Wind Load Paths on Wood Buildings

Ioannis G. Zisis

A Thesis
In the Department
of
Building, Civil and Environmental Engineering

Presented in Partial Fulfillment of the Requirements
For the Degree of
Doctor of Philosophy (Building Engineering) at
Concordia University
Montreal, Quebec, Canada

September 2011

CONCORDIA UNIVERSITY
SCHOOL OF GRADUATE STUDIES

This is to certify that the thesis prepared

By: Ioannis Zisis

Entitled: Wind Load Paths on Wood Buildings

and submitted in partial fulfillment of the requirements for the degree of

Doctor of Philosophy (Building Engineering)

complies with the regulations of the University and meets the accepted standards with respect to originality and quality.

Signed by the final examining committee:

Dr. W. Ghaly — Chair

Dr. Gregory Kopp — External Examiner

Dr. George Vatistas — External to Program

Dr. Ashutosh Bagchi — Examiner

Dr. Lucia Tirca — Examiner

Dr. Ted Stathopoulos — Thesis Supervisor

Approved by

Chair of Department or Graduate Program Director

Dean of Faculty

ABSTRACT

Wind load paths on wood buildings

Ioannis G. Zisis, PhD.

Concordia University, 2011

Wind-induced natural disasters have been frequently reported as some of the most fatal and costly catastrophes. Of particular intensity was the disastrous effect on low-rise residential properties that suffered in several cases from a complete damage. The intense research efforts of the wind engineering community contributed significantly towards the development of more complex yet safer wind standards and building codes of practice. Numerous studies have been carried out focusing on the estimation of wind-induced envelope pressures using in most cases wind tunnel experimental techniques and less often field studies. A key component that has not yet been investigated adequately is the flow of wind-induced forces through the structural system and their attenuation due to dynamic and other structural aspects of light frame construction.

The field monitoring of a low-rise wood building provided valuable information related to its wind-induced structural response. The building was equipped with a state-of-the-art data acquisition system to monitor weather, pressure and force data. In addition, detailed wind tunnel tests on a scaled model and finite element analysis were used to study the wind effects in a simulated environment.

Despite the vast amount of field data that were acquired, only a limited number was qualified as stationary and considered for further interpretation. The analysis revealed a

non-uniform upstream exposure which was incorporated in the wind tunnel experiments and improved the agreement between the two experimental approaches. Of particular importance were the findings related to wind-induced uplift force distribution, especially those related to the attenuation of the wind load. For this analysis, data from pressure taps and foundation load cells were considered and incorporated in the finite element analysis. A significant reduction was identified as the wind-induced load is transferred through structural and non-structural elements to the foundation level. This attenuation was evident in the field data but was not predicted by finite element analysis, indicating that wind design practices based on static analysis of structural systems will tend to conservatively estimate actual building performances. Another interesting finding was that the wind load is transferred predominantly to the two side walls whereas the end walls have a significantly smaller contribution. Last but not least, the comparisons of the findings to current wind provisions, such as ASCE 7 and NBCC, revealed that in certain cases the recommended by the standards values could underestimate the total uplift wind force.

ACKNOWLEDGEMENTS

During the course of my graduate studies, I was fortunate to be advised by an excellent researcher and mentored by a wonderful teacher. My greatest appreciation goes to my supervisor Dr. Ted Stathopoulos.

I would also like to dedicate this dissertation to my family. Their endless support and love throughout the years kept me motivated and helped me succeed in my endeavors.

The guidance and support from Dr. Ian Smith and Dr. Ghasan Doudak was of great importance for the completion of this work. Many thanks are due to my dear friends and colleagues as well as the lab technicians at Concordia University and University of New Brunswick.

Last but not least, I would like to thank Yen for her unconditional encouragement, support and patience.

There is a continuing need to maintain an adequate source of full-scale data so that new theories and modelling procedures can be tested. Such data should preferably include results from experiments on several structures so as to reduce the uncertainty. Conclusions reached from an ensemble of full-scale experiments are likely to be of significantly greater value than those reached from any individual experiment. The sharing of full-scale data should be encouraged.

Alan G. Davenport (1975)

TABLE OF CONTENTS

LIST OF FIGURES

LIST OF TABLES

NOMENCLATURE

A	Projected area of the building	(m^2)
$A_{eff,i}$	Effective roof pressure tap area	(m^2)
c_f	Force coefficient	
$c_{f,max}$	Maximum force coefficient	
$c_{f,mean}$	Mean force coefficient	
$c_{f,min}$	Minimum force coefficient	
$c_{f,peak}$	Peak force coefficient	
$c_{f,rms}$	Root mean square force coefficient	
$c_{f,z}$	Total uplift force coefficient	
c_g	Gust coefficient	
c_p	Pressure coefficient	
$c_{p,max}$	Maximum pressure coefficient	
$c_{p,mean}$	Mean pressure coefficient	
$c_{p,min}$	Minimum pressure coefficient	
$c_{p,peak}$	Peak pressure coefficient	
$c_{p,rms}$	Root mean square pressure coefficient	
F	Wind-induced force	(N)
H	Height	(m)
$I(z)$	Longitudinal turbulence intensity	
k	Von Karman constant	
L	Length	(m)
L_u^x	Longitudinal scale of turbulence	(m)

p_a	Atmospheric pressure	(Pa)
p_i	Internal pressure	(Pa)
p_{mean}	Mean pressure	(Pa)
p_{peak}	Peak pressure	(Pa)
p_{rms}	Root mean square pressure	(Pa)
p_s	Stagnation pressure	(Pa)
$R_u(\tau)$	Auto-covariance function	
$R_{xx}(\tau)$	Autocorrelation function	
$R_{xy}(\tau)$	Crosscorrelation function	
s_x^2	Variance	
S(n)	Spectrum of wind turbulence	
$\overline{V}(z)$	Constant component of the wind speed	(m/s)
V(t)	Fluctuating component of the wind speed	(m/s)
V*	Friction velocity	(m/s)
V, V_i	Wind speed at any height z_i	(m/s)
V_g	Gradient wind speed	(m/s)
W	Width	(m)
$\overline{x^2}$	Mean square value	
$\bar{x}$	Mean value	
z_o	Roughness length	(m)
α	Power law exponent	
δ	Atmospheric boundary layer thickness	(m)
ρ	Air density	(kg/m^3)
σ_x	Standard deviation	

CHAPTER 1
INTRODUCTION

1.1 Overview

The majority of residential construction in North America is based on wood products. As a result, common dwelling houses are light-weight, low-rise structures of simple geometry and layout. Construction techniques also show many similarities, especially for older construction that followed prescriptive rather than performance based code guidelines. The proper design of this broad group of structures is of major significance, first for the safety of the occupants and then for the nation's economy.

The characteristics of these light-weight structures make them vulnerable to high winds. Design codes have been revised numerous times the past few decades, resulting into a more complex yet safer and more economical design process. Recent extreme wind events and growth of wind-related losses indicates that this process still needs further refinement and attention. In addition, the concept of efficient design is no longer a conceptual process for wind engineers. The demand to reduce costs at every possible stage, including the design stage, is more pronounced than ever. Wind-structure interaction and wind-induced loads must be examined and studied extensively in order to achieve that level of detail and confidence, required for the safe and efficient design of low-rise structures.

1.2 Safety and Cost

Wind engineering research is, unfortunately, closely related to tragic events. The past few decades several wind related catastrophes initiated long lasting studies and resulted in the revision of building codes. Unfortunate events have been evaluated mainly by insurance agencies and the numbers show a significant amount of losses. Both tornado and hurricane events caused extensive house damages the past ten years. The frequency of occurrence of these events creates even more concerns and the up to date available data indicate a significant increase of damages (see Figure 1.1). The insured losses in the United States for 2006 were more than 8 billion dollars (A.M. Best 2007), the highest amount ever recorded, with an average property/casualty claims of 4.9 billion dollars for the period 2001 to 2007. Moreover, the same report indicated that the 57% of losses due to natural catastrophes since 1953 are related to extreme wind effects. These numbers are significantly higher if actual (not insured) losses are considered, reaching the 150 billion dollars for the period 2004-2005 (Pielke et al. 2008).

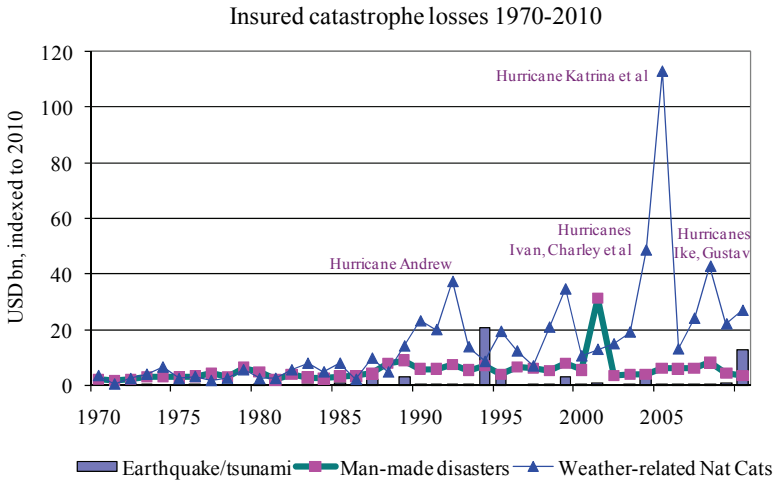

Figure 1.1 Insured losses from weather-related and other catastrophes (modified from Sigma -Swiss Re 2010).

1.3 Full-Scale Studies and Wind Load Paths Concept

Wind effects on buildings have been examined extensively the past few decades. The availability of boundary layer wind tunnels had also significant influence to the current wind standards. In addition, several full-scale studies were carried out and contributed in the verification process of the simulation studies. The potential of wind-structure interaction through full-scale studies was acknowledged and proposed by researchers as the most reliable tool to validate wind tunnel experiments (e.g. Davenport 1975 and 2002 - see Figure 1.2).

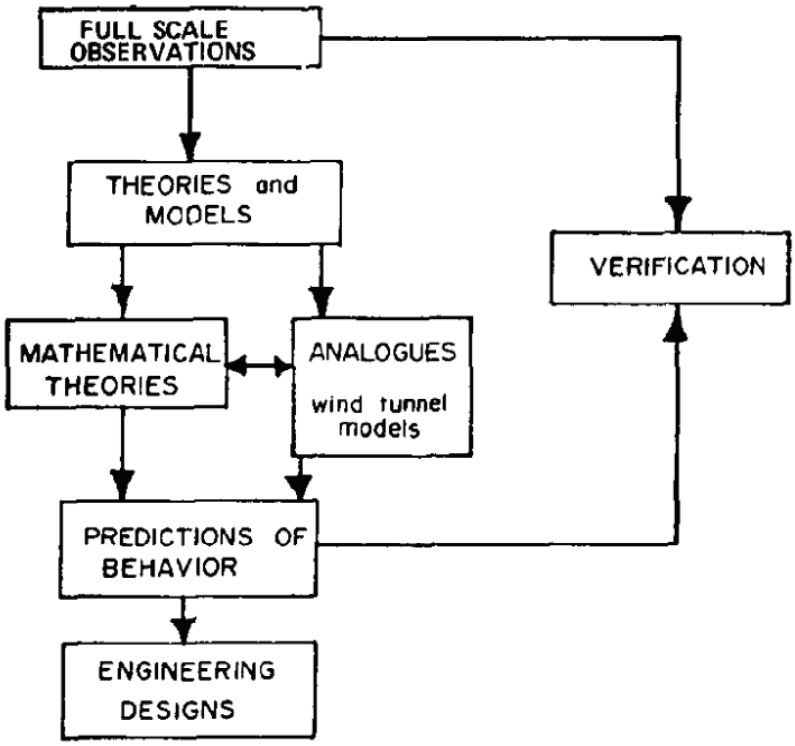

Figure 1.2 The scientific method to study wind-induced loading (reprinted from Davenport 1975).

The NSERC Collaborative Research and Development (CRD) Project "Load Paths in Wood Buildings" (2002-2006) and "Engineering Design of Low-Rise Wood Buildings" (2006-2009) awarded to a consortium of Canadian Universities including Concordia, entails the monitoring and collection of data from three light frame wood buildings to assess the application of environmental loads and their actual transferring through the buildings' elements to their foundation. Structure 1 is an existing industrial single-storey, light-frame shed located in Saint Foy, Quebec and owned by Forintek Canada Corp (currently FPInnovation). This shed was monitored for wind pressures and structural responses to natural, as well as artificial loading, since 2000 (Doudak 2005 and Doudak et al. 2005). Structure 2 has been constructed in Fredericton, New Brunswick and is the case study for this thesis. Structure 3 is a single-storey, light-frame building with post frame construction and duo-pitch roof in Winnipeg, Manitoba.

This study aims to determine how wind-induced loads affect a typical wood building. Understanding the interaction between the wind load and the structure is considered critical in the evaluation of wind load paths in buildings. Full-scale measurements on Structure 2, wind tunnel studies and numerical analysis are used to understand and define the nature of this complex subject. Through this study, the importance of the wind-induced pressure acting on the surface of a building will be examined, i.e. how this pressure is distributed on the structure and, finally, how the structural system resists to the applied load.

1.4 Research Objectives

The research objectives of this thesis are the following:

- Examine and identify the actual wind load paths.
- Identify and quantify the concept of structural attenuation of the wind-induced load.
- Better understand wind-induced structural response of low-rise buildings through full-scale monitoring.
- Compare the experimental and numerical findings to those proposed by current wind standards and building codes of practice.
- Increase confidence of simulation studies and validate the results through full-scale experiments.
- Develop a detailed numerical model to be used in accordance to wind tunnel findings and accurately simulate available full-scale scenarios.

1.5 Thesis Outline

The thesis consists of seven chapters. Following the introduction, a comprehensive review of full-scale pressure and structural monitoring studies is discussed. Then, in Chapter 3 some necessary theoretical background related to the current study is presented. In Chapter 4, a detailed description of the research tools is provided, including all three major elements of this study; i.e. full-scale facilities, wind tunnel experiments and finite element modeling. Some important experimental- and methodology-related verifications are described in Chapter 5 followed by the research findings and their critical discussion in Chapter 6. Last but not least, the conclusions along with the contributions and some recommendations for future work are closing the thesis.

CHAPTER 2
PAST STUDIES

2.1 Introduction

Wind engineering is a relatively recent field of study and has as one of its main objectives to examine the wind-structure interaction. It is closely related to meteorological and statistical sciences and structural engineering. These disciplines are some of the tools wind engineers use to study how wind action will affect structural integrity and human safety and comfort. Over the past 60 years, following Jensen (1958) and Jensen and Franck (1965) and his first attempts to perform experiments in boundary layer wind tunnels, the wind engineering community has grown rapidly and tremendous advancement has been achieved. One of the most important contributions of this discipline is the development and continuous revision of wind related building standards.

Most of the code-related studies have been established on a wind tunnel basis (Stathopoulos 1984). The validation of the simulated tests, the increase of confidence, the availability of advanced instrumentation and recent extreme wind events lead researchers into field studies. The time and cost difficulties related to full-scale experiments are the main reasons for the limited number of such studies. In addition, the majority of these projects focused either to wind-terrain characteristics or wind-induced pressures on buildings. Attempts to directly monitor wind-induced stresses on structural systems are limited and the quality in some cases is questionable (Mehta 2004).

In the following sections a critical description of full-scale experimental studies followed by wind tunnel simulations will be presented. The classification is based on each study's initiation year - considering those that were initiated after the 1950's - and attention is paid mainly to complete structure projects rather than structural component testing.

2.2 National Bureau of Standards (US)

One of the very first attempts to evaluate wind pressures through full-scale tests was made by Marshall (1975 and 1977). A low-rise rectangular shape dwelling located at Malmstorm (Montana, US) was instrumented with ten pressure taps and weather monitoring equipment. In addition to the field tests, scaled models were tested in wind tunnels (Marshall 1975, Tieleman et al 1978, Roy 1983) at Colorado State University, University of Western Ontario and James Cook University.

Although the full-scale tests were compromised by limited instrumentation and problematic configuration (reference pressure on top of the building), the findings provided wind engineers valuable information regarding full-scale tests and proper simulation of the terrain in wind tunnel tests. Surry and Johnson (1986) discuss in detail the strengths and weaknesses of the particular full-scale study as well as some of the supporting wind tunnel simulation efforts.

2.3 The Aylesbury Experiment

A very important and detailed study carried out on a full-scale low-rise structure was the Aylesbury project. This study started in the 1970s, following a series of full-scale

wind pressure measurements on tall buildings, and the data collected were used and compared with wind tunnel studies for nearly three decades. The test building was a two-storey house, located in Aylesbury, UK. It was a rectangular-shaped building (13.0 x 7.0 meters) and had a variable pitch roof ranging from 5 to 45 degrees. Details of the full-scale experiments are presented by Eaton and Mayne (1975).

Full-scale data were collected by the Building Research Establishment (BRE-UK). In addition to the experimental house, other similar houses in the proximity were instrumented in order to compare the effect of terrain variation on the pressure measurements. The experimental house was equipped with 72 transducers and 12 load cells. The frequency response of the transducers used was up to 32 Hz. The ambient atmospheric pressure was the reference for the differential pressure transducers and the location of the reference pressure manhole was approximately 80 meters east of the house.

The first wind tunnel simulation results of the Aylesbury house were presented in the late 70's (Holmes and Best 1978, Apperley et. al. 1979). The latter tests were conducted at the UWO boundary layer wind tunnel using a 1:500 scale model. Several discrepancies between full-scale and wind tunnel mean and peak pressure coefficients were found (see Figure 2.1). The authors presented discrepancies even between two full-scale records with similar wind conditions. Most importantly, these tests revealed the importance of accurate terrain simulation, which proved to be key variable for successful comparison between full-scale and wind tunnel results.

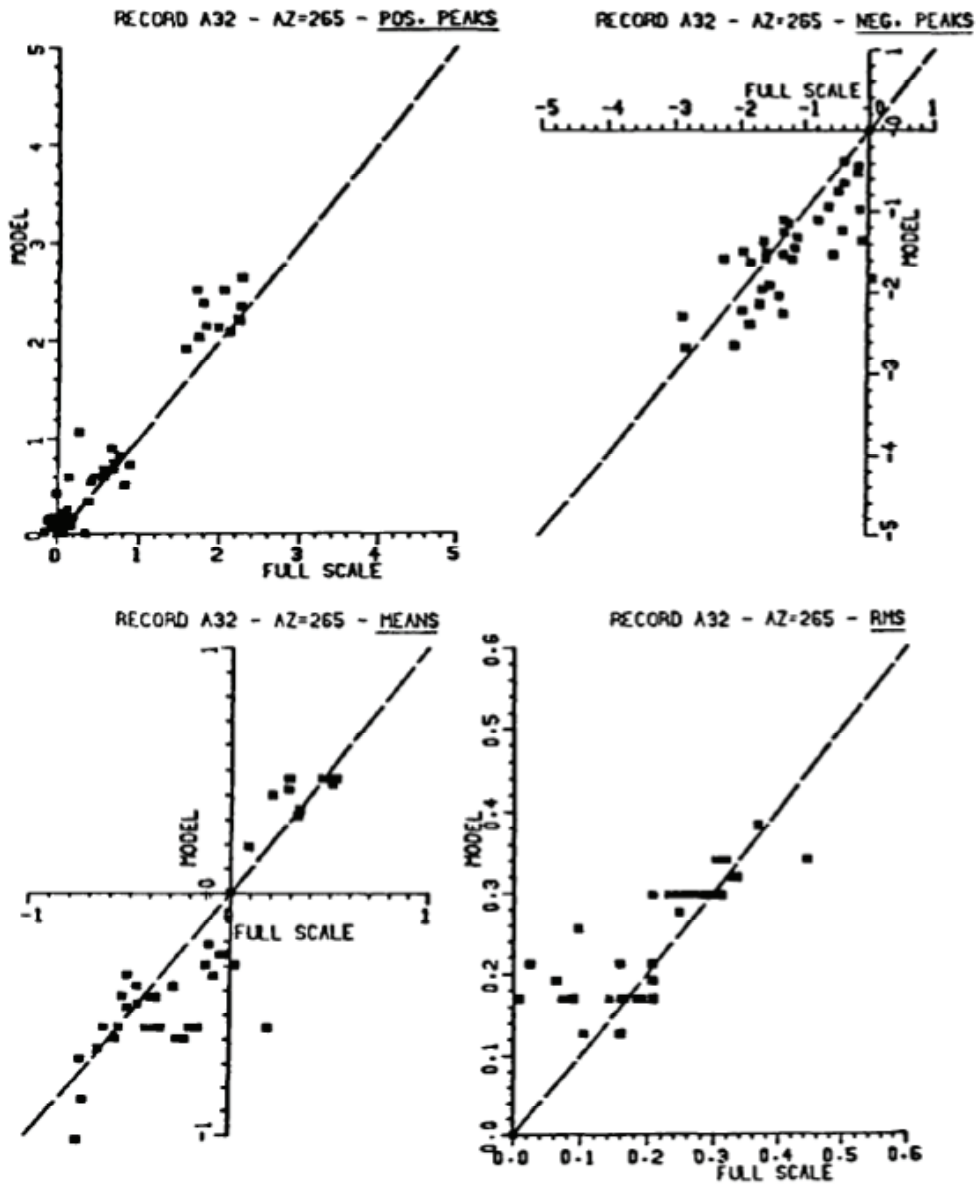

Figure 2.1 Comparison of wind tunnel and full-scale peak, mean and rms pressure coefficients for roof slope 22.5 degrees (reprinted from Apperley et. al. 1979).

Additional wind tunnel tests were carried out for almost a decade by several laboratories (Vickery and Surry 1983, Hansen and Sorensen 1985, Mousset 1986) followed by the Aylesbury Comparative Experiment (Sill et al. 1989 and 1992). This study compared full-scale measurements with wind tunnel results from 17 different

laboratories. The most important outcome of this comparison was the problematic behaviour of the reference static pressure box location and construction. This was found to be the main reason for the differences between the model scale and the full-scale results. Another interesting point of this experiment was the discrepancies of the results between the different wind tunnel studies, which for some cases were up to 40% (mean pressure coefficients).

It appears that the Aylesbury project was the forerunner for the wind pressure monitoring in full-scale low rise buildings. The location of the reference static pressure box in the full-scale house was the weakest point of this study. The interpretation and analysis of the full-scale and model scale data was also another reason for the discrepancy between the results, especially for the peak pressures. Finally, it should be mentioned that although the Aylesbury building was instrumented with load cells at both foundation and roof level no results were ever presented or published corresponding to this instrumentation.

2.4 The Texas Tech University Project (TTU)

The Texas Tech University performed extensive experiments on more than one full-scale structure. The first experimental effort was performed in the late 70's on a flat roof box-shaped building located in an open field (Kim and Mehta 1977). The building had external dimensions of 4.9 x 4.9 x 3.0 meters (16 x 16 x 10 ft) and was equipped with roof load cells which were used to measure the roof uplift forces. The findings indicated that the normalized wind speed and wind-induced load spectra showed high similarities.

The authors proposed a statistical model to predict peak roof loads which was also compared to design standards, a wind tunnel test and a previous full-scale experiment.

The second and significantly more extensive project initiated in the 1980s and had as main objective to extract accurate field data that describe the wind distribution on the surface of a low rise building and define the appropriate terrain characteristics for proper simulation in boundary layer wind tunnels (Ng 1990 and Levitan et. al. 1990).

The Wind Engineering Research Field Laboratory (WERFL) was constructed in Lubbock, Texas and was equipped with state-of-the-art instruments. In addition to the actual house, a meteorological tower was also recording weather data at various heights. The prefabricated metal house had a rectangular shape with external dimensions of 9.1 x 13.7 x 4.0 meters (B x L x H). The roof was almost flat and the building was resting on a concrete slab. A very interesting and unique characteristic of the facility was the unrestrained base which allowed the rotation of the building to any desired orientation. The researchers could easily adjust the direction of the house based on the approaching wind. Initially the building was instrumented with 40 pressure taps (Levitan et al. 1990) but the following years the monitoring equipment was upgraded significantly (Levitan and Mehta 1992 - Part I and Part II). The reference pressure for the measurements was the ambient atmospheric pressure. As mentioned previously, this was one of the main problems for other full-scale studies. For this particular study, a box below ground was used. This box had a lid with a small hole and was placed 23 meters west of the center of the test building. Special attention was given to the location of the reference pressure box to avoid any influence of the wind flow by the building.

During the first years of the project, a significant amount of time was spent on the verification of the data acquisition system. The majority of the early publications dealt with data quality issues and improvement of the monitoring techniques i.e. some frequency related sampling methods (Ng 1990, Levitan et al 1991, Letchford et al. 1992).

The acquisition of the early full-scale data (Levitan et al 1990 and 1991, Letchford et al 1992, Mehta et al 1992) triggered a number of wind tunnel studies, starting with Surry at University of Western Ontario (1991) and followed by Cochran and Cermak (1992), Okada and Ha (1992) and Bienkiewicz and Sun (1992). In the years following these studies additional wind tunnel tests have been carried out addressing various issues related to full-scale measurements (Lin et al. 1995, Cheung et al 1997, Tieleman et al 1998). The majority of all simulation attempts can be summarized as follows: the mean pressure distribution was accurately predicted by wind tunnel studies for all examined wind angles of attack. The positive pressure coefficients comparison between full-scale and wind tunnel results showed also satisfactory agreement. The negative peak pressure results was the only significantly varied component of the full-scale studies and in most wind tunnel tests was underestimated (see Figure 2.2). The discrepancies were higher for corner and ridge regions, where studies addressed factors up to two between full-scale and wind tunnel values (Cochran and Cermak 1992, Bienkiewicz and Sun 1992). Initially the differences were attributed to unsuccessful simulation of the terrain characteristics (mainly turbulence), non-stationarity of full-scale data (Surry 1991) and frequency related issues during full-scale and wind tunnel sampling (Cochran and Cermak 1992). Contrary to these conclusions, a later study that followed an eigenvector analysis approach concluded that the discrepancies should not be attributed to instrumentation, peak

pressure definition or selective isolation of peaks and suggested that further investigation and analytical work is required (Letchford and Mehta 1993).

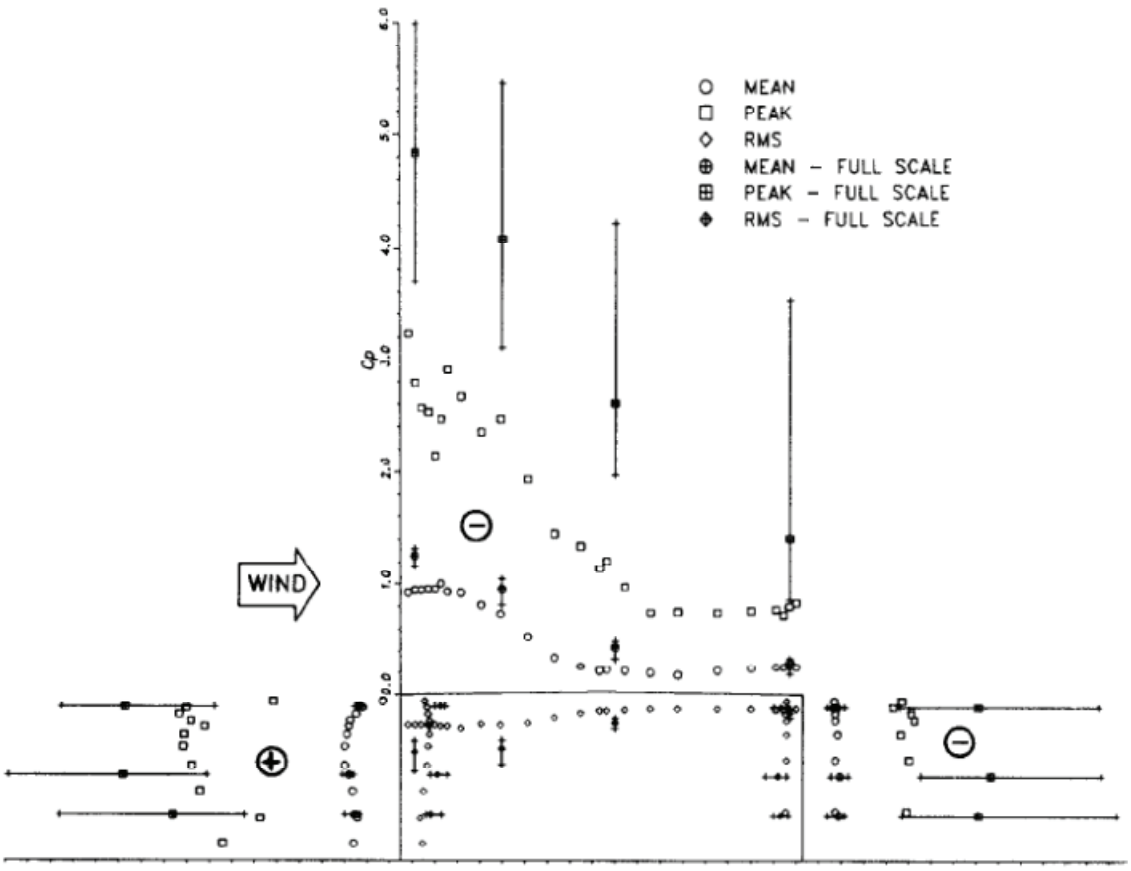

Figure 2.2 Comparison of wind tunnel and full-scale mean, peak and rms pressure coefficients for oblique wind direction (reprinted from Surry 1991).

Further studies after 1995 (Lin et al. 1995, Cheung et al 1997, Tieleman et al 1998, Ham and Bienkiewicz 1998, Endo et al. 2006) attempted to justify the discrepancies on the peak pressure results. These studies experimented with various terrain configurations and managed to reduce the span between full-scale and wind tunnel studies.

The availability of a large number of field data made also possible the completion of several other studies related to data handling and analysis techniques (Letchford et al 1993), internal pressures (Yeatts and Mehta 1993, Smith et al 1994, Ginger et al. 1997, Sharma and Richards 2003), net pressures (Ginger and Letchford 1999, Ginger 2000) and development of design databases (Chen et al 2003, Ho et al 2005).

Of greater interest to the current study were the efforts to evaluate the overall wind load on the structural system of the test building (Fagan 2001). Although the building was instrumented with four load cells only overall results integrated for all strain gages were reported. The individual traces of each cell were contaminated with noise and other temperature-related effects and this was one of the main drawbacks of this study. The use of ARX system identification models provided some valuable insight to the wind-induced response of the test building. A very interesting outcome from the specific study was that no attenuation of wind-induced forces occurs for frequencies less than 0.05 Hz (Fagan et al 2001).

2.5 The Silsoe Structures

Another important project, connecting full-scale with model-scale studies, started in the Silsoe Research Institute (formerly AFRC Institute of Engineering Research) in the late 1980's (Robertson and Glass 1988). Although there was more than one instrumented building, the main test structure was the Silsoe experimental building located at the Silsoe Institute, Wrest Park, Silsoe, UK on a relatively open field site. This building was designed specifically for wind load monitoring, including both pressure taps and strain gages (Hoxey 1991). A basic characteristic of the building was the choice of curved or

sharp eave detail configuration. The house was steel framed and clad structure of rectangular shape, 24.0 meters long by 13.9 meters wide and the ridge height was 5.3 meters. The duo pitch roof had a 10-degree inclination.

The researchers, having already the experience of previous full-scale studies and knowing the problems created by the reference static pressure box location, decided to mount the reference pressure probe 20 meters upstream of the house at the same height with the ridge. This distance and position assured that the influence of the building was negligible. Some of the later studies evaluated this assumption by performing detailed analysis of wind velocity data (Hoxey and Richards 1992, 1993) and tried to correlate the measurements from the probe with various wind tunnel simulations (location of static and dynamic reference pressure - Richardson and Surry 1992).

Field data were used extensively for wind velocity and upstream terrain analysis (Hoxey and Richards 1992 and 1993, Richardson and Surry 1992, Richardson and Blackmore 1995, Dalley 1996). These studies focused on the characteristics of boundary layer and its effect to the wind tunnel tests. The full-scale measurements were also supported by several wind tunnel studies (Richardson and Surry 1991, 1992 and 1994, Richards and Hoxey 1992, Richardson and Blackmore 1995, Dalley 1996, Richardson et al. 1997). The most extensive data analysis and comparison was mainly conducted from tests at the UWO and the BRE wind tunnel facilities. Two models were constructed at the BRE, one with curved and one with sharp eaves. Both models were made at a 1:100 geometric scale. The same models but with different tubing sensor systems were used for both studies at UWO and BRE wind tunnels. The curved-eave model had a total of 81 pressure taps and the sharp-eave model had a total of 74 pressure taps. For both tests,

special attention was paid to the accurate simulation of the upstream terrain characteristics and different tests covered a number of upstream terrain configurations.

Most of the comparisons referred mainly to the mean pressure coefficients and in several cases a spectral approach was selected. Moreover several references (Richardson and Surry 1991 and 1992, Richards and Hoxey 1992, Richardson and Blackmore 1995, Richardson et. al. 1997) mentioned that the flow separation and recirculation cannot be properly simulated in the wind tunnel tests resulting in underestimation of mean pressure coefficient especially in corner roof regions (see Figure 2.3). In agreement to previous studies, peak pressure coefficient comparisons are also problematic for certain wind directions.

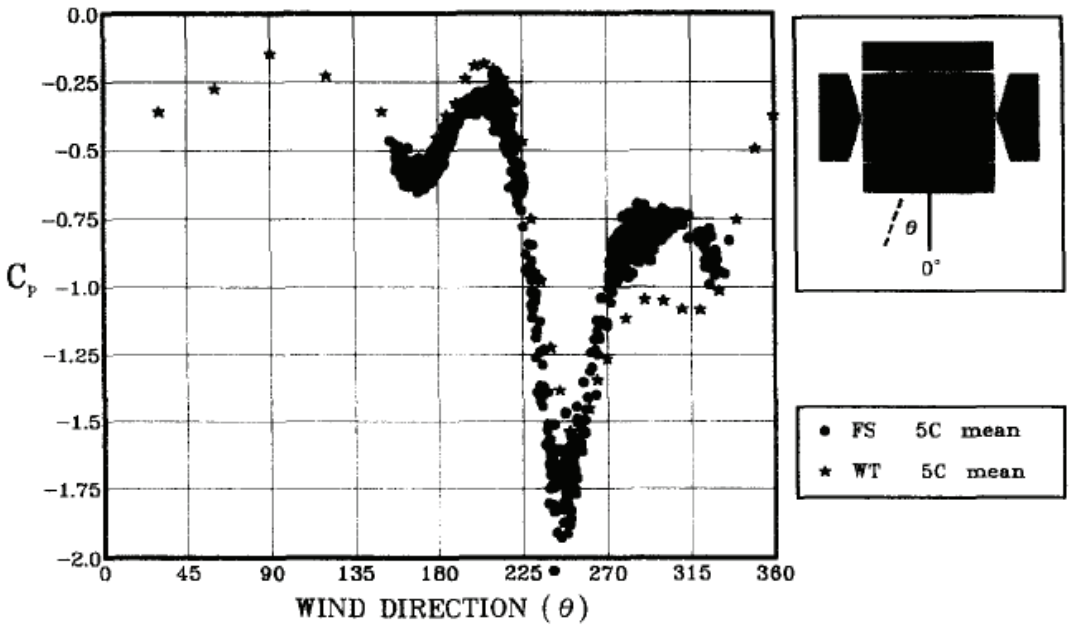

Figure 2.3 Comparison of mean pressure coefficients for a gable-end tap in Silsoe structure (after Richardson and Blackmore 1995).

The Silsoe building was also equipped with strain gages but only one study presented results from such experiments (Hoxey 1991). This study used both pressure and strain measurements from the mid-building-length frame and evaluated the applicability of quasi-static design approach and the importance of the base fixity conditions during modeling. The preliminary results showed that the quasi-static method could lead into proper design with the wall-to-foundation restraint conditions playing a significant role into the successful verification of this method. Other studies, using only pressure measurements, evaluated the quasi-static method and concluded in similar outcomes with additional comments related to power attenuation phenomena in the mid-frequency range (Hoxey and Richards 1995).

The experience gained through this study was significant, not only for the full-scale but for the wind tunnel tests as well. Many of the full-scale results, especially for the mean pressure coefficients, were in good agreement with the simulated tests. Finally, CFD studies were also carried out and results were compared to the available field data (Richards and Hoxey 1992, Hoxey and Richards 1993).

In addition to the Silsoe Structure, the Silsoe Cube was another full-scale experimental structure that was used to monitor the wind-induced pressures on its envelope (Richards et al. 2001). The 6-meter cube was placed in an open terrain exposure and was instrumented with several pressure taps. The simplified geometry of the building made possible the comparison of the field data to various wind tunnel studies of cubic models. The results of the field and simulation studies were discussed by Richards et al. (2001) and Hoxey et al. (2002). In general the agreement was found to be satisfactory, with some discrepancies to occur for wind directions perpendicular to a face. These discrepancies

were mainly attributed to the flow properties (i.e. Reynolds number and flow reattachment). Moreover, this study was used for validation of computational simulation (Richards et al. 2002 and Lim et al. 2009).

2.6 Southern Shores Project (North Carolina)

One more interesting study, started in 2000, is the Southern Shores project. An existing residential building located in the town of South Shores (North Carolina) was selected for full-scale monitoring. The two-storey building has a relatively complex geometry and is instrumented with meteorological, pressure, strain and deformation transducers (see Figure 2.4). The focus of this project was mainly to examine extreme wind effects, therefore the pressure equipment was selected based on a large dynamic range criterion. As a result, low wind monitoring was practically impossible (Caracoglia and Jones 2004). It should also be noted that the instrumentation was mainly located on the second floor and the southeast corner of the house. That specific location was chosen because of the steel framed construction and the less complex characteristics of the upstream terrain. Details of the building and the instrumentation used can be found in Porterfield and Jones (2001).

The field monitoring started in 1997 and during the first three years more than 8000 records were available, including three hurricane events (Bonnie, Dennis and Floyd). More recently published papers (Caracoglia et al. 2008, Caracoglia and Jones 2009) present results from the analysis of the above records and comparisons with current wind provisions. The findings showed a reasonable agreement for the walls and higher discrepancies for the roof pressure taps (see Figure 2.5). In addition to the pressure

coefficient detailed comparisons, the authors performed a simplified model analysis and compared stress and deformation findings with simulation results. The discrepancies of the later comparison were justified by the modeling simplifications, the definition of tributary areas and the averaging method of local pressures.

This study, which has not been supported by any wind tunnel tests up to this date, presents significant pressure and load findings during hurricane events. The complexity of the geometry and topography along with the limitation on the number of transducers and strain gages are considered as the main difficulties in the data interpretation process.

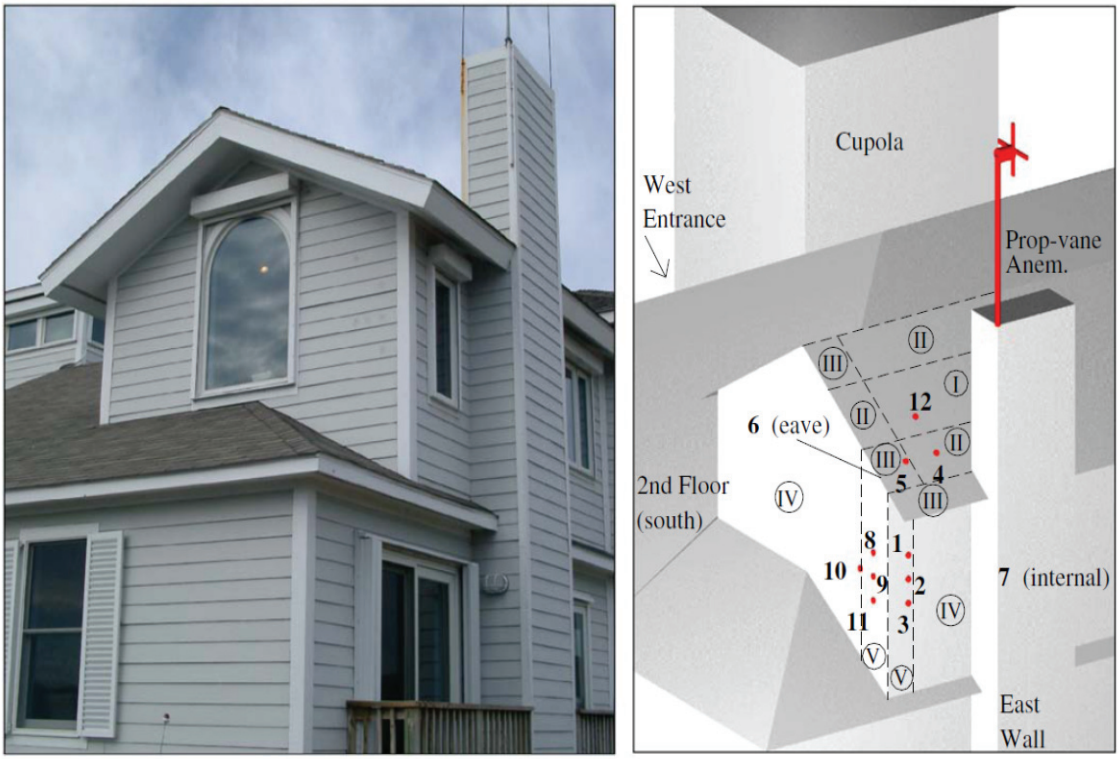

Figure 2.4 Test building and location of roof pressure taps (after Caracoglia and Jones 2009).

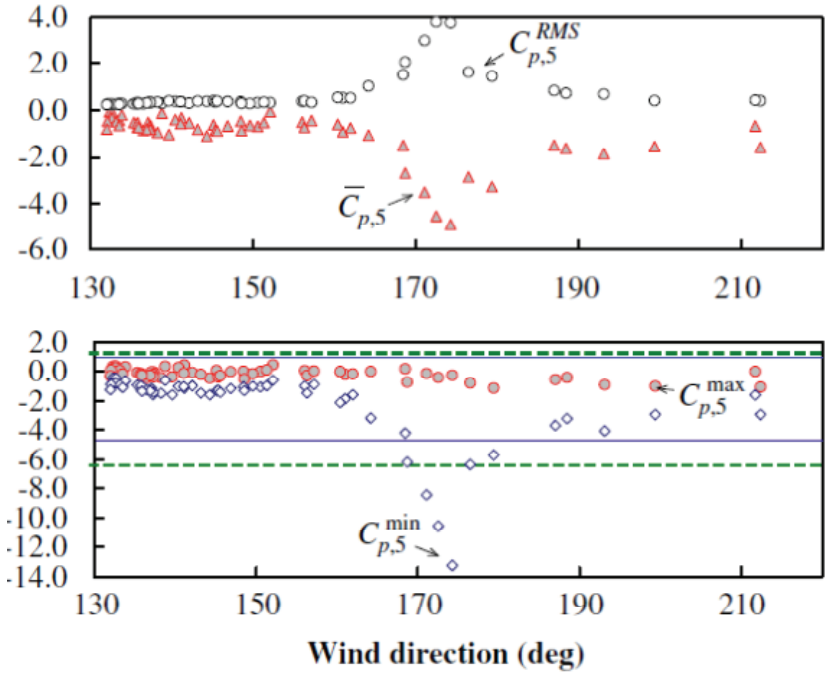

Figure 2.5 Mean, RMS and peak Cp's for a roof pressure tap ($C_{p,5}$, tap 5) and ASCE-7 predictions (after Caracoglia and Jones 2009).

2.7 Florida Coastal Monitoring Program (FCMP)

The Florida Coastal Monitoring Program is a collaborative project started in 1998. The participants are Clemson University, University of Florida, Florida International University, Florida Institute of Technology and Institute for Business and Home Safety. The objectives of this project are to collect field wind speed and pressure data and compare them to scale model test results. Of great interest to the research team is to track hurricane events and record data during extreme wind phenomena. Moreover, an evaluation of current construction practices and building codes is attempted through a damage assessment process after major hurricane events.

The project makes use of six mobile tower systems that are able to monitor detailed weather data (wind speed, direction, temperature, atmospheric pressure etc.). Results related to the wind field were presented by Yu et al. (2008) and Masters et al. (2010). In addition, a large number of occupied residences are instrumented with pressure monitoring equipment. These houses are located in Florida (thirty two) and in North and South Carolina (six). The location of the pressure taps was chosen based on expected higher suction regions on the roof. Details of weather and pressure instrumentation as well as results related to the pressure measurements have been reported in several sources (Dearhart 2003, Aponte-Bermoudez 2006, Datin et al. 2006, Liu 2006, Liu et al. 2009).

The field collected data were supported by wind tunnel tests conducted at Clemson University. A test model of 1:50 geometric scale of one of the instrumented houses (FL27 – see Figure 2.6) was tested and preliminary results were presented by Datin et al. (2006) and Liu et al. (2009). The conclusions of these articles can be summarized as follows; mean and RMS pressure coefficients from field and wind tunnel tests are in very good agreement. Similar to some past studies, positive and negative peak pressure coefficients are consistently underestimated by wind tunnel simulation (Figure 2.7). The experimental findings were also compared to the recommended by ASCE 7 values concluding that the standard may provide non-conservative values for peak uplift local loads, i.e. Components and Cladding (Aponte Bermoudez 2006, Liu et al. 2009).

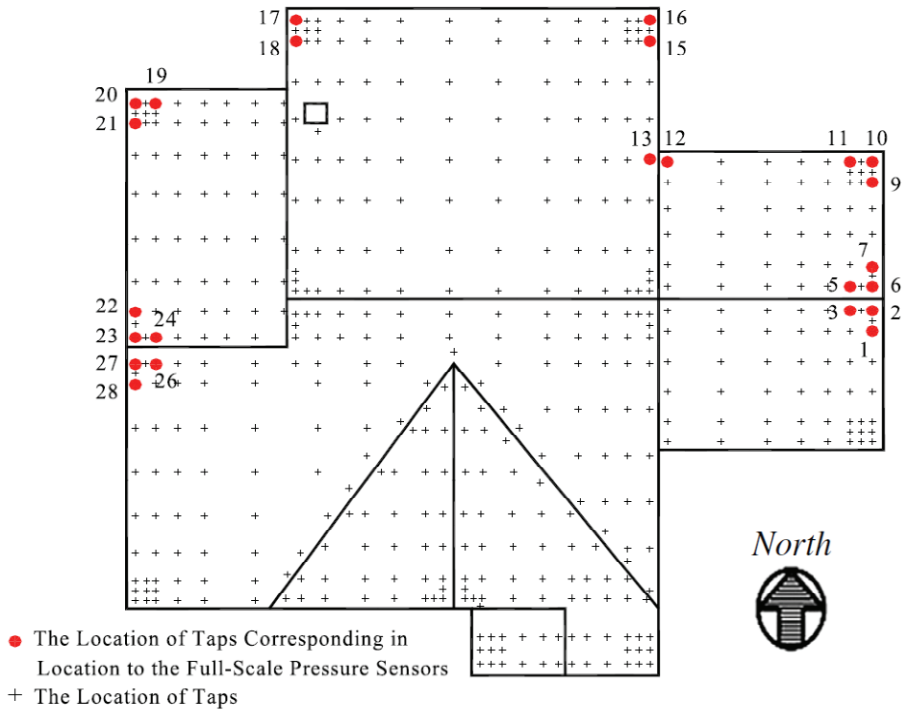

Figure 2.6 Plan view of wind tunnel model indicating the position of the roof pressure taps (after Liu et al. 2009).

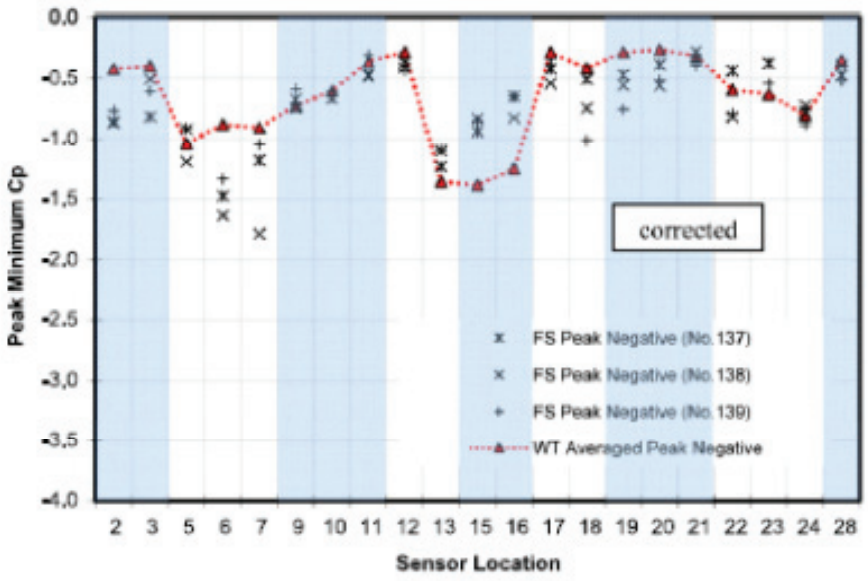

Figure 2.7 Negative peak Cp's for full-scale monitoring and wind tunnel tests (after Liu et al. 2009).

2.8 The Load Paths Project (Structure 1 - Saint Foy QC)

This study is part of an NSERC Collaborative Research and Development (CRD) project and refers to the first of the three wooden structures tested since 2000. The test structure is an existing industrial single storey, light frame shed, located in Saint Foy, Quebec and owned by Forintek Canada Corporation (currently FPInnovations). This building is a typical storage shed, constructed in 1998 (Figure 2.8). It has a rectangular plan with external dimensions of 8.0 by 15.0 meters. The roof is flat and has a height of 5.1 meters with a 0.5 meters high parapet.

The area surrounding the building consists mainly of similar low-rise storage and industrial buildings and low dense plantation. The test building is equipped with 20 pressure taps, 14 of which located on the walls and the rest on the roof. The pressure taps are connected with differential pressure transducers, which were calibrated at the Building Aerodynamics Laboratory of Concordia University. The ambient atmospheric pressure was used as reference pressure for the transducers and it was measured in a box located about 25 meters from the test building. The shed is also equipped with Linear Variable Displacement Transducers (LVDT) that can measure the displacements of the structure at desired key points. Meteorological data have been collected by a weather station close to the south-west face of the building. The station is equipped with a propeller anemometer, mounted at 10 meters above the ground. In addition to this station, data are also provided by two other stations; the local airport, located west of the building site and Laval's University weather station.

Figure 2.8 Experimental structure located in Saint Foy, QC (after Doudak et al. 2005).

Wind pressure records have been collected but only for a few wind directions. The lack of high winds for other directions made the collection of more pressure data almost impossible. Mean and peak pressure coefficients were calculated and compared to the wind tunnel test results.

The model scale tests were conducted at the Building Aerodynamics Laboratory of Concordia University. The 1:200 building model was equipped with 20 pressure taps located at the same points as the full-scale structure. A surroundings model was also constructed and the upstream terrain characteristics were simulated based on the full-scale wind data. Wind tunnel data were obtained for more than 15 directions using an interval of 10-15 degrees. The data were recorded at a frequency of 250 Hz. Mean and peak wind tunnel pressure coefficients showed good agreement with corresponding full-scale results. A typical comparison record is presented in Figure 2.9.

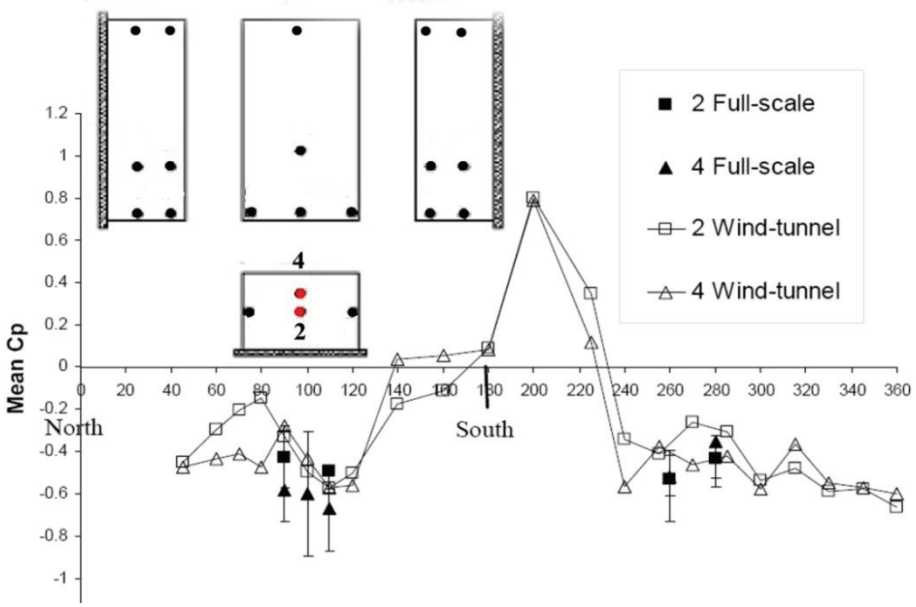

Figure 2.9 Comparison of full-scale and wind tunnel results (reprinted from Doudak 2005).

A finite element model was also prepared and used for comparison with the full and model-scale results. The outcomes of this study are presented in detail by Doudak (2005), Doudak et al. (2005) and Doudak et al. (2009).

2.9 International Hurricane Research Center and Florida International University

One more hurricane-related project has been initiated by the International Hurricane Research Center (IHRC) and Florida International University in 2003. The two partners suggested that the demand of a full-scale testing facility reproducing controlled but realistic hurricane events could be fulfilled under a reasonable cost (Leatherman et al. 2007). This effort created the Wall of Wind (WoW) testing apparatus that in

collaboration with the FCMP project is aiming to reproduce the wind field characteristics acquired during hurricane events (Leatherman et al. 2007, Chowdhury et al. 2009, Bitsuamlak et al. 2009).

The WoW apparatus consisted initially of two fans - recently upgraded to six fans (see Figure 2.10). In the current stage the WoW is capable of replicating Category 1 hurricanes (Saffir-Simpson) while maintaining realistic turbulence intensity levels. Additional research is required to allow simulation of more severe hurricane winds (Chowdhury et al. 2010).

The up-to-date results are related to destructive tests of roof components such as roof tiles (Huang et al. 2009), effectiveness of aerodynamic roof edge devices in load reduction (Blessing et al. 2009) and assessment of wind-driven rain intrusion through the building envelope and roof vents (Bitsuamlak et al 2009, Chowdhury et al 2010).

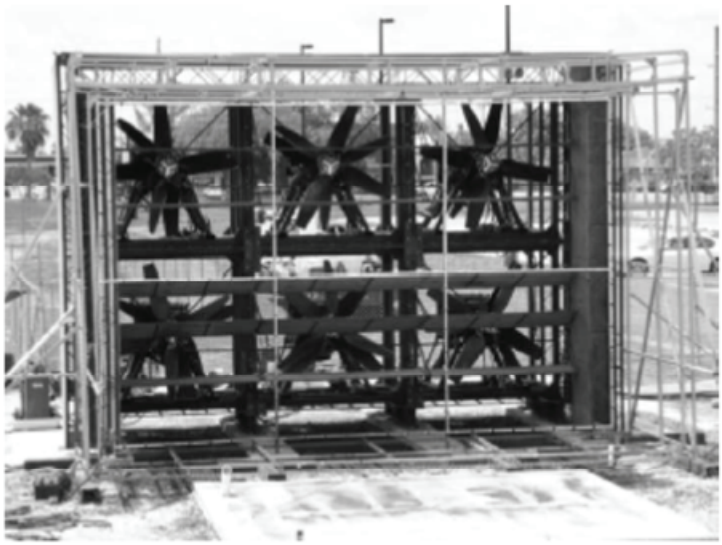

Figure 2.10 Testing apparatus consisting of six fans – Wall of Wind (reprinted from Chowdhury et al. 2010).

2.10 Insurance Research Lab for Better Homes (Three Little Pigs Project)

A highly promising project was established at University of Western Ontario under the name “Three Little Pigs” at the Insurance Research Lab for Better Homes. The main goal of this study is to mitigate wind damage on residential construction (Bartlett et al. 2007, Kopp et al. 2010). This multi-million project simulates wind pressure time histories and apply these loads directly on full-scale test structures (Figure 2.11). The generation of the fluctuating pressures is provided by pressure loading actuators (PLA’s). The pressure signal that the actuators reproduce is based on wind tunnel tests, field measurements or available pressure coefficient databases. Details regarding the technical specifications and function of the actuators can be found in Kopp et al. (2010). The up to date tests include PLA loads applied on full structures in order to evaluate the performance of individual components, such as roof cladding, toe-nailed roof-to-wall connections and glass specimens (Kopp et al. 2010, Morrison and Kopp 2011, Gavanski and Kopp 2011a and 2011b).

Figure 2.11 The Insuranse Research Lab for Better Homes full-scale testing facilities (reprinted from Kopp et al. 2010).

2.11 Wind Simulator (University of Florida - UF)

A very interesting and closely related to the current study effort has been initiated in University of Florida. The particular study aims to examine the response of a low wood building subjected to wind loads, as well as to investigate how this wind-induced load is transferred through the structural system. More specifically, the UF facilities include a 1/3 scaled model of a wood building instrumented with pressure and load monitoring equipment. The wind load is generated by a wind simulator which was designed to primarily test window and door panels. Consequently the flow does not simulate the atmospheric boundary layer and lacks the turbulent characteristics of natural winds. Details related to the experimental facilities are presented in Datin (2010) and Mensah (2010). In addition to the 1/3 building model, a 1:50 wind tunnel model was tested in a boundary layer wind tunnel (Clemson University) and the findings were used for further comparisons (Datin 2010, Mensah et al. 2011). Finally, the study also examines the applicability of a Database-Assisted-Design (DAD) methodology in conjunction to the simulation studies to predict the structural response of a low-rise wood building.

2.12 Insurance Institute for Business and Home Safety (IBHS)

The most recent of the full-scale experimental efforts was initiated in South Carolina in which a full-scale wind tunnel was constructed. The open-jet wind tunnel features 105 fans that can operate in variable wind speeds in order to replicate the atmospheric boundary layer. The test chamber has dimensions 44 by 44 meters and can accommodate up to two-story houses. Preliminary results reported issues related to proper replication of

higher frequency components of wind (Liu et al. 2011) and presented some early pressure coefficient comparisons to results from the TTU building (Brown et al. 2011).

2.13 Concluding remarks

Previous studies have shown that there are many full-scale experimental efforts carried out over the past few decades. Contributions from these studies are of major importance and have been used mainly to verify and improve wind tunnel simulation techniques. However, a very limited number of results have been reported from other full-scale experimental buildings subjected to actual wind loads and monitoring both wind-induced pressures and forces at various levels. Therefore, the present study attempts to identify the wind load paths for the case of low-rise wood buildings.

CHAPTER 3
THEORETICAL BACKGROUND

3.1 Introduction

In this chapter, a brief introduction related to the basic concepts of wind engineering will be discussed. Most of the definitions and knowledge presented in the following sections have been based on the material extracted from three excellent sources (Simiu and Scanlan 1996, Holmes 2001, Liu 1996) as well as by Zisis (2007). It should be noted that the scope of this dissertation is to examine the wind-induced response of low-rise wood buildings from the wind engineering perspective rather than study in detail the dynamics of such structural system. For this reason, a detailed discussion of the dynamic response of wood-frame construction is beyond the scope of this dissertation.

3.2 Wind Structure and the Atmospheric Boundary Layer (ABL)

The discipline of wind engineering is predominantly associated with the lower layers of the atmosphere. Despite the fact that more and more structures are pushing the height limits set in the previous century, still the majority of construction around the world deals with lower height structures (i.e. low-rise buildings and other structures). To this effect the upper layers of the atmosphere are not of particular interest to wind engineers compared to the very first of the atmospheric layers, the so called atmospheric boundary layer (ABL). The ABL's depth is ranging between a few hundred meters to several

kilometres, depending mainly on the terrain characteristics, such as topography and roughness.

The main property of the atmospheric boundary layer is that the wind speed increases with respect to the height – see Figure 3.1. Thus, the surface wind speed at the ground level (zero reference height) is assumed to be zero and as the height increases and reaches the end of the atmospheric boundary layer, the wind speed reaches its maximum value which is referred as gradient wind speed (V_G). Above the atmospheric boundary layer, the wind speed is assumed to be constant. The thickness of the boundary layer is denoted as "δ" in most of wind engineering bibliographic resources. There are two main approaches for the approximation of the wind speed profile. The first is the logarithmic law (Equation 3.1) and the second is the power law (Equation 3.2).

$$V(z) = \frac{1}{k} V_* \ln \frac{z}{z_0} \tag{3.1}$$

$$V(z) = V_i \left(\frac{z}{z_i}\right)^{\alpha} \tag{3.2}$$

where k is the Von Karman constant (equal to approximately 0.4), V_* is the friction velocity, z_o is the roughness length, V_i is the wind speed at any height z_i and α is the power law exponent. Due to its simplicity and its use by the National Building Code of Canada (NBCC 2005), the power law was selected for the analysis of the data hereafter.

The gradient height of the atmospheric boundary layer and consequently the development of the wind speed profile are directly related to the surface roughness. The logarithmic law equation describes the effect of the surface roughness with respect to the roughness length; larger values of roughness shift the wind speed profile to greater heights. This can also be shown using the power law, by setting as reference height the

thickness δ of the atmospheric boundary layer and as reference wind speed the gradient speed (Eq. 3.3).

$$V(z) = V_g(\frac{z}{\delta})^{\alpha} \qquad 3.3$$

The values of α and δ are directly affected by the terrain roughness. A summary of suggested values for the above characteristics of the atmospheric boundary layer in codes and standards can be found in Table 3.1.

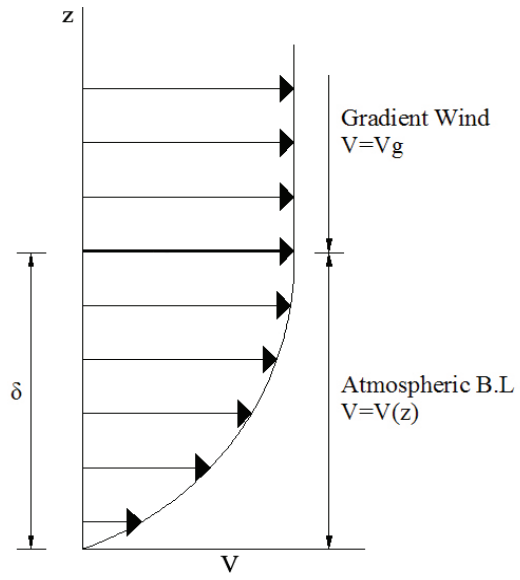

Figure 3.1 Atmospheric boundary layer.

The wind flow in the atmospheric boundary layer is characterized by high fluctuations and random behavior, which are identified as wind turbulence. This fluctuating nature of wind requires the use of statistical tools in order to define the mean, peak and RMS components of wind speed and to precisely quantify its effects on structures. The first and most important definition is the mean wind speed: the average over certain duration of a wind speed record. The most common averaging periods are the 10-minute and 1-hour

mean values. The mean wind speed has the tendency to remain relatively steady over smaller periods of time (i.e. 10 minutes to an hour) which is described as the so-called stationarity of wind speed. This property can be attributed to the time scale of the processes that generate the mean component of the wind flow which are significantly higher than the 1 hour mark. The full wind spectrum presented originally by van der Hoven (1957) depicts the energy contained in different frequencies (see Figure 3.2).

Table 3.1 Power law exponent, terrain roughness and boundary layer thickness suggested values (from Liu 1991)

Exposure Category	Power Law Exponent (α)	Terrain Roughness (z_0) - cm	Atmospheric B.L. Thickness (δ) - m
A	0.33	80	457
B	0.22	20	366
C	0.14	3.5	274
D	0.1	0.7	213

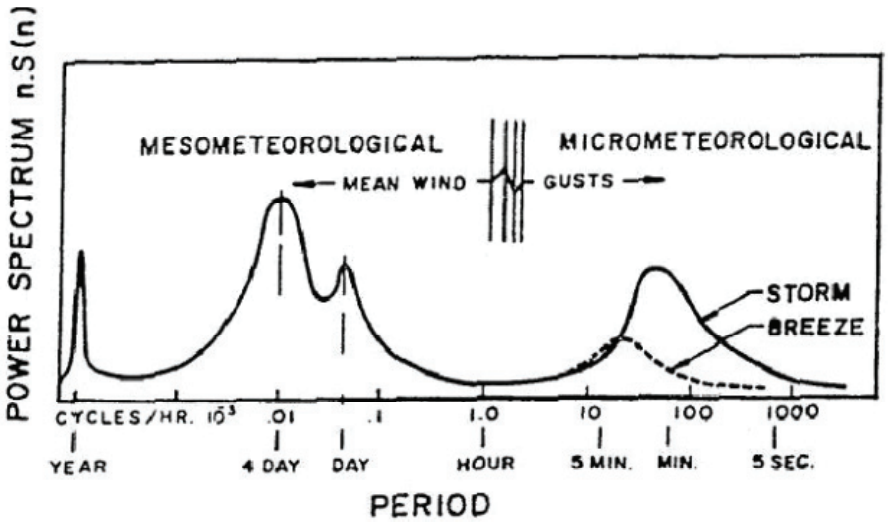

Figure 3.2 Wind spectrum (after van der Hoven 1957).

Although the mean wind speed is useful for describing climate characteristics, structural engineers are mainly interested in the peak values of the wind speed. The peak wind speeds can be defined in a number of different ways, again depending on the duration of the record and also the statistical tools used. In general, for a random wind speed record, the peak wind speed for a given return period is inversely proportional to the averaging time.

In order to describe the turbulence over a given terrain, the turbulence intensity was introduced. As mentioned previously, the wind speed has a fluctuating nature; especially for regions near the ground surface the flow is highly fluctuating and the speed can be described by:

$$V(z,t) = \overline{V}(z) + V(t) \tag{3.4}$$

where $\overline{V}(z)$ is the mean component of the wind speed and V(t) the fluctuations.

The longitudinal turbulence intensity is defined as:

$$I(z) = \frac{\sqrt{\overline{V^2(z,t)}}}{\overline{V}(z)} \tag{3.5}$$

where $\sqrt{\overline{V^2(z,t)}}$ is the root mean square value of the wind speed at the elevation z.

The turbulent nature of wind is also described by the integral scales of turbulence and the spectrum of turbulence which is expressed by its power spectral density. The fluctuation of the wind flow results from the superposition of eddies on the mean wind. Each of these eddies has a characteristic amplitude and frequency n and all together contribute to the total kinetic energy of the fluctuating motion.

The integral scales of turbulence measure the average size of eddies. Since there are three dimensions and three different components for the flow fluctuations (longitudinal, transverse and vertical) a total of nine different scales of turbulence exist. The most common is the longitudinal scale of turbulence, defined as:

$$L_u^x = \frac{1}{\sqrt{\overline{V^2}}} \int_0^\infty R_u(\tau)\, d\tau \tag{3.6}$$

where $R_u(\tau)$ is the autocoveriance function of the fluctuation V(z,t).

The spectrum of wind turbulence is used to describe the total energy generated by the eddies and for convenience is defined by (Liu 1991):

$$V_l = \sqrt{\overline{V(t)^2}} = \int_0^\infty S_l(n)\, dn \tag{3.7}$$

The most common expressions of the power spectra of longitudinal velocity used for structural design purposes are the following (from Simiu and Scanlan, 1996):

- Davenport Equation:

$$\frac{nS(z,n)}{V_*^2} = 4\frac{x^2}{(1+x^2)^{\frac{4}{3}}} \tag{3.8}$$

where: $x = \frac{1200 \times n}{V(10)}$, n in (Hz) and V(10) the mean wind speed in m/sec at z=10m

- Von Karman Equation:

$$\frac{nS(n)}{V_*^2} = 4\frac{\beta \frac{nL_u^x}{U}}{\left[1+70.8\left(\frac{nL_u^x}{V}\right)^2\right]^{\frac{5}{6}}} \tag{3.9}$$

- Kaimal Equation (Kaimal et al. 1972):

$$\frac{nS(n)}{V_*^2} = \frac{105n}{(1+33n)^{5/3}} \qquad 3.10$$

3.3 Bluff Body Aerodynamics

The wind-induced effects on buildings and other structures are generated principally due to their non-streamlined shape. Scope of wind engineering is to study the aerodynamics of bluff bodies and define theoretically and experimentally the wind field around these bodies. The characteristics and properties of the wind flow are of particular importance and closely related to the wind-induced pressures on the surfaces of a bluff body. An example of such flow, for the case of a boundary layer flow, is presented in Figure 3.3 (two-dimensional) and Figure 3.4 (three-dimensional). The windward wall, as expected, is subjected to positive pressures whereas the effect of flow separation generates high suctions on the roof and lower suctions on the side and leeward walls.

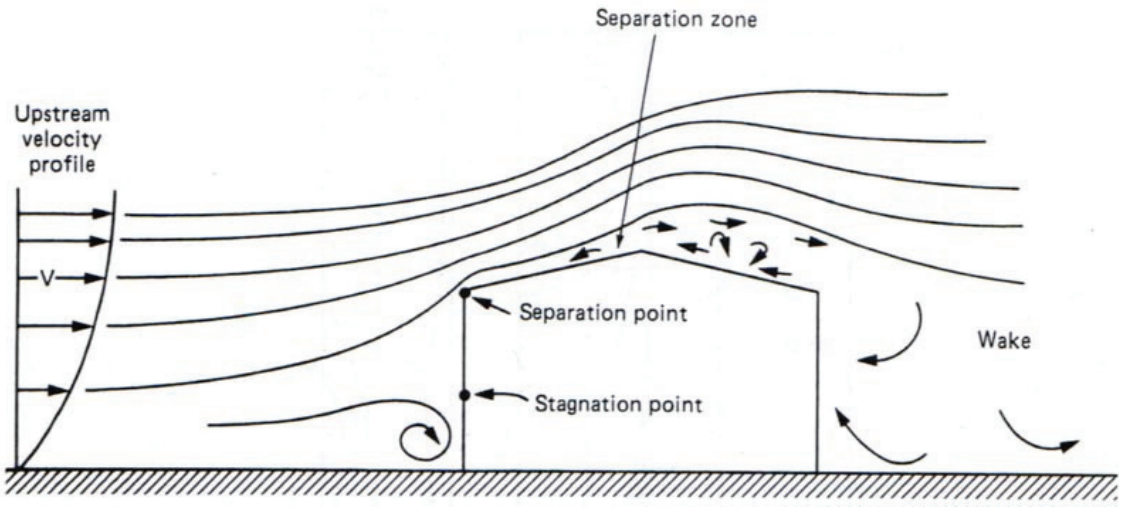

Figure 3.3 Boundary layer 2-D wind flow around a low-rise structure (after Liu 1991).

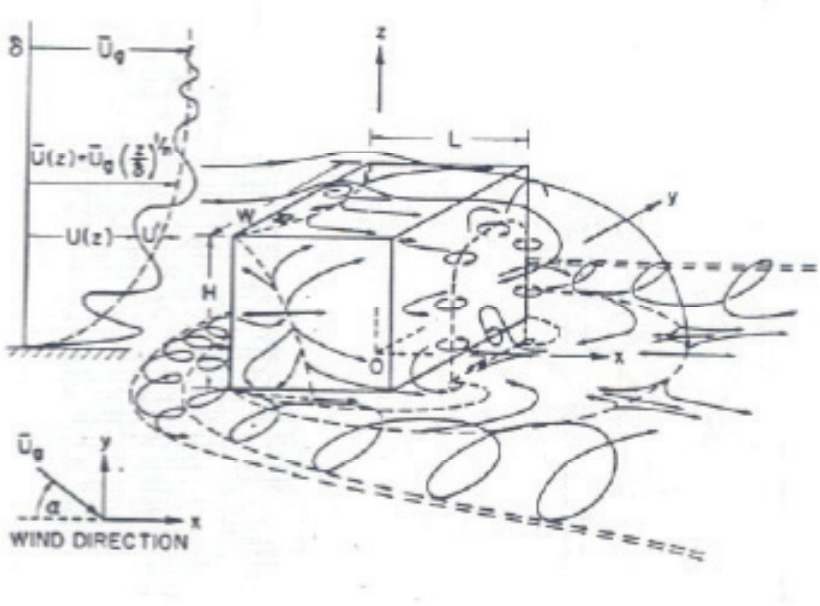

Figure 3.4 Boundary layer 3-D wind flow around a cubic structure (after Woo et al. 1977).

3.4 Wind-Induced Pressures and Forces on Buildings

The presence of a bluff body, e.g. a low-rise building, inside a boundary layer wind flow has as a result the formation of a complex flow field similar to that of Figure 3.4. Consequently, the building envelope is subjected to positive and negative pressures whereas the structural system needs to withstand the local and total wind-induced forces and moments. More specifically, the wind pressure or suction (negative pressure) needs to be defined with respect to a reference pressure and for wind engineering applications the ambient atmospheric pressure is selected. It should be noted that this atmospheric pressure should be considered without the presence of any obstacles in the near flow field. This is particularly important in field studies for which precise monitoring requires measurement of the ambient atmospheric pressure without any effects of separation or

wake of adjacent structures or buildings. The use of the atmospheric pressure as reference justifies the positive and negative pressures acting on the building envelope.

In order to define the pressure and suctions acting on the surface of the structure, the wind flow is assumed to be steady and uniform. Applying Bernoulli's equation for the flow:

$$p_a + \frac{1}{2}\rho V^2 = p_s \tag{3.11}$$

where p_a is the atmospheric pressure, ρ is the air density and p_s is the stagnation pressure.

For convenience, dimensionless coefficients have been introduced and these coefficients help to evaluate and compare the effects of wind on structures. Thus, the mean pressure coefficient is defined as:

$$c_{p,mean} = \frac{p_{mean} - p_a}{\frac{1}{2}\rho V^2} \tag{3.12}$$

Peak and RMS pressure coefficients are defined as:

$$c_{p,peak} = \frac{p_{peak} - p_a}{\frac{1}{2}\rho V^2} \tag{3.13}$$

$$c_{p,rms} = \frac{p_{rms} - p_a}{\frac{1}{2}\rho V^2} \tag{3.14}$$

Internal pressure coefficient is defined as:

$$c_{p,i} = \frac{p_i - p_a}{\frac{1}{2}\rho V^2} \tag{3.15}$$

In addition to pressure coefficients, the overall wind-induced force exerted on a building can be expresses in dimensionless form using the force coefficient which is defined as:

$$c_F = \frac{F}{(\frac{1}{2}\rho V^2)A} \qquad 3.16$$

where F is the wind-induced force (x, y or z-direction) and A is the projected area of the building, usually at the foundation level.

As mentioned previously, the averaging period over which the mean wind velocity is considered ranges from 3 seconds to 1 hour. The numerous national and international standards and building codes are using different averaging periods, therefore comparisons between these standards and experimental studies requires particular scrutiny. The widely used Durst gust duration curve (Durst 1960) is suggested for conversion of the mean hourly wind speed to wind speeds over other averaging time (see Figure 3.5).

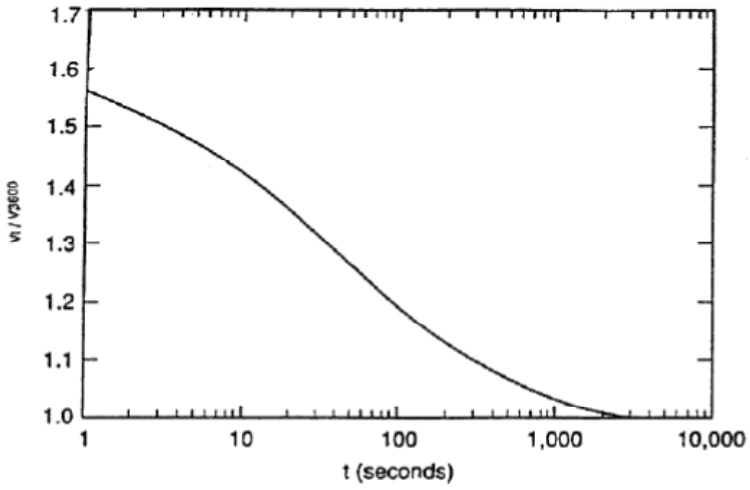

Figure 3.5 Gust duration curve (after Durst 1960).

3.5 Boundary Layer Wind Tunnels

Although wind tunnel testing of small or larger scaled models has a long history in various engineering disciplines – but predominantly in aeronautics – it was only in the

last few decades that boundary layer wind tunnels were established and used to perform extensive testing on buildings and other structures exposed to wind. The boundary layer wind tunnels have basic requirements related to their dimensions and capabilities in order to simulate properly the characteristics of the atmospheric boundary layer (velocity profile, turbulence intensity and power spectra of turbulence). In addition to these basic flow properties, there are certain similarity parameters that need to be reproduced during a wind tunnel study. The basic scale factors are the length, velocity, air density, frequency and time factors. It should be noted that these parameters are not independent from each other.

The geometric scales used for wind tunnel modeling vary from 1:10 down to 1:500. The proper scale should be selected after taking into consideration the size of the wind tunnel and the size of the examined building or structure. Of particular importance is the type of the wind tunnel study which should also be considered before selecting the proper geometric scale. Despite the small size of wind tunnel models, recent technological progress has changed drastically the equipment capabilities, and more importantly their size, allowing for high frequency sampling on several hundreds of miniature pressure sensors. Last but not least, sophisticated data acquisition systems support the high frequency sampling and storage of excessive amounts of data.

CHAPTER 4
PROJECT DESCRIPTION

4.1 Introduction

In this section a description of the test facilities and experimental procedures will be presented. Various modifications and upgrades have been undertaken on the test building since the initiation of the project. Structural and equipment characteristics have been presented in detail by Zisis (2006) but will also be discussed here in order to track recently added components and other structural modifications.

4.2 Full-scale Studies

4.2.1 Site characteristics

The location of the full-scale experimental facilities is Fredericton, New Brunswick. The facilities include a test building and two weather masts. The site is in the proximity of the Hugh John Fleming Forestry Centre which is affiliated to the University of New Brunswick. The building is surrounded predominantly by low-rise industrial buildings and forest areas. More particularly, the South-East region is dominated by a relatively dense forest area with trees of approximately 20 meters height. The rest of the surroundings include either low-rise buildings of average height between 5 and 10 meters or smaller forest areas. A detailed description of the surroundings is presented in Figure 4.1 and Table 4.1.

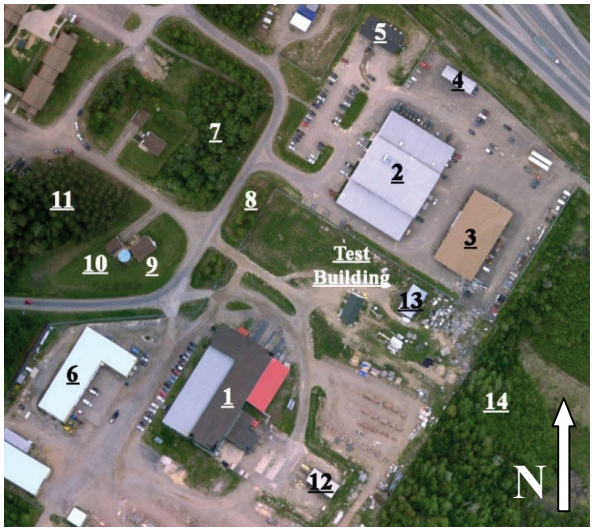

Figure 4.1 Aerial view of the full-scale test facilities and the surroundings.

Table 4.1 Description and height of the surroundings of the test building.

ID (see Figure 4.1)	Description	Approximate External Dimensions (m)	Approximate Height (m)
1	Industrial building	54 x 85	11.5
2	Industrial building	45 x 65	10
3	Industrial building	27 x 46	7
4	Industrial building	6 x 20	6
5	Industrial building	12 x 25	6
6	Industrial building	36 x 55	7
7	Forest area	75 x 75	< 20
8	Forest area	12 x 33	< 15
9	Residential building	10 x 14	6
10	Residential building	6 x 8	6
11	Forest area	65 x 80	< 25
12	Storage space	9 x 18	6.5
13	Storage space	9 x 12	6
14	Forest area	-	< 20

4.2.2 Test building and instrumentation

The building geometry was selected to be of rectangular shape with a gable roof and the platform construction method was used to form the structural system. This particular technique is currently the most conventional construction method in which the wall framing is erected on top of the floor system. The building has external dimensions of 8.6 x 17.2 x 5.6 meters (W x L x H) and a duo-pitch roof of 4/12 slope. It is resting on a concrete foundation wall 0.225 m thick and 1.225 m deep. The geometry and dimensions of the building are shown in Figure 4.2.

The floor system of the test building consists of 43 I-joists directed along the small side of the structure. The I-joists (JSI 40) have a total height of 508 mm and they are spaced at 406 mm (centre-to-centre distance). On the top of the I-joists, 15 mm thick OSB (Oriented Strand Board) panels 1.22x2.44 m have been nailed and create a solid diaphragm on the floor.

The wall system consists of wall frames, sheathing and siding panels. The wall frames are assembled from 38x89 mm studs spaced at 600 mm. The studs are made by spruce-pine-fir lumber (S-P-F). Studs are also used for bottom (one stud 38x89 mm) and top (two studs 38x89 mm) plates in order to form the framing wall system. On the exterior side of the wall, OSB panels of 9.5 mm thickness are used to cover the framing. A final layer of stained wood is used as siding. The internal side of the frame walls and the ceiling are covered with plasterboards of 9.5 mm thickness. No partition walls are installed thus only the exterior walls serve as lateral force resisting system.

The ceiling of the test building consists of a grid of 38x89 mm and 19x89 mm studs, which are fastened to the bottom of the roof trusses. The roof trusses are prefabricated fink trusses (W-trusses) spaced at 600 mm and comprised of 38x89 mm lumber elements.

Two door openings exist on the building, one door on the east and the other on the west wall. The orientation of the building is 43 degrees right of the geometric North which was assumed to be the reference zero point for all direction measurements. More details about the construction of the test building can be found in Doudak (2005) and Zisis (2006).

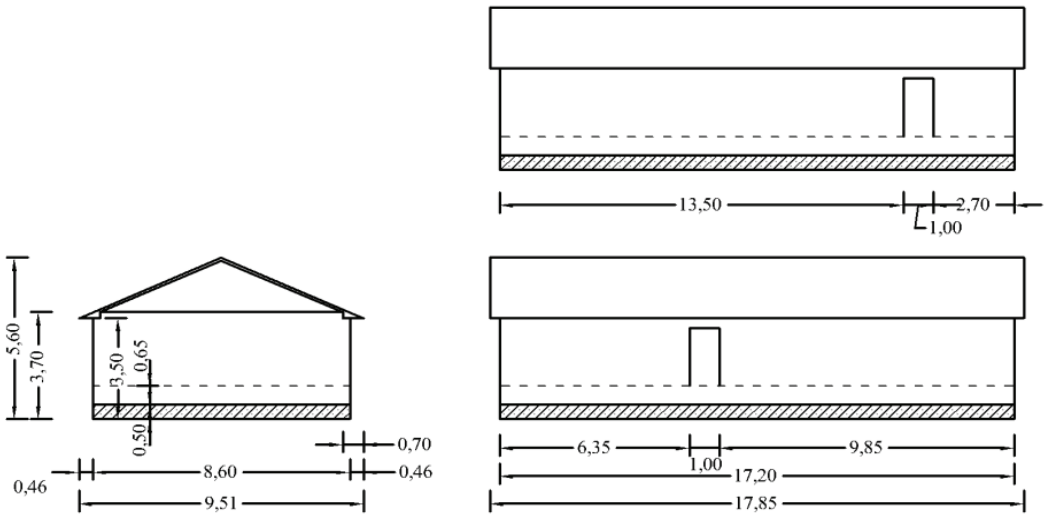

Figure 4.2 External dimensions of the experimental building.

The test building is equipped with 40 pressure taps, 12 of them on the wall and 28 on the roof, as shown in Figure 4.3. The pressure taps were installed at an earlier stage of the project and the installation of additional sensors, although very desirable, was not really possible considering the general system configuration (limited number of ports available in the data acquisition system). The majority of the roof pressure taps were distributed on top of three pre-selected frames and were equally spaced from each other. The closest tap to the eave of the roof was at a distance of 1.6 meters and the closest to the ridge at a distance of 0.2 meters. The system consists of 4.8 mm inside diameter plastic tubes mounted on the wall and roof surface and connected to differential pressure transducers

(Micro Switch 160PC). These transducers use as reference pressure the ambient atmospheric pressure, which is provided by the barometric pressure scanning system.

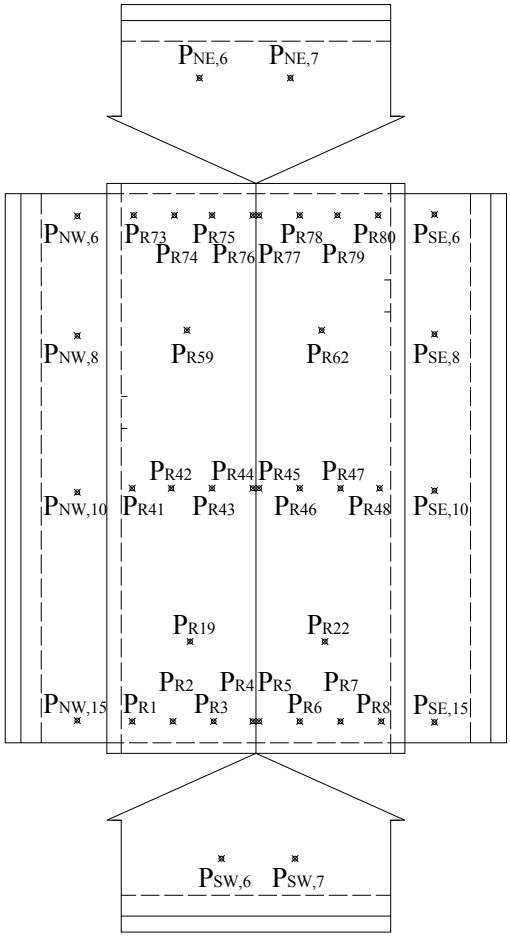

Figure 4.3 Pressure tap location on the test building.

Particular attention was given to the protection of the tubing from humidity, condensation, dust and section obstruction. For this reason, special techniques were used for the roof pressure taps to drain the rain water from them and protect also the transducers.

Full-scale pressure measurements are highly affected by the way of measuring the reference atmospheric pressure. The differential pressure transducers measure surface

wind pressure using as reference the ambient atmospheric pressure. Therefore, the test building was equipped with a Young (R. M. Young Company, 2001) barometric pressure sensor, monitoring the ambient atmospheric pressure. The sensor is located outside the building and is mounted on the south wall. The combination of a regular pressure sensor (Young - model 61202) housed in a waterproof molded case and a pressure port (Young - model 61002) minimized significantly the dynamic pressure errors due to wind. The pressure port uses two parallel plates in order to reduce significantly the approaching wind velocity before it hits the pressure inlet. In addition an internal baffle system protects the barometer from water and snow penetration.

The load cell system is an innovative part of this study. A total number of twenty-seven 3-D load cells were placed around the perimeter of the building at the foundation-to-wall interface (Figure 4.4a). Another six 1-D load cells were also installed between the wall top plate and three of the roof trusses (Figure 4.4b). The location of the load cells is shown in Figure 4.5. It should be mentioned that the building is completely isolated from the foundation and the only points of contact are the 3-D load cells. This construction detail assures the transfer of the applied load to the foundation only through the load cells.

In addition to the pressure and stress sensors, temperature monitoring equipment is also used. Thermocouples are installed in such way so monitoring of internal, external, foundation concrete wall and foundation load cell housing can be monitored simultaneously to the rest of the sensors.

(a)  (b) 

Figure 4.4 (a) Foundation and (b) roof load cells placed in the foundation to wall and wall to roof interfaces.

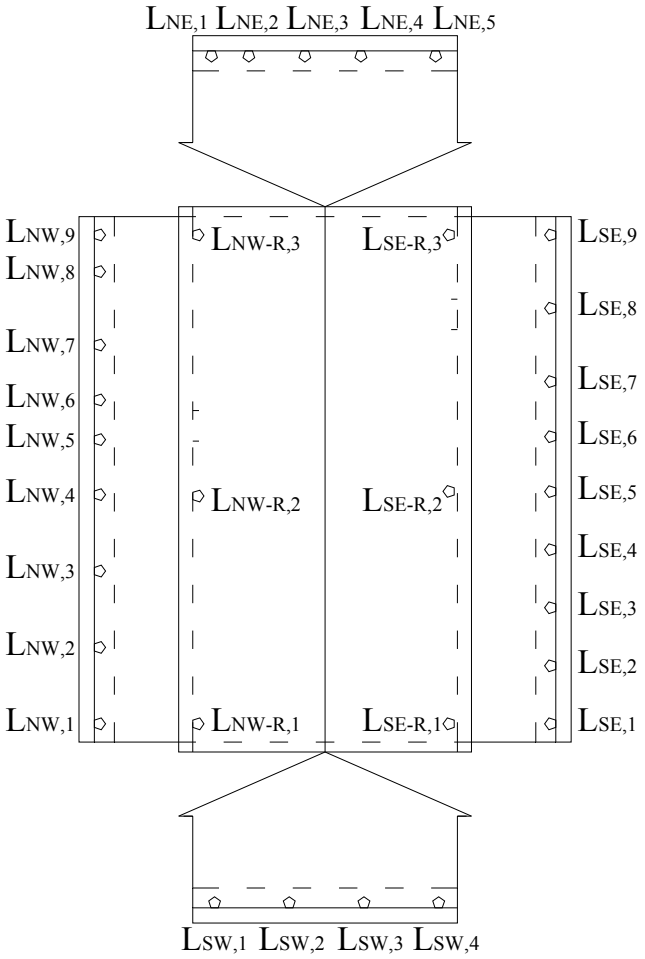

Figure 4.5 Roof and foundation load cell location on the test building.

Finally, the System 5000 (Vishay System Model 5000, Intertechnology) was used for data acquisition and reduction. This stress analysis data system is able to accept simple strain gages (load cells), linear variable differential transformers (LVDT's) and high frequency sensors (pressure tap transducers). The system is operated by sophisticated software (Strainsmart Software) provided by the same company. This Windows-based software can export the acquired data in different formats (ASCII, EXCEL, ACCESS database).

4.2.3 Weather and structural monitoring

The wind characteristics were monitored using four propeller anemometers. Three of them are mounted on a 10-meter mast on the North-West side of the building at 5.5, 6.5 and 10.0 meters height and the fourth is mounted on the top of a 5.5-meter post on the South-East side of the building. An aerial view of the facilities with the actual building North view and the meteorological towers on the North-West and South-East sides of the building, at a distance of approximately 20 meters, are shown in Figure 4.6. Special attention was paid regarding the location of the towers close to obstructions in order to avoid contaminating the wind regime by eddies generated from adjacent structures or trees.

The data acquisition system was set to monitor at 5 Hz. The total number of the monitored sensors was approximately 150 and the duration of each scanning session was at least 10 minutes. In the early phase of the project an advanced triggering system was used to either initiate or extend the scanning session if the wind speed at 10 meters height was exceeding a predefined limit. This option was abandoned and a continuous

monitoring of 24 hours duration was selected during 2008 and 2009. Although the extended acquisition duration generated enormous amounts of recorded data, it allowed the identification and isolation of some – in some cases significant – temperature effects on the distribution of the foundation forces.

Figure 4.6 Aerial view with test building and weather tower locations.

4.3 Wind Tunnel Simulation

In addition to the field studies, several wind tunnel tests were conducted in the Building Aerodynamics Laboratory (BAL-Concordia University) to evaluate the wind-induced pressures on a scaled model of the test building. The particular boundary layer wind tunnel is 12.0 meters long and has a test section 1.8 meters wide and 1.8 meters high. A turntable of 1.20-meter diameter is located on the test section of the tunnel and allows testing of models for different angles of attack. The wind speed of the wind tunnel

ranges between 4.0 and 14.0 m/sec. The ceiling of the wind tunnel is adjustable in order to provide the minimum possible pressure gradient along the test section. A detailed description of the specific boundary layer wind tunnel can be found in Stathopoulos (1984).

4.3.1 Test building and surroundings model

The building model and the surroundings were constructed using a 1:200 geometric scale. The model was metallic with a duo pitch roof of 4:12 slope and external dimensions of 86.5 mm by 42.5 mm and a total height of 24.35 mm. The model was equipped with 80 roof and 46 wall pressure taps respecting the location of the available taps on the full-scale test building. The location of the roof and wall pressure taps along with their notation is shown in Figure 4.7. The 15 mm diameter taps were connected to the pressure transducers by using flexible urethane tubing and a metallic restrictor to filter the fundamental frequency response.

In addition to the building model, a proximity model of 1:200 scale was constructed. Considering the scale of the test building and the size of the wind tunnel test section, a circular wood base of 1.60-meter diameter and 3.0 mm thickness was used to place all surrounding structures and tree elements on it. Styrofoam was used for the construction of the surrounding building models and wood sticks and wire wool (scourer) for the vegetation. A space at the center of the wood base was left open in order to be able to place the test building model and pass all the tubing system underneath the turntable. A plan and isometric view of the proximity model are shown in Figure 4.8 and the actual maquette placed in the test section of the wind tunnel is shown in Figure 4.9.

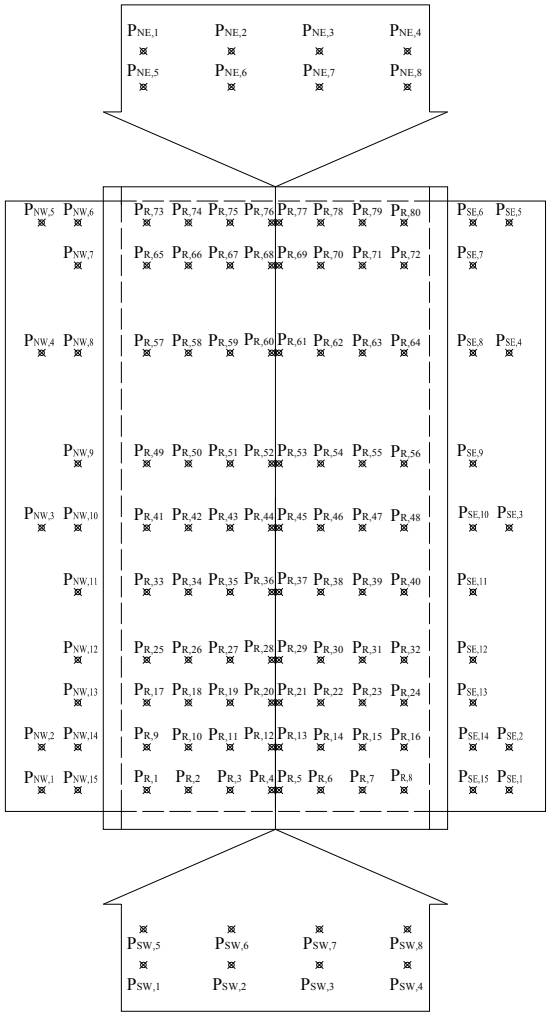

Figure 4.7 Exploded view of the wind tunnel building model and location of pressure taps.

4.3.2 Upstream terrain simulation

The wind tunnel tests were carried out for three different upstream terrain configurations. The selection of these terrains was based on the observations acquired from the anemometers located in the field facilities (see Figure 4.6). The appropriate roughness elements were placed upstream to the test section of the wind tunnel creating the three distinct boundary layer profiles, i.e. open, light suburban and heavy suburban.

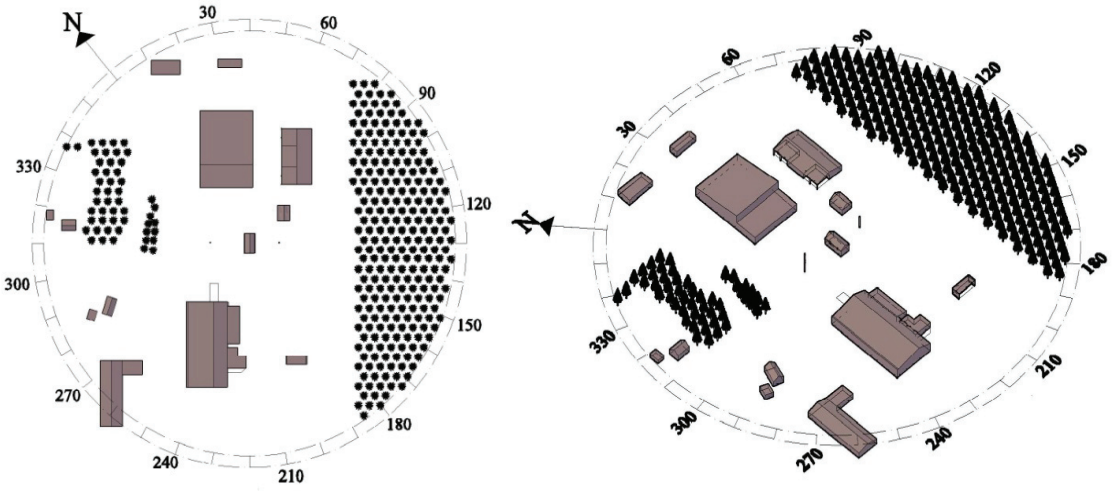

Figure 4.8 Wind tunnel proximity model and orientation of the test building.

Figure 4.9 Test building and surroundings model placed in the wind tunnel.

For the open terrain exposure, the default carpet setting was selected resulting in a power law exponent of 0.16 (Figure 4.10a). The mean wind speed and turbulence intensity profiles are shown in Figure 4.10b. For the light and heavy suburban exposure the power law exponents were estimated to be equal to 0.22 and 0.28 respectively (Figure 4.11a and Figure 4.12a). The plotted mean wind speed and turbulence intensity profiles are presented in Figure 4.11b and Figure 4.12b. The roughness length and turbulence intensity values for each of the three simulated terrain are presented in Table 4.2.

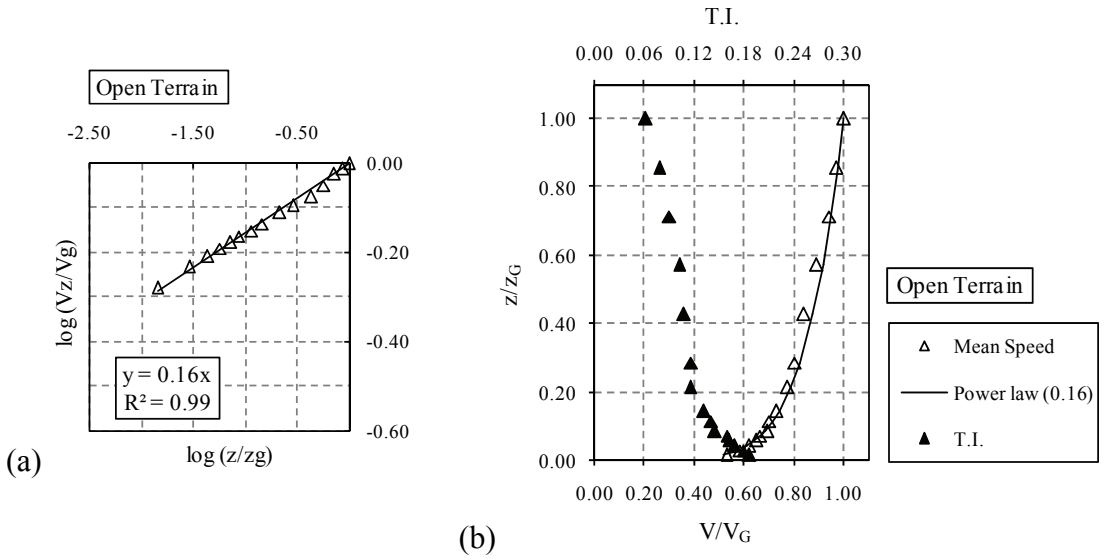

Figure 4.10 (a) Power law exponent and (b) mean wind speed profile and turbulence intensity profile for open terrain simulation.

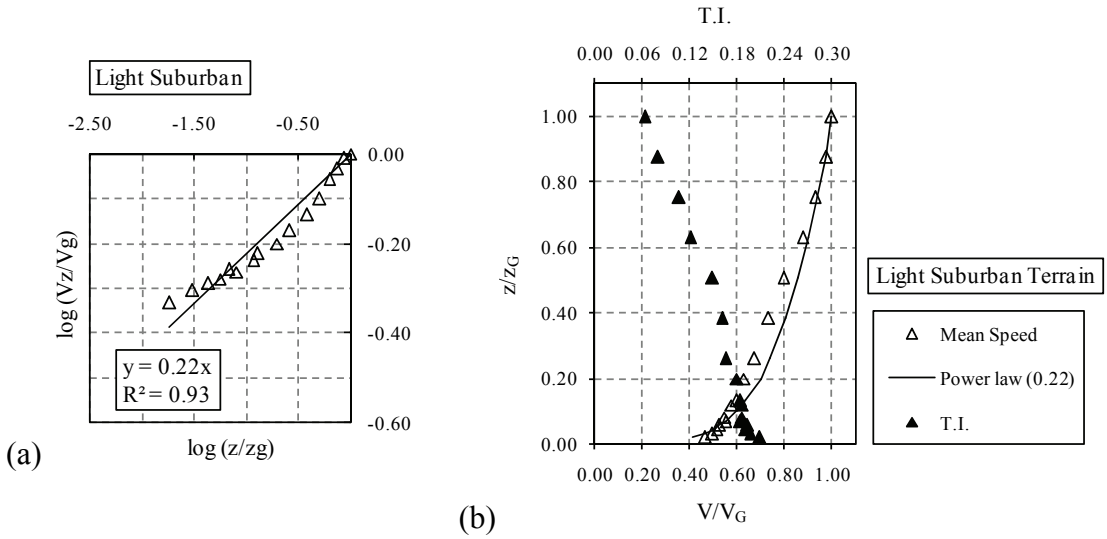

Figure 4.11 (a) Power law exponent and (b) mean wind speed profile and turbulence intensity profile for light suburban terrain simulation.

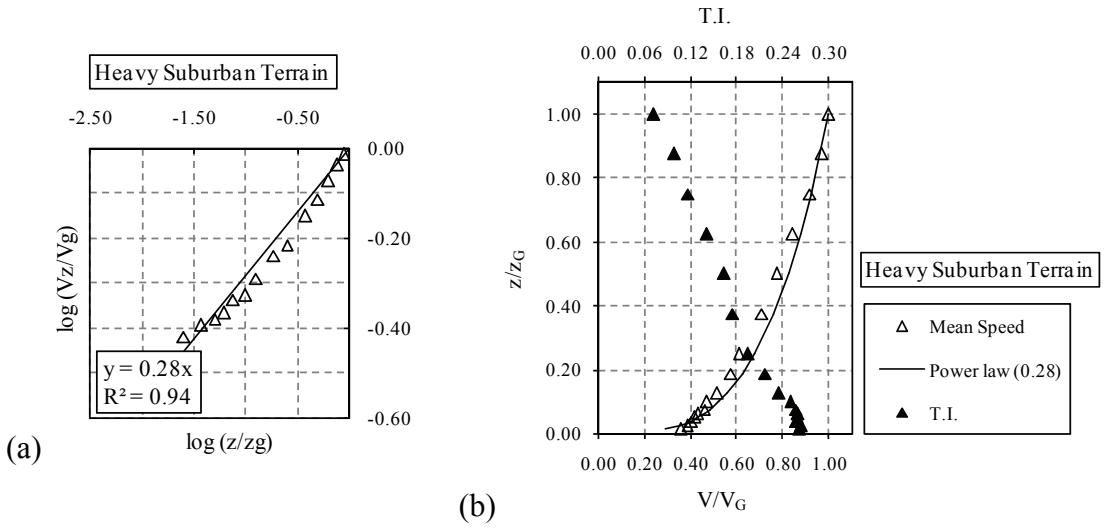

Figure 4.12 (a) Power law exponent and (b) mean wind speed profile and turbulence intensity profile for heavy suburban terrain simulation.

Table 4.2 Power law exponent, terrain roughness and turbulence intensity at ridge height experimental values.

Terrain	Power Law Exponent (α)	Terrain Roughness (z_0) - cm	Turbulence Intensity (Ridge Height) - %
Open	0.16	0.012	17.9
Light Suburban	0.22	0.069	20.2
Heavy Suburban	0.28	0.198	26.4

The verification of an adequate simulation of the boundary layer was examined by comparing the wind tunnel along wind velocity spectrum to those suggested in literature (e.g. Simiu and Scanlan 1996, Holmes 2001). The longitudinal velocity spectrum was measured at 0.05 meters in the wind tunnel which corresponds to 10 meters height in full scale for a 1:200 building model scale. It should be mentioned that the agreement to the

Von Karman and Davenport spectra was improved for the geometric scale of 1:400. Due to the relatively small building size, the scale of 1:200 was selected considering that this scale relaxation will have minimal effect on the local and area averaged pressure results (Stathopoulos and Surry 1983).

In all three terrains the wind tunnel energy levels compare well to those obtained by the analytical and empirical expressions. A representative spectrum for the light suburban case is shown in Figure 4.13. The experimental spectrum shows a particular agreement for mid- to high-range wave numbers (1-10 Hz/m/s). The Von Karman and Davenport spectrum show a more consistent energy distribution whereas the Kaimal model is consistently shifted towards a higher reduced frequency.

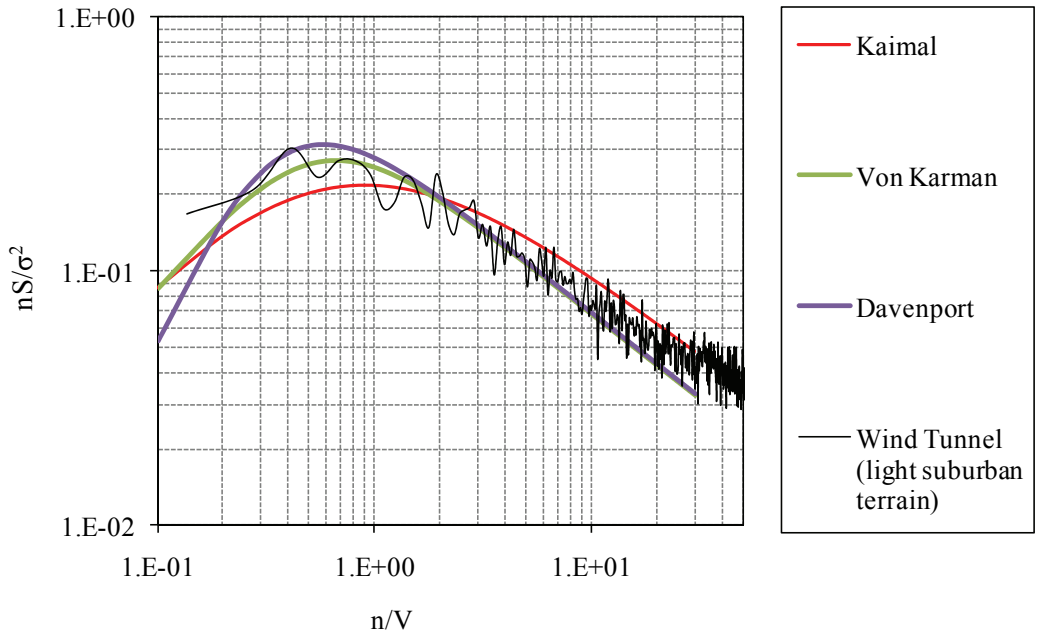

Figure 4.13 Experimental, analytical and empirical velocity spectra for light suburban terrain simulation.

4.3.3 Wind tunnel testing

The wind tunnel experiments were conducted using sophisticated scanning and data acquisition systems. The wind velocity measurements, such as wind speed and turbulence profiles and spectra, were measured using the 4-hole Cobra probe (Turbulent Flow Instrumentation). The sampling rate for the velocity measurements was 1000 Hz and the duration of each run was at least 30 seconds. The gradient mean wind velocity for all three terrains was approximately 13.6 m/s.

The pressure measurements were conducted using the updated version of Scanivalve's Digital Service Module (DSM 3400) with two ZOC33/64Px miniature pressure scanners (Figure 4.14). The scanning period was set at 50 micro-seconds resulting in a sampling frequency of 312.5 Hz. The duration of each run was 26.2 seconds and the total number of frames scanned was 8192. In all cases the model was tested for 36 wind directions (10 degrees direction intervals – see Figure 4.8). The building model was connected to the two ZOC 33/64Px scanners using flexible urethane tubing and the scanners were connected to the main DSM unit. The data acquisition system was operated by a host computer through Ethernet connection and the data were saved in binary format to avoid a buffer overflow. A schematic of the testing apparatus is presented in Figure 4.15.

(a) 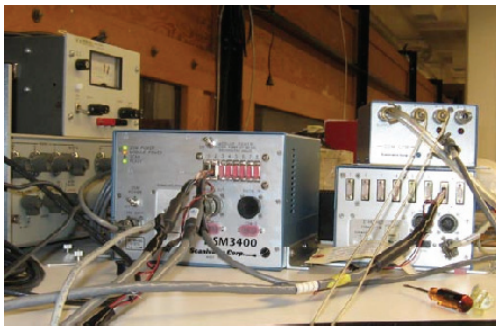

(b) 

Figure 4.14 (a) Miniature pressure scanning system DSM 3400 and (b) ZOC33/64Px.

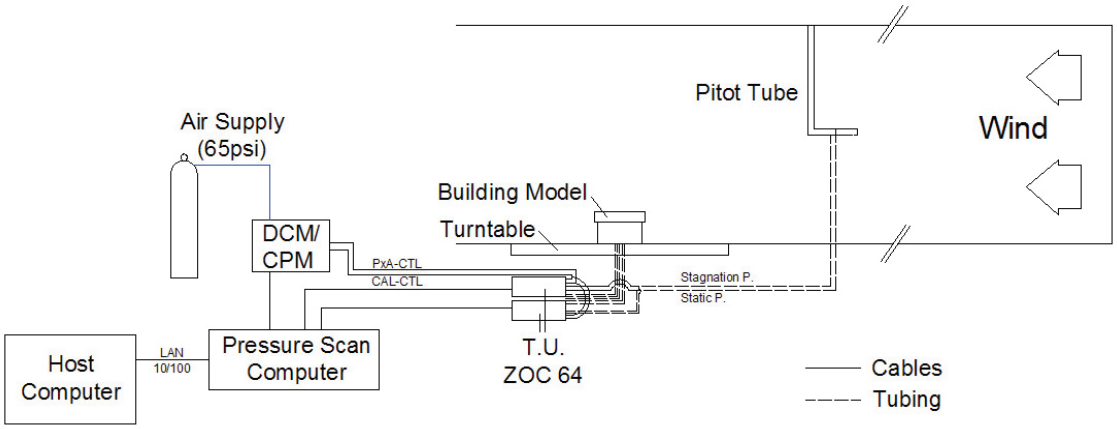

Figure 4.15 Instrumentation schematic of the wind tunnel experiments (after Zisis 2006).

4.4 Numerical Simulation (FEA)

4.4.1 Model description

The field facilities provided detailed information regarding the wind-induced loads not only on the surface of the test building but at various locations of the structural system as well. On the contrary, the wind tunnel experiments estimated only the applied wind load on the surface of the building model without any information on how this load is distributed to other structural members and eventually to the foundation. Therefore, it was of immediate interest to the present study to develop a numerical model which could be compared and validated by the full-scale and wind tunnel studies.

The numerical model was developed using the commercial software SAP 2000 (Computers and Structures, Inc.). The scope of the current research project was to improve significantly the level of modeling accuracy of previously developed models (Zisis 2006) as well as to deliver a highly detailed model which can be used for further analysis and verification in future studies. Particular attention was paid towards the "one-by-one" consideration of all primary and secondary elements of the test building during

the development of the numerical model. As a result, a total of 19,157 joints and 22,012 elements were incorporated in the model replicating in the highest possible way the actual test building (Figure 4.16).

More specifically, five additional material properties were added and used throughout the model. Their properties were retrieved from the literature (e.g. Doudak 2005, Canadian Wood Council, Canadian Plywood Association) and recent studies conducted at the Engineered Timber Structures Research Group (University of New Brunswick). The predefined material properties for steel were used and in addition the following materials were added; spruce-pine-fir lumber (SPF), laminated vaneer lumber (LVL), oriented strand board (OSB) and plasterboard. Some of these materials properties are presented in Table 4.3. All materials were assumed to be isotropic i.e. the material orientation and the direction of the loading do not affect their behaviour.

Table 4.3 Material properties used in the numerical modeling.

Material	Unit Weight (kN/m^3)	Modulus of Elasticity (kN/m^2)	Shear Modulus (kN/m^2)
Steel	78.5	199.9×10^6	76.885×10^6
SPF	5.69	10.5×10^6	4.038×10^6
LVL	7.45	10.5×10^6	4.038×10^6
OSB	6.87	5.5×10^6	2.115×10^6
Plasterboard	7.35	199.9×10^3	76.884×10^3

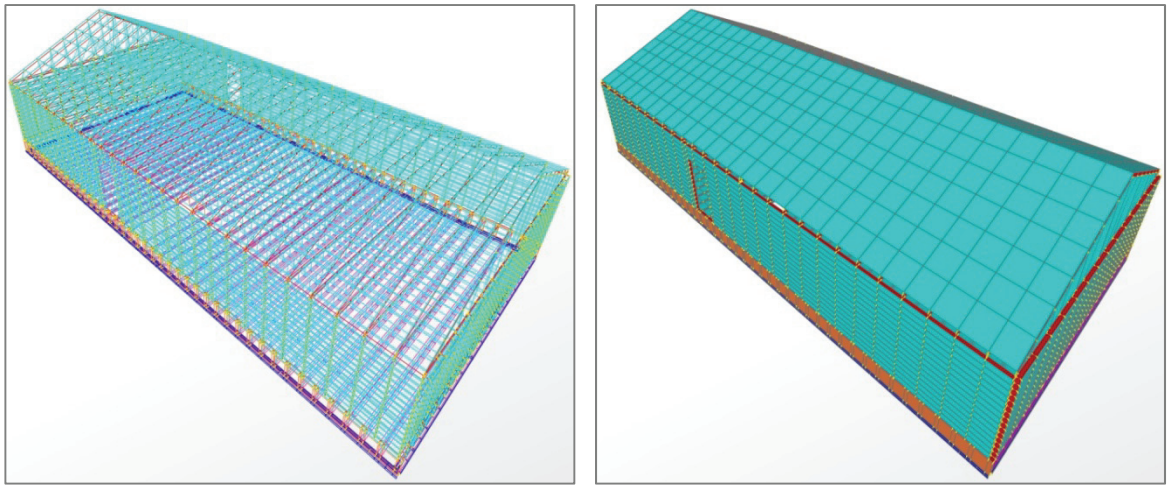

Figure 4.16 Wireframe and conceptual views of the test building model.

The model was formed using both frame and shell elements. The frame sections were mostly used for the truss formation and some of the wood stud framing. The majority of the floor, ceiling, roof and walls were modeled as area sections. The option of the thick shell was selected for all members/panels excluding the plasterboard which was modeled as a membrane. In all cases the thickness for both the membrane and bending behaviour had the same nominal value and the material angle was set to zero. The stiffness modifiers for the shell elements were not changed whereas the mass modifiers were altered to account for the additional moisture content of some elements. The total weight of the test building was verified through the full scale dead load monitoring. Finally, the frame and shell elements were interconnected by using rigid links. These links were placed at the exact same locations as in the test building representing the nail/bolt connections. For the scope of the current study, the links were fixed in all six directions and were assumed to have a linear behaviour. The only links that had particular degrees of freedom were those connecting the load cells to the system of I-joists. The specific

bolted connections had one rotational and one translational degree of freedom with zero damping properties. The links were grouped based on the two connected members allowing a future modification of their linearity.

4.4.2 Loading of the numerical model

The load applied on the finite element model was obtained through either the field monitoring or the wind tunnel experiments. In both cases the wind-induced load recorded by the pressure taps was distributed over the area elements (shell elements) using the equivalent area principle. Based on this approach, each pressure tap had its own area of influence which was consequently loaded with the recorded pressure signal. The level of approximation in this approach is directly related to the number of available pressure taps. Therefore the wind tunnel model which was equipped with 132 pressure taps provided a significantly more detailed loading grid compared to the 40 pressure tap scheme on the full scale test building.

As previously mentioned, the pressure measurements were acquired in the form of time series (e.g. 26.2 seconds duration in the wind tunnel or 10 minutes duration in full scale). In order to be able to compare the load cell readings to those derived by the numerical model the option of the linear direct integration history analysis was selected. The particular type of analysis was computationally intense but had the advantage to estimate the structural response in the form of time series and therefore allow us to directly compare the experimental to the numerical results on an instantaneous basis. In order to use the particular method of analysis, each of the equivalent areas was loaded with each individual pressure trace. As a result, for the case of the full scale analysis, 40

pressure traces of 3000 time steps each were applied to the surface of the numerical model. The linear analysis was carried out using the Hilber-Hughes-Taylor built-in time integration method.

CHAPTER 5
VERIFICATION OF TESTING AND MODELING PROCESSES

5.1 Introduction

The research project incorporates multiple experimental procedures, as well as computer-based modeling. It was of great importance to verify the functionality of the experimental facilities and validate the accuracy of the developed numerical model. This chapter presents several verifications carried out at various stages of the study.

5.2 Verification of Full-scale Facilities

5.2.1 Weather tower monitoring system

The four anemometers, the barometric pressure port and the five thermocouples are the main components of the weather monitoring system. Special attention is paid to the condition of the pressure port, since all pressure measurements are using this port as reference. All wind speed and direction data are isolated and imported to a dedicated database which is used to verify the exposure characteristics (power law exponent, turbulence intensity, surface roughness, power spectra etc).

In order to validate the reliability of the weather tower monitoring system, collected data are compared to those from the closest weather stations operated by Environment Canada (Fredericton Airport and CDA-CS stations). These stations provide wind speed and direction data at 10 meters height and are based on the last five-minute averages of

each hour. Data collected during the period October 21-31, 2008 were analyzed and 5-minute averages of wind speed and wind direction were calculated.

The anemometers selected for this comparison are those located at 5.5- and 10.0-meter height. In order to be able to compare the acquired data to those recorded by Environment Canada, appropriate transformations using the power law velocity profile (Equation 3.3) were incorporated. More specifically, the transformation took into consideration the upstream terrain (e.g. open vs. suburban) and the height difference between the anemometers (e.g. 5.5 meters vs. 10.0 meters). The comparison between the experimental building data and local weather stations is shown in Figure 5.1 (wind speed) and Figure 5.2 (wind direction). It should be noted that a total of 1906 5-minute sets have been analyzed using data from the weather tower monitoring system. The agreement for both wind speed and direction signals is very good and validates the accuracy of the data recorded by the weather tower monitoring system.

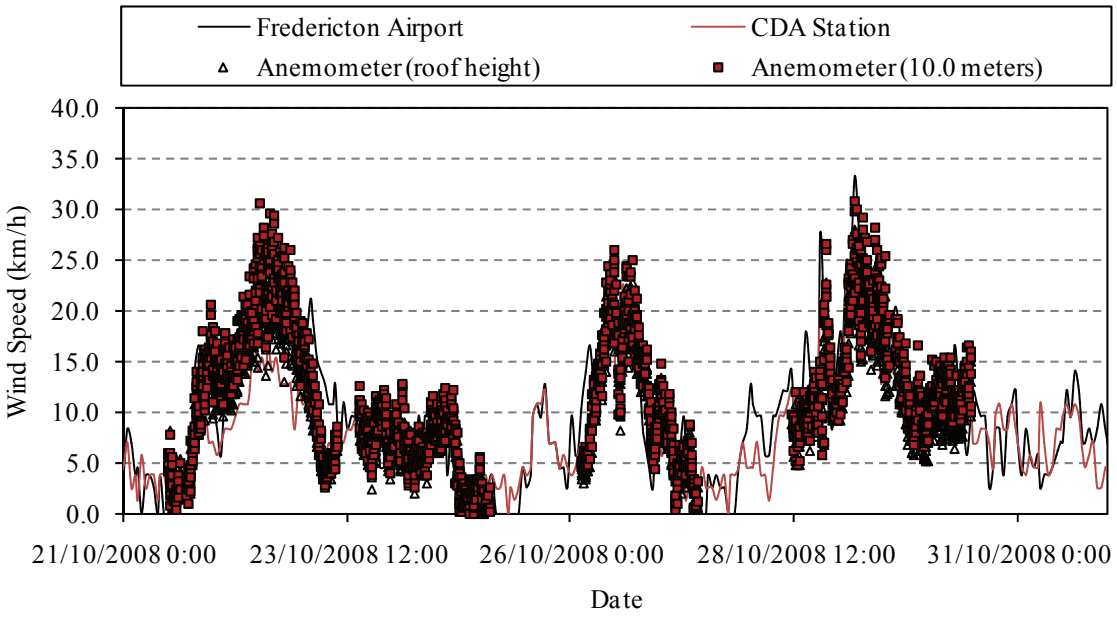

Figure 5.1 Wind speed comparison (5-minute averaged values).

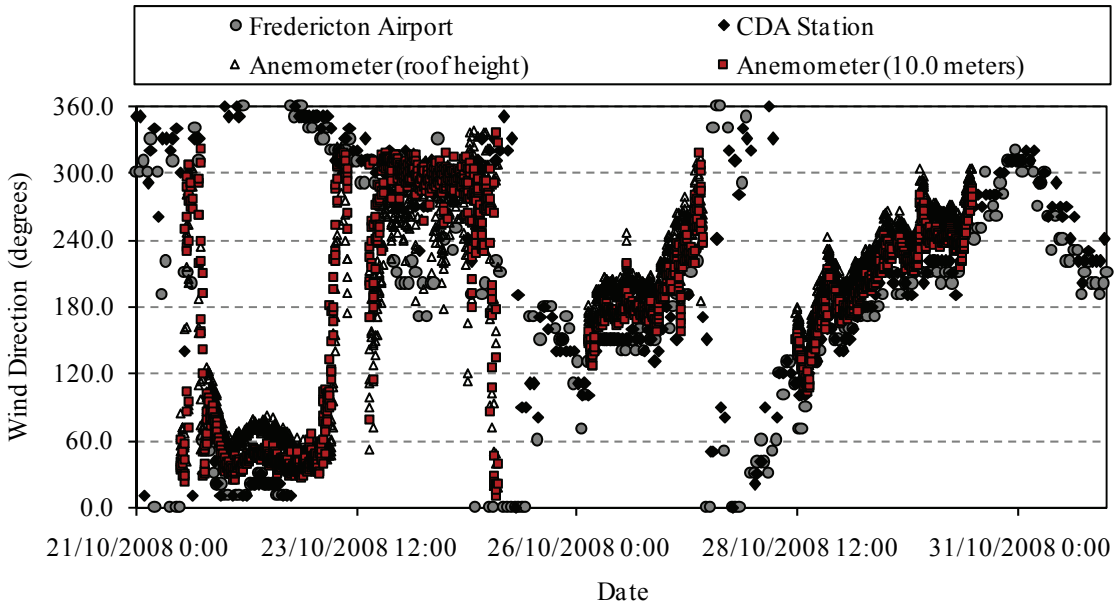

Figure 5.2 Wind direction comparison (5-minute averaged values).

5.2.2 Static load tests

The test building is resting on top of the 27 foundation load cells. As previously described, there is no other point of contact between the foundation wall and the superstructure besides these load cells. To verify their accuracy and performance a series of controlled tests were carried out. More specifically, the test building was subjected to a static ramp load using an external loader (Figure 5.3). The point of application was at the top of the wall close to the wall-to-roof intersection. The applied load was monitored by using a "pancake" type tension/compression load cell connected to the main data acquisition system. The load level was controlled by the loader driver and was increased periodically using intervals of approximately 60 seconds and a load step of 1 kN.

Figure 5.3 Application of static ramp load at the top of the North-West and South-East walls.

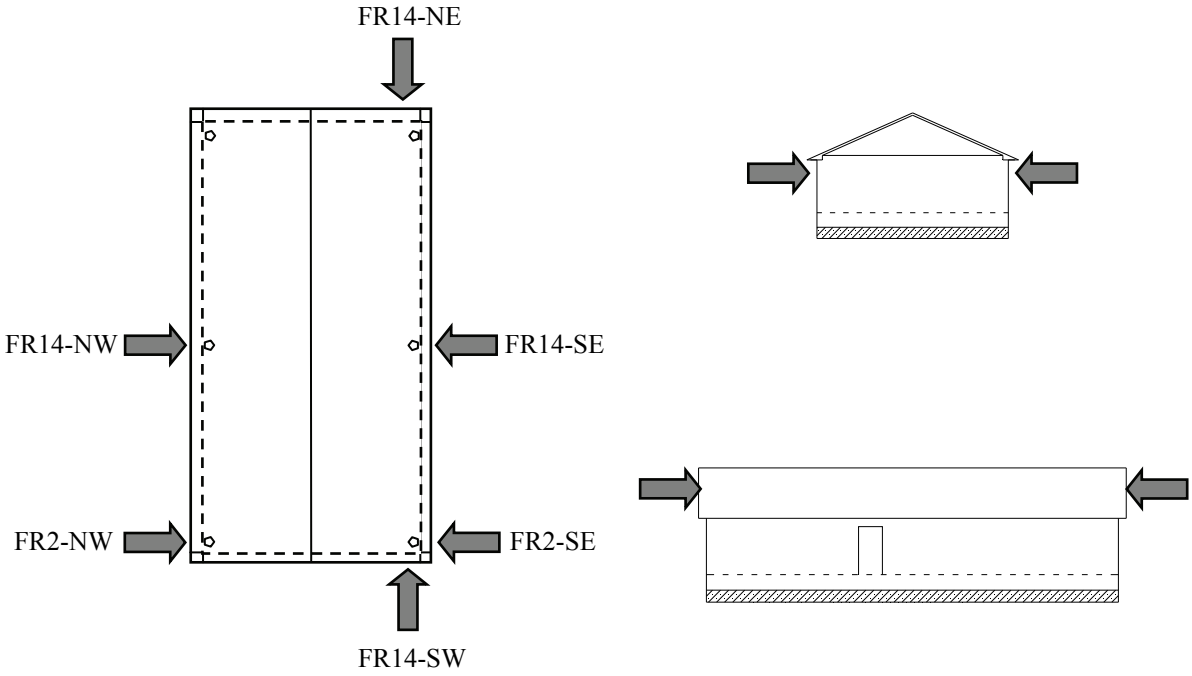

Figure 5.4 Location of static load test application points (plan and side views).

The location of the application points is presented in Figure 5.4. In total, six tests will be reported examining the performance of the load cells in the two horizontal directions. Although the vertical direction was of greater importance to this study, it was not possible

to perform a vertical load test due to unavailability of a static load frame and appropriate equipment. The notation used for the tests comprised by the frame number and the orientation of the wall that the load is applied to. For example, for static load test FR14-NW the point of application is on the 14th frame of the North-West wall. The results are presented in Figure 5.5 to Figure 5.7. The maximum load applied was determined based on the shear wall capacity (i.e. non-destructive maximum deflection) on the direction tested and was ranging between 1.5 and 8.0 kN.

The tests performed on the North-West and South-East walls show excellent agreement between the externally applied and the recorded by the load cells total foundation load. It should be mentioned that the measured (by the load cells) load is fluctuating, as it includes a wind-induced load component. Despite the efforts to conduct the static load tests during relatively calm wind periods, the duration of each test made it almost impossible to exclude some wind gust effects from the load monitoring. This effect is more pronounced in tests FR2-SE and FR14-SE (Figure 5.6), during which the wind speed reached the 25 km/h level. The other two tests were performed in the longitudinal direction which allowed reaching higher load levels. As it can be seen in Figure 5.7, the agreement between the applied load and that recorded by the load cells is excellent for lower stress levels. The two signals diverge when the applied load exceeds the 4-5 kN level, which indicates a possible unlocking of some internal stresses (e.g. temperature deformations). Another possibility could be a contact point at the foundation level during large diaphragmatic deformations. In any case, the particular phenomenon occurs for significantly high structural system deformations, which could only be generated by very high intensity winds (over 90 km/h).

The above comparisons verified that the foundation load cell array performs exceptionally well in both horizontal directions. The fact that the two horizontal components do not show any indications of malfunction or a non-proper placement to achieve structural isolation (foundation wall to rigid floor interface), provides equal confidence for their functionality in the vertical direction. In addition, the total vertical measured load by the foundation load cells was found to be in agreement with the approximate estimation of the dead and equipment loads.

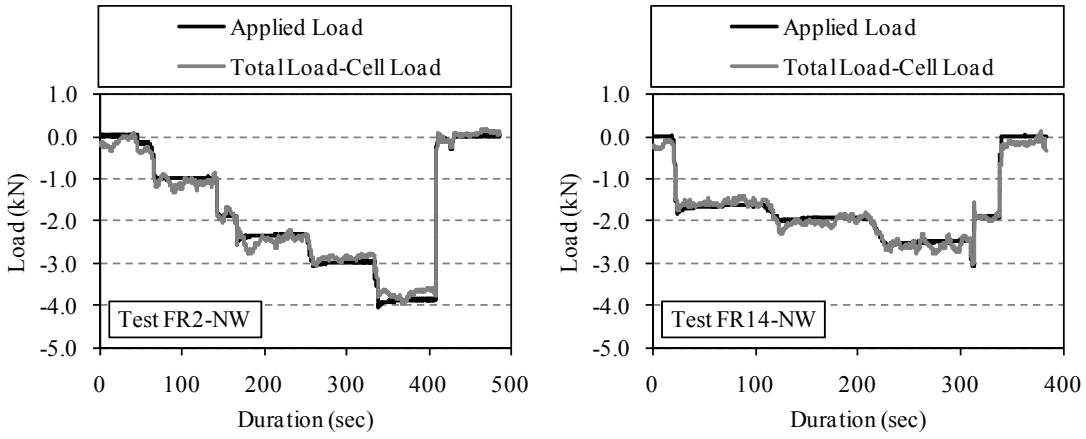

Figure 5.5 Static load test verification results for FR2-NW and FR14-NW tests.

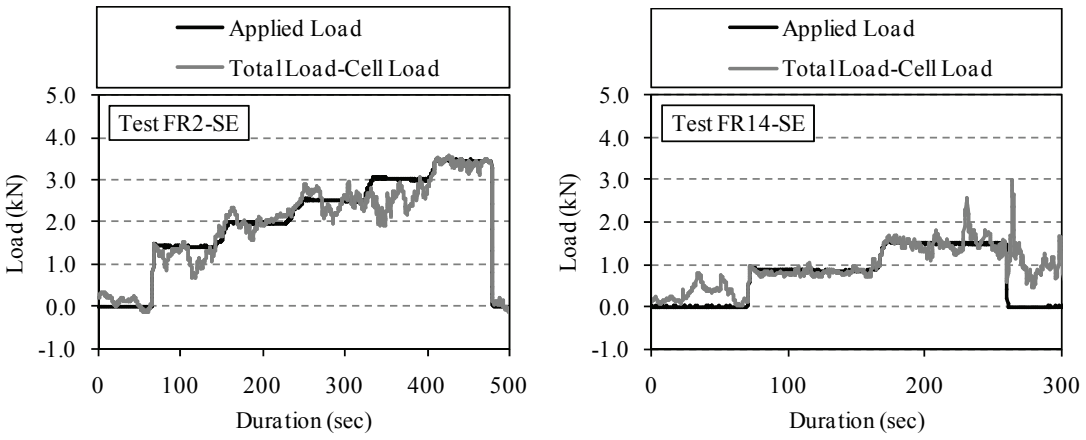

Figure 5.6 Static load test verification results for FR2-SE and FR14-SE tests.

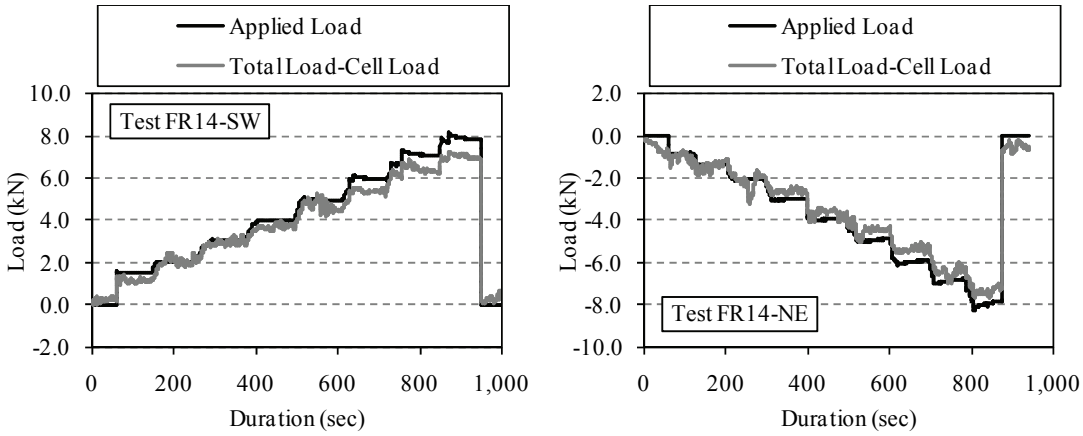

Figure 5.7 Static load test verification results for FR14-SW and FR14-NE tests.

5.3 Verification of Field Records

5.3.1 Stationarity on field records

Field studies and full-scale data are of extreme importance and in most cases demand a considerable amount of time and resources to be invested. Furthermore, these studies suffer from several equipment-related issues that could potentially compromise the quality of the acquired information. More specifically, wind and load monitoring data collected through the various instruments installed on the weather towers and the test building had to be verified before proceeding with a more detailed analysis and interpretation. Increased attention was paid to the inspection of the anemometer data (i.e. wind speed and direction) which also was the checkpoint for the qualification of the complete data set/record for further analysis.

All data acquired from the sensors were exported in the form of time histories. These functions can be considered as random processes with specific statistical properties (Figure 5.8 – note that the DADiSP data analysis software was used to derive these properties) highly influenced by the nature of the processed signal. For wind-related

studies an important aspect of the time-history is its stationarity. In order to characterise a random process as stationary its statistical properties should not be dependent on the selected time origin. Two basic statistical properties of a random process used to evaluate stationarity are the mean (first moment - $\mu_x(t_1)$) and the autocorrelation function (joint moment - $R_{xx}(t_1,t_1+\tau)$). If these two descriptive statistical properties do not vary with time the random process is called stationary. There are two forms of stationarity i.e. weak and strong. As Bendat and Piersol (2010) indicate, in most of the practical applications the strong stationarity criterion can be assumed often after proving the weak stationarity existence.

For wind-related studies the stationarity criterion is verified for both wind speed and wind direction and it is computationally efficient to examine the mean square value instead of the autocorrelation (Levitan 1988). There are also various methods to verify if a record of specific duration is stationary or not. The first, rather subjective, step is the visual inspection of the signal trace which helps to identify significant trends in the data. This process is also useful to diagnose problematic sensor behaviour or other physical instabilities that make the use of the recorded data unreliable. The visual inspection is followed by a more detailed analytical procedure using two non-parametric tests i.e. the RUN and the TREND (Reverse Arrangements) tests. As previously mentioned, these tests are applied for both mean and mean square values. Although both tests are used to identify non-stationarity of a random process, the RUN test is particularly efficient on revealing fluctuating trends, whereas the TREND test spots any underlying monotonic trend (Murphy, 1971).

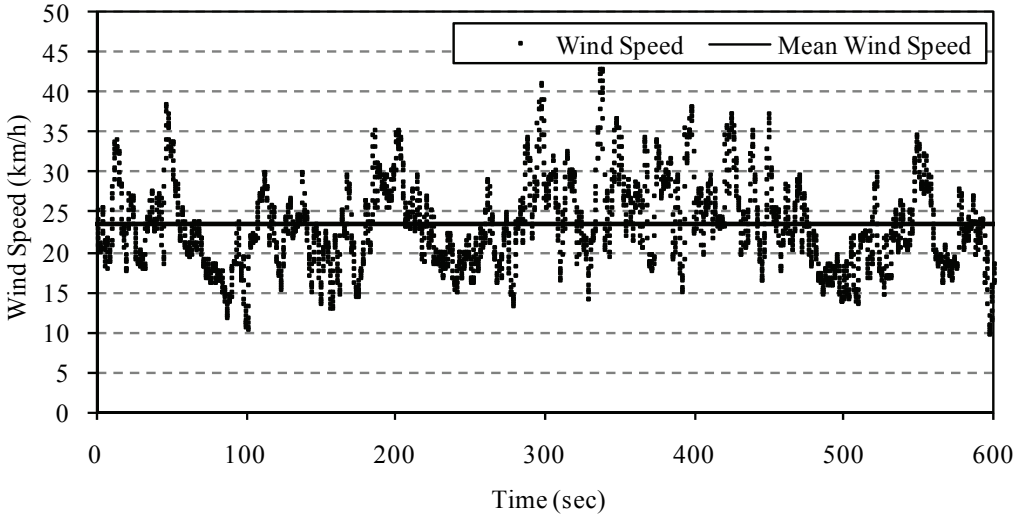

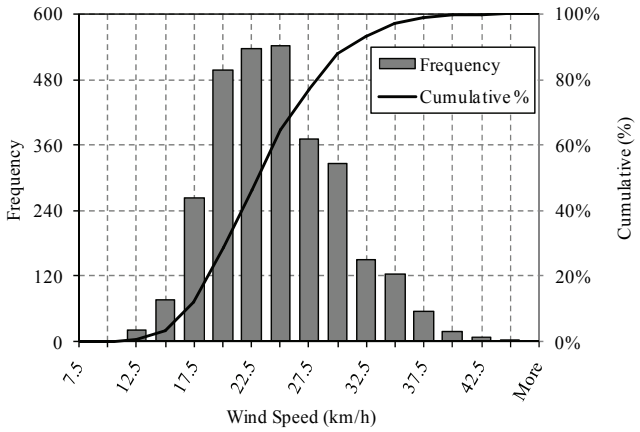

Mean	23.52
Standard Error	0.10
Median	22.89
Mode	18.98
Standard Deviation	5.44
Sample Variance	29.59
Kurtosis	0.06
Skewness	0.50
Range	33.27
Minimum	9.89
Maximum	43.16
Sum	70556.27
Count	3000.00
Largest (1)	43.16
Smallest (1)	9.89
Confidence Level (95.0%)	0.19

Figure 5.8 Descriptive statistics of a 10-minute wind speed record.

Table 5.1 Descriptive statistical properties for random data (after Bendat and Piersol, 2010).

Mean value	$\bar{x} = \frac{1}{T}\int_0^T x(t)dt$
Mean square value	$\overline{x^2} = \frac{1}{T}\int_0^T x^2(t)dt$
Variance	$s_x^2 = \frac{1}{T}\int_0^T [x(t) - \bar{x}]^2 dt$
Standard deviation	$\sigma_x = \sqrt{s_x^2}$
Moving average	The n-order moving average function of a sequence $\{x_i\}_{i=1}^{N}$ is a new sequence $\{y_i\}_{i=1}^{N-n+1}$ where y_i is given by: $y_i = \frac{1}{n}\sum_{j=1}^{i+n-1} x_j$
Cross-correlation function (of two quantities x(t) and y(t))	$R_{xy}(\tau) = \frac{1}{T}\int_0^T x(t)y(t+\tau)dt$ τ is the delay and can be either negative or positive
Auto-correlation function	$R_{xx}(\tau) = \frac{1}{T}\int_0^T x(t)x(t+\tau)dt$ τ is the delay and can be either negative or positive

5.3.2 Description of stationarity checks

The field monitoring produced a vast amount of data which, as a result, made their handling and interpretation a time consuming and computationally demanding process. The primary filtering criterion applied to the available records was the stationarity

verification. The identification was performed in two phases, namely Phase I which includes the preliminary visual and moving average slope inspections, and Phase II which includes the RUN and TREND tests. Furthermore these verifications were performed for the mean and mean square values of both wind speed and wind direction.

5.3.3 Visual inspection and moving average slope

Due to the large number of available records an analytical routine was developed to divide longer traces into 10-minute duration segments and estimate their linear moving average slope. Then the qualified segments were inspected visually for abnormalities or sudden instabilities (e.g. spikes, steps etc).

In more detail, the data acquisition system was set to monitor for approximately 24 hours with a sampling rate of 5 readings per second (5 Hz). The acquired block of data was then saved in binary format and then the system was restarted for the new scanning session. Wind speed and direction data (at 5.5 and 10 meters height) were extracted from each master file and used to further extract the 10-minute duration segments (3000 scanning frames) at a rate of 12 seconds (60 scanning frames). This approach was used to increase the segment sampling grid from 10 minutes (i.e. simply divide the master file into 3000 scanning frames segments) to 12 seconds (i.e. extract 3000 scanning frames every 60 frames). The next step was to compute the 30-second average and standard deviation values of each 10-minute segment, which resulted into a sequence of 20 discrete points. These points were then plotted and a least squares polynomial fit was performed to estimate the slope of the sequence. The qualification criterion for this slope was set to ±2.5% of the mean sequence value (Figure 5.9). Qualified 10-minute segments

were those which fulfilled the ±2.5% slope criterion for the mean and standard deviation sequences of the wind speed and direction values, both at 10 meters height. Moreover, only records maintained a mean wind speed over 15 km/h were considered. Finally, a schematic of the process is shown in Figure 5.10.

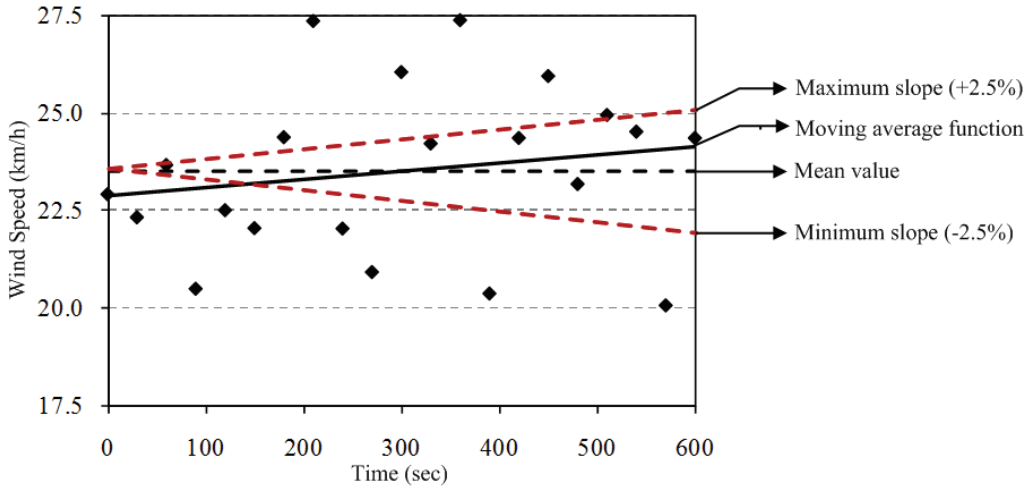

Figure 5.9 Qualification criterion for the first phase stationarity check.

5.3.4 RUN and TREND tests

The second and more detailed phase of stationarity verification was conducted to the visually inspected and PHASE I qualified records by using the RUN and TREND tests. Both tests were applied to a sequence of independent sample measurements, i.e. wind speed and direction, for both mean and mean square values. Special attention was paid to properly identify the interval length and assure independence of the sequential data. The process described by Levitan (1988) has been implemented to identify the interval length based on the field observations.

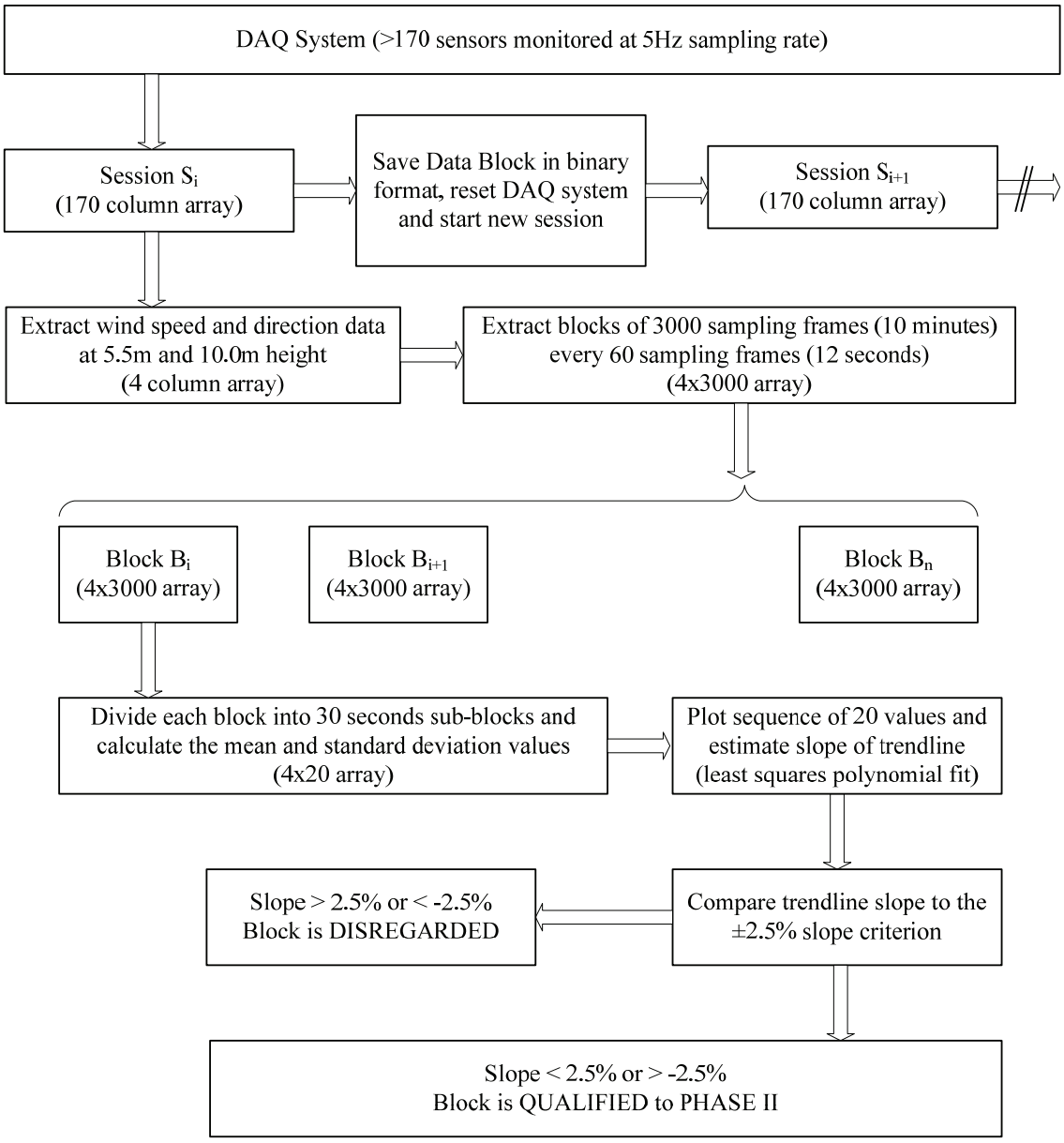

Figure 5.10 Schematic process of the first phace stationarity check.

Several representative wind speed and direction records have been selected and used to plot the variation of the autocorrelation function with respect to time. Two representative plots are presented in Figure 5.11 and Figure 5.12 and include wind speed and direction for records acquired during October 2008 and May 2009. As the plots

indicate the time lag should be at least 25 seconds to assure independence between the samples used in both RUN and TREND tests. To better demonstrate the effect of the time lag, three intervals were considered, starting from 30 seconds and then move to 40 and 50 seconds. Before presenting the results from these two tests a brief description of the computational process will be provided.

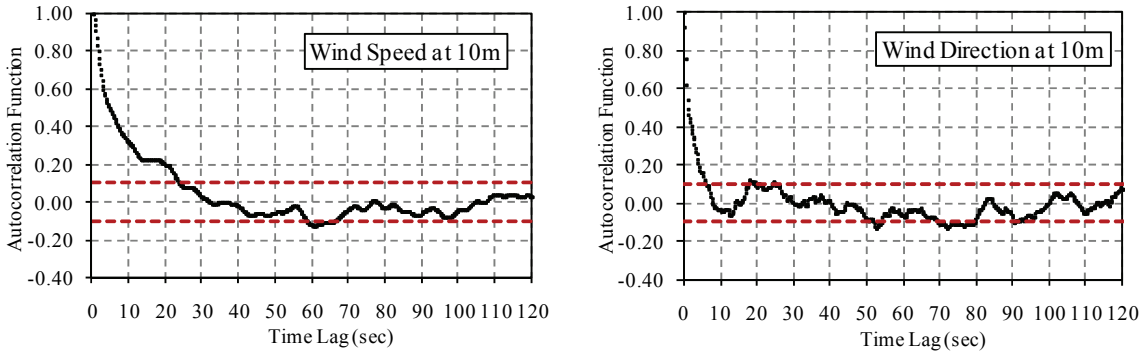

Figure 5.11 Autocorrelation function of the wind speed and direction at 10 meters height (October 29, 2008).

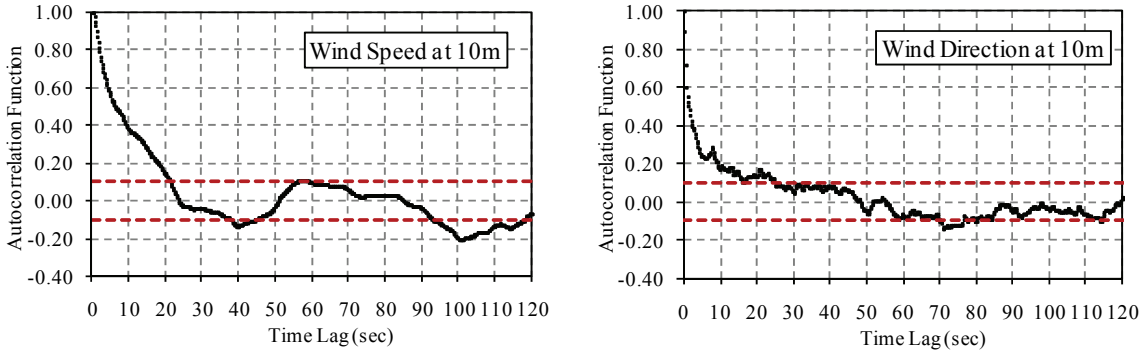

Figure 5.12 Autocorrelation function of the wind speed and direction at 10 meters height (May 21, 2009).

RUN test

The RUN test is preferably used to identify fluctuating trends. The examined record is divided into N equal independent intervals and then the mean and mean square values are calculated. This provides a sequence of N mean and mean square values which are used as input data to the RUN test and to identify the number of same sign observations. Denoting x_i and x_i^2 as the random mean and mean square variables with i = 1, 2, ..., N and $\bar{x}$ and $\overline{x^2}$ as the mean values of the mean and mean square sequence, the following two conditions are examined:

$$x_i > \bar{x} \tag{5.1}$$

$$x_i^2 > \overline{x^2} \tag{5.2}$$

If the first condition is satisfied we assign in the RUN sequence a "+" sign whereas in the case where the second condition is valid we assign a "-". After evaluating the conditions for all random variables of each sequence (mean and mean square values) we count the number "runs" i.e. the number of sequences with identical observation (either "+" or "-"). This number is then compared to the critical values $r_{N/2;1-\alpha/2}$ and $r_{N/2;\alpha/2}$, provided by the table "Percentage points of RUN distribution" (APPENDIX A), for level of significance "α". The stationarity criterion is satisfied, if the number of "runs", denoted as r, satisfies the following condition:

$$r_{N/2;1-a/2} < r < r_{N/2;a/2} \tag{5.3}$$

For the case where r falls outside the two limits, the "runs" are not independent and the record is considered as non-stationary.

TREND test

In a similar manner the TREND test, or also known also as Reverse Arrangement test, is used to identify monotonic trends in the sequence of the mean and mean square values. For this test we need to count the number of reverse arrangements using the following process.

Denoting as N the number of independent random observations (mean and mean square values), and x_i and x_i^2 the random mean and mean square variables with i = 1, 2, ..., N, the condition $x_i > x_j$ where j>i is considered. The factor h_{ij} is introduced and is defined as:

$$h_{ij} = \begin{cases} 1 \; if \; x_i > x_j \\ 0 \; if \; x_i < x_j \end{cases} \tag{5.4}$$

whereas the number of reverse arrangements is then given by:

$$A = \sum_{i=1}^{N-1} \left(\sum_{j=i+1}^{N} h_{ij} \right) \tag{5.5}$$

The stationarity criterion is satisfied, if the number of reverse arrangements satisfies the following condition:

$$A_{N;1-a/2} < A < A_{N;a/2} \tag{5.6}$$

where $A_{N;1-\alpha/2}$ and $A_{N;\alpha/2}$, are the critical values provided by the table "Percentage points of TREND distribution" (APPENDIX A), for level of significance "α". For the case where A falls outside the two limits, the record is considered as non-stationary.

5.3.5 Final selection

The PHASE I selection resulted in 163 qualified records, out of which 41 were acquired in 2008 and 122 in 2009. The records are presented in Figure 5.13 in a polar plot where both the mean wind speed and direction (10 minutes duration) are identified. It should be noted that the majority of the records have a North-West angle of approach and that only six records exceeded the mean wind speed of 30 km/h (246.5 to 13.5 degrees). Figure 5.14 presents the same records indicating the 3-second gust speed which exceeded the 60 km/h in only 7 cases.

The 163 qualified records were then considered for the RUN and TREND tests. The confidence level for both tests was 95% and three time lag cases were examined, i.e. 30, 40 and 50 seconds time lag. The first case resulted in 87 stationary records (Figure 5.15), the second case in 93 stationary records (Figure 5.16) and the last one in 106 stationary records (Figure 5.17). Detailed results of both PHASE I and II stationarity checks can be found in APPENDIX A. It should be mentioned at this point that, after considering the autocorrelation function of several records (see Figure 5.11 and Figure 5.12), the records of the 30 seconds time lag were selected for further analysis. Moreover, only a limited number of these records were acquired with the pressure taps open, i.e. no precipitation was expected therefore the taps were not protected. These records were used for both pressure and load data interpretation whereas the rest of the stationary records were considered for load and wind data analysis.

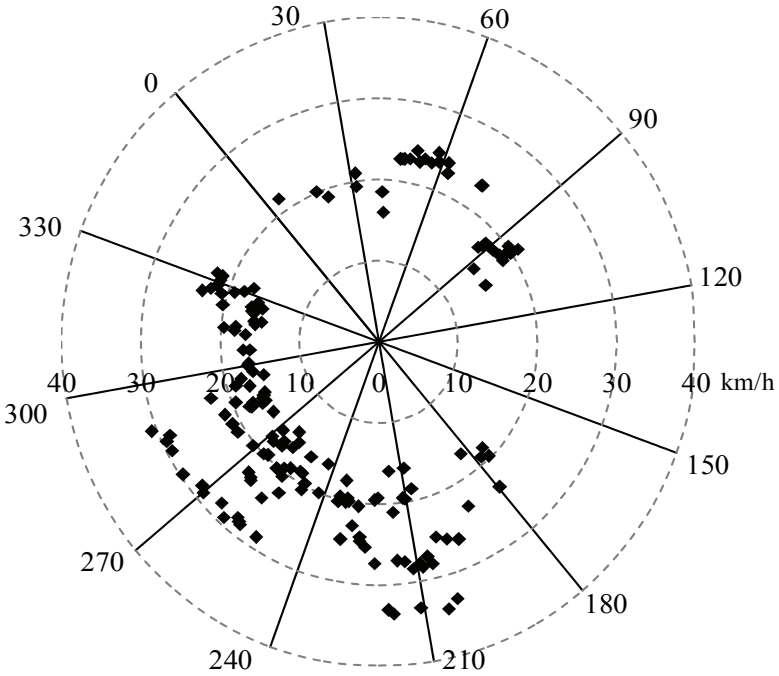

Figure 5.13 Mean wind speed and direction of PHASE I records.

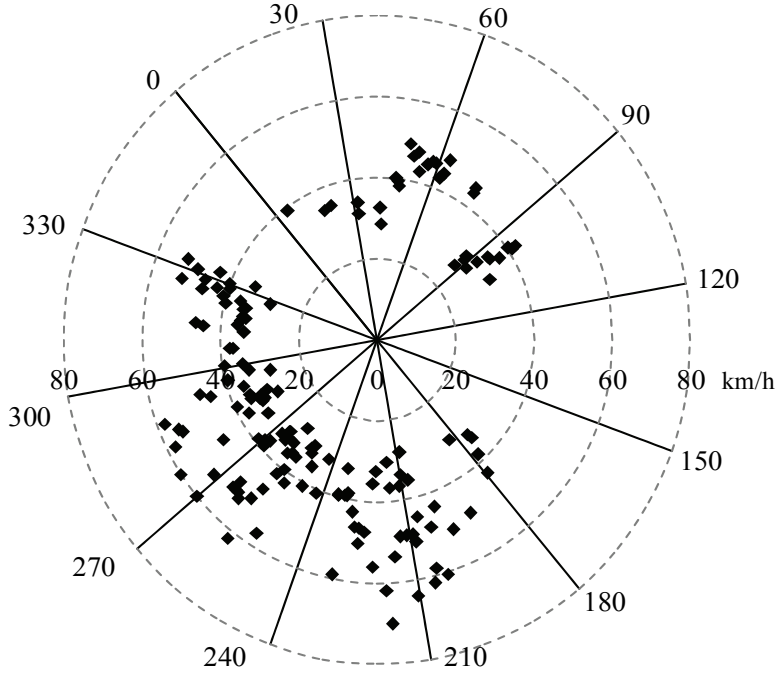

Figure 5.14 Gust speed and direction of PHASE I records.

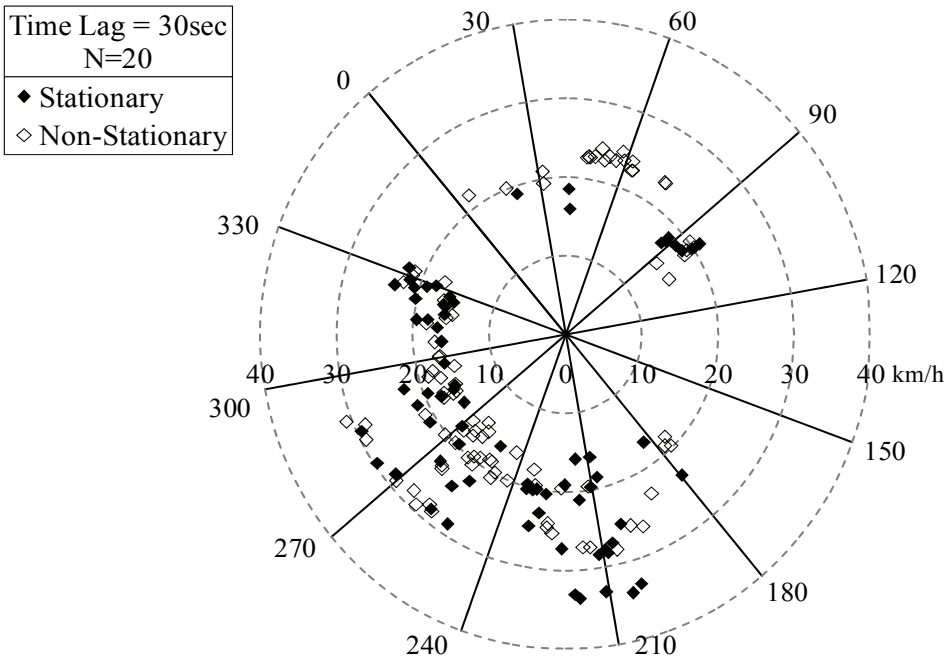

Figure 5.15 Stationary and non-stationary records of RUN/TREND tests for 30-sec time lag.

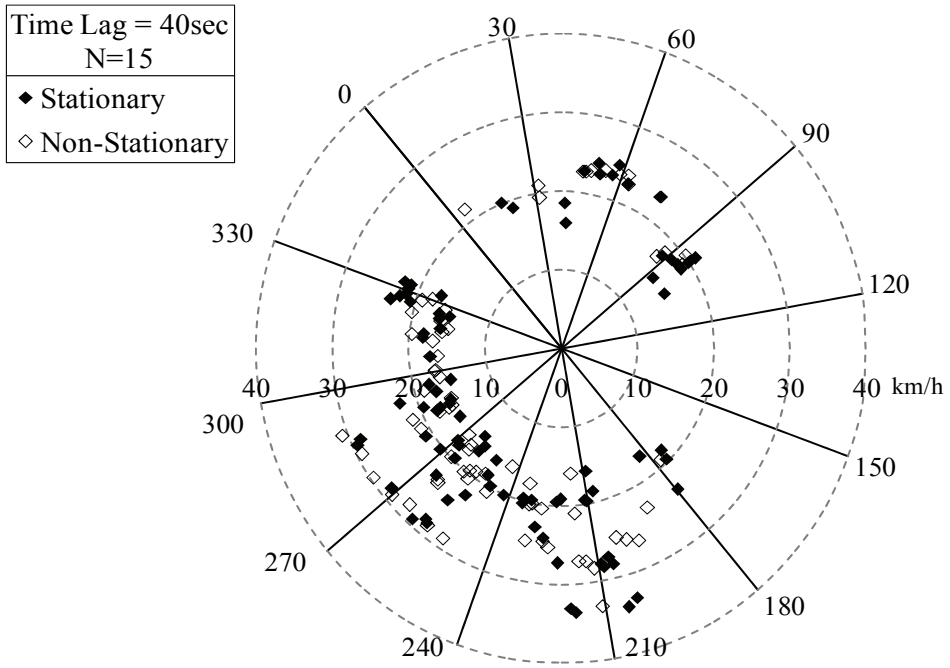

Figure 5.16 Stationary and non-stationary records of RUN/TREND tests for 40-sec time lag.

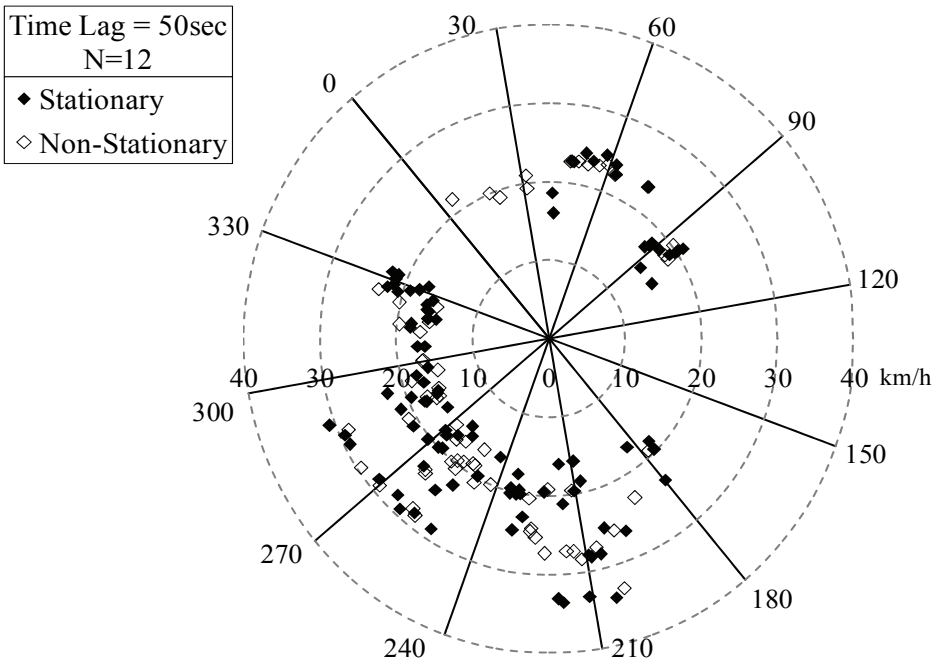

Figure 5.17 Stationary and non-stationary records of RUN/TREND tests for 40-sec time lag.

5.4 Wind Tunnel Simulation

5.4.1 Repeatability

The wind tunnel experiments were conducted in several stages taking always in consideration updates from the field monitoring. The repeatability of the tests was verified on several occasions showing that the obtained results are in good agreement regardless of the period they were carried out. To demonstrate this agreement the results from two wind tunnel runs are compared in terms of mean and peak local pressure coefficients. This comparison includes all wall and roof pressure taps and is presented in Figure 5.18 to Figure 5.20. As the mean pressure coefficients scatter plots reveal, the repeatability for all three simulated terrains (i.e. Open, Light Suburban and Heavy Suburban) is excellent. The peak pressure coefficients, as expected, compare very well

with only few outlined points from the 45-degree line. Similar results have been observed for other wind directions as well.

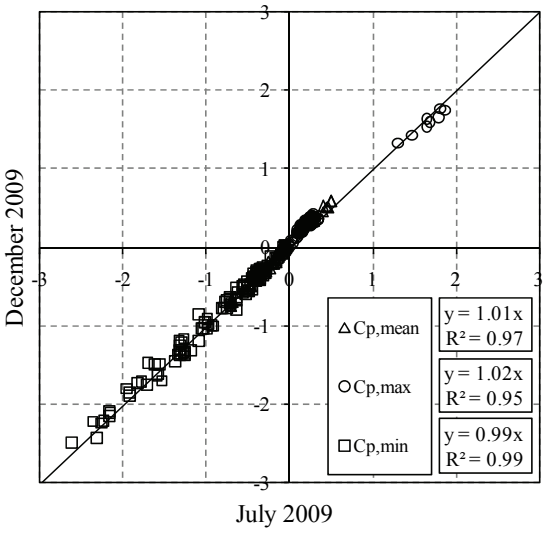

Figure 5.18 Roof and wall local pressure coefficients for Open Terrain exposure (220 degrees wind direction).

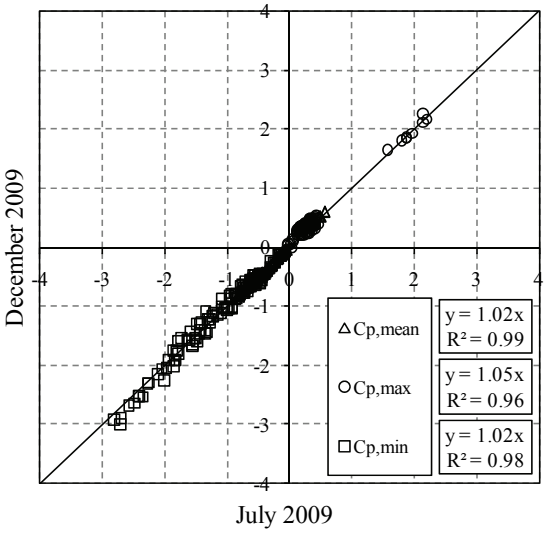

Figure 5.19 Roof and wall local pressure coefficients for Light Suburban Terrain exposure (220 degrees wind direction).

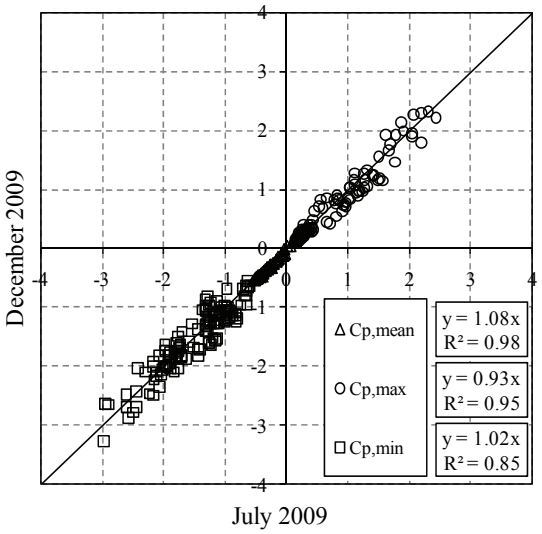

Figure 5.20 Roof and wall local pressure coefficients for Heavy Suburban Terrain exposure (130 degrees wind direction).

5.5 Numerical Simulation

5.5.1 Dead load distribution

For the vertical direction (i.e. uplift foundation forces), the verification of the numerical model was performed by using the dead load distribution as the static load tests were only available for the two horizontal directions. Several full-scale records with low wind speed were selected and the dead load distribution was measured by the 27 foundation load cells. The comparison between the individual load cell readings for these records and the numerical simulation results for low wind load is presented in Figure 5.21 and Figure 5.22. The agreement for most of the reactions is satisfactory with some higher discrepancies occurring on the South-East wall. In addition, the total vertical load for the full-scale case is equal to 187 kN, whereas the estimated by the numerical model dead load is 180 kN.

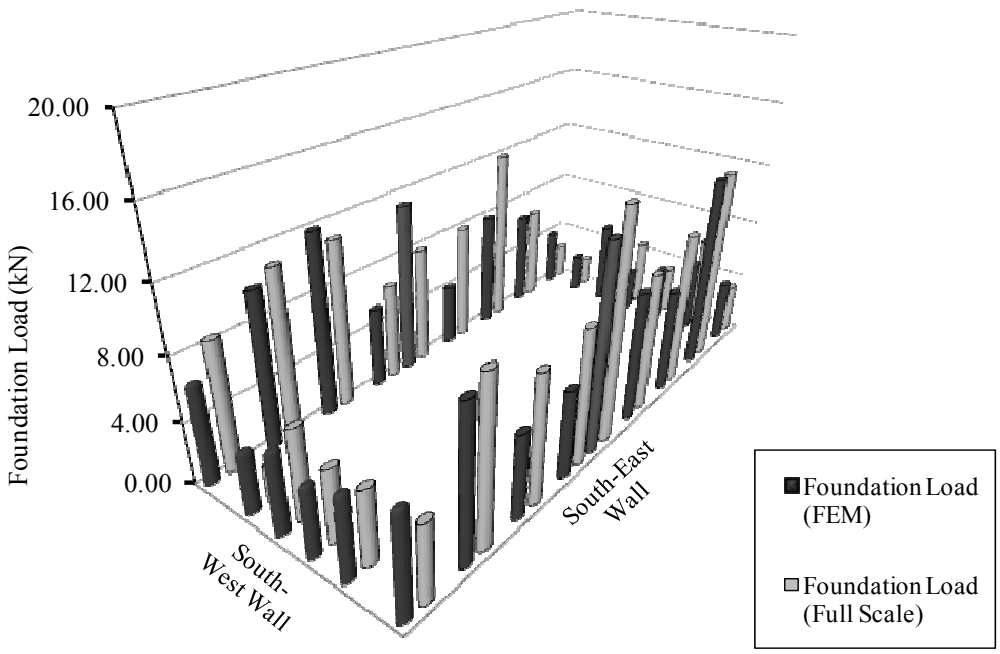

Figure 5.21 Dead load distributions in test building and finite element model.

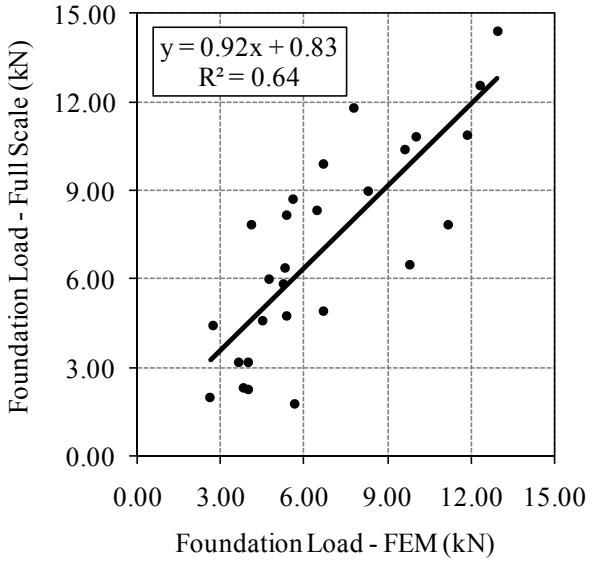

Figure 5.22 Comparison of foundation dead load measured by individual load cells and that estimated by FEA.

CHAPTER 6
EXPERIMENTAL AND NUMERICAL SIMULATION RESULTS AND DISCUSSION

6.1 Introduction

The effect of wind-induced pressures on structures has been studied thoroughly. Almost all of the conducted studies have been focusing extensively on how the pressure distribution can be precisely and accurately predicted, initially through wind tunnel studies and later through -limited- full-scale experiments. The limitation of all wind tunnel pressure studies was the fact that it was not possible to examine the wind-induced forces in the structural system and foundation. Moreover, as discussed in Chapter 2, almost all of the full-scale studies, related to low-rise buildings, did not incorporate any force measurements in the field monitoring process.

The most important concept of the current thesis is the wind load path. Lack of significant full-scale studies related to wind load paths, initiated this collaborative effort which has as main objective to better understand and define how wind pressure is transformed to actual load and transferred through building elements to the foundation level. This path can only be captured by monitoring real wind events using strain sensors at key points of the structural system. In addition to the envelope pressure characteristics, strain data provide the appropriate information to successfully map the wind load flow. Each of the structural components has its own importance and effect in the total response and reaction of the structure. Dissipation of the applied energy occurs at various stages

and in most cases is part of a highly non-linear process. In some cases these phenomena are treated from current provisions by approximations; e.g. the 30% reduction of the effective wind load for the design of the foundation, suggested by National Building Code of Canada (NBCC 2005, Users Guide - figure I-7).

There was a vast amount of data acquired through the field monitoring as well as in the wind tunnel experiments. In the following sections, results from all three approaches, i.e. field studies, wind tunnel simulation and finite element analysis, are presented and compared. The results identify important parameters related to the exposure characteristics which need to be considered in the wind tunnel simulation process. Then, findings are grouped in two main sections; those related to envelope pressures and those describing the wind-induced uplift forces at the roof and foundation levels. Of particular importance, is the identification of the wind load distribution to the concrete foundation walls as well as the attenuation identified as the wind load is transferred through the structural system.

6.2 Weather Tower Monitoring

6.2.1 Exposure characteristics

The experimental building is located in a light suburban area with some low-height obstacles in close proximity. In order to verify this subjective observation, the basic exposure characteristics (power law exponent, turbulence intensity and roughness length) were evaluated using field data acquired from the two anemometers of the North-West meteorological tower (at 6.5 and 10.0 meters height). Records collected during October to November 2008 and April to June 2009 were considered for this study and only those

which fulfilled the stationarity criteria were used for further analysis. Using the 10-minute averaged statistical values (mean and standard deviation), filtered to retain data with mean wind speeds over 4 m/s (at 6.5-meter height), the power law exponent, turbulence intensity and roughness length values were calculated with respect to the approaching wind direction. During the period between December 2008 and March 2009 the data acquisition system was not operational due to lower temperatures and snow accumulation on top of the roof.

The results are plotted in terms of power law exponent, turbulence intensity and roughness length for all available full-scale wind directions and are presented in Figure 6.1 to Figure 6.3 respectively. The power law exponent ranges from 0.10 to 0.50, the turbulence intensity from 24% to 47% and the roughness length from a few millimeters up to 0.90 meters. Even if the data are grouped within a wind direction range that results in similar properties (e.g. South-West region) the mean values still vary significantly. For instance, the power law exponent takes its highest mean value of 0.36 (0.08 standard deviation – see Figure 6.1) for the wind direction range 230 to 290 degrees, whereas the lowest mean value of 0.20 (0.05 standard deviation) occurs at the 70 to 125 degrees wind direction range. Similar findings occur for the roughness length distribution over different wind angles of attack. As Figure 6.3 shows, the roughness length takes values from a few centimetres up to 0.9 meters. As expected, the higher roughness lengths correspond to those wind directions for which a higher power law exponent was estimated (e.g. 230 to 290 degrees wind direction range). On the contrary, the turbulence intensity levels are more consistent with lower variations. The estimated values range between 32% and 37%, at roof height, for all wind direction ranges (Figure 6.2).

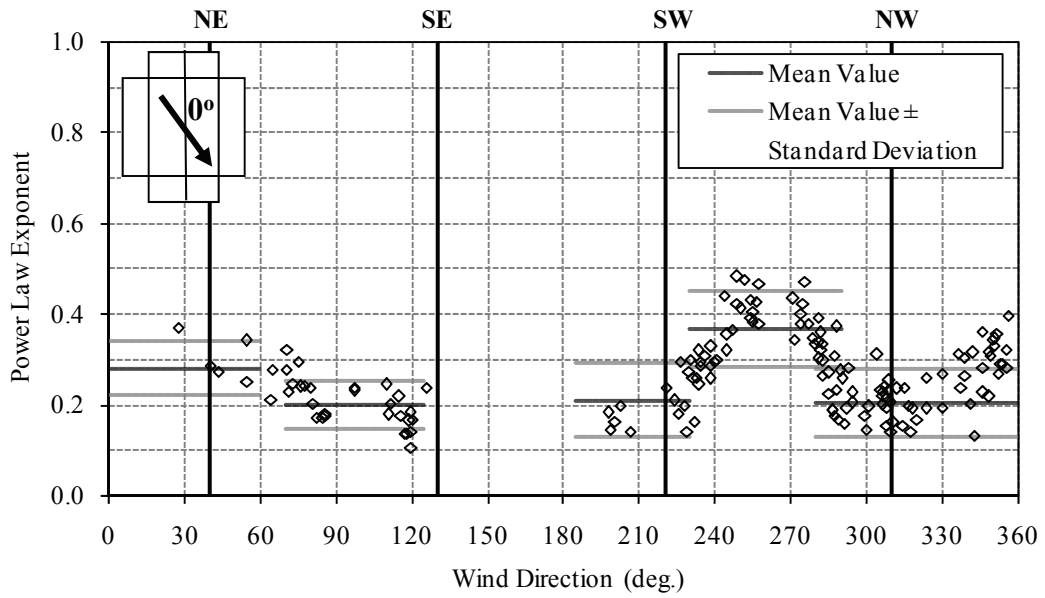

Figure 6.1 Power law exponent variation with respect to direction.

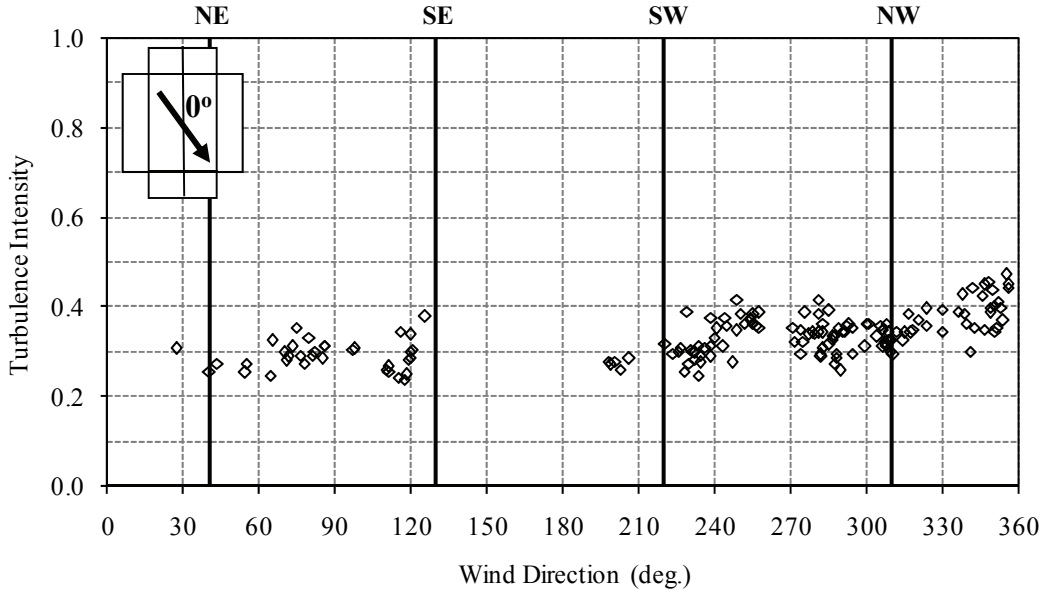

Figure 6.2 Turbulence intensity (roof height) variation with respect to direction.

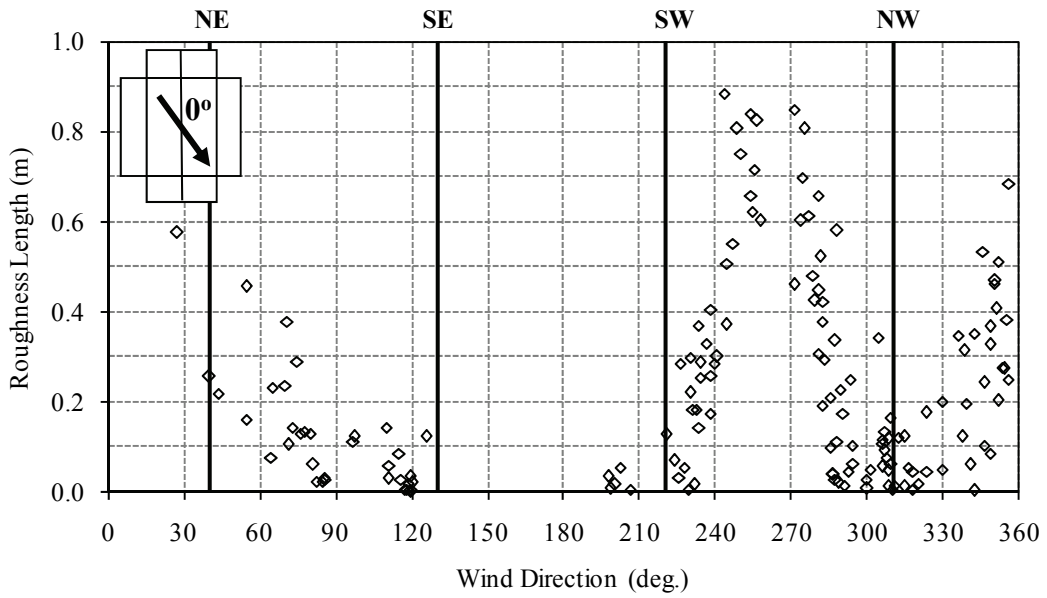

Figure 6.3 Roughness length variation with respect to direction.

It is quite interesting to examine how these properties vary for different angles of attack, considering that the test building, as previously indicated, is located in a light suburban area with only a few low-rise buildings and medium height trees in the proximity. Following current wind provision guidelines and "common" wind engineering sense, the terrain would be classified in the open to suburban region expecting a power law exponent in the range of 0.20. The higher variations should be clearly attributed to the influence of adjacent buildings (north and south sides) and forestry area (east side) located inside a radius of 300-400 meters fetch. These deviating terrain properties indicate that complex terrains need to be examined carefully in order to properly conduct scaled model tests and to successfully compare full-scale and wind tunnel results. Regarding the wind tunnel tests of the particular study, these upstream terrain properties were the basis for the selection of the three major simulated terrains that were selected; i.e. open, light suburban and heavy suburban.

6.3 Wind-induced Envelope Pressures

6.3.1 General

To verify the agreement between the field and model scale pressure results, the field records were compared to three wind tunnel test exposures (open, light suburban and heavy suburban). Only stationary full-scale records with the pressure taps open (i.e. no rain or snow was expected during the day) were used for this analysis. The mean pressure coefficients were calculated using Equation 3.12 and the peak pressure coefficients were estimated using the method proposed by Wang (2005). It should be noted that only representative graphical results are presented in this chapter. All results available are presented in APPENDIX B.

6.3.2 Comparison between full-scale and wind tunnel pressure coefficients for individual pressure taps

The first comparison between wind tunnel experiments and full-scale pressure monitoring was performed in terms of mean and peak pressure coefficients, considering each of the forty full-scale pressure taps individually. The notation of the pressure taps can be seen in Figure 4.7. As previously discussed, the field records were of 10-minute duration, therefore the mean pressure coefficient was calculated by dividing the 10-minute average surface pressure recorded by the pressure tap by the 10-minute average dynamic pressure at the roof height. The peak pressure coefficient was the ratio of the 3-second peak pressure (i.e. 3-sec moving average peak) recorded within the 10-minute record to the 10-minute average dynamic pressure at roof height. The wind tunnel pressure coefficients were estimated following the same approach. The thirty-six wind

directions tested in the wind tunnel allowed the formation of three discrete pressure coefficient trends for each of the upstream terrains; i.e. open, light suburban and heavy suburban. The field data were then added as single points representing the values of 10-minute records of specific wind incidents.

In Figure 6.4, results from a representative roof pressure tap ($P_{R,2}$) are presented. The mean pressure coefficients show an excellent agreement for most of the available stationary field records. The variation between the three wind tunnel pressure trends is not significant for most of the wind directions, therefore there is no particular improvement in the comparisons for any of the three simulated terrains. The comparison of peak pressure coefficients is characterized as satisfactory for both maximum and minimum values. The full-scale minimum pressure coefficients are in closer agreement to the heavy suburban wind tunnel results. As can be seen in Figure 6.4, a limited number of field values exceed the estimated wind tunnel minimum pressure coefficients by as much as 25%. These discrepancies can be attributed to the fact that for most field records the wind direction was variable and the standard deviation had values of 15-25 degrees which, of course, was not the case in the wind tunnel experiments where the wind direction remained practically constant.

Representative pressure coefficient results are presented in Figure 6.5 for a wall pressure tap ($P_{SW,6}$). Similar to the roof pressure tap, the full-scale mean pressure coefficients compare very well with wind tunnel values. Once more, the wind tunnel curves for the three different upstream terrains are in close agreement with each other as well as with the field values. As far as the peak pressure coefficients are concerned, the agreement is considered very good with most of the field values to be located close to the

wind tunnel curves. Both minimum and maximum full-scale pressure coefficients seem to be in closer agreement to the light suburban wind tunnel values, particularly for the region between 280-290 degrees for which the power law exponent seems to be decreasing towards the 0.20 mark (see Figure 6.1).

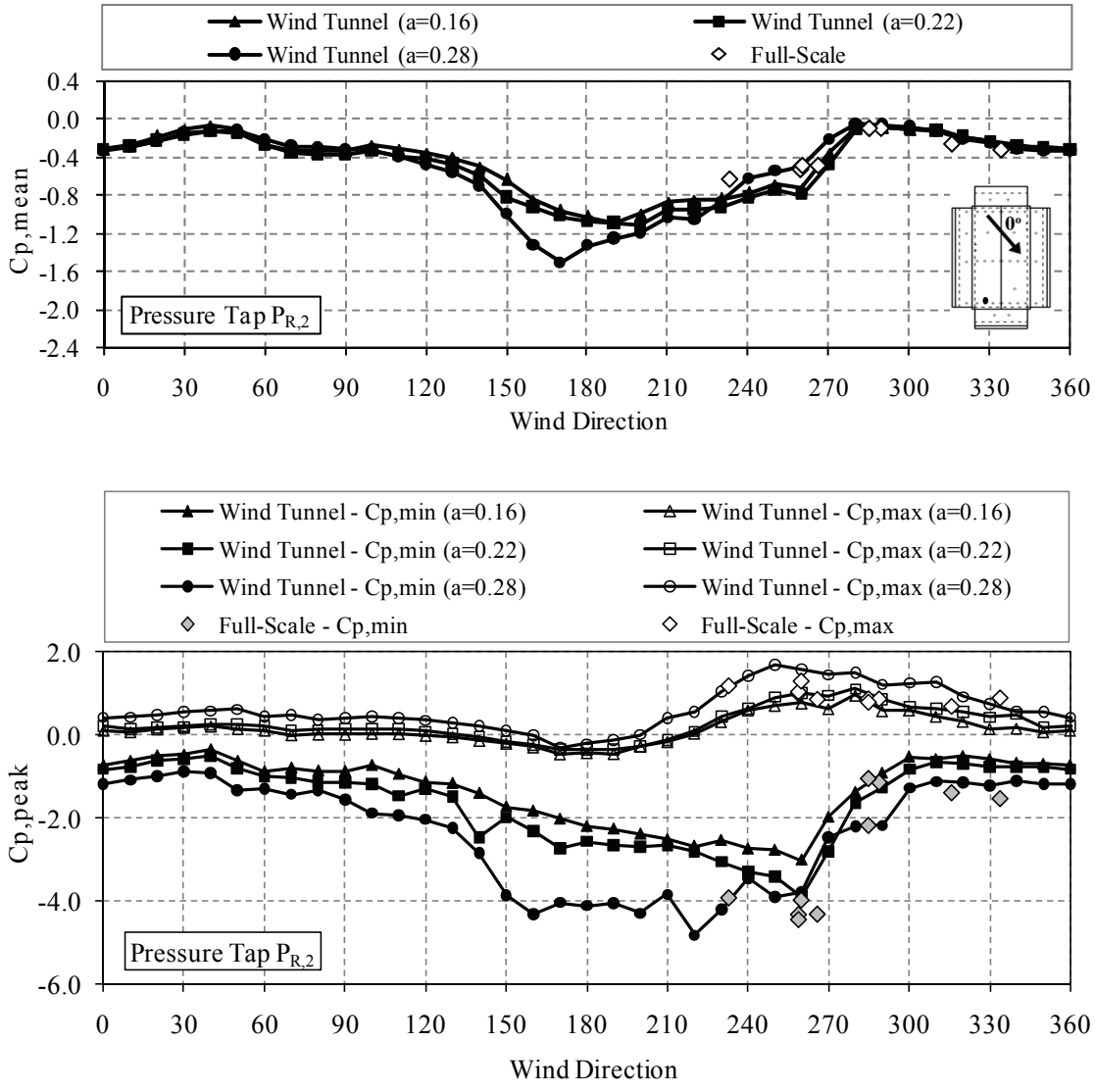

Figure 6.4 Mean and peak pressure coefficient variation for roof pressure tap $P_{R,2}$.

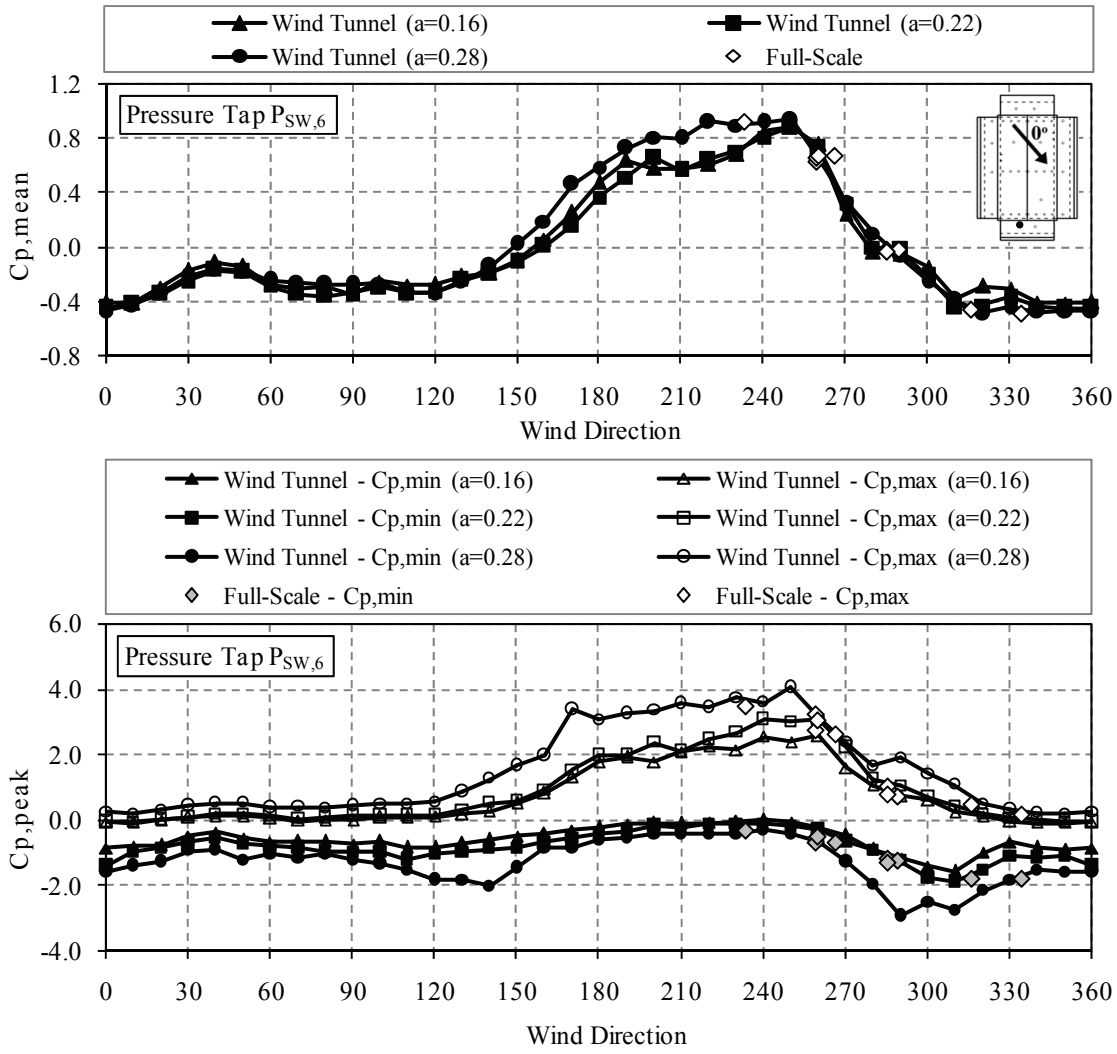

Figure 6.5 Mean and peak pressure coefficient variation for wall pressure tap $P_{SW,6}$.

The results of the rest of the thirty-eight roof and wall pressure taps are presented in APPENDIX B. In general, the majority of the mean pressure coefficients are in good agreement with most of the field values to be very close to the light/heavy suburban wind tunnel curves. The limited discrepancies occur mainly on roof pressure taps and only for a single wind direction. Regarding the peak pressure coefficients, the comparisons indicate a satisfactory agreement for most of the wall and roof pressure taps. As it has been reported in previous field studies (Cochran and Cermak 1992, Bienkiewicz and Sun

1992), the comparison becomes problematic for pressure taps located close to the ridge or the corners of the roof. In particular, roof pressure taps $P_{R,4}$, $P_{R,44}$ and $P_{R,76}$ show significant departure of the field values from the heavy suburban wind tunnel curve. The discrepancies between the field and wind tunnel minimum pressure coefficients for certain directions exceed a factor of two (e.g. $P_{R,4}$). It should be noted that such discrepancies occur only for pressure taps located on the windward side of the roof. Corner and close to the ridge roof pressure taps located on the leeward side of the building do not show any particular deviation.

6.3.3 Comparison between full-scale and wind tunnel pressure coefficients for all pressure taps

In addition to the individual pressure tap and frame comparisons, the wind tunnel tests are verified by comparing mean and peak pressure coefficients from all wall and roof pressure taps. As was presented and discussed in the previous comparisons, some of the discrepancies between the field and wind tunnel pressure coefficients were attributed to the fluctuations of the wind direction in the 10-minute full-scale records. More specifically, the wind tunnel tests were conducted at thirty-six distinct wind angles of attack whereas field records were characterized by high variability in wind direction even during shorter periods of time. To account for these directional fluctuations the field mean and peak pressure coefficients from 10-minute records were compared to a range of wind tunnel directions (with ± 20 degrees of any nominal direction - which is close to the standard deviation of the wind direction in most field records). Therefore, for this analysis a single full-scale record was compared to five different wind tunnel cases and

this process was repeated for each of the forty pressure taps. The final scatter plot, for all 40 pressure taps, was formed only with the results corresponding to the wind direction that seemed to be predominant through each individual comparison.

A representative comparison is presented in Figure 6.6, in which a 10-minute record from May 21, 2009 is compared to the wind tunnel results. For the specific record, the mean wind speed at 10 meters height was 28.0 km/h and the mean wind direction at the same height was 259.4 degrees with a standard deviation equal to 14.9 degrees. Considering the mean wind direction of approximately 260 degrees the full-scale mean and peak pressure coefficients were compared to the wind tunnel results for the range of 240 to 280 degrees. By following this approach the agreement between the two experimental results is significantly improved. As the graph clearly shows, positive and negative peak values compare quite well with only few outliers from the generally tight correlation between field and wind tunnel pressure coefficients. The coefficients of determination (i.e. R^2) are equal to 0.99, 0.92 and 1.00 for the cases of the mean, minimum and maximum pressure coefficients respectively. The agreement is particularly good even for the extreme peak values, such as the absolute minimum and maximum pressure coefficients, which for the specific record reach the values of -4.7 and +2.7 respectively.

Additional full-scale records were plotted using the same approach and are presented in APPENDIX B. These records were recorded during October 2008 and June 2009 and in all cases the agreement is very good. Discrepancies occurred for pressure taps close to the ridge and roof corners and discussed in the previous sections seem to be reduced when additional wind tunnel cases are considered in the comparison. There are still some

- limited – single pressure taps that deviate from the 45-degrees center line which indicate that for certain wind directions and pressure tap locations, the wind tunnel cannot adequately reproduce particularly high suctions.

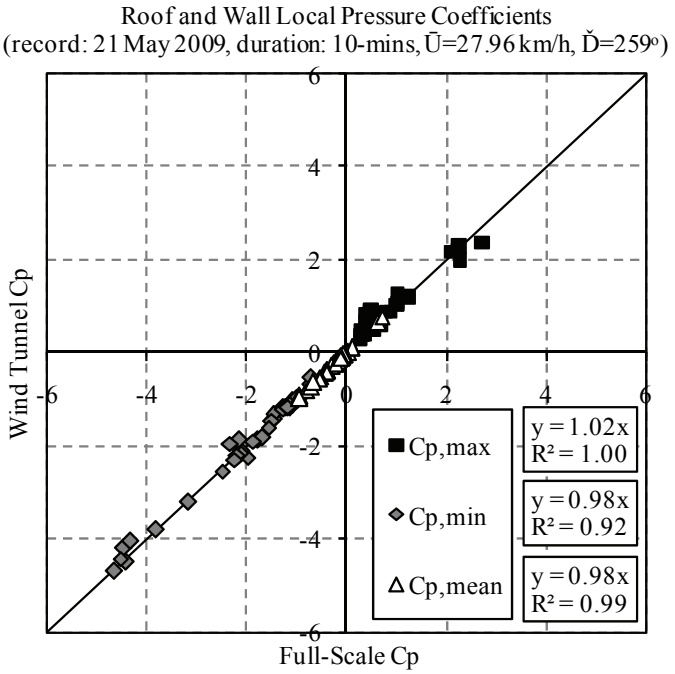

Figure 6.6 Comparison of wind tunnel and field mean and peak pressure coefficients (21 May, 2009).

6.3.4 Comparison between full-scale and wind tunnel pressure coefficients for individual frames

The results from the individual pressure tap comparisons were grouped in such manner so as to demonstrate the agreement or discrepancies of three main frames of the test building. The frames, namely Frame 2, 14 and 28 (Figure 6.7), were instrumented with roof load cells at the truss to wall interface and foundation load cells directly below them between the I-Joist wall and the concrete foundation wall. Furthermore, each frame has

two wall and eight roof pressure taps along its center-line which makes possible the real-time monitoring of the applied and induced wind structural forces. This is of particular interest to further analyse the structural behaviour of these frames using finite element analysis.

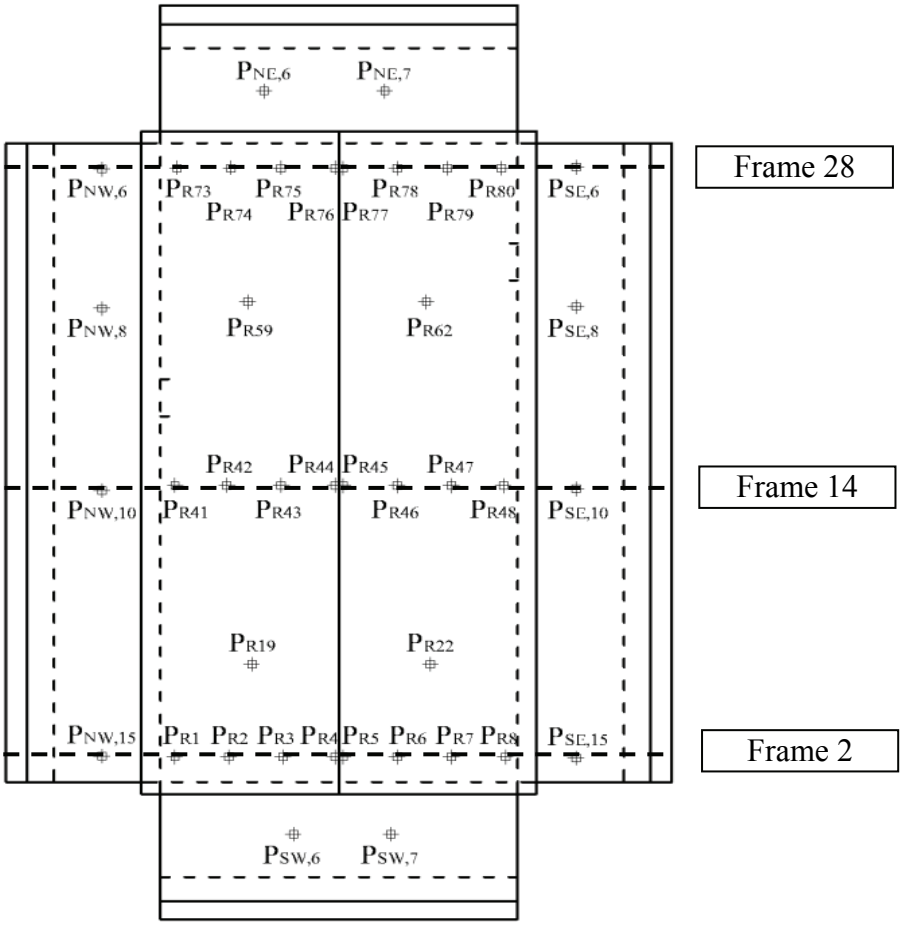

Figure 6.7 Instrumented frames in full-scale test building.

Four representative full-scale records were considered and compared to the wind tunnel results. More specifically, 10-minute full-scale records, from May and June 2009, were selected and the mean and peak pressure coefficients were calculated using the

method discussed in the previous section. The wind direction of the field records was fluctuating, therefore only the average value was considered for selection of the appropriate wind tunnel case. The results include all three wind tunnel upstream terrain cases and the field values are depicted as single points for each individual pressure tap. One of the four cases is presented in Figure 6.8 (mean pressure coefficients) and Figure 6.9 (peak pressure coefficients) for Frame 14. This particular case refers to an average wind direction of 240 degrees. As Figure 6.8 clearly shows, the agreement is excellent for the mean pressure coefficient comparison. Full-scale values for all pressure taps are in close agreement to the heavy suburban wind tunnel mean pressure coefficients. The peak pressure coefficients show an excellent agreement for the pressure taps located on the leeward side of Frame 14 (i.e. South-East side – see Figure 6.9). The rest of the pressure taps are in close agreement with the highest discrepancies occurring on the windward wall and the close to the ridge roof pressure tap. These discrepancies can be justified if we consider the higher wind direction fluctuation in the full-scale record. The rest of the examined frames and wind direction cases are presented in APPENDIX B. In most cases the agreement between the field and heavy suburban wind tunnel mean pressure coefficients is particularly good whereas the peak pressure coefficient comparisons indicate, in agreement to the previous section's results, that close to the ridge and corners suctions tend to be underestimated by wind tunnel experiments. This can be clearly seen in the case of 260 degrees wind direction, in which the field peak pressure coefficient for Frame 28 is close to -2.0 whereas the heavy suburban wind tunnel coefficient is just over -1.0. Similar values are presented for other wind directions as well.

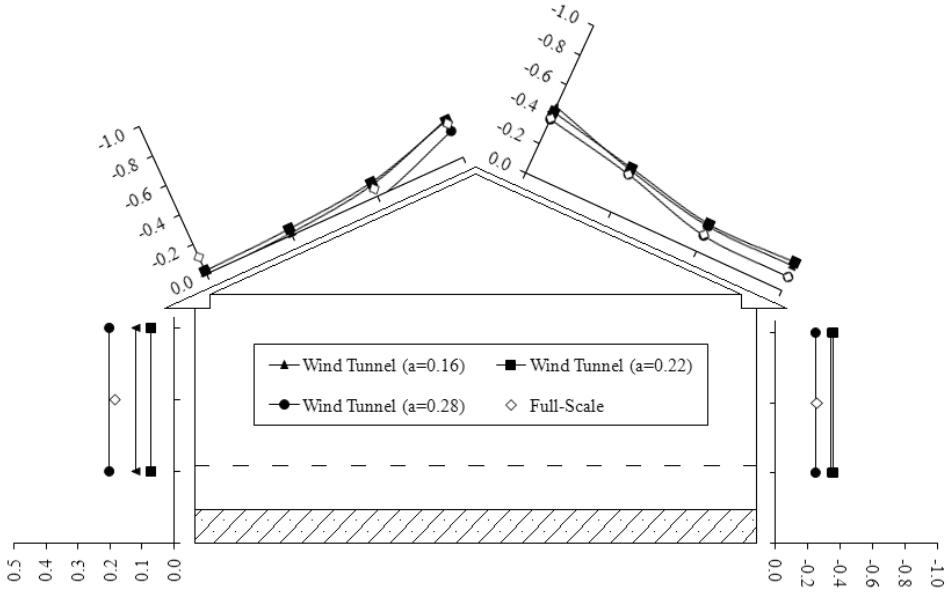

Figure 6.8 Mean pressure coefficients for Frame 14 (240 degrees wind direction).

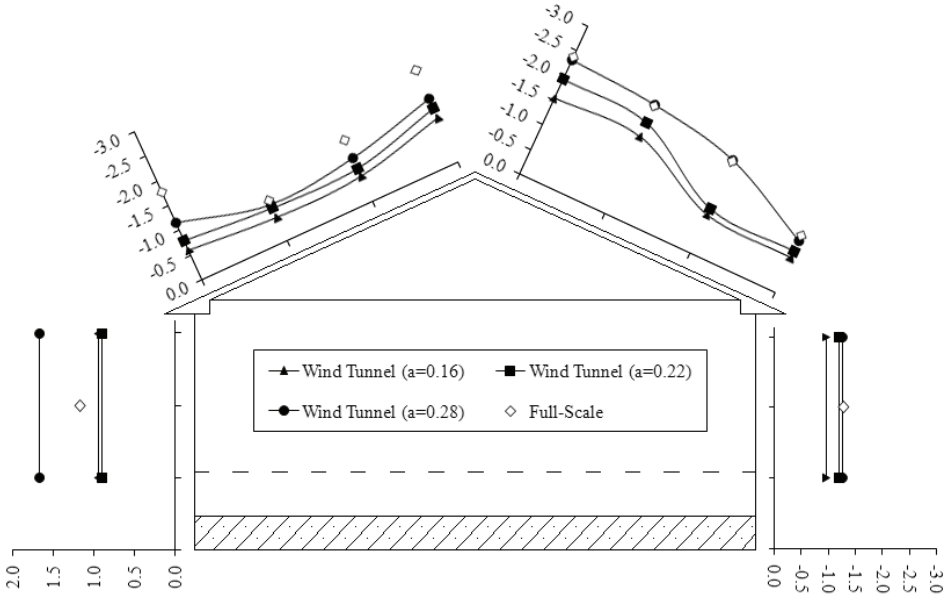

Figure 6.9 Peak pressure coefficients for Frame 14 (240 degrees wind direction).

6.4 Wind Uplift Force Distribution

6.4.1 General

The test building was equipped with twenty-seven foundation load cells and six roof load cells. The particular characteristic was unique for wind-induced pressure and force monitoring. While exposure and pressure measurements were of great importance, particularly on the verification process of the wind tunnel experiments, the load cell measurements offered the ability to study how wind-induced forces flow within the structural system of low-rise wood buildings. Data from both roof and foundation load cells were acquired and processed to identify possible patterns and correlation between various building locations and levels. As previously mentioned, the horizontal foundation loads were excluded from the analysis in the current study due to contamination of the signals with non-linear temperature related deformation and consequently internal stresses.

6.4.2 Uplift load correlation between roof and foundation load cells

As a first approach towards the identification of wind load paths, i.e. wind-induced force flow field, a total of twenty-two 10-minute full-scale records were selected on the basis of the stationarity criterion and the weather conditions (e.g. rain did not allow the pressure monitoring). The records used and details about the wind characteristics at 10 meters height are presented in Table 6.1. These records were acquired during May and June of 2009. Scope of this analysis was to examine how well correlated are the traces recorded at the roof level and at the foundation level. This would help us identify how a specific roof-to-wall vertical load is affected, and possibly attenuated, as it is transferred

down to the foundation level through various structural and non-structural components. Therefore, the cross correlation between the roof load cells located on Frame 14 ($L_{NW\text{-}R,2}$ and $L_{SE\text{-}R,2}$ – see Figure 4.5) and each of the foundation load cells located on the foundation wall below them was evaluated. For the calculation of the cross correlation the convolution method was used and the results were normalized from -1 to 1.

Table 6.1 Records considered for correlation analysis between roof and foundation load cell records.

Record ID	Start Date	Record Date	Record Time	Point ID	V_{10m} (km/h)				D_{10m} (deg.)	
					Mean	St.Dev.	Min.	Max.	Mean	St.Dev.
1	14-May-09	14-May-09	17:13:29	106081	34.0	7.9	14.4	58.2	204.9	13.7
2	14-May-09	15-May-09	1:26:42	30001	24.2	7.6	3.4	50.5	225.7	17.9
3	14-May-09	15-May-09	3:22:05	64621	22.9	6.9	6.5	43.0	228.6	18.0
4	20-May-09	20-May-09	14:18:08	110581	17.2	5.4	4.4	36.0	291.5	20.5
5	21-May-09	21-May-09	16:35:12	110281	28.0	7.8	9.4	50.7	259.4	14.9
6	22-May-09	22-May-09	11:10:26	48181	17.5	5.5	3.6	32.7	285.0	20.3
7	22-May-09	24-May-09	13:58:53	120241	20.3	6.9	3.2	39.5	234.6	20.4
8	25-May-09	25-May-09	12:41:17	87241	18.2	6.1	3.2	35.9	316.1	23.7
9	25-May-09	25-May-09	16:34:35	54901	21.4	7.9	4.2	48.8	330.8	30.6
10	27-May-09	27-May-09	18:06:19	74641	19.6	4.3	6.8	33.8	210.2	14.8
11	01-Jun-09	01-Jun-09	8:50:45	13021	23.0	7.2	7.6	51.6	265.5	15.0
12	01-Jun-09	01-Jun-09	15:29:04	109321	30.8	9.4	9.1	58.1	289.0	18.1
13	02-Jun-09	02-Jun-09	16:16:46	99421	21.4	5.9	8.6	39.3	285.2	16.4
14	03-Jun-09	03-Jun-09	14:49:34	49921	16.2	5.8	3.9	33.3	284.5	19.3
15	04-Jun-09	04-Jun-09	12:16:25	30241	15.7	4.9	5.1	30.5	286.6	22.9
16	08-Jun-09	08-Jun-09	11:02:15	41041	18.1	5.4	4.6	32.9	284.0	16.1

17	08-Jun-09	08-Jun-09	15:47:51	126721	17.1	6.4	4.2	33.8	333.0	34.1
18	17-Jun-09	18-Jun-09	12:08:18	74101	20.2	5.5	4.1	36.1	259.4	15.6
19	17-Jun-09	18-Jun-09	13:41:42	102121	17.6	5.3	2.6	32.6	233.4	21.5
20	19-Jun-09	21-Jun-09	16:51:02	516061	24.5	6.5	9.7	46.3	58.1	18.2
21	19-Jun-09	22-Jun-09	0:46:02	658561	22.8	7.0	7.7	47.6	53.0	17.5
22	22-Jun-09	22-Jun-09	1:38:13	185341	24.1	7.4	7.7	46.3	51.8	16.4

In Table 6.2, representative results are presented for both roof load cells. The third column indicated the cross correlation factors between roof load cell $L_{NW\text{-}R,2}$ and each of the foundation load cells located on North-West wall and the fourth column the cross correlation between roof load cell $L_{SE\text{-}R,2}$ and each of the foundation load cells located on the South-East wall. The results are sorted with respect to the direction which also helps to compare the correlation distribution between records with similar mean wind direction. It should be noted, that for clarity only cases with higher correlation were included in the results (i.e. values exceeding the value of 0.9). By carefully examining these results we can make the following comments:

- There is a smaller correlation between the roof load cells and the foundation load cells located directly below them, when the wind is approaching from South-West (i.e. perpendicular to the South-West wall). For example, the cross correlation factor takes its minimum value of 0.90 for the case of North-West wall when the wind direction is approximately 225 degrees, whereas the corresponding value for the South-East wall is even below 0.90. This is an indication that the two longitudinal walls act as rigid diaphragms when the load is parallel to the ridge, resulting into the spread of the vertical load to further foundation load cells but at the same time with smaller correlation.

- The foundation load cells of the windward wall, i.e. North-West wall for the most examined records, show the highest correlation for oblique directions. This is clearly demonstrated in case 18 (mean wind direction 259.4 degrees) in which eight out of nine foundation load cells exceed the value of 0.9.
- The foundation load cells of the leeward wall, i.e. South-East wall for most of the examined records, are in general highly correlated to the roof load recorded by the load cell located on top of the specific wall (i.e. $L_{SE\text{-}R,2}$). In most of the records the cross correlation factor exceeds the value of 0.95 for at least two of the adjacent to the mid-foundation load cell. A representative example is that of case 14 (mean wind direction of 284.5 degrees) for which the cross correlation factors for five foundation load cells are over 0.98.

Table 6.2 Cross correlation factors between roof and foundation load cell records for North-West and South-East walls.

Date (ID)	D_{10m} (deg.)	North-West wall	South-East wall
1	204.9	0.98 0.98 0.99 0.98 0.92	0.91 0.95 0.97 0.98 0.97 0.96 0.90
2	225.7	0.92 0.95 0.94 0.90 0.91	0.93 0.97 0.96 0.93
3	228.6	0.95 0.97 0.96 0.92 0.92	0.93 0.96 0.93
19	233.4	0.92 0.92 0.95 0.95	0.92 0.93 0.92 0.91
7	234.5	0.95 0.96 0.98 0.93 0.91	0.94 0.97 0.97 0.94
18	259.4	0.91 0.94 0.95 0.97 0.99 0.98 0.97 0.92	0.95 0.99 0.99 0.99 0.97 0.95

5	259.4	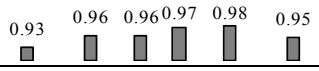	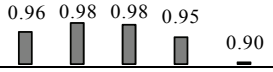
16	284.0	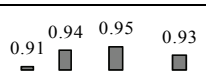	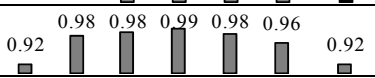
14	284.5		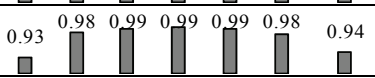
13	285.2	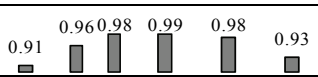	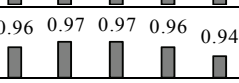
15	286.6	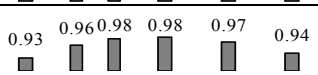	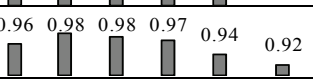
12	289.0	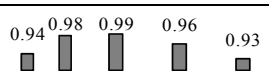	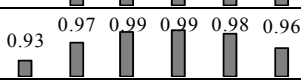
4	291.5	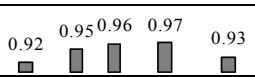	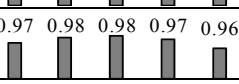
8	316.1	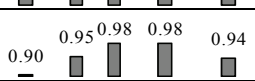	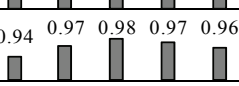
9	330.8	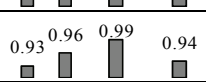	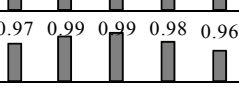
17	333.0	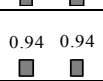	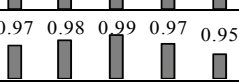

In addition to the individual foundation load cells, the cross correlation analysis was carried out considering records from the roof load cells located on Frame 14 ($L_{NW\text{-}R,2}$ and $L_{SE\text{-}R,2}$ – see Figure 4.5) and those of the sum of the foundation load cell records for each of the four foundation walls as well as the total foundation load. More specifically, the foundation load cells were grouped based on their location in order to calculate the total uplift force and the force of each foundation wall i.e. North-East, South-East, South-West and North-West walls. These five records were then compared to the load recorded from each of the roof load cells and the cross correlation factor was estimated for all 22 records presented in Table 6.1. The results of this analysis are presented in detail in Table 6.3. As expected, the highest correlation is observed between the roof load cell record and that of the wall located below the load cell. The cross correlation factors for this case are in most records over 0.90. Similar levels of correlation are observed also for the total foundation load. The wall opposite to the considered roof load cell has slightly lower correlation

values, whereas the two endwalls (North-East and South-West walls) indicate a significantly lower correlation for almost all records (<0.90).

Table 6.3 Cross correlation factors between local roof and foundation wall load records.

Date (ID)	D_{10m} (deg.)	Foundation Wall / Roof load Cell	North-East	South-East	South-West	North-West	Total
22	51.8	$L_{NW-R,2}$	0.69	0.94	0.82	0.95	0.94
21	53.0	$L_{NW-R,2}$	0.82	0.96	0.72	0.97	0.96
20	58.1	$L_{NW-R,2}$	0.76	0.97	0.87	0.97	0.96
1	204.9	$L_{NW-R,2}$	0.68	0.95	0.74	0.95	0.94
10	210.2	$L_{NW-R,2}$	0.68	0.92	0.62	0.92	0.89
2	225.7	$L_{NW-R,2}$	0.63	0.91	0.77	0.93	0.91
3	228.6	$L_{NW-R,2}$	0.72	0.92	0.73	0.95	0.92
19	233.4	$L_{NW-R,2}$	0.74	0.90	0.67	0.90	0.87
7	234.5	$L_{NW-R,2}$	0.77	0.90	0.62	0.93	0.90
18	259.4	$L_{NW-R,2}$	0.71	0.91	0.62	0.96	0.92
11	265.5	$L_{NW-R,2}$	0.16	0.89	0.99	0.87	0.91
16	284.0	$L_{NW-R,2}$	0.64	0.81	0.77	0.89	0.86
14	284.5	$L_{NW-R,2}$	0.71	0.88	0.80	0.95	0.94
6	285.0	$L_{NW-R,2}$	0.75	0.91	0.99	0.88	0.92
13	285.2	$L_{NW-R,2}$	0.78	0.88	0.83	0.94	0.92
15	286.6	$L_{NW-R,2}$	0.78	0.92	0.79	0.96	0.95
12	289.0	$L_{NW-R,2}$	0.59	0.88	0.87	0.93	0.92
4	291.5	$L_{NW-R,2}$	0.80	0.86	0.79	0.92	0.90
4	291.5	$L_{NW-R,2}$	0.69	0.92	0.71	0.97	0.95
8	316.1	$L_{NW-R,2}$	0.79	0.84	0.80	0.94	0.91
9	330.8	$L_{NW-R,2}$	0.71	0.77	0.70	0.90	0.86
17	333.0	$L_{NW-R,2}$	0.55	0.59	0.63	0.80	0.73
22	51.8	$L_{SE-R,2}$	0.57	0.92	0.83	0.82	0.86
21	53.0	$L_{SE-R,2}$	0.76	0.96	0.75	0.92	0.93
20	58.1	$L_{SE-R,2}$	0.75	0.98	0.89	0.96	0.96
1	204.9	$L_{SE-R,2}$	0.69	0.96	0.70	0.93	0.93
10	210.2	$L_{SE-R,2}$	0.71	0.89	0.57	0.84	0.83
2	225.7	$L_{SE-R,2}$	0.52	0.96	0.81	0.94	0.94
3	228.6	$L_{SE-R,2}$	0.69	0.93	0.72	0.90	0.90
19	233.4	$L_{SE-R,2}$	0.66	0.90	0.66	0.87	0.86
7	234.5	$L_{SE-R,2}$	0.67	0.94	0.64	0.93	0.92
18	259.4	$L_{SE-R,2}$	0.65	0.94	0.60	0.91	0.90

11	265.5	$L_{SE\text{-}R,2}$	0.38	0.95	0.85	0.99	0.98
16	284.0	$L_{SE\text{-}R,2}$	0.76	0.98	0.84	0.94	0.96
14	284.5	$L_{SE\text{-}R,2}$	0.65	0.96	0.82	0.89	0.93
6	285.0	$L_{SE\text{-}R,2}$	0.85	0.96	0.87	0.99	0.99
13	285.2	$L_{SE\text{-}R,2}$	0.75	0.99	0.89	0.94	0.97
15	286.6	$L_{SE\text{-}R,2}$	0.76	0.98	0.76	0.93	0.95
12	289.0	$L_{SE\text{-}R,2}$	0.52	0.98	0.90	0.92	0.95
4	291.5	$L_{SE\text{-}R,2}$	0.79	0.97	0.83	0.91	0.93
4	291.5	$L_{SE\text{-}R,2}$	0.60	0.98	0.72	0.94	0.95
8	316.1	$L_{SE\text{-}R,2}$	0.75	0.97	0.82	0.91	0.94
9	330.8	$L_{SE\text{-}R,2}$	0.68	0.98	0.85	0.90	0.94
17	333.0	$L_{SE\text{-}R,2}$	0.59	0.98	0.86	0.87	0.92

6.4.3 Uplift load correlation between foundation load cells

The correlation of the load transferred to the four foundation walls was examined by comparing the ratios of instantaneous force coefficients. More specifically, load data acquired from the twenty-seven foundation load cells were grouped in four sets, each corresponding to an individual foundation wall (see Figure 6.10), and normalized by the instantaneous dynamic pressure and the area of the test building in order to get dimensionless force coefficients. These data were also sorted with respect to the wind direction at 10 meters height. The comparison was performed in the form of scatter plots where the distribution and the correlation of various cases were examined.

The results of this analysis are presented in Figure 6.11 to Figure 6.14 and were grouped using as reference the approaching wind direction. In Figure 6.11 the case of incidents approaching from the North-East (i.e. 13.5 to 66.5 degrees) are considered and the three scatter plots compare the correlation between the two sidewalls, between the windward wall and the two sidewalls and finally between the two endwalls and the two sidewalls. The comparison between the two sidewalls, i.e. North-West and South-East walls, indicates a high correlation with the coefficient of determination to be equal to

0.82. It is also clear that for the specific range of directions the North-West wall carries more than 20% of the wind-induced uplift force compared to the South-East wall. When the load of the windward wall (North-East wall) is compared to the sum of the load of the two sidewalls (North-West and South-East walls) it is quite clear that the contribution of the endwall is minimal compared to that of the sidewalls. The same conclusion is drawn when the load from both endwalls is compared to that of the two sidewalls, despite the fact that the correlation is improved in this case (0.67 coefficient of determination).

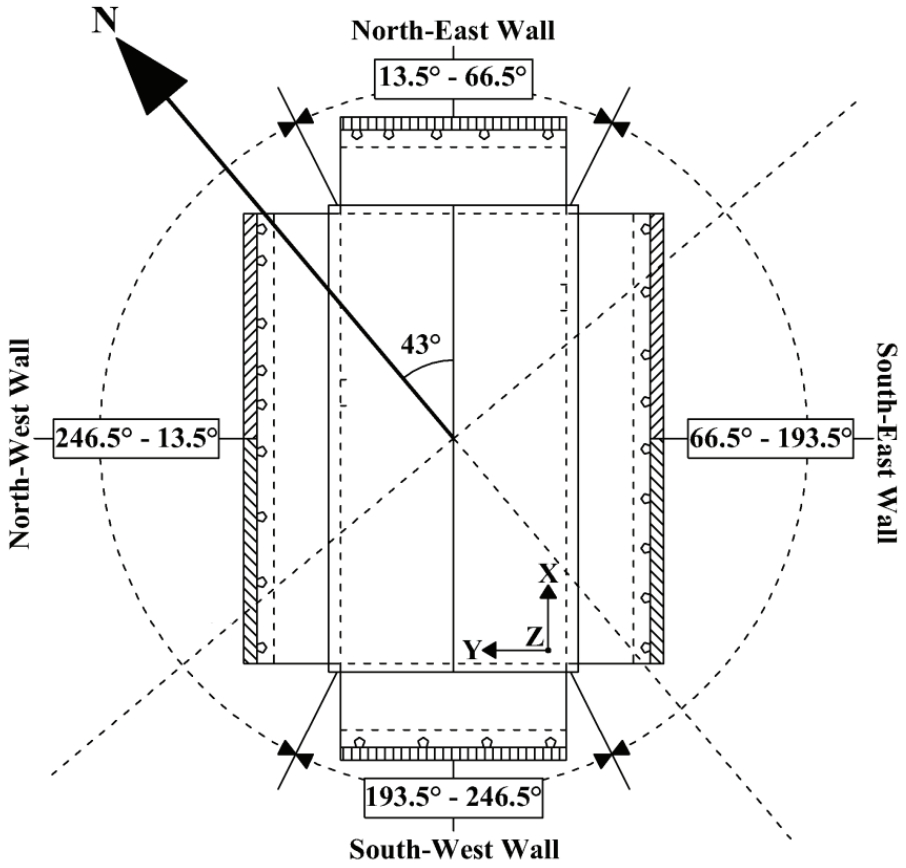

Figure 6.10 Test building and foundation wall notations.

The next range of wind direction considered was the South-East (66.5 to 193.5 degrees – see Figure 6.12). For this case the comparison between the South-East and the North-West walls indicates that the windward side of the building (i.e. South-East) carries most of the wind-induced uplift forces. Moreover, the load transferred to the two sidewalls, and consequently to the foundation walls below them, is significantly higher than the load transferred to the two endwalls (South-West and North-East walls). The other two wind direction ranges are presented in Figure 6.13 (wind approaching from South-West) and Figure 6.14 (wind approaching from North-West). The scatter plots reveal similar findings such as the minimal load transferred to the two endwalls and the increased (by approximately 25%) load transferred to the windward sidewall (North-West wall in Figure 6.14). Last but not least, it should be noted that for all wind direction cases the correlation between the two sidewalls is high, with an estimated coefficient of determination over 0.76.

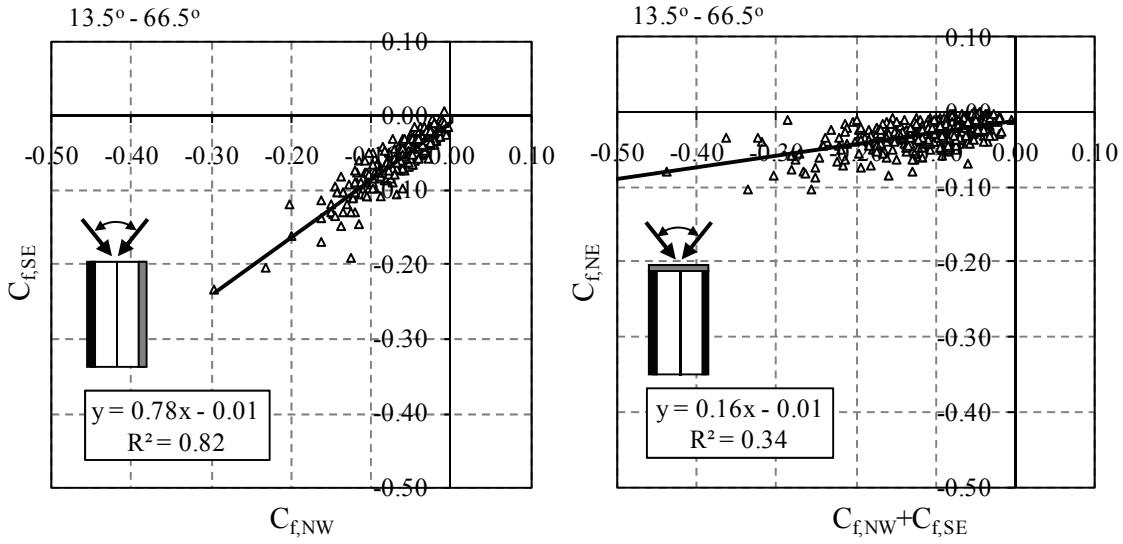

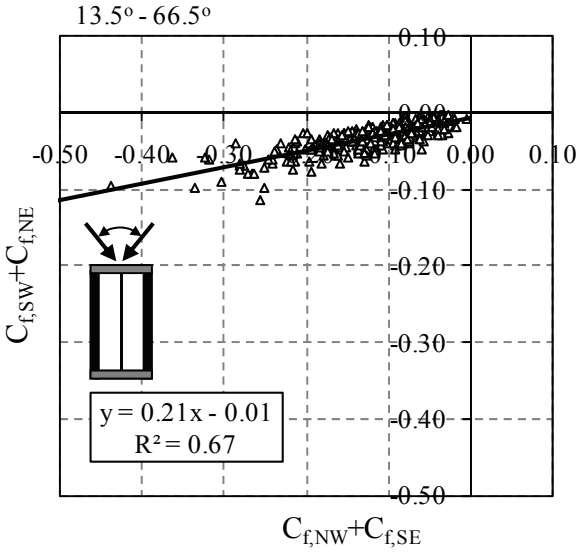

Figure 6.11 Correlation of wall segment force coefficients (13.5 to 66.5 degrees wind direction range).

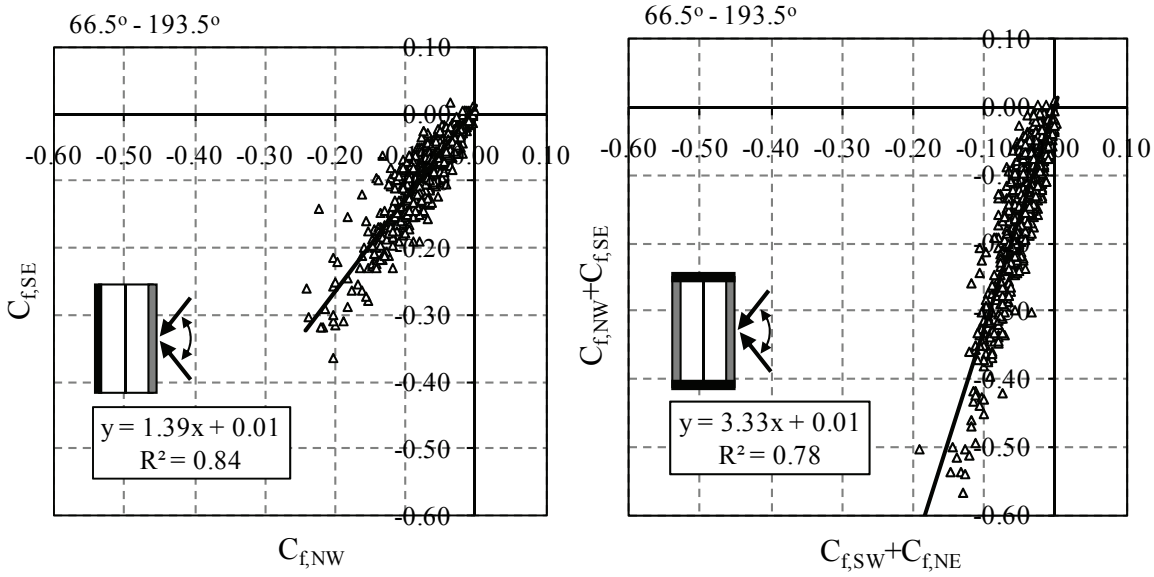

Figure 6.12 Correlation of wall segment force coefficients (66.5 to 193.5 degrees wind direction range).

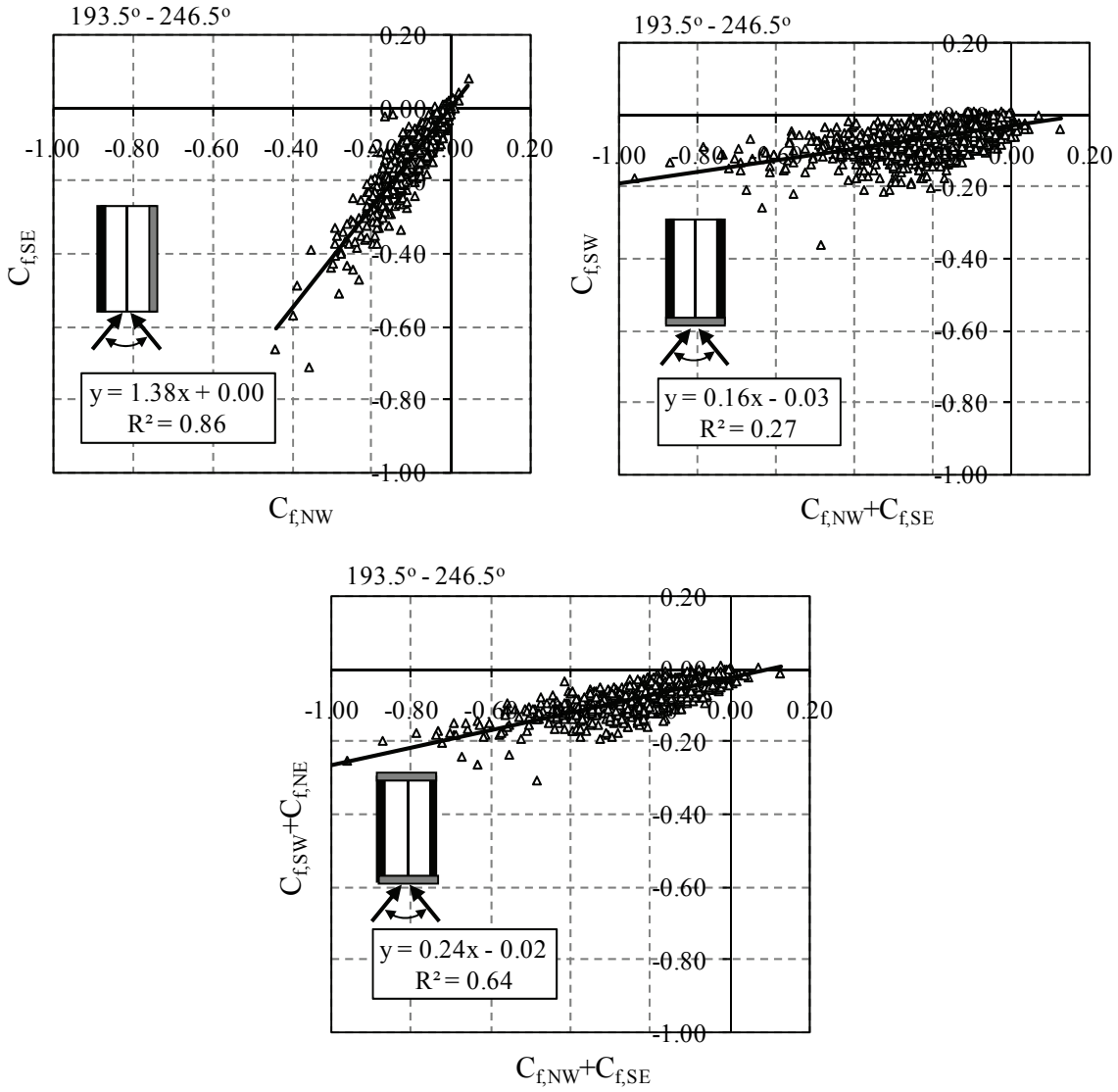

Figure 6.13 Correlation of wall segment force coefficients (193.5 to 246.5 degrees wind direction range).

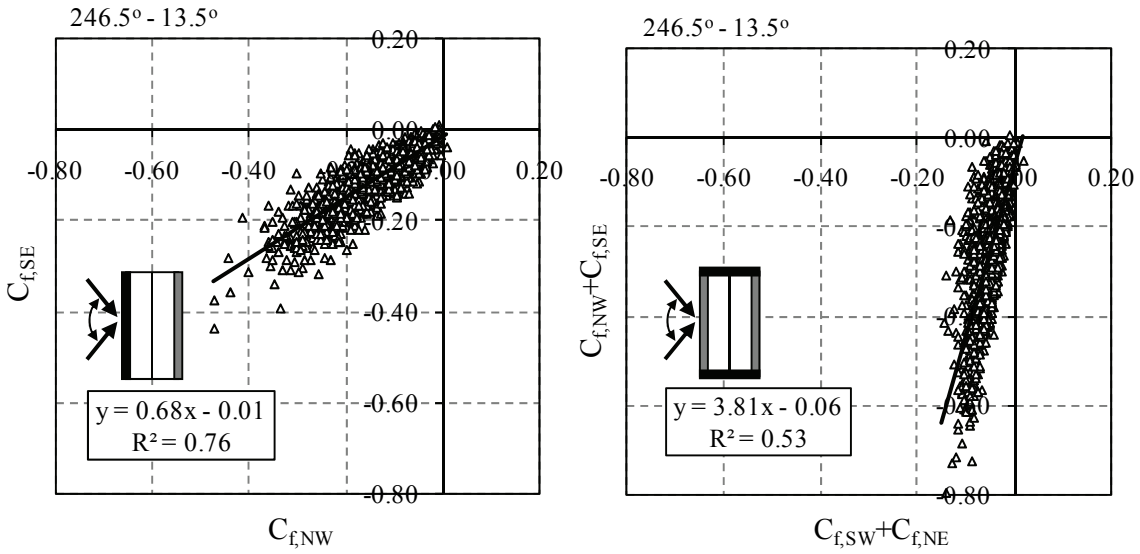

Figure 6.14 Correlation of wall segment force coefficients (246.5 to 13.5 degrees wind direction range).

6.4.4 Partitioning of uplift wind force between the foundation wall and the superstructure

In this last comparison, the participation of each foundation wall on the total wind-induced uplift force was evaluated. This analysis included load cell data acquired during the Fall 2008 (October and November) and Spring 2009 (April to June) used to evaluate the uplift force partitioning between foundation walls and the superstructure during strong wind events with respect to the approaching wind angle of attack. This time the 27 foundation load cells were grouped into six main sets, namely North-East, South-East (N) and South-East (S) refer to the north and south half of the South-East wall respectively, South-West and finally North-West (N) and North-West (S) refer to the north and south half of the North-West wall. The participation of each foundation wall segment in the uplift structural resistance was evaluated by considering the ratios of the instantaneous uplift force coefficient acting simultaneously on each wall segment to the instantaneous

total uplift force coefficient. The results were grouped with respect to the approaching wind angle of attack and then the average value was estimated for every 10-degree angle range.

The first comparison was performed for the two side walls (South-East and North-West) considering their half length segments. As Figure 6.15 indicates, the wall segment located on the windward side of the building in most cases carries the highest wind load; e.g. for the range of 180 to 240 degrees the South-East (S) wall segment has at least a 30% contribution compared to the total uplift wind load whereas the North-West (N) wall segment barely exceeds the 10% mark. It is quite interesting as well to detect a symmetrical behaviour for wind direction normal to the side wall. Therefore, for 310 degrees wind direction, i.e. the approaching wind is normal to the North-West wall, the two halves of the North-West wall have an almost equal contribution of 25%. This is not the case for the leeward side of the building, for which the south part of the South-East wall seems to carry approximately 10% higher load than its north portion.

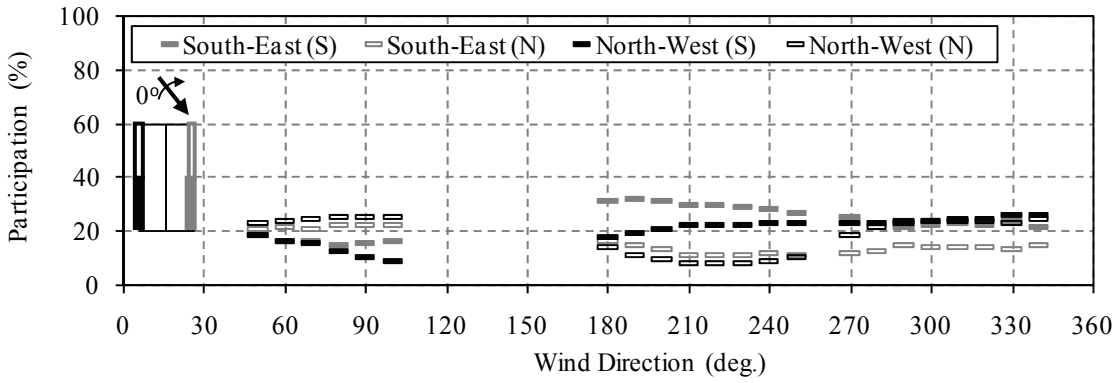

Figure 6.15 Foundation wall segment participation (South-East S/N and North-West S/N).

The participation of the two entire side walls (South-East and North-West walls) is examined in Figure 6.16 and that of the end walls (South-West and North-East walls) in Figure 6.17. The results show that the dominant foundation load is transferred towards the side walls, as opposed to the minimal contribution from the endwalls. Specifically, the South-East wall resists 47% of the total uplift wind load for a wind direction of 180 degrees while it takes its minimum value of 36% as a leeward wall (270 to 330 degrees). The North-West foundation wall performs in a similar manner, i.e. a participation of 50% is reached when the wind is approaching from the North-West direction (i.e. located on the windward side) and a minimum of 30% is reached for anti-diametric wind directions. In both cases, the overturning caused by wind action is apparent through the increased participation of the windward over the leeward foundation wall. Finally, the end walls (South-West and North-East) have significantly lower participation with their maximum combined ratio to the total uplift force reaching 29%. This is in agreement with the results presented in the previous section in the form of scatter plots. If considered separately, the North-East reaches its maximum value of 26% and the South-West the value of 27.5% as windward walls.

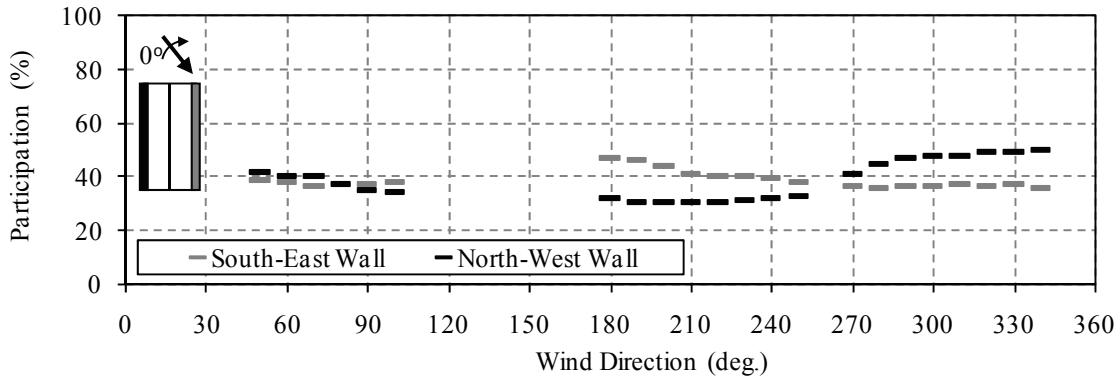

Figure 6.16 Foundation wall segment participation (South-East and North-West).

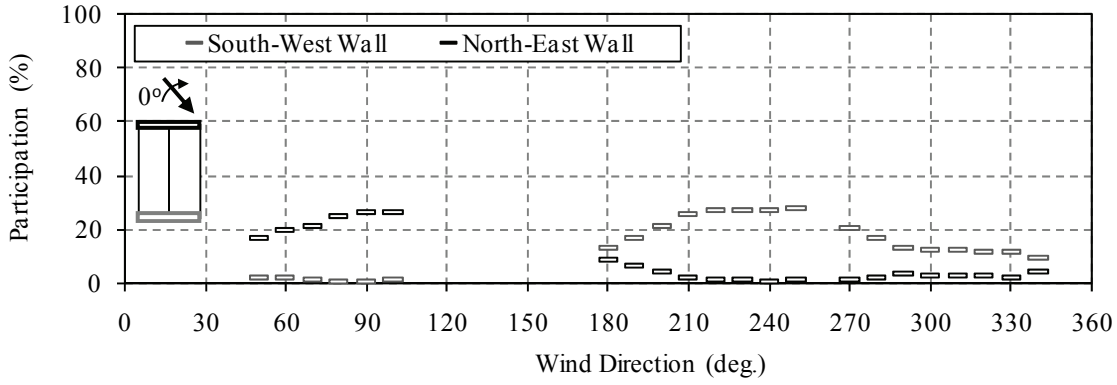

Figure 6.17 Foundation wall segment participation (South-West and North-East).

6.5 Wind Uplift Force Comparisons

6.5.1 General

A more quantitative analysis approach was selected to evaluate two major concepts in this study. The first is related to structural attenuation, a phenomenon incorporated in the National Building Code of Canada but never experimentally justified by any previous study. The second concept is related to the integration of wind tunnel tests into the field force monitoring and the verification of the simulation approach through the comparison to the field results as well as current building codes and wind standards.

6.5.2 Structural attenuation of wind uplift force

The main interest in this study was to examine how the applied wind load is transferred through the building superstructure and down to the foundation (wind load paths). By investigating the load transfer mechanisms it was possible to identify, and most importantly, quantify the degree of wind load attenuation as this load reaches the foundation level. The concept of structural attenuation was examined by using finite

element simulation tools and by comparing the findings from the different experimental approaches.

The results presented here are based on comparisons between the load cell measurements and those derived by applying the acquired full-scale pressure traces to the finite element model surfaces. In more detail, the data acquired from the forty pressure taps on the full-scale building were applied as individual time series on forty effective surface areas, and the analysis was performed using the Hilber-Hughes-Taylor (Hilber et al. 1977) time integration method. Considering the sampling rate of 5 Hz for the field monitoring, a 10-minute record consisted of forty 3000-point time series applied as surface pressures simultaneously on shell elements representing the outer building surface. Using this particular method of analysis it was possible to numerically derive internal force and foundation reaction time histories, which were compared to the data captured by the load cells installed in the test building. All force values were normalized by the mean dynamic pressure at the roof level in order to transform them in their dimensionless form (i.e. force coefficient).

Figure 6.18, Figure 6.19 and Figure 6.20 show representative results, for a stationary 10-minute record, which were acquired on June 4, 2009. The mean wind speed for that record is 15.6 km/h and the mean wind direction 286 degrees at 10 meters height. More specifically, Figure 6.18 compares force data for Frame 14 (see Figure 6.18) at the roof level ($L_{NW\text{-}R,2}$ and $L_{SE\text{-}R,2}$); Figure 6.19 at the foundation level ($L_{NW,4}$ and $L_{SE,5}$); and Figure 6.20 the total uplift foundation force $\Sigma\{L_{SE,i}+L_{SW,i}+L_{NE,i}+L_{NW,i}\}$. - Note: The terminology frame as used here signifies an arrangement of structural components that lie in a vertical cross-section through the building “cut” normal to the ridgeline. - Figure

6.18a, Figure 6.19a and Figure 6.20a clearly illustrate good general agreement between the two traces, especially for lower force levels. Importantly however, for most peak values the predicted force exceeds the observed forces captured by the load cells. This behaviour identifies that although the applied load should generate predicted responses at various components, (e.g. roof to wall, wall to foundation interfaces) the actual force monitoring reveals attenuation of peak forces and reactions. The ratios between the load cell and the FEA values range from 0.6 to 0.7 for Frame 14 roof and foundation level and from 0.7 to 0.8 for the total uplift foundation force. It should be noted here, that the lower ratios observed in Frame 14 compared to the total foundation uplift force, indicate that a considerable portion of the wind load transferred from the envelope to the truss and walls, spreads in the adjacent frames. This effect has the result that FEA predicts higher local loads for Frame 14 whereas in reality the forces captured in the specific frame are somewhat smaller. This was also demonstrated in section 6.3.2 where the correlation between the various roof and foundation load cells was examined. The physical explanation for the attenuation of force magnitudes, as the effects of wind pressures flow from exterior surfaces through the superstructure and into the foundation, is believed to be the result of dynamic fluctuation in surface pressures and dynamic (kinetic) force flows with the structural system. Both of those are effects that the finite element model does not incorporate. By implication, it can be expected that wind design practices based on static analysis of structural systems will tend to conservatively estimate true building performances, in the present and other contexts.

Attenuation of internal peak forces is also demonstrated by the scatter plots presented in Figure 6.18b, Figure 6.19b and Figure 6.20b. Those plots include all 3,000 data points

with each corresponding to a 10-minute record. The ratios in this case (unconstrained linear regression analysis) are 0.73, 0.72 and 0.86 for the cases of roof level (Frame 14), foundation level (Frame 14) and total foundation uplift respectively. The coefficients of determination range from 0.78 to 0.86, which indicates cohesive relationships between full-scale and FEA values.

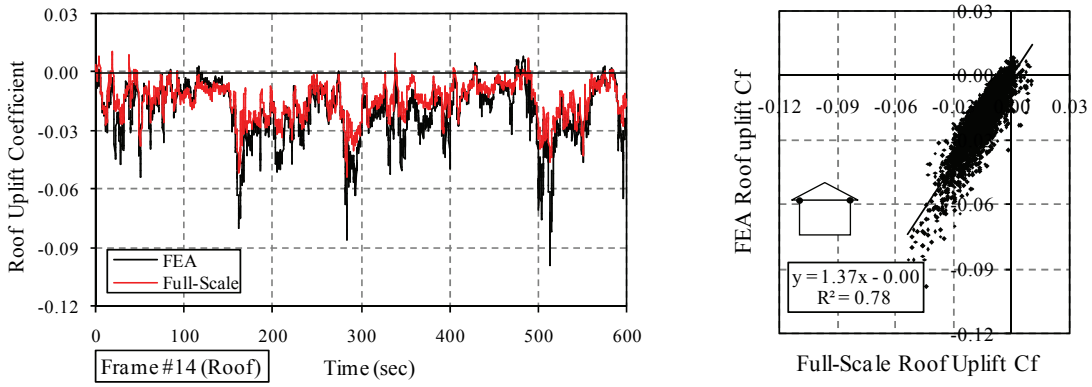

(a) (b)

Figure 6.18 (a) Frame 14 load cell and finite element roof uplift forces and (b) scatter plots (FEA: finite element model predictions).

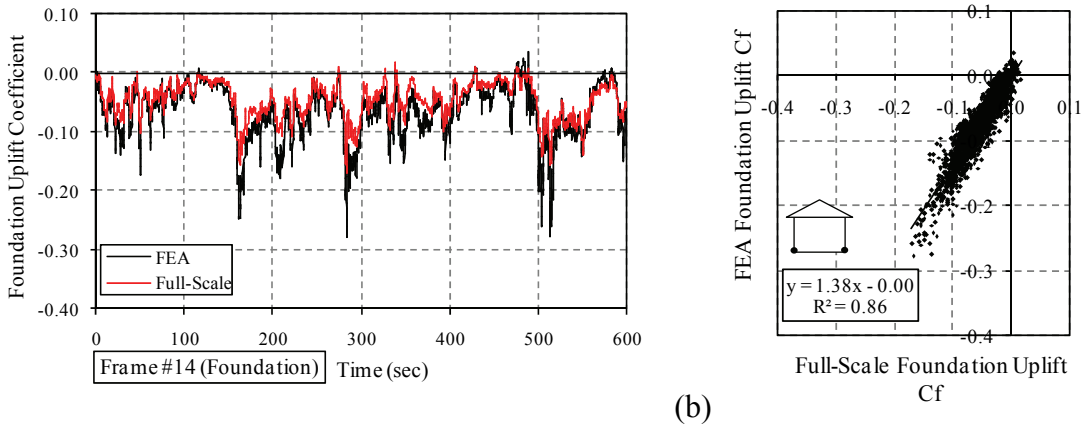

(a) (b)

Figure 6.19 (a) Frame 14 load cell and finite element foundation uplift forces and (b) scatter plots (FEA: finite element model predictions).

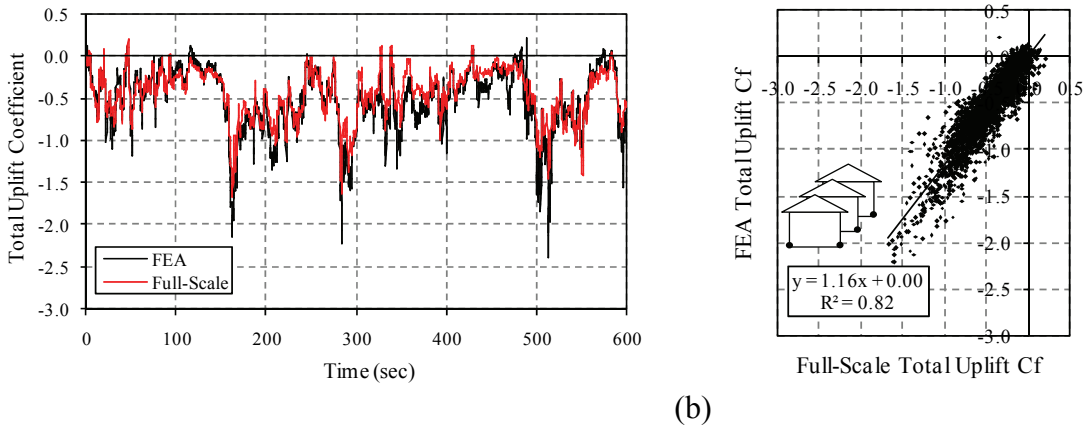

(a) (b)

Figure 6.20 (a) Load cell and finite element total foundation uplift forces and (b) scatter plots (FEA: finite element model predictions).

In addition to the June 4th record, the same analysis was carried out for another ten records. The results are presented in APPENDIX C for all three cases; i.e. Frame 14 roof uplift forces, Frame 14 foundation uplift forces and total uplift force. For all field records considered, the attenuation is apparent and the numerically estimated peak values consistently overestimate the real forces acquired by the roof and foundation load cells. In particular, the FEA over full-scale total uplift ratio ranges from 1.03 to 1.23 if all 3000 sets of values are considered; i.e. even lower magnitude forces are included in the linear regression analysis.

In order to precisely estimate the degree of attenuation in the available full-scale records we had to examine the variation of the FEA to full-scale force ratio when higher magnitude forces are induced by wind action. Therefore, out of the 3000 points assembling each record the first 300 peaks (10% of the sample) were isolated and the ratio of the FEA to full-scale uplift force was calculated. The average value of these peaks was then calculated for several averaging sets, starting from 5 (i.e. the average of

the first five ratios) up to 300 (the average of all 300 ratios). The results of this analysis along with their descriptive statistics are presented in Figure 6.21 (Frame 14 roof uplift force), Figure 6.22 (Frame 14 foundation uplift force) and Figure 6.23 (total foundation uplift force). The roof uplift ratios for all 11 records converge after the averaging of the first 100 peaks indicating an average ratio of 1.46 to 1.72 (standard error of 0.028) which corresponds to 32% - 42% reduction of the numerically estimated roof uplift force. As previously discussed, this reduction is overestimated due to the fact that in reality more roof load escapes from trusses adjacent to Frame 14 and this has as a result to capture lower magnitude loads from the roof load cells compared to those estimated in FEA. Regarding the foundation uplift force in Frame 14, Figure 6.22 indicates that the ratios of the peak values converge after the averaging of the first 150 points. The range of the average attenuation factor is significantly broader in this case, taking values from 0.65 to 0.85 (ratios range from 1.18 to 1.54 with a standard error of 0.039) or equivalent reduction of 15% to 35%. The particular span indicates a higher sensitivity to the wind direction resulting which can be also justified by the poor in some cases ability of the finite element model to replicate sufficiently the force distribution to adjacent foundation load cells. Finally, Figure 6.23 presents the variation of the FEA to full-scale total uplift force ratio with respect to the number of averaging points. In this case the ratios of the peak values converge between the 100 and 150 points and the attenuation factor takes values between 0.73 to 0.83 (ratios range from 1.20 to 1.37 with a standard error of 0.018). Considering these average ratios, the reduction is estimated to 17% to 27%; i.e. at least 17% of the numerically estimated uplift peak force was not detected by the foundation load cells. Indeed the particular finding is of significant importance for the

design of low-rise buildings and is expected, for very first time, to partially justify the 30% reduction of the effective wind load for the design of the foundation, suggested by the National Building Code of Canada (NBCC 2005, Users Guide - Figure I-7).

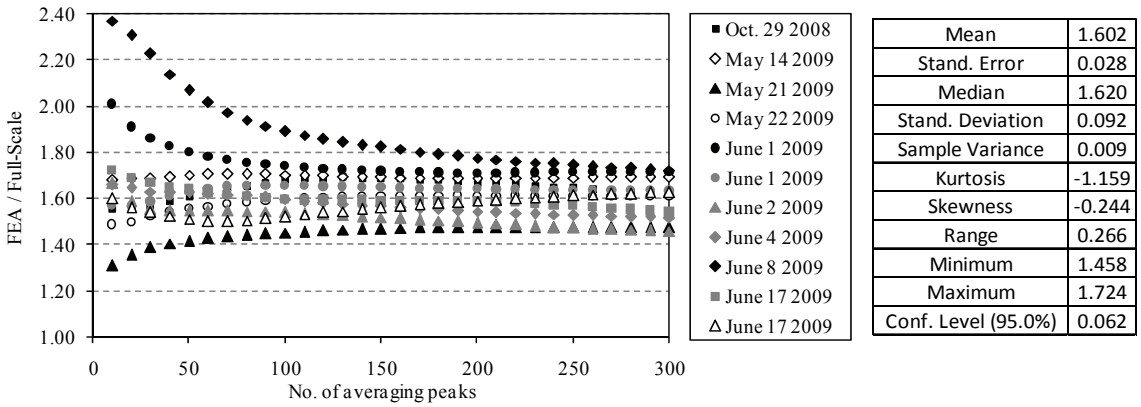

Mean	1.602
Stand. Error	0.028
Median	1.620
Stand. Deviation	0.092
Sample Variance	0.009
Kurtosis	-1.159
Skewness	-0.244
Range	0.266
Minimum	1.458
Maximum	1.724
Conf. Level (95.0%)	0.062

Figure 6.21 Finite element to load cell roof uplift peak force ratio variation (Frame 14).

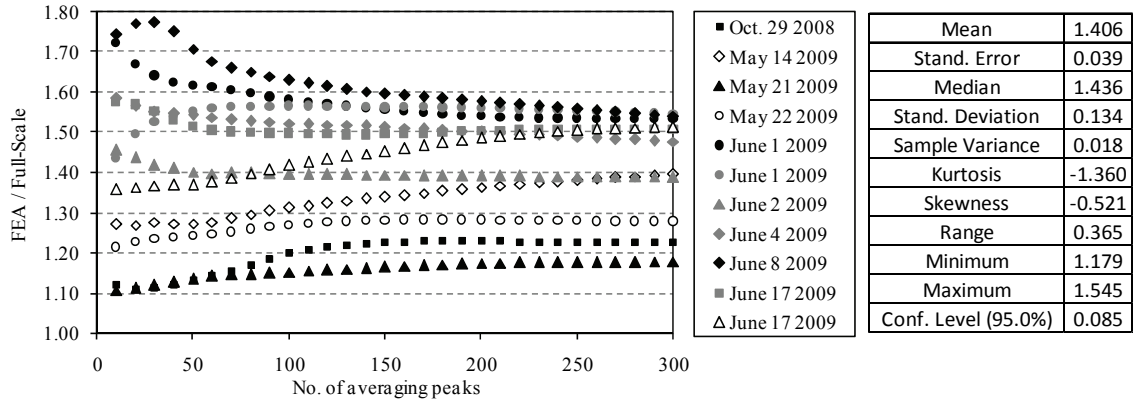

Mean	1.406
Stand. Error	0.039
Median	1.436
Stand. Deviation	0.134
Sample Variance	0.018
Kurtosis	-1.360
Skewness	-0.521
Range	0.365
Minimum	1.179
Maximum	1.545
Conf. Level (95.0%)	0.085

Figure 6.22 Finite element to load cell foundation uplift peak force ratio variation (Frame 14).

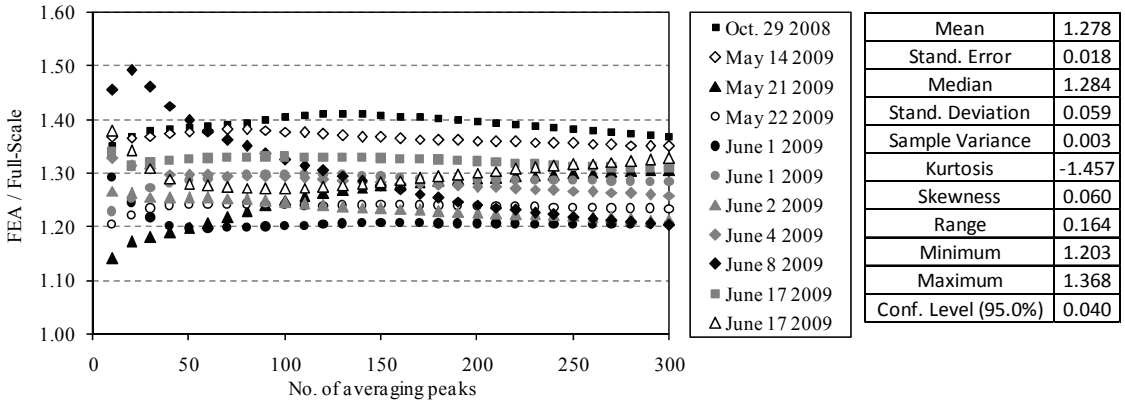

Mean	1.278
Stand. Error	0.018
Median	1.284
Stand. Deviation	0.059
Sample Variance	0.003
Kurtosis	-1.457
Skewness	0.060
Range	0.164
Minimum	1.203
Maximum	1.368
Conf. Level (95.0%)	0.040

Figure 6.23 Finite element to load cell total uplift peak force ratio variation (all foundation load cells).

6.5.3 Uplift force spectra comparisons

The attenuation related findings were also identified in terms of force spectra. Figure 6.24 presents the normalized spectra of both FEA and full-scale total foundation uplift force. Figure 6.25 shows the spectra of FEA and full-scale foundation and roof uplift force on Frame 14 (both load cells included) and finally Figure 6.26 presents the normalized spectra of the foundation and roof uplift force on the South-East side of Frame 14 (one load cell considered). In all cases, the two spectra compare well for lower frequencies indicating a very similar trend. However, the attenuation effect becomes clear in the higher frequency range depicted by a rapid drop of the full-scale spectra compared to that estimated by finite element analysis. It is also quite interesting that this drop is more dominant in the cases of foundation forces (Figure 6.25a and Figure 6.26a), whereas in the case of the roof force spectra (Figure 6.25b and Figure 6.26b) the departure of the full-scale curve is shifted towards the higher frequency region.

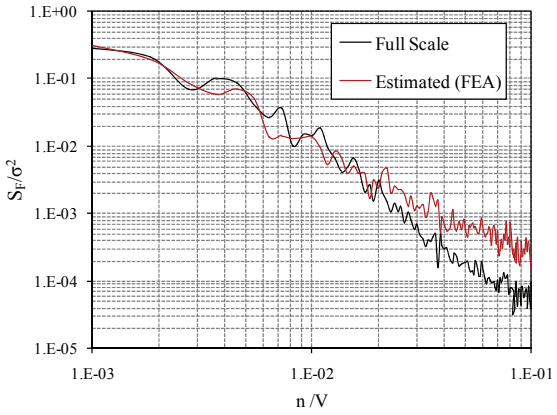

Figure 6.24 Field and numerically estimated total uplift force spectra (all foundation load cells).

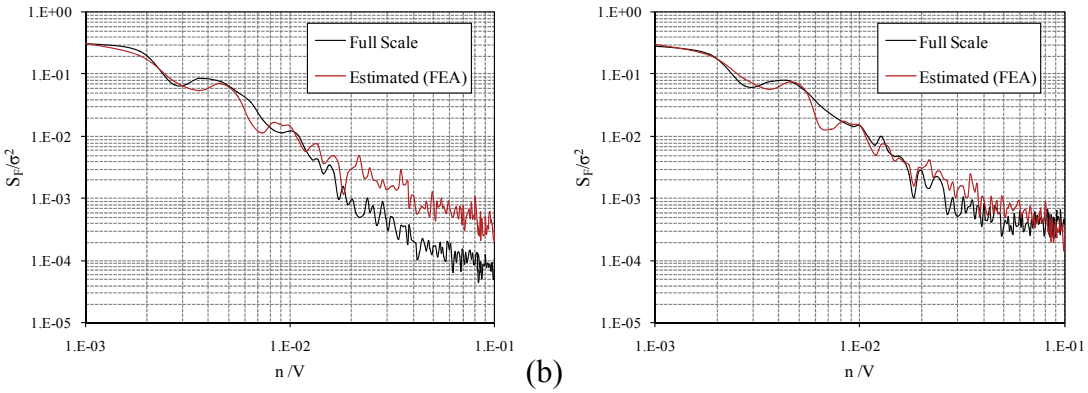

Figure 6.25 Field and numerically estimated (a) foundation and (b) roof force spectra at Frame 14 (two foundation and two roof load cells).

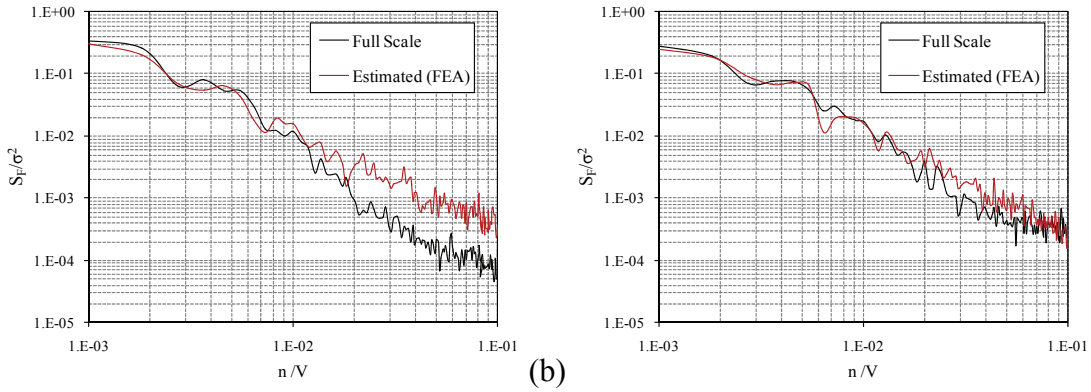

Figure 6.26 Field and numerically estimated (a) foundation and (b) roof force spectra at South-East side of Frame 14 (single foundation and roof load cell).

Additional results from other full-scale records are presented in APPENDIX C. In all cases, numerically estimated force spectrum attains more energy in higher frequencies compared to the load cell force spectrum. It should be noted that similar findings have been reported by Robertson et al. (1998) when the wind-induced response of a free-standing wall was estimated using both pressure transducers and load cells. The authors of that study indicated that the higher energy depicted by the pressure based finite element analysis may be related to the sensitivity of higher envelope suctions to sudden wind direction changes which when uncorrelated result to lower intensity base reactions.

6.5.4 Total uplift force coefficient comparisons

In this last part of the uplift force verification process, the wind tunnel simulation is incorporated to the finite element analysis in order to estimate the total uplift force. As previously discussed, full-scale data were acquired using both pressure and force sensors, whereas wind tunnel tests produced only envelope pressures. In addition to the verification of the wind tunnel simulation in the form of pressure coefficient

comparisons, the total instantaneous uplift force on the building was compared to the available full-scale load data by integrating the measured envelope pressures obtained in the wind tunnel over the roof surface. Consequently, the total uplift force coefficient was calculated, and compared to that calculated directly by the load cell data, for each upstream terrain case using the following equation:

$$c_{f,z} = \frac{\sum c_{p,i} A_{eff,i}}{A} \qquad 6.1$$

where $c_{p,i}$: instantaneous pressure coefficient, $A_{eff,i}$: effective roof pressure tap area (m^2) and A: horizontal projected area of the roof (m^2). It should be noted that dynamic and attenuation effects occurring as the wind load is transferred from the various structural and non-structural components to the foundation walls are not considered in the wind tunnel approach (instantaneous static analysis). Similarly to the previous comparisons, for the full-scale calculations the mean force values were based on a 10-minute average and the instantaneous peak force values on a 3-second gust, both obtained from the available stationary full-scale records. The field data were filtered to retain only those for wind speeds over 4 m/sec (at 10 meters height). The dynamic pressure was always averaged on a 10-minute basis and was referenced to the roof height. Moreover, field data were integrated over a wind angle of attack of 10-degree range to account for the higher standard deviation values of the wind direction and to be directly compared to wind tunnel tests carried out using intervals of 10 degrees. To account for the varying characteristics of the full-scale results, the range (maximum and minimum values) of the integrated values of each set of data was considered in addition to the mean values.

The comparison of the mean total uplift force coefficients presented in Figure 6.27, shows that all three wind tunnel upstream exposure configurations are close to the range

of the field values. The discrepancies are somewhat higher for the South-West to North-West region (230 to 270 degrees) where the mean full-scale values are up to 35% and 40% higher compared to the light and heavy suburban terrain wind tunnel tests respectively. The peak uplift force coefficient comparison is presented in Figure 6.28 and shows better agreement compared to the mean values. Both positive and negative peak wind tunnel results are in most cases within the range of the field data. The agreement for both positive and negative peak uplift force coefficients is particularly improved for the light suburban terrain simulation. It should be noted that the full-scale values are always lower compared to the heavy suburban terrain wind tunnel tests. This finding is quite interesting, considering that the full-scale mean and peak pressure coefficients were in better agreement with the heavy suburban wind tunnel case. As indicated above the use of wind tunnel pressure coefficient in the finite element analysis does not incorporate any attenuation effect similar to those described in the previous sections. Therefore, by using the pressures obtained in the wind tunnel the total uplift force may be overestimated by at least 20% (see section 6.5.2) and this could justify the discrepancies between the heavy suburban wind tunnel force values and those obtained by the foundation load cells.

In addition to the experimental findings, the estimated total uplift force coefficients derived from the NBCC 2005 building code and ASCE 7-10 standard were also plotted in Figure 6.28. For the NBCC 2005 calculations, the external peak composite pressure-gust coefficients (C_pC_g) from Figure I-7 were used to calculate the total uplift force coefficient. The averaging period for the reference wind pressure was adjusted from hourly to 10-minute mean (Figure C26.5-1, ASCE 7-10). In a similar manner, the external pressure coefficients (GC_{pf}) from Figure 28.4-1 (ASCE/SEI 7-10) were

considered and the total uplift force coefficient was computed. For this comparison the velocity pressure was adjusted to account for the averaging period of 10 minutes instead of the 3-sec gust considered in the ASCE standard. It should be noted that on the estimation of the total uplift force using NBCC and ASCE 7-10 two cases were considered, those with and without the contribution of the internal pressures. For the case of full-scale force measurements, the load cells capture the total effect including both external and internal pressures applied on the wall and roof surfaces whereas in the wind tunnel experiments only external pressures are considered.

As Figure 6.28 indicates (note that NBCC* and ASCE* refer to the cases where internal pressures were considered), the estimated NBCC 2005 and ASCE 7-10 values appear to be conservative in relation to the field measurements. However, wind tunnel values, particularly for the case of the heavy suburban terrain, exceed the recommended code provisions. The ASCE 7-10* uplift force coefficient value of -2.03 is higher (absolute value) than the open and light suburban terrain wind tunnel curves and for most of the directions is also higher than the heavy suburban terrain wind tunnel curves. On the other hand, the NBCC 2005* value of -1.60 compares slightly worse than ASCE with the heavy suburban terrain values, whereas the light suburban terrain wind tunnel force coefficients is again below the estimated NBCC 2005 values. This underestimation will become even more critical if the NBCC 2005 values are adjusted for the exposure using the factors provided in Sentence (5) of section 4.1.7.1 (NBCC 2005). For the particular building the exposure factor, which is equal to 0.90 for open terrain and 0.70 for rough terrain, would further reduce the estimated force coefficient by an additional 30% resulting in values that are lower than the experimental findings. It should be noted that

similar observations (non-conservative code recommendations – particularly for the ASCE 7 standard) have been reported by other studies in the past (e.g. Liu et al 2009, Caracoglia and Jones 2009, Mensah et al 2010).

As previously addressed by Zisis and Stathopoulos (2009) the discrepancies between the experimental procedures can be partially attributed to the relatively complex surrounding region. The analysis of wind velocity and direction data from the weather tower indicated a non-uniform variation of the basic exposure parameters (power law exponent, turbulence intensity and roughness length) with respect to the wind direction. Significant roughness amplification was denoted for the wind direction range from 240 to 300 degrees which coincides with the region where the discrepancies between the full-scale and wind tunnel values are of higher order. Finally, higher fluctuations of the wind direction in the field data should also be addressed and considered accountable for discrepancies between the wind tunnel and field values.

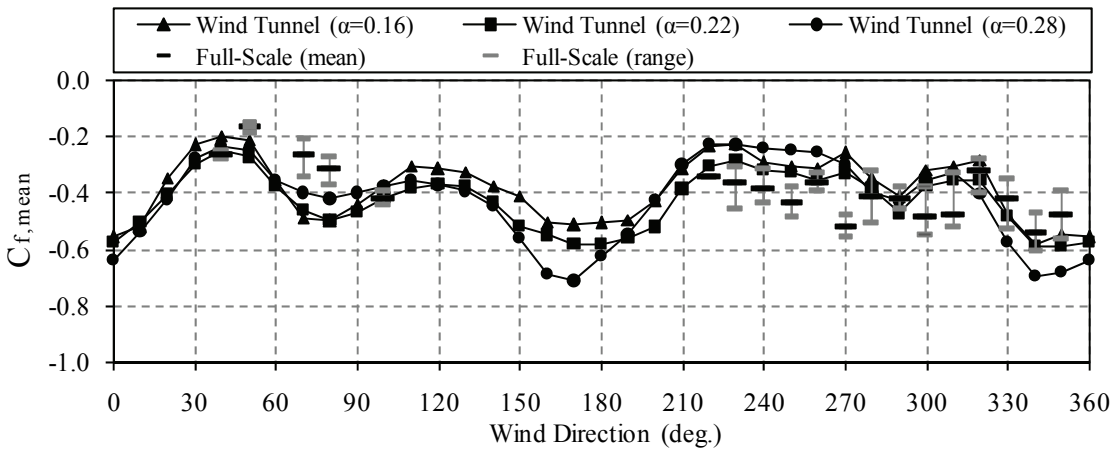

Figure 6.27 Mean total uplift force coefficient comparison.

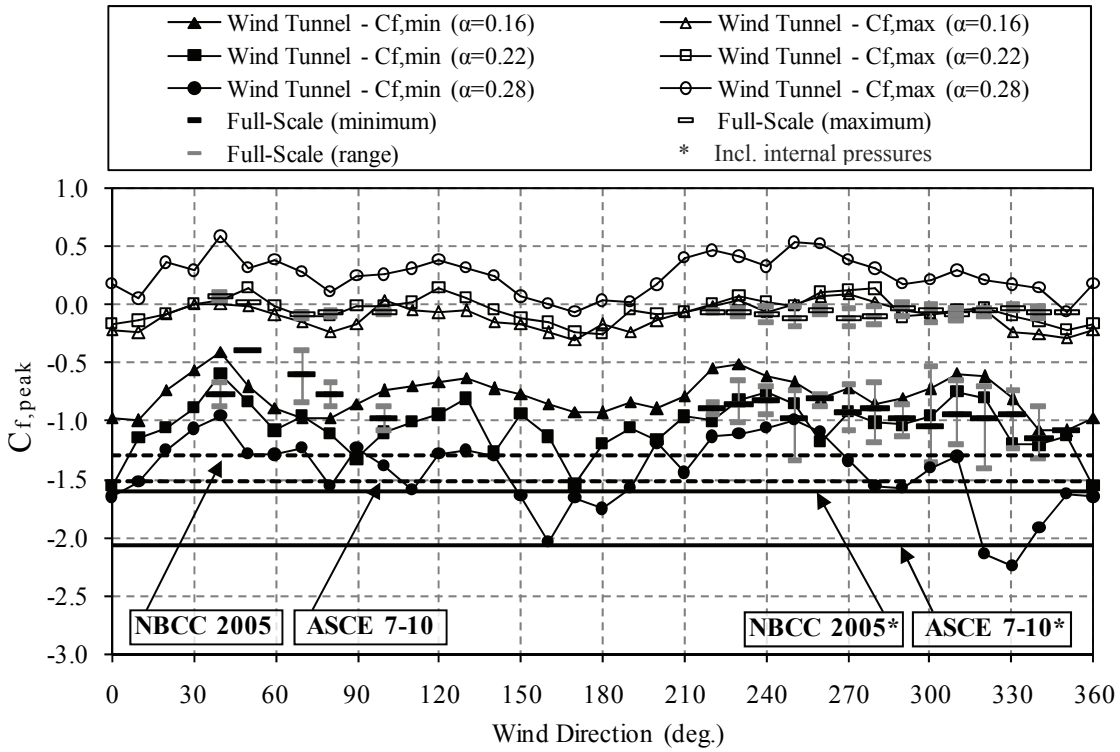

Figure 6.28 Minimum and maximum peak total uplift force coefficient comparison.

CHAPTER 7
CONCLUSIONS

7.1 Research Summary and Contributions

The structural monitoring of a low wood building under wind loads provided invaluable information related to the wind-induced envelope pressures and structural roof and foundation uplift forces. The concepts of wind load paths and structural attenuation of wind-induced forces were defined for very first time by using unique full-scale facilities. The field facilities include two weather stations and a test building equipped with load and pressure sensors. The building rests on top of twenty-seven load cells and is structurally isolated, i.e., the only points of contact between the foundation wall and the superstructure are the foundation load cells. Simultaneously to the load monitoring, forty pressure taps are recording the envelope pressures both on the roof and the wall surfaces. In addition to the field monitoring, a scaled model of the building was tested in a boundary layer wind tunnel using three different upstream terrain configurations that provided varying levels of turbulence characteristics suitable for comparisons with full-scale values. Finally, a detailed finite element model was developed and used to estimate the response of the building for several real and simulated wind load scenarios.

Several verifications were incorporated at various stages of this study, providing confidence in the experimental processes and equipment performance. The analysis of a considerable amount of experimentally and numerically acquired data generated findings of significant importance.

The contributions of this research work can be summarized as follows:

Facilities:

- A unique field facility was implemented, including a test building instrumented with foundation load cells which was structurally isolated. Most importantly, the test building was exposed to real - and not artificial or simulated - wind action.
- The monitoring of the test building provided invaluable information regarding wind-induced envelope pressures and structural loads at roof and foundation levels, both recorded simultaneously.

Methodology:

- The proposed methodology of considering a range of wind directions for the wind tunnel pressure coefficients for comparison with full-scale pressure coefficients performed adequately.
- The numerical model performed adequately as a supplement to wind tunnel and field studies.

Findings

- The attenuation of wind-induced load as it is transferred through structural and non-structural elements to the foundation level was identified and quantified. It was estimated that the reduction of the wind load as it reaches the foundation level is at least 17%.
- The wind load paths were examined and identified in terms of distribution and correlation of uplift roof and foundation forces. Irrespective of the wind direction, the majority of the wind uplift force is transferred to the two side

walls whereas the end walls have a significantly smaller contribution (less than 30% of the total wind uplift force).

- The total uplift force was estimated and compared to wind tunnel simulation and building codes. The comparison revealed that in certain cases those recommended by the standards values could underestimate the total uplift wind force. Particular attention is required for the case of NBCC 2005 which recommends a 30% reduction of the effective wind load for the design of foundations.
- The wind tunnel simulation was verified in terms of pressure coefficients and force coefficients. The agreement with full scale was particularly good for the case of mean and peak pressure coefficients, especially when a range of wind tunnel wind directions was compared to the field record.
- Exposure characteristics were examined and significant variations were identified. The deviating terrain properties indicate that complex terrains need to be examined carefully in order to properly conduct scaled model tests and to successfully compare full-scale and wind tunnel results.

7.2 Limitations and Recommendations for Future Work

The limitations of the current study and therefore, the recommendations for future work, can be summarized as follows:

- The temperature-related deformations of the structural system, particularly at the foundation level, introduced force components of significant magnitude. The variation of these forces was highly non-linear, making the data

conditioning almost impossible. A more sophisticated and possibly automated data acquisition system could potentially handle such effect by removing the temperature drift from the load cells strain gages on a regular basis provided that the wind speed remains low.

- The response of the experimental building to extreme wind effects could probably provide additional confidence and insight regarding the structural attenuation effect and the wind load paths. The available records had in most cases moderate wind speeds with gusts reaching up to 70 km/h. Moreover, the majority of the field records were approaching from the South to West range. As a result, very few records were available for the rest of the wind angles of attack.
- The finite element model was not developed on a component-based approach. In order to study in detail the wind-induced response of the test building as well as its dynamic properties, additional verifications need to be performed. Laboratory tests of shear walls and truss to wall connections should provide the basis for the adjustment of the links incorporated in the finite element model of this study.
- At this stage only six roof load cells were installed. The installation of additional roof load cells could expand the range of findings as far as the wind load paths are concerned.
- Of great interest will be to study the effect of additional openings and internal partitions to the findings of the current study. These construction details should

also be accompanied by detailed internal pressure measurements in order to be able to examine in detail the net pressure effect on the building envelope.

- Last but not least, as in any full-scale study, the findings are closely dependent to the geometry and properties of the specific test building. Additional field monitoring and research should be carried out to comprehend and support this effort.

  *"To test the validity of theories for wind loading, it appears that we need not one full-scale test, no matter how exhaustive, but several covering ranges of different conditions expected in practice" (*Davenport 1975).

References

A.M. Best. (2007). Toto...we're not in new jersey anymore. No. Special Report: U.S. Tornadoes, A.M. Best.

Aponte-Bermúdez, L. D. (2006). Measured Hurricane Wind Pressure on Full-Scale Residential Structures: Analysis and Comparison to Wind Tunnel Studies and ASCE-7. PhD Thesis, University of Florida, Department of Civil and Coastal Engineering, Gainesville, FL.

Apperley, L., Surry, D., Stathopoulos, T. & Davenport, A.G. (1979). Comparative measurements of wind pressure on a model of the full-scale experimental house at Aylesbury, England. Journal of Wind Engineering and Industrial Aerodynamics, 4(3-4), 207-228.

ASCE/SEI 7-05 (2005). Minimum Design Loads for Building and Other Structures, American Society of Civil Engineers, Reston, Virginia, USA.

ASCE/SEI 7-10 (2010). Minimum Design Loads for Building and Other Structures, American Society of Civil Engineers, Reston, Virginia, USA.

Bartlett, F. M., Galsworthy, J. K., Henderson, D., Hong, H. P., Iizumi, E., & Inculet, D. R. (2007). The three little pigs project: A new test facility for full-scale small buildings. 12th International Conference on Wind Engineering, Cairns, Australia. 1623-1630.

Bendat, J. & Piersol, A. (2010). Random data: Analysis and measurement procedures. John Wiley & Sons, Hoboken, New Jersey.

Bienkiewicz, B., & Sun, Y. (1992). Local wind loading on the roof of a low-rise building. Journal of Wind Engineering and Industrial Aerodynamics, 45(1), 11-24.

Bitsuamlak, G. T., Chowdhury, A. G., & Sambare, D. (2009). Application of a full-scale testing facility for assessing wind-driven-rain intrusion. Building and Environment, 44, 2430-2441.

Blessing, C., Chowdhury, A. G., Lin, J., & Huang, P. (2009). Full-scale validation of vortex suppression techniques for mitigation of roof uplift. Engineering Structures, 31, 2936-2946.

Brown, T.M., Liu, Z., Morrison, M.J., Cope, A.D., Smith, D.A. (2011). Comparison of field and full-scale laboratory pressure data at the IBHS research center. 13th International Conference on Wind Engineering, Amsterdam, Netherlands.

CAMBELL SCIENTIFIC INC, 05103, 05106 and 05305 R. M. Young Wind Monitors, Instruction Manual, Revision: 11/05.

Canadian Wood Council <http://www.cwc.ca/?Language=EN>, retrieved on August 2011.

Canadian Plywood Association <http://www.canply.org/english/>, retrieved on August 2011.

Caracoglia, L., & Jones, N. (2004). Full-scale pressure measurement during hurricanes. Proceedings of 5th Intern. Colloquium on Bluff Body Aerodynamics & Applications, Ottawa, ON, Canada. pp.485-488.

Caracoglia, L., Sangree, R. H., Jones, N. P., & Schafer, B. W. (2008). Interpretation of full-scale strain data from wind pressures on a low-rise structure. Journal of Wind Engineering and Industrial Aerodynamics, 96(12), 2363-2382.

Caracoglia, L., & Jones, N. P. (2009). Analysis of full-scale wind and pressure measurements on a low-rise building. Journal of Wind Engineering and Industrial Aerodynamics, 97, 157-173.

Chen, Y., Kopp, G. A., & Surry, D. (2003). Interpolation of pressure time series in an aerodynamic database for low buildings. Journal of Wind Engineering and Industrial Aerodynamics, 91(6), 737-765.

Cheung, J. C. K., Holmes, J. D., Melbourne, W. H., Lakshmanan, N., & Bowditch, P. (1997). Pressures on a scale model of the Texas Tech building. Journal of Wind Engineering and Industrial Aerodynamics, 69-71, 529-538.

Chowdhury, A. G., Simiu, E., & Leatherman, S. P. (2009). Destructive testing under simulated hurricane effects to promote hazard mitigation. Natural Hazards Review, 10 (1), 1-10.

Chowdhury, A. G., Bitsuamlak, G. T., Fu, T-C, & Kawade, P. (2010). A study on roof vents subjected to simulated hurricane effects. Natural Hazards Review, in press.

Cochran, L. S., & Cermak, J. E. (1992). Full- and model-scale cladding pressures on the Texas Tech university experimental building. Journal of Wind Engineering and Industrial Aerodynamics, 43(1-3), 1589-1600.

Computers and Structures, Inc., CSI. (1997), SAP®2000, Integrated Structural Analysis and Design Software. CSI, Berkeley, CA, USA.

Computers and Structures, Inc. CSI, (1998), SAP®2000, Basic Analysis Reference, CSI, Berkeley, CA, USA.

DADiSP, DSP Development Corporation, Newton, MA, USA

Dalley, S. (1996). Surface pressure spectra on a model of the Silsoe structures building and comparison with full-scale. Journal of Wind Engineering and Industrial Aerodynamics, 60, 177-187.

Datin, P. L., Liu, Z., Prevatt, D. O., Masters, F. J., Gurley, K., & Reinhold, T. A. (2006). Wind loads on single-family dwellings in suburban terrain: Comparing field data and wind tunnel simulation. Structures Congress 2006, St. Louis, Missouri, USA.

Datin, P. L. (2010). Structural load paths in low-rise, wood-framed structures. PhD Thesis, University of Florida, Department of Civil and Coastal Engineering, Gainesville, FL. Department of Civil and Coastal Engineering, Gainesville, FL.

Davenport, A. G. (1975). Perspectives on the full-scale measurement of wind effects. Journal of Wind Engineering and Industrial Aerodynamics, 1, 23-54.

Davenport, A. G. (2002). Past, present and future of wind engineering. Journal of Wind Engineering and Industrial Aerodynamics, 90(12-15), 1371-1380.

Dearhart, E. (2003). Comparison of Field and Model Wind Pressure on Residential Buildings in Tropical Storm Winds. Masters Thesis, Clemson University, Department of Civil Engineering, Clemson, SC.

Doudak, G. (2005). Field determination and modeling of load paths in wood light-frame structures. PhD Thesis, McGill University, Montreal, QC, Canada.

Doudak, G., Ghallagher, A., Kasal, B., McGlure, G., Mohhamad, M., Smith, I., Stathopoulos, T., & Zisis, I. (2005). Towards wind load paths on wood buildings. The Fourth European & African Conference on Wind Engineering, Prague, CZ.

Doudak, G., McClure, G., Smith, I., Hu, L., & Stathopoulos, T. (2005). Monitoring structural response of a wooden light-frame industrial shed building to environmental loads. Journal Structural Engineering, 131(5), 794-805.

Doudak, G., McGlure, G., Smith, I., & Stathopoulos, T. (2009). Comparison of field and wind tunnel pressure coefficients for a light-frame industrial building. Journal of Structural Engineering, ASCE, 135 (10), 1301-1304.

Durst, C.S. (1960). Wind speeds over short periods of time. Meteorological Magazine, 89, 181-186.

Eaton, K. J., & Mayne, J. R. (1975). The measurement of wind pressures on two-storey houses at Aylesbury. Journal of Wind Engineering and Industrial Aerodynamics, 1, 67-109.

Environment Canada Weather Office, Natural Resources Canada (NRC)

Endo, M., Bienkiewicz, B., & Ham, H. J. (2006). Wind tunnel investigation of point pressure on TTU test building. Journal of Wind Engineering and Industrial Aerodynamics, 94, 553-578.

Fagan, R., Smith, D. A., & Mehta, K. C. (2001). Field measurements of total wind forces on buildings. Structures Congress 2001, Washington, DC, USA. , 109(40558) 102.

Fagan, R. (2001). A model for time varying wind loads on a low-rise structure. PhD Thesis, Texas Tech University, Lubbock, Texas, USA.

Gavanski, E. & Kopp, G.A. (2011a). Glass breakage tests under fluctuating wind loads, ASCE Journal of Architectural Engineering, 17, 34-41.

Gavanski, E. & Kopp, G.A. (2011b). Examination of load resistance in window glass design, ASCE Journal of Architectural Engineering, 17, 42-50.

Ginger, J. D., Mehta, K. C., & Yeatts, B. B. (1997). Internal pressures in a low-rise full-scale building. Journal of Wind Engineering and Industrial Aerodynamics, 50, 213-224.

Ginger, J. D., & Letchford, C. W. (1999). Net pressures on a low-rise full-scale building. Journal of Wind Engineering and Industrial Aerodynamics, 83(1-3), 239-250.

Ginger, J. D. (2000). Internal pressures and cladding net wind loads on full-scale low-rise building, Journal of Structural Engineering, 126(4), 538-543.

Ham, H. J., & Bienkiewicz, B. (1998). Wind tunnel simulation of TTU flow and building roof pressure. Journal of Wind Engineering and Industrial Aerodynamics, 77-78, 119-133.

Hansen, S. O., & Sørensen, E. G. (1986). The Aylesbury experiment. Comparison of model and full-scale tests. Journal of Wind Engineering and Industrial Aerodynamics, 22(1), 1-22.

Hilber, H. M., Hughes, T. J. R. & Taylor, R. L. (1977). Improved numerical dissipation for time integration algorithms in structural dynamics. Earthquake Engineering and Structural Dynamics, 5, 283–292.

Ho, T. C. E., Surry, D., Morrish, D., & Kopp, G. A. (2005). The UWO contribution to the NIST aerodynamic database for wind loads on low buildings: Part 1. Archiving format

and basic aerodynamic data. Journal of Wind Engineering and Industrial Aerodynamics, 93(1), 1-30.

Holmes, J. D., & Best, R. J. (1978). Pressure measurements on wind tunnel models of the aylesbury experimental house. Wind Engineering, 2(4), 203-220.

Holmes, J. D. (2001). Wind loading of structures. Spon Press, New York.

Hoxey, R. P. (1991). Structural response of a portal framed building under wind load. Journal of Wind Engineering and Industrial Aerodynamics, 38(2-3), 347-356.

Hoxey, R. P., & Richards, P. J. (1992). Structure of the atmospheric boundary layer below 25 m and implications to wind loading on low-rise buildings. Journal of Wind Engineering and Industrial Aerodynamics, 41(1-3), 317-327.

Hoxey, R. P., & Richards, P. J. (1993). Flow patterns and pressure field around a full-scale building. Journal of Wind Engineering and Industrial Aerodynamics, 50, 203-212.

Hoxey, R. P., & Richards, P. J. (1995). Full-scale wind load measurements point the way forward. Journal of Wind Engineering and Industrial Aerodynamics, 57(2-3), 215-224.

Hoxey, R. P., Richards, P. J., & Short, L. J. (2002). A 6 m cube in an atmospheric boundary layer flow - Part 1. Full-scale and wind-tunnel results. Wind and Structures, Vol. 5, No. 2-4, 165-176.

Huang, P., Mirmiran, A., Chowdhury, A. G., Abishdid, C., & Wang, T. L. (2009). Performance of roof tiles under simulated hurricane impact. Journal of Architectural Engineering, ASCE, 15 (1), 26-34.

Jensen, M. (1958). The model-law for phenomena in natural wind. Ingenioren - International Edition, 2(4), 121-128.

Jensen, M., & Franck, N. (1965). Model-scale tests in turbulent wind. Part II. Danish Technical Press.

Kaimal, J.C., Wyngaard, J.C., Izumi, Y., & Coté O.R. (1972), Spectral Characteristics of Surface Layer Turbulence, Quarterly Journal of the Royal Meteorological Society, 98, 563-589.

Kim, S. I., & Mehta, K. C. (1977). Wind loads on flat roof area through full-scale experiment. Institute for Disaster Research, Texas Tech University, Lubbock, Texas.

Kopp, G. A., Morrison, M. J., Gavanski, E., Henderson, D. J., & Hong, H. P. (2010). "Three little Pigs" Project: Hurricane risk mitigation by integrated wind tunnel and full-scale laboratory tests. Natural Hazards Review, 11 (4), 151-161.

Leatherman, S. P., Gan Chowdhury, A., & Robertson, C. J. (2007). Wall of wind full-scale destructive testing of coastal houses and hurricane damage mitigation. Journal of Coastal Research, 23(5), 1211-1217.

Leatherman, S., Robertson, C., Chowdhury, A. G., Simiu, E., Bitsuamlak, G., & Huang, P. (2008). Full-scale destructive testing of houses to hurricane-force wind and rain. Solutions to Coastal Disasters Congress 2008, Oahu, Hawaii. , 312(40968) 73.

Letchford, C. W., & Ginger, J. D. (1992). Wind loads on planar canopy roofs — part 1: Mean pressure distributions. Journal of Wind Engineering and Industrial Aerodynamics, 45(1), 25-45.

Letchford, C. W., Iverson, R. E., & McDonald, J. R. (1993). The application of the quasi-steady theory to full scale measurements on the Texas Tech building. Journal of Wind Engineering and Industrial Aerodynamics, 48(1), 111-132.

Letchford, C. W., & Mehta, K. C. (1993). The distribution and correlation of fluctuating pressures on the Texas Tech building. Journal of Wind Engineering and Industrial Aerodynamics, 50, 225-234.

Letchford, C. W., Sandri, P., Levitan, M. L., & Mehta, K. C. (1992). Frequency response requirements for fluctuating wind pressure measurements. Journal of Wind Engineering and Industrial Aerodynamics, 40(3), 263-276.

Levitan, M. L. (1988). Statistical analysis to validate full scale wind and structural response data. MSc Thesis, Texas Tech University, Department of Civil Engineering, Lubbock, TX.

Levitan, M. L., Mehta, K. C., Vann, W. P., & Holmes, J. D. (1991). Field measurements of pressures on the Texas Tech building. Journal of Wind Engineering and Industrial Aerodynamics, 38(2-3), 227-234.

Levitan, M. L., & Mehta, K. C. (1992). Texas Tech field experiments for wind loads part 1: Building and pressure measuring system. Journal of Wind Engineering and Industrial Aerodynamics, 43(1-3), 1565-1576.

Levitan, M. L., & Mehta, K. C. (1992). Texas Tech field experiments for wind loads part II: Meteorological instrumentation and terrain parameters. Journal of Wind Engineering and Industrial Aerodynamics, 43(1-3), 1577-1588.

Levitan, M. L., Mehta, K. C., Chok, C. V., & Millsaps, D. L. (1990). An overview of Texas Tech's wind engineering field research laboratory. Journal of Wind Engineering and Industrial Aerodynamics, 36(Part 2), 1037-1046.

Lim, H. C., Thomas, T. G., & Castro, I. P. (2009). Flow around a cube in a turbulent boundary layer: LES and experiment. Journal of Wind Engineering and Industrial Aerodynamics, 97, 96-109.

Lin, J. X., Surry, D., & Tieleman, H. W. (1995). The distribution of pressure near roof corners of flat roof low buildings. Journal of Wind Engineering and Industrial Aerodynamics, 56(2-3), 235-265.

Liu, H. (1991). Wind Engineering: A Handbook for Structural Engineers, Prentice Hall, New Jersey.

Liu, Z., Prevatt, D., Aponte, L., Reinhold, T., Gurley, K., & Masters, F. (2006). Wind load determination using field data and wind tunnel studies on residential buildings. Fourth LACCEI International Latin American and Caribbean Conference for Engineering and Technology, Puerto Rico.

Liu, Z. (2006). Field measurements and wind tunnel simulation of hurricane wind loads on single family dwellings. PhD. Thesis, Clemson University, Department of Civil Engineering, Clemson, SC.

Liu, Z., Prevatt, D. O., Aponte-Bermúdez, L. D., Gurley, K. R., Reinhold, T. A., & Akins, R. E. (2009). Field measurement and wind tunnel simulation of hurricane wind loads on a single family dwelling. Engineering Structures, 31, 2265-2274.

Liu, Z., Brown, T.M., Cope, A.D. & Reinhold, T.A. (2011). Commissioning of the wind test capabilities of the IBHS Research Center, 13th International Conference on Wind Engineering, Amsterdam, Netherlands.

Marshall, R. D. (1975). A study of wind pressures on a single-family dwelling in model and full scale. Journal of Wind Engineering and Industrial Aerodynamics, 1, 177-199.

Marshall, R. D. (1977). The measurements of wind loads on a full-scale mobile home. Washington DC: National Bureau of Standards.

Masters, F. J., Tieleman, H. W., & Balderrama, J. A. (2010). Surface wind measurements in three Gulf Coast hurricanes of 2005. Journal of Wind Engineering and Industrial Aerodynamics, 98, 533-547.

Mehta, K. C., Levitan, M. L., Iverson, R. E., & McDonald, J. R. (1992). Roof corner pressures measured in the field on a low building. Journal of Wind Engineering and Industrial Aerodynamics, 41(1-3), 181-192.

Mehta, K. C., & Smith, D. A. (2004). Full-scale measurements for wind effects on buildings. Earth & Space 2004, Houston, TX, USA. , 153(40722) 27.

Mensah, A. F. (2010). Determination of wind uplift forces using database assisted design (DAD) approach for light framed wood structures. Master of Science Thesis, University of Florida, Department of Civil and Coastal Engineering, Gainesville, FL.

Mensah, A. F., Datin, P. L., Prevatt, D. O., Gupta, R., & van de Lindt, J. W. (2011). Database-assisted design methodology to predict wind-induced structural behavior of a light-framed wood building. Engineering Structures, 33, 674-684.

Morrison, M. J., Kopp, G. A., (2011). Performance of toe-nail connections under realistic wind loading. Engineering Structures, 33, 69-76.

Mousset, S. (1986). The international Aylesbury collaborative experiment in C.S.T.B. Journal of Wind Engineering and Industrial Aerodynamics, 23, 19-36.

Murphy, N. R. (1971). Dynamics of wheeled vehicles: A statistical analysis of terrain-vehicle-speed systems. Technical Report M-68-1, U.S. Army Engineers Waterways Experiment Section, Vicksburg, Mississippi.

National Building Code of Canada - NBCC (2005). National Research Council of Canada (NRCC), Ottawa, Canada.

Ng, H. H. T., & Mehta, K. C. (1990). Pressure measuring system for wind-induced pressures on building surfaces. Journal of Wind Engineering and Industrial Aerodynamics, 36(1-3), 351-360.

Okada, H., & Ha, Y. (1992). Comparison of wind tunnel and full-scale pressure measurement tests on the Texas Tech building. Journal of Wind Engineering and Industrial Aerodynamics, 43(1-3), 1601-1612.

Pielke, J.,Roger A., Gratz, J., Landsea, C. W., Collins, D., Saunders, M. A., & Musulin, R. (2008). Normalized hurricane damage in the United States: 1900-2005. Natural Hazards Review, 9(1), 29-42.

Porterfield, M., & Jones, N. (2001). The development of a field measurement instrumentation system for low-rise construction. Wind and Structures, 4(3), 247-14.

Richards, P. J., & Hoxey, R. P. (1992). Computational and wind tunnel modeling of mean wind loads on the Silsoe structures building. Journal of Wind Engineering and Industrial Aerodynamics, 43(1-3), 1641-1652.

Richards, P. J., Hoxey, R. P., & Short, L. J. (2001). Wind pressures on a 6m cube. Journal of Wind Engineering and Industrial Aerodynamics, 89, 1553-1564.

Richards, P. J., Quinn, A. D. & Parker, S. (2002). A 6 m cube in an atmospheric boundary layer flow - Part 1. Computational solutions. Wind and Structures, Vol. 5, No. 2-4, 177-192.

Richardson, G. M., & Blackmore, P. A. (1995). The Silsoe structures building: Comparison of 1:100 model-scale data with full-scale data. Journal of Wind Engineering and Industrial Aerodynamics, 57(2-3), 191-201.

Richardson, G. M., Hoxey, R. P., Robertson, A. P., & Short, J. L. (1997). The Silsoe structures building: Comparisons of pressures measured at full scale and in two wind tunnels. Journal of Wind Engineering and Industrial Aerodynamics, 72, 187-197.

Richardson, G. M., & Surry, D. (1991). Comparisons of wind-tunnel and full-scale surface pressure measurements on low-rise pitched-roof buildings. Journal of Wind Engineering and Industrial Aerodynamics, 38(2-3), 249-256.

Richardson, G. M., & Surry, D. (1992). The Silsoe building: A comparison of pressure coefficients and spectra at model and full-scale. Journal of Wind Engineering and Industrial Aerodynamics, 43(1-3), 1653-1664.

Richardson, G. M., & Surry, D. (1994). The Silsoe structures building: Comparison between full-scale and wind-tunnel data. Journal of Wind Engineering and Industrial Aerodynamics, 51(2), 157-176.

R. M. YOUNG COMPANY, 05103Model 61202L Barometric pressure Sensor, Instruction Manual, October 2001

Robertson, A. P., & Glass, A. G. (1988). The Silsoe structures building - its design, instrumentation and research facilities. AFRC Inst. Engng. Res., Silsoe, Div. Note DN 1482

Robertson, A.P., Hoxey, R.P., Short, J.L., Ferguson, W.A., & Blackmore, P.A. (1998). Prediction of structural loads from fluctuating wind pressures: Validation from full-scale force and pressure measurements. Journal of Wind Engineering and Industrial Aerodynamics, 74-76, 631-640.

Roy, R. J. (1983). Wind tunnel measurements on total loads on a mobile home. Journal of Wind Engineering and Industrial Aerodynamics, 13, 327-338.

Scanivalve Corporation, ZOC 33/64Px – Electronic Pressure Scanning Module, Instruction and Service Manual

Scanivalve Corporation, DSMLINK V2.90, Installation and Operation Manual

Scanivalve Corporation, DSM 3000 – Digital Service Module, Instruction and Service Manual

Sill, B. L., Cook, N. J., & Blackmore, P. A. (1989). IAWE Aylesbury comparative experiment — preliminary results of wind tunnel comparisons. Journal of Wind Engineering and Industrial Aerodynamics, 32(3), 285-302.

Sill, B. L., Cook, N. J., & Fang, C. (1992). The Aylesbury comparative experiment: A final report. Journal of Wind Engineering and Industrial Aerodynamics, 43(1-3), 1553-1564.

Simiu, E., & Scanlan, R. H. (1996). Wind Effects on Structures: Fundamentals and Applications to Design. John Wiley & Sons, New York.

Sharma, R. N., & Richards, P. J. (2003). The influence of Helmholtz resonance on internal pressures in a low-rise building. Journal of Wind Engineering and Industrial Aerodynamics, 91, 807-828.

Smith, D. A., Mehta, K. C., Yeatts, B. B., & Bhavaraju, S. V. (1994). Area-averaged and internal pressure coefficients measured in the field. Journal of Wind Engineering and Industrial Aerodynamics, 53(1-2), 89-103.

Stathopoulos, T. & Surry, D. (1983). Scale effects in wind tunnel testing of low buildings. Journal of Wind Engineering and Industrial Aerodynamics, 13(1-3), 313-326.

Stathopoulos, T. (1984). Design and fabrication of a wind tunnel for building aerodynamics. Journal of Wind Engineering and Industrial Aerodynamics, 16(2-3), 361-376.

Surry D., & Johnson G.L. (1986). Comparisons between wind tunnel and full-scale estimates of wind loads on a mobile home. Journal of Wind Engineering and Industrial Aerodynamics, 23, 165-180.

Surry, D. (1991). Pressure measurements on the Texas Tech building: Wind tunnel measurements and comparisons with full scale. Journal of Wind Engineering and Industrial Aerodynamics, 38(2-3), 235-247.

Sigma – Swiss Re (2011). Natural catastrophes and man-made disasters in 2010. No1/2011, Swiss Reinsurance Company td, Zurich, Switzerland.

Tieleman, H. W., Hajj, M. R., & Reinhold, T. A. (1998). Wind tunnel simulation requirements to assess wind loads on low-rise buildings. Journal of Wind Engineering and Industrial Aerodynamics, 74-76, 675-685.

Tieleman, H. W., Reinhold, T. A., & Marshall, R. D. (1978). On the wind-tunnel simulation of the atmospheric surface layer for the study of wind loads on low-rise buildings. Journal of Wind Engineering and Industrial Aerodynamics, 3(1), 21-38.

Van der Hoven, I. (1957). Power spectrum of wind velocities fluctuations in the frequency range from 0.0007 to 900 Cycles per hour. Journal of Meteorology, 14, 160-164.

Vickery, P. J., & Surry, D. (1983). The Aylesbury experiments revisited — further wind tunnel tests and comparisons. Journal of Wind Engineering and Industrial Aerodynamics, 11(1-3), 39-62.

VISHAY, StrainSmart Software Specification/Features Version 3.1, Bulletin 256S, Vishay Measurements Group

VISHAY, System 5000 Hardware Specifications, Bulletin 257H, Vishay Measurements Group

Wang, K. (2005). Modeling terrain effects and application to the wind loading of low buildings. PhD Thesis, Concordia University, Montreal, QC, Canada.

Woo, H. G. C., Peterka, J. A., & Cermak, J. E. (1977). Wind-tunnel measurements in the wakes
of structures. NASA Contractor Rep. NASA CR~2806.

Yeatts, B. B., & Mehta, K. C. (1993). Field experiments for building aerodynamics. Journal of Wind Engineering and Industrial Aerodynamics, 72, 163-174.

Yu, B., Chowdhury, A. G., & Masters, F. J. (2008). Hurricane wind power spectra, cospectra, and integral length scales. Boundary Layer Meteorology, 129, 411-430.

Zisis, I. (2006). Structural monitoring and wind tunnel studies of a low wooden building. MASc Thesis, Concordia University, Montreal, QC, Canada.

Zisis, I., & Stathopoulos, T. (2009). Wind-induced cladding and structural loads on low-wood building. Journal of Structural Engineering, 135(4), 437-447.

APPENDIX A

Stationarity of Full-Scale Records

This appendix presents supplementary results to Section 5.3.

A.1 Phase I inspection

Table A.1 Qualified records from PHASE I visual and moving average slope inspection (*V>15 km/h).

Start Date	Record Date	Time	Point ID	V10m (km/h)				D10m (deg.)	
				Mean	StDev	Min	Max	Mean	StDev
2008									
28-Oct-08	29-Oct-08	03:43:15	296161	23.14	6.56	8.00	48.90	190.81	16.24
		03:51:03	298501	23.52	5.44	9.89	43.16	179.49	16.76
		06:38:03	348601	26.37	7.97	5.13	50.67	197.45	15.80
		07:15:39	359881	25.11	7.33	4.82	48.16	203.28	16.98
		13:14:39	467581	20.42	6.72	6.84	46.45	227.14	18.64
29-Oct-08	29-Oct-08	15:28:47	5941	20.22	6.73	4.88	39.13	232.09	20.78
		15:30:23	6421	20.02	6.55	5.80	38.64	230.97	19.81
		17:10:23	36421	15.92	5.28	3.24	30.34	215.45	18.38
	30-Oct-08	05:46:23	263221	16.31	4.82	5.98	31.86	242.92	16.50
		09:52:11	336961	15.92	3.93	5.86	28.14	258.96	14.15
07-Nov-08	07-Nov-08	17:08:42	125221	18.55	4.46	8.73	32.54	41.45	12.11
		18:46:36	154591	16.00	4.70	5.49	28.69	41.94	14.36
17-Nov-08	17-Nov-08	13:31:41	35281	17.67	5.53	2.56	34.06	263.51	16.82
19-Nov-08	20-Nov-08	01:19:47	248791	19.17	5.92	2.99	39.80	328.61	25.20
		02:30:29	270001	18.01	6.64	2.08	40.04	330.22	27.83
		02:47:29	275101	15.93	4.72	3.54	28.69	327.70	24.28
		03:32:47	288691	15.75	4.13	4.40	35.16	317.86	18.85
		05:52:05	330481	16.00	5.88	1.83	34.00	319.08	24.78
		11:41:53	435421	16.62	6.66	2.69	39.43	300.74	21.94

		14:05:29	478501	19.51	5.66	4.21	34.98	287.48	14.52
21-Nov-08	22-Nov-08	14:09:40	288091	20.15	6.32	1.71	39.68	323.24	24.29
		15:52:58	319081	19.66	7.65	2.26	46.39	315.39	23.63
	23-Nov-08	04:12:34	540961	17.03	4.07	7.45	31.50	264.26	12.81
		05:40:58	567481	19.99	4.34	5.43	33.63	266.39	13.96
		05:46:58	569281	19.69	4.64	5.43	31.80	264.98	14.59
		07:21:46	597721	16.49	4.60	3.72	30.64	251.02	16.18
		09:59:40	645091	20.90	7.63	5.80	46.27	277.95	18.89
		14:15:40	721891	22.25	7.33	3.48	44.68	291.80	19.47
24-Nov-08	25-Nov-08	14:59:06	645481	18.34	4.01	6.04	28.81	92.01	12.59
		19:06:54	719821	19.92	5.98	7.02	41.14	96.67	13.99
		19:10:06	720781	20.96	6.08	9.71	41.14	96.77	13.48
		19:32:06	727381	18.62	5.64	5.31	37.05	97.16	13.70
		21:57:54	771121	18.23	4.47	5.13	30.83	87.76	12.47
25-Nov-08	26-Nov-08	01:59:46	59101	18.58	4.62	5.43	34.98	95.13	13.13
		05:15:04	117691	15.00	4.62	5.31	31.80	92.87	15.40
		05:38:04	124591	17.69	4.39	7.20	29.67	88.25	13.94
		06:29:22	139981	17.09	3.66	8.30	27.16	86.94	12.20
		09:09:04	187891	20.14	4.76	8.73	34.79	93.99	13.44
		09:27:58	193561	19.15	4.99	7.02	40.41	95.87	15.14
		09:43:10	198121	20.23	6.25	6.35	42.12	96.54	15.13
		10:12:58	207061	15.21	5.63	3.85	32.47	102.63	15.95
2009									
24-Apr-09	25-Apr-09	13:15:14	396661	24.64	8.02	3.60	46.70	225.77	19.91
		13:28:50	400741	27.86	7.21	6.04	48.90	209.35	16.34
		13:32:26	401821	28.32	7.73	6.04	48.90	211.21	16.29
		13:33:26	402121	27.21	8.23	2.99	48.90	213.15	18.77
		13:47:14	406261	25.74	6.92	5.98	43.65	200.64	16.17
		14:02:50	410941	27.20	6.11	9.40	44.81	206.85	15.28
25-Apr-09	26-Apr-09	11:15:15	263941	21.74	6.49	2.87	39.07	4.33	33.58
		13:53:39	311461	20.12	4.88	5.62	34.61	17.10	22.13
		15:26:15	339241	20.99	4.76	10.13	34.12	31.74	15.74
		16:04:15	350641	19.02	4.99	7.08	35.16	20.45	24.79
		17:57:39	384661	19.36	4.38	8.00	31.56	31.53	14.67
14-May-09	14-May-09	13:02:53	30901	28.29	8.37	5.68	50.79	208.63	17.40
		13:14:29	34381	33.18	9.02	7.57	64.03	210.65	16.35
		14:09:29	50881	33.17	9.93	5.25	60.62	202.64	13.98
		15:13:29	70081	33.08	10.99	5.37	61.90	217.74	17.06

		15:41:17	78421	33.58	10.39	7.69	70.20	216.74	19.65
		16:17:17	89221	28.17	10.85	7.08	61.71	206.09	16.15
		16:29:41	92941	27.11	8.51	1.83	53.66	215.06	19.18
		17:13:29	106081	34.03	7.91	14.35	58.23	204.89	13.68
14-May-09	15-May-09	00:10:17	7081	27.29	9.60	5.07	56.04	221.18	17.88
		01:26:42	30001	24.15	7.61	3.36	50.48	225.68	17.93
		02:06:17	41881	24.78	8.09	6.17	59.03	231.21	19.13
		02:53:29	56041	25.34	6.72	10.26	47.49	223.91	15.92
		03:22:05	64621	22.90	6.92	6.47	42.97	228.62	18.03
		12:57:41	237301	22.45	6.89	2.93	42.55	254.04	18.98
16-May-09	17-May-09	05:20:12	206401	17.15	5.04	4.76	30.83	183.16	19.00
		06:10:24	221461	19.73	5.10	5.80	32.78	175.51	14.56
		06:57:00	235441	19.20	5.38	8.55	38.27	177.54	14.48
		08:04:36	255721	18.38	5.03	5.62	34.18	174.87	17.55
		10:09:00	293041	18.56	5.35	1.77	35.47	207.12	15.69
		10:35:12	300901	19.50	5.49	6.23	36.56	211.15	13.44
20-May-09	20-May-09	14:18:08	110581	17.22	5.40	4.40	35.95	291.48	20.52
21-May-09	21-May-09	12:01:00	28021	24.27	6.90	4.03	41.75	257.73	16.45
		14:29:00	72421	28.49	9.49	5.55	62.02	257.97	18.31
		15:36:12	92581	28.26	7.16	7.14	46.88	258.53	15.74
		16:07:12	101881	28.64	7.99	5.92	56.71	252.75	17.53
		16:35:12	110281	27.96	7.77	9.40	50.73	259.44	14.88
		17:14:48	122161	28.06	7.29	5.86	49.51	264.98	15.94
22-May-09	22-May-09	09:16:34	16021	15.03	5.23	4.88	28.38	294.70	20.10
		10:44:10	42301	16.49	5.20	4.33	32.78	282.90	20.06
		11:10:26	48181	17.54	5.51	3.60	32.66	284.99	20.26
		12:01:38	63541	15.03	5.47	1.10	34.79	319.47	24.14
22-May-09	24-May-09	13:21:41	109081	19.61	6.14	3.30	39.43	234.57	21.06
		13:58:53	120241	20.29	6.91	3.24	39.49	234.55	20.39
		15:01:29	139021	21.04	5.72	5.43	36.63	215.24	19.02
		15:22:29	145321	19.63	5.84	2.62	39.19	231.52	23.27
		16:23:29	163621	19.52	5.99	4.03	35.59	221.69	20.70
25-May-09	25-May-09	11:40:05	68881	16.12	5.62	3.11	34.79	322.65	26.53
		11:55:29	73501	16.55	6.12	2.01	36.20	325.35	26.76
		12:41:17	87241	18.18	6.07	3.17	35.89	316.07	23.74
		12:55:29	91501	15.21	5.60	0.18	40.59	325.54	30.00
25-May-09	25-May-09	14:59:35	26401	22.23	7.66	3.48	42.91	327.46	28.76
		15:20:11	32581	20.67	8.60	0.06	52.13	326.91	31.74

		15:46:11	40381	23.20	8.44	3.78	46.33	325.77	28.04
		15:51:35	42001	21.45	8.72	1.22	46.33	328.88	30.09
		16:34:35	54901	21.40	7.93	4.21	48.83	330.82	30.62
		16:52:35	60301	21.30	9.31	3.36	52.25	332.37	32.47
		17:59:59	80521	22.12	8.86	0.43	43.28	332.66	36.25
27-May-09	27-May-09	17:58:31	72301	15.88	4.62	5.13	28.38	208.36	18.63
		18:06:19	74641	19.61	4.30	6.78	33.76	210.17	14.76
		18:21:07	79081	19.17	4.89	6.10	32.47	220.41	16.32
01-Jun-09	01-Jun-09	08:50:45	13021	22.99	7.15	7.57	51.64	265.50	15.02
		08:53:33	13861	23.20	6.93	7.57	51.64	264.19	15.52
		08:55:21	14401	23.50	6.95	7.57	51.64	263.41	15.48
01-Jun-09	01-Jun-09	10:37:16	21781	29.13	8.28	6.84	52.86	262.16	14.41
		12:04:52	48061	28.44	7.99	7.87	53.35	271.34	19.54
		13:22:28	71341	28.93	10.11	9.10	59.88	270.02	19.84
		14:17:28	87841	29.57	9.76	3.85	60.19	276.44	19.92
		15:12:28	104341	29.36	8.86	5.74	54.51	285.35	20.23
		15:29:04	109321	30.75	9.40	9.10	58.11	289.01	18.07
		15:37:16	111781	29.33	9.25	7.87	57.81	282.80	16.61
		17:25:16	144181	28.68	7.97	5.80	55.24	286.36	19.87
02-Jun-09	02-Jun-09	12:49:10	37141	17.87	5.03	6.84	32.05	283.44	17.47
		14:36:58	69481	18.78	7.02	4.64	47.19	293.34	22.22
		15:27:34	84661	16.26	5.99	1.71	36.87	306.72	27.60
		16:03:10	95341	17.17	6.36	2.99	37.54	306.77	24.06
		16:16:46	99421	21.41	5.90	8.61	39.31	285.18	16.42
		16:23:46	101521	18.00	5.91	3.60	39.31	295.24	22.79
		16:48:22	108901	21.01	6.07	5.13	37.42	281.14	17.83
		17:04:46	113821	16.85	5.79	3.42	34.92	300.36	25.45
03-Jun-09	03-Jun-09	13:38:10	28501	16.32	5.85	2.01	33.57	297.09	25.61
		14:16:58	40141	15.83	5.84	3.72	33.09	276.93	21.69
		14:49:34	49921	16.22	5.82	3.85	33.33	284.53	19.31
04-Jun-09	04-Jun-09	11:13:01	11221	15.87	4.81	2.62	35.34	285.85	22.73
		11:56:25	24241	17.78	6.13	5.13	37.66	269.32	17.60
		12:16:25	30241	15.69	4.90	5.07	30.52	286.61	22.85
07-Jun-09	07-Jun-09	13:28:01	15241	20.32	6.64	4.15	38.76	271.09	19.96
		14:39:25	36661	18.10	6.34	2.32	36.93	267.52	25.71
		15:44:37	56221	16.29	5.47	1.22	39.01	267.88	24.22
08-Jun-09	08-Jun-09	11:02:15	41041	18.05	5.38	4.64	32.90	284.04	16.14
		13:01:03	76681	16.84	5.85	2.38	34.00	313.14	28.12

		14:27:15	102541	16.46	7.09	0.79	34.37	323.24	34.57
		15:02:15	113041	18.26	7.33	0.61	44.44	314.48	30.32
		15:47:51	126721	17.09	6.40	4.21	33.76	333.01	34.13
17-Jun-09	17-Jun-09	13:24:59	96361	16.95	5.97	3.60	33.27	259.90	21.09
		13:55:47	105601	15.99	5.02	3.48	28.51	283.24	24.16
		18:04:47	180301	15.02	5.23	3.91	33.15	262.12	17.95
17-Jun-09	18-Jun-09	12:08:18	74101	20.19	5.48	4.09	36.14	259.44	15.60
		12:49:30	86461	18.79	5.74	3.11	32.60	250.91	18.53
		13:17:30	94861	18.69	4.63	4.52	31.38	251.89	16.64
		13:41:42	102121	17.59	5.33	2.62	32.60	233.39	21.50
18-Jun-09	18-Jun-09	15:52:34	11881	20.64	5.08	5.55	35.53	248.17	16.82
		16:11:22	17521	20.04	6.58	5.68	40.90	242.26	18.52
		16:18:10	19561	19.19	6.20	3.30	35.65	255.64	21.06
		16:31:46	23641	20.52	6.55	5.31	39.80	256.44	18.50
		18:15:34	54781	19.61	6.25	3.42	35.47	257.70	15.09
		18:29:10	58861	19.79	5.97	3.85	40.96	248.01	18.78
19-Jun-09	21-Jun-09	14:13:50	468901	23.25	6.60	7.45	45.05	73.96	17.04
		14:58:38	482341	23.29	6.69	7.26	43.77	74.25	18.36
		16:51:02	516061	24.52	6.49	9.71	46.27	58.07	18.18
		17:41:14	531121	23.45	6.66	9.64	45.97	59.14	16.48
		18:42:14	549421	22.61	6.57	5.98	47.92	62.84	19.54
		18:50:14	551821	23.76	6.29	5.43	43.04	61.92	17.11
		19:48:02	569161	22.61	6.60	8.55	44.32	62.70	16.93
	22-Jun-09	00:46:02	658561	22.77	6.98	7.69	47.55	53.04	17.46
22-Jun-09	22-Jun-09	01:38:13	185341	24.10	7.44	7.69	46.33	51.79	16.42
		12:02:41	189481	22.92	6.69	10.44	49.08	49.97	16.06
		14:55:05	237061	23.04	6.51	7.63	45.11	56.79	18.93
		16:08:53	259201	22.77	6.32	3.11	39.49	47.74	15.55
		16:36:53	267601	22.72	6.01	8.24	40.17	47.03	13.27
		17:28:17	283021	23.34	6.08	10.87	42.97	54.53	16.77
		23:39:05	394261	22.77	6.63	8.12	38.46	48.28	11.99

Table A.2 Percentage points of RUN distribution.

n = N/2	0.99	0.975	0.95	0.05	0.025	0.01
5	2	2	3	8	9	9
6	2	3	3	10	10	11
7	3	3	4	11	12	12
8	4	4	5	12	13	13
9	4	5	6	13	14	15
10	5	6	6	15	15	16
11	6	7	7	16	16	17
12	7	7	8	17	18	18
13	7	8	9	18	19	20
14	8	9	10	19	20	21
15	9	10	11	20	21	22
16	10	11	11	22	22	23
18	11	12	13	24	25	26
20	13	14	15	26	27	28
25	17	18	19	32	33	34
30	21	22	24	37	39	40
35	25	27	28	43	44	46
40	30	31	33	48	50	51
45	34	36	37	54	55	57
50	38	40	42	59	61	63
55	43	45	46	65	66	68
60	47	49	51	70	72	74
65	52	54	56	75	77	79
70	56	58	60	Al	83	85
75	61	63	65	86	88	90
80	65	68	70	91	93	96
85	70	72	74	97	99	101
90	74	77	79	102	104	107
95	79	82	84	107	109	112
100	84	86	88	113	115	117

Table A.3 Percentage points of TREND distribution.

N	0.99	0.975	0.95	0.05	0.025	0.01
10	9	11	13	31	33	35
12	16	18	21	44	47	49
14	24	27	30	60	63	0.66
16	34	38	41	78	81	85
18	45	50	54	98	102	107
20	59	64	69	120	125	130
30	152	162	171	263	272	282
40	290	305	319	460	474	435
50	473-	495	514	710	729	751
60	702	731	756	1013	1038	1064
70	977	1014	1045	1369	1400	1437
80	1299	1344	1382	1777	1815	1360
90	1668	1721	1766	2238	2283	2336
100	2083	2145	2198	2751	2804	2865

A.2 Phase II selection (RUN and TREND tests)

Table A.4 RUN and TREND tests (time lag = 30 sec and N = 20).

Start Date	Date	Time	Point ID	V6.5m				D6.5m				V10m				D10m			
				RUN		TREND		RUN		TREND		RUN		TREND		RUN		TREND	
				Mean	M. Sq.	Mean	M. Sq.	Mean	M. Sq.	Mean	M. Sq.	Mean	M. Sq.	Mean	M. Sq.	Mean	M. Sq.	Mean	M. Sq.
2008																			
28-Oct-08	29-Oct-08	03:43:15	296161	S	S	S	S	NS	NS	NS	NS	S	S	S	S	S	S	NS	NS
		03:51:03	298501	S	S	S	S	S	S	S	S	S	S	S	S	S	S	S	S
		06:38:03	348601	S	S	S	S	S	S	NS	S	S	S	S	S	S	S	S	S
		07:15:39	359881	S	S	S	S	S	S	S	S	S	S	S	S	S	S	S	S
		13:14:39	467581	S	S	S	S	S	S	S	S	S	S	S	S	S	S	S	S
29-Oct-08	29-Oct-08	15:28:47	5941	S	S	S	S	S	S	S	S	S	S	S	S	S	S	S	S
		15:30:23	6421	S	S	S	S	S	S	S	S	S	S	S	S	S	S	S	S
		17:10:23	36421	S	S	S	S	S	S	S	S	S	S	S	S	S	S	S	S
	30-Oct-08	05:46:23	263221	S	S	S	S	S	NS	S	S	S	S	S	S	NS	S	S	S
		09:52:11	336961	S	S	S	S	S	S	NS	S	S	S	S	S	NS	NS	S	S
07-Nov-08	07-Nov-08	17:08:42	125221	S	S	S	S	S	S	S	S	S	S	S	S	S	S	S	S
		18:46:36	154591	S	S	S	S	S	S	S	S	S	S	S	S	S	S	S	S
17-Nov-08	17-Nov-08	13:31:41	35281	S	S	S	S	S	S	S	S	S	S	S	S	NS	NS	S	S
19-Nov-08	20-Nov-08	01:19:47	248791	S	S	S	S	S	S	S	S	S	S	S	S	S	S	S	S
		02:30:29	270001	S	S	S	S	S	S	S	S	S	S	S	S	S	S	S	S
		02:47:29	275101	S	S	S	S	S	S	S	S	S	S	S	S	S	S	S	S
		03:32:47	288691	S	S	S	S	NS	S	S	S	S	S	S	S	S	S	S	NS
		05:52:05	330481	S	S	S	S	S	S	S	S	S	S	S	S	S	S	S	S
		11:41:53	435421	NS	NS	S	S	NS	S	NS	NS	S	NS	S	S	S	S	S	S
		14:05:29	478501	S	S	S	S	S	S	S	S	S	S	S	S	S	S	S	S
21-Nov-08	22-Nov-08	14:09:40	288091	S	S	S	S	S	S	S	S	S	S	S	S	S	S	S	S
		15:52:58	319081	S	S	S	S	S	S	S	S	S	S	S	S	S	S	S	S

	23-Nov-08	04:12:34	540961	S	S	S	S	NS	NS	S	S	S	S	S	S	S	S	S	S
		05:40:58	567481	S	S	S	S	S	S	S	S	NS	NS	S	S	S	S	S	S
		05:46:58	569281	S	S	S	S	S	S	S	S	S	S	S	S	S	S	S	S
		07:21:46	597721	S	S	S	S	S	S	S	S	S	S	S	S	S	S	S	S
		09:59:40	645091	S	S	S	S	S	S	S	S	S	S	S	S	S	S	S	S
		14:15:40	721891	S	S	S	S	S	S	S	S	S	S	S	S	S	S	S	S
24-Nov-08	25-Nov-08	14:59:06	645481	S	S	S	S	S	S	S	S	S	S	S	S	S	S	S	S
		19:06:54	719821	S	S	S	S	S	S	S	S	S	S	S	S	S	S	S	S
		19:10:06	720781	S	S	S	S	S	S	S	S	S	S	S	S	S	S	S	S
		19:32:06	727381	NS	NS	S	S	S	S	S	S	NS	NS	S	S	S	S	S	S
		21:57:54	771121	S	S	S	S	S	S	S	S	S	S	S	S	S	S	S	S
25-Nov-08	26-Nov-08	01:59:46	59101	S	S	S	S	S	S	S	S	S	S	S	S	S	S	S	S
		05:15:04	117691	NS	NS	S	S	S	S	S	S	NS	NS	S	S	S	S	S	S
		05:38:04	124591	S	S	S	S	S	S	S	S	S	S	S	S	S	S	S	S
		06:29:22	139981	S	S	S	S	S	S	S	S	S	S	S	S	S	S	S	S
		09:09:04	187891	NS	NS	S	S	S	S	NS	NS	S	NS	S	S	S	NS	S	S
		09:27:58	193561	S	S	S	S	S	S	S	S	S	S	S	S	S	NS	S	S
		09:43:10	198121	S	NS	S	S	S	S	S	S	S	S	S	S	S	S	S	S
		10:12:58	207061	S	S	S	S	S	S	S	S	NS	S	S	S	S	S	S	S
2009																			
24-Apr-09	25-Apr-09	13:15:14	396661	NS	NS	S	S	S	S	NS	NS	S	S	S	S	S	S	S	S
		13:28:50	400741	S	S	S	S	S	S	S	S	S	S	S	S	S	S	S	S
		13:32:26	401821	S	S	S	S	S	S	S	S	S	S	S	S	S	S	S	S
		13:33:26	402121	S	S	S	S	S	S	NS	NS	S	S	S	S	S	S	S	S
		13:47:14	406261	S	S	S	S	S	S	NS	NS	S	S	S	S	S	S	NS	NS
		14:02:50	410941	S	S	S	S	S	S	S	S	S	S	S	S	S	S	S	S
25-Apr-09	26-Apr-09	11:15:15	263941	NS	NS	S	S	NS	NS	S	S	NS	NS	S	S	S	S	S	S
		13:53:39	311461	S	S	S	S	NS	NS	S	S	S	S	S	S	S	S	S	S
		15:26:15	339241	S	S	S	S	S	S	S	S	S	S	NS	S	S	S	S	S
		16:04:15	350641	S	S	S	S	S	S	S	S	S	S	S	S	S	S	S	S

		17:57:39	384661	S	S	S	S	NS	NS	S	S	S	S	S	S	S	NS	S	S
14-May-09	14-May-09	13:02:53	30901	S	S	S	S	S	S	S	S	S	S	S	S	S	S	S	S
		13:14:29	34381	S	S	S	S	S	S	S	S	S	S	S	S	S	S	S	S
		14:09:29	50881	S	S	S	S	S	S	S	S	S	S	S	S	S	S	S	S
		15:13:29	70081	S	S	S	S	S	S	S	S	S	S	S	S	S	S	S	S
		15:41:17	78421	S	S	S	S	S	S	S	S	S	S	S	S	S	S	S	S
		16:17:17	89221	NS	NS	S	S	S	S	S	S	NS	NS	S	S	S	S	S	S
		16:29:41	92941	S	S	S	S	S	S	NS	NS	S	S	S	S	S	S	NS	NS
		17:13:29	106081	S	S	S	S	S	S	S	S	S	S	S	S	S	S	S	S
14-May-09	15-May-09	00:10:17	7081	S	S	S	S	S	S	S	S	S	S	S	S	S	S	S	S
		01:26:42	30001	S	S	S	S	S	S	S	S	S	S	S	S	S	S	NS	NS
		02:06:17	41881	S	S	S	S	S	S	S	S	S	S	S	S	S	S	S	S
		02:53:29	56041	S	S	S	S	S	S	S	S	S	NS	S	S	S	S	S	S
		03:22:05	64621	S	S	S	S	S	S	S	S	S	S	S	S	S	S	S	S
		12:57:41	237301	S	S	S	S	S	S	S	S	S	S	S	S	S	S	S	S
16-May-09	17-May-09	05:20:12	206401	S	S	S	S	S	S	S	S	S	S	S	S	S	S	S	S
		06:10:24	221461	S	S	S	S	S	S	S	S	S	S	S	S	NS	NS	S	S
		06:57:00	235441	S	S	S	S	S	S	NS	NS	S	S	S	S	S	S	NS	NS
		08:04:36	255721	S	S	S	S	NS	S	S	S	S	S	S	S	S	S	S	S
		10:09:00	293041	S	S	S	S	S	S	S	S	S	S	S	S	S	S	S	S
		10:35:12	300901	S	S	S	S	S	S	S	S	NS	NS	S	S	S	S	S	S
20-May-09	20-May-09	14:18:08	110581	S	NS	S	S	S	S	S	S	S	S	S	S	S	S	S	S
21-May-09	21-May-09	12:01:00	28021	S	S	S	S	S	S	S	S	S	S	S	S	S	S	S	S
		14:29:00	72421	NS	NS	S	S	NS	NS	S	S	S	S	S	S	NS	NS	NS	NS
		15:36:12	92581	S	S	S	S	S	S	S	S	S	S	S	S	S	S	S	S
		16:07:12	101881	S	S	S	S	S	S	S	S	S	S	S	S	S	S	S	S
		16:35:12	110281	S	S	S	S	NS	NS	S	S	S	NS	S	S	NS	NS	S	S
		17:14:48	122161	S	S	S	S	S	S	S	S	NS	NS	S	S	S	S	S	S
22-May-09	22-May-09	09:16:34	16021	S	S	S	S	NS	S	S	S	S	S	S	S	S	S	S	S
		10:44:10	42301	S	S	S	S	S	S	S	S	S	S	S	S	S	S	NS	NS

		11:10:26	48181	S	S	S	S	S	S	S	S	NS	NS	S	S	NS	NS	S	NS
		12:01:38	63541	S	S	S	S	S	S	S	S	S	S	S	NS	S	S	S	S
22-May-09	24-May-09	13:21:41	109081	S	S	S	S	S	S	S	S	S	S	S	S	S	S	S	S
		13:58:53	120241	S	S	S	S	S	S	S	S	S	S	S	S	S	S	S	S
		15:01:29	139021	S	S	S	S	S	S	S	S	S	S	S	S	S	S	S	S
		15:22:29	145321	S	S	S	S	S	S	S	S	S	S	S	S	NS	NS	S	S
		16:23:29	163621	S	S	S	S	S	NS	S	S	S	S	S	S	S	S	S	S
25-May-09	25-May-09	11:40:05	68881	S	S	S	S	S	S	S	S	S	S	S	S	S	S	S	S
		11:55:29	73501	S	S	S	S	S	S	S	S	S	NS	S	S	S	S	S	S
		12:41:17	87241	S	S	S	S	S	S	S	S	S	S	S	S	S	S	S	S
		12:55:29	91501	S	S	S	S	S	S	S	S	S	S	S	S	S	S	S	S
25-May-09	25-May-09	14:59:35	26401	S	S	S	S	S	S	S	S	NS	NS	S	S	S	S	S	S
		15:20:11	32581	S	S	S	S	S	S	S	S	S	S	S	S	S	S	S	S
		15:46:11	40381	S	S	S	S	S	S	S	S	S	S	S	S	S	S	S	S
		15:51:35	42001	S	S	S	S	S	S	S	S	S	S	S	S	S	S	S	S
		16:34:35	54901	S	S	S	S	S	S	S	S	NS	S	S	S	S	S	S	S
		16:52:35	60301	S	S	S	S	S	NS	S	S	NS	NS	S	S	NS	NS	S	S
		17:59:59	80521	S	S	S	S	S	S	S	S	S	S	S	S	S	S	S	S
27-May-09	27-May-09	17:58:31	72301	S	S	S	S	S	S	S	S	S	S	S	S	S	S	S	S
		18:06:19	74641	S	S	S	S	S	S	S	S	S	S	S	S	S	S	S	S
		18:21:07	79081	S	S	S	S	S	S	S	S	S	S	S	S	S	S	S	S
01-Jun-09	01-Jun-09	08:50:45	13021	S	S	S	S	S	S	S	S	S	S	S	S	S	S	S	S
		08:53:33	13861	S	S	S	S	S	S	NS	NS	S	S	S	S	S	S	NS	NS
		08:55:21	14401	S	S	S	S	NS	NS	NS	NS	S	S	S	S	NS	NS	NS	NS
01-Jun-09	01-Jun-09	10:37:16	21781	S	S	S	S	S	S	S	S	S	S	S	S	S	NS	S	S
		12:04:52	48061	S	S	S	S	S	S	S	S	S	S	S	S	S	S	S	S
		13:22:28	71341	S	S	S	S	S	S	NS	NS	S	S	S	S	NS	NS	NS	NS
		14:17:28	87841	S	S	S	S	S	S	S	S	S	S	S	S	S	S	S	S
		15:12:28	104341	S	S	S	S	S	S	S	S	S	S	S	S	S	S	S	S
		15:29:04	109321	S	S	S	S	S	S	S	S	S	NS	S	S	S	S	S	S

		15:37:16	111781	S	S	S	S	S	S	NS	NS	NS	NS	S	S	S	S	S	S
		17:25:16	144181	S	S	S	NS	S	S	S	S	S	S	S	S	S	S	S	S
02-Jun-09	02-Jun-09	12:49:10	37141	S	S	S	S	S	S	S	S	NS	NS	S	S	S	S	S	S
		14:36:58	69481	S	S	S	S	S	S	S	S	S	S	S	S	S	S	NS	NS
		15:27:34	84661	S	S	S	S	S	S	S	S	S	S	S	S	S	S	S	S
		16:03:10	95341	S	S	S	S	S	NS	S	S	S	S	S	S	S	NS	S	S
		16:16:46	99421	S	S	S	S	S	S	S	S	S	S	S	S	S	S	S	S
		16:23:46	101521	S	S	S	S	NS	S	S	S	S	S	S	S	S	S	S	S
		16:48:22	108901	S	S	S	S	NS	S	S	NS	NS	NS	S	S	NS	NS	NS	NS
		17:04:46	113821	NS	NS	S	S	S	S	S	S	S	S	S	S	S	NS	NS	NS
03-Jun-09	03-Jun-09	13:38:10	28501	S	S	S	S	S	S	S	S	S	S	S	S	S	S	S	S
		14:16:58	40141	S	S	S	S	S	S	S	S	S	S	S	S	S	S	S	S
		14:49:34	49921	S	S	S	S	S	S	S	S	S	S	S	S	S	S	S	S
04-Jun-09	04-Jun-09	11:13:01	11221	S	S	S	S	S	S	S	S	S	S	S	S	S	S	S	S
		11:56:25	24241	S	S	S	S	S	S	S	S	S	S	S	S	S	S	S	S
		12:16:25	30241	S	S	S	S	S	S	S	S	S	S	S	S	S	S	NS	NS
07-Jun-09	07-Jun-09	13:28:01	15241	NS	NS	S	S	S	NS	S	S	S	NS	S	S	S	S	S	S
		14:39:25	36661	S	S	S	S	S	S	S	S	S	S	S	S	NS	NS	S	S
		15:44:37	56221	S	S	S	S	S	NS	S	S	S	S	S	S	S	S	S	S
08-Jun-09	08-Jun-09	11:02:15	41041	S	S	S	S	S	S	S	S	S	S	S	S	S	S	S	S
		13:01:03	76681	S	S	S	S	S	S	S	S	S	S	S	S	S	S	S	S
		14:27:15	102541	S	S	S	S	S	S	S	S	S	S	S	S	S	S	S	S
		15:02:15	113041	S	S	S	S	NS	NS	S	S	S	S	S	S	S	S	S	S
		15:47:51	126721	S	S	S	S	S	S	S	S	S	S	S	S	S	S	S	S
17-Jun-09	17-Jun-09	13:24:59	96361	S	S	S	S	S	S	S	S	S	S	S	S	S	S	S	S
		13:55:47	105601	S	S	S	S	S	S	S	S	S	S	S	S	S	S	S	S
		18:04:47	180301	S	S	S	S	S	NS	S	S	NS	NS	S	S	S	S	S	S
17-Jun-09	18-Jun-09	12:08:18	74101	S	S	S	S	S	S	S	S	S	S	S	S	S	S	S	S
		12:49:30	86461	S	S	S	S	NS	S	S	S	S	S	S	S	S	S	S	S
		13:17:30	94861	S	S	NS	NS	NS	NS	NS	NS	S	S	S	S	NS	NS	NS	NS

		13:41:42	102121	S	S	S	S	S	S	S	S	S	S	S	S	S	NS	S	S
18-Jun-09	18-Jun-09	15:52:34	11881	S	S	S	S	NS	NS	S	S	S	S	S	S	NS	NS	S	S
		16:11:22	17521	S	S	S	S	S	S	S	S	S	S	S	S	S	S	S	S
		16:18:10	19561	NS	S	S	S	NS	NS	NS	NS	NS	NS	S	S	NS	NS	NS	NS
		16:31:46	23641	S	S	S	S	NS	NS	NS	NS	S	S	S	S	NS	NS	NS	NS
		18:15:34	54781	S	S	S	S	NS	S	S	S	S	S	S	S	S	S	S	S
		18:29:10	58861	S	S	S	S	S	S	S	S	S	S	S	S	S	S	S	S
19-Jun-09	21-Jun-09	14:13:50	468901	S	NS	S	S	S	S	S	S	S	S	S	S	NS	NS	S	S
		14:58:38	482341	S	S	S	S	S	S	S	S	S	S	S	S	S	S	S	S
		16:51:02	516061	S	S	S	S	S	S	S	S	S	S	S	S	S	S	S	S
		17:41:14	531121	NS	NS	S	S	S	S	S	S	NS	NS	S	S	S	S	S	S
		18:42:14	549421	S	S	S	S	S	S	S	S	S	S	S	S	S	S	S	S
		18:50:14	551821	S	S	S	S	S	S	S	S	S	S	S	S	S	NS	S	S
		19:48:02	569161	S	S	S	S	NS	S	S	S	S	S	S	S	S	S	S	S
	22-Jun-09	00:46:02	658561	S	NS	S	S	S	S	S	S	S	S	S	S	NS	S	S	S
22-Jun-09	22-Jun-09	01:38:13	185341	S	S	S	S	S	S	S	S	S	S	S	S	S	S	S	S
		12:02:41	189481	S	S	S	S	S	S	S	S	S	S	S	S	S	S	S	S
		14:55:05	237061	S	S	S	S	S	S	S	S	S	S	S	S	S	S	S	S
		16:08:53	259201	S	S	S	S	S	S	S	S	S	S	S	S	S	S	S	S
		16:36:53	267601	S	S	S	S	NS	NS	S	S	S	S	S	S	S	S	S	S
		17:28:17	283021	NS	NS	S	S	NS	NS	S	S	S	S	S	S	NS	NS	S	S
		23:39:05	394261	S	S	S	S	S	S	S	S	S	S	S	S	S	S	S	S

Table A.5 RUN and TREND tests (time lag = 40 sec and N = 15).

Start Date	Date	Time	Point ID	V6.5m				D6.5m				V10m				D10m			
				RUN		TREND		RUN		TREND		RUN		TREND		RUN		TREND	
				Mean	M. Sq.	Mean	M. Sq.	Mean	M. Sq.	Mean	M. Sq.	Mean	M. Sq.	Mean	M. Sq.	Mean	M. Sq.	Mean	M. Sq.
2008																			
28-Oct-08	29-Oct-08	03:43:15	296161	S	S	S	S	S	S	NS	NS	S	S	S	S	S	S	NS	NS
		03:51:03	298501	S	S	S	S	S	S	S	S	S	S	S	S	S	S	S	S
		06:38:03	348601	S	S	S	S	S	S	NS	NS	S	S	S	S	S	S	S	S
		07:15:39	359881	S	S	S	S	S	S	NS	NS	S	S	S	S	S	S	NS	NS
		13:14:39	467581	NS	NS	S	S	S	S	S	S	NS	NS	S	S	S	S	S	S
29-Oct-08	29-Oct-08	15:28:47	5941	S	S	S	S	S	S	S	S	S	S	S	S	S	S	NS	NS
		15:30:23	6421	S	S	S	S	S	S	NS	NS	S	S	S	S	S	S	S	S
		17:10:23	36421	S	S	S	S	S	S	S	S	S	S	S	S	S	S	NS	S
	30-Oct-08	05:46:23	263221	S	S	NS	NS	S	S	S	S	S	S	S	S	S	S	S	S
		09:52:11	336961	S	S	S	S	S	S	S	S	S	S	S	S	S	S	S	S
07-Nov-08	07-Nov-08	17:08:42	125221	S	S	S	S	S	S	S	S	S	S	S	S	S	S	S	S
		18:46:36	154591	S	S	S	S	S	S	S	S	S	S	S	S	S	S	S	S
17-Nov-08	17-Nov-08	13:31:41	35281	S	S	S	S	S	S	S	S	NS	NS	S	S	S	S	S	S
19-Nov-08	20-Nov-08	01:19:47	248791	S	S	S	S	S	S	NS	NS	S	S	S	S	S	S	S	S
		02:30:29	270001	S	S	S	S	S	S	NS	NS	S	S	S	S	S	S	S	S
		02:47:29	275101	S	S	S	S	NS	NS	S	S	S	S	S	S	S	S	S	S
		03:32:47	288691	S	S	S	S	S	S	S	S	S	S	S	S	S	S	NS	NS
		05:52:05	330481	S	S	S	S	S	S	S	S	S	S	S	S	S	S	S	S
		11:41:53	435421	NS	NS	NS	NS	S	S	NS	NS	NS	NS	NS	NS	S	S	S	S
		14:05:29	478501	S	S	S	S	S	S	S	S	S	S	S	S	S	S	S	S
21-Nov-08	22-Nov-08	14:09:40	288091	S	S	S	S	S	S	S	S	S	S	S	S	S	NS	S	S
		15:52:58	319081	S	S	S	S	NS	S	S	S	S	S	S	S	S	S	S	S
	23-Nov-08	04:12:34	540961	S	S	S	S	S	S	S	S	S	S	S	S	S	NS	S	S

		05:40:58	567481	S	S	S	S	S	S	S	S	S	S	S	S	S	S	NS	NS
		05:46:58	569281	S	S	S	S	S	S	S	S	S	S	S	S	S	S	S	S
		07:21:46	597721	S	S	S	S	S	S	S	S	S	S	S	S	S	S	S	S
		09:59:40	645091	S	S	S	S	S	S	S	S	S	S	S	S	S	S	S	S
		14:15:40	721891	S	S	S	S	S	S	S	S	S	S	S	S	S	S	S	S
24-Nov-08	25-Nov-08	14:59:06	645481	S	S	S	S	S	S	S	S	S	S	S	S	S	S	S	S
		19:06:54	719821	S	S	S	S	S	S	S	S	S	S	S	S	S	S	S	S
		19:10:06	720781	S	S	S	S	S	S	S	S	S	S	S	S	S	S	S	S
		19:32:06	727381	S	S	S	S	S	S	S	S	S	S	S	S	S	S	S	S
		21:57:54	771121	S	S	S	S	S	S	NS	NS	S	S	S	S	S	S	S	NS
25-Nov-08	26-Nov-08	01:59:46	59101	S	S	S	S	S	S	S	S	S	S	S	S	S	S	S	S
		05:15:04	117691	S	S	S	S	S	S	S	S	S	S	S	S	S	S	S	S
		05:38:04	124591	S	S	S	S	S	S	S	S	S	S	S	S	S	S	S	S
		06:29:22	139981	S	S	S	S	S	S	NS	S	NS	S	S	S	S	S	NS	NS
		09:09:04	187891	S	S	S	S	S	S	S	NS	S	NS	S	S	S	NS	S	S
		09:27:58	193561	S	S	S	NS	S	S	S	S	S	S	S	S	S	S	S	S
		09:43:10	198121	S	S	S	S	S	S	S	S	S	S	S	S	S	S	S	S
		10:12:58	207061	S	S	S	S	S	S	S	S	S	S	S	S	S	S	S	S
2009																			
24-Apr-09	25-Apr-09	13:15:14	396661	S	S	S	S	S	S	NS	NS	S	S	S	S	S	S	NS	NS
		13:28:50	400741	S	S	S	S	S	S	S	S	S	S	S	S	S	S	S	S
		13:32:26	401821	S	S	S	NS	S	S	S	S	S	S	S	S	S	S	S	S
		13:33:26	402121	S	S	NS	S	NS	NS	S	S	S	S	S	S	S	S	S	S
		13:47:14	406261	S	S	S	S	S	S	NS	NS	S	S	S	S	S	S	NS	NS
		14:02:50	410941	S	S	S	S	S	S	S	S	S	S	S	S	S	S	S	S
25-Apr-09	26-Apr-09	11:15:15	263941	S	S	S	S	S	S	NS	NS	S	S	S	S	S	S	NS	S
		13:53:39	311461	S	S	S	S	S	S	S	S	S	S	S	S	S	S	S	S
		15:26:15	339241	S	S	S	S	S	S	NS	NS	S	S	S	S	S	S	NS	S
		16:04:15	350641	S	S	S	S	S	S	S	S	S	S	S	S	S	S	S	S
		17:57:39	384661	NS	NS	NS	NS	S	S	NS	NS	S	S	NS	NS	S	S	NS	S

14-May-09	14-May-09	13:02:53	30901	S	S	S	S	S	S	S	S	S	S	S	S	S	S	S	S
		13:14:29	34381	S	S	S	S	S	S	S	NS	S	S	S	S	S	S	S	S
		14:09:29	50881	S	S	S	S	S	S	S	S	S	S	S	S	S	S	S	S
		15:13:29	70081	S	S	S	S	S	S	S	S	S	S	S	S	S	S	S	S
		15:41:17	78421	S	S	S	S	S	S	S	S	S	S	S	S	S	S	S	S
		16:17:17	89221	S	S	S	S	S	S	S	S	S	S	S	S	S	S	S	S
		16:29:41	92941	S	S	S	S	S	S	NS	NS	S	S	S	S	S	S	NS	NS
		17:13:29	106081	S	S	S	S	S	S	S	S	S	S	S	S	S	S	S	S
14-May-09	15-May-09	00:10:17	7081	S	S	S	S	S	S	S	S	S	S	S	S	S	S	S	S
		01:26:42	30001	S	S	S	S	S	S	S	S	S	S	S	S	S	S	S	S
		02:06:17	41881	S	S	NS	NS	S	S	S	S	S	S	NS	NS	S	S	S	S
		02:53:29	56041	S	S	NS	NS	S	S	NS	NS	S	S	NS	NS	S	S	NS	NS
		03:22:05	64621	S	S	S	S	S	S	S	S	S	S	S	S	S	S	S	S
		12:57:41	237301	S	S	S	S	S	S	S	S	S	S	S	S	S	S	S	S
16-May-09	17-May-09	05:20:12	206401	S	S	S	S	S	S	S	S	S	S	S	S	S	S	S	S
		06:10:24	221461	S	S	S	S	S	S	S	S	S	S	S	S	S	S	S	S
		06:57:00	235441	S	S	S	S	S	S	NS	NS	S	S	S	S	S	S	S	NS
		08:04:36	255721	S	S	S	S	S	S	S	S	S	S	S	S	S	S	S	S
		10:09:00	293041	S	S	S	S	S	S	S	S	S	S	S	S	S	S	S	S
		10:35:12	300901	S	S	S	S	S	S	S	S	S	S	S	S	S	S	S	S
20-May-09	20-May-09	14:18:08	110581	S	S	S	S	S	S	S	S	S	S	S	S	S	S	S	S
21-May-09	21-May-09	12:01:00	28021	S	S	S	S	S	S	S	S	S	S	S	S	S	S	S	S
		14:29:00	72421	S	S	S	S	S	S	S	S	S	S	S	S	S	S	NS	NS
		15:36:12	92581	S	S	S	S	S	S	S	S	S	S	S	S	S	S	S	S
		16:07:12	101881	NS	S	S	S	S	S	S	S	S	S	S	S	S	S	S	S
		16:35:12	110281	S	S	S	S	S	S	S	S	S	S	S	S	S	S	S	S
		17:14:48	122161	S	S	S	S	NS	S	S	S	S	S	S	S	S	S	S	S
22-May-09	22-May-09	09:16:34	16021	S	S	S	S	S	S	S	S	S	S	S	S	S	S	S	S
		10:44:10	42301	S	S	S	S	S	S	S	S	S	S	S	S	S	S	NS	NS
		11:10:26	48181	S	S	S	S	S	S	S	S	S	S	S	S	S	S	S	S

		12:01:38	63541	S	S	NS	NS	S	S	S	S	S	S	NS	NS	S	S	S	S
22-May-09	24-May-09	13:21:41	109081	S	S	S	S	S	S	S	S	S	S	S	S	S	S	S	S
		13:58:53	120241	S	S	S	S	S	S	S	S	S	S	S	S	S	S	S	S
		15:01:29	139021	S	S	NS	NS	S	S	S	S	S	S	NS	NS	S	S	S	S
		15:22:29	145321	S	S	S	S	S	S	S	S	S	S	S	S	S	S	S	S
		16:23:29	163621	S	S	S	S	S	S	S	S	S	S	S	S	S	S	S	S
25-May-09	25-May-09	11:40:05	68881	S	S	S	S	S	S	S	S	S	S	S	S	S	S	S	NS
		11:55:29	73501	S	S	S	S	S	S	S	S	S	S	S	S	S	S	S	S
		12:41:17	87241	S	S	S	S	S	S	S	S	S	S	S	S	S	S	S	S
		12:55:29	91501	S	S	S	S	S	S	S	S	S	S	S	S	S	S	S	S
25-May-09	25-May-09	14:59:35	26401	S	S	S	S	S	S	S	S	S	S	S	S	S	S	S	S
		15:20:11	32581	S	S	S	S	S	S	S	S	S	S	S	S	S	S	S	S
		15:46:11	40381	S	S	S	S	S	S	S	S	S	S	S	S	S	S	S	S
		15:51:35	42001	S	S	S	S	S	S	S	S	S	S	S	S	S	S	S	S
		16:34:35	54901	S	S	S	S	S	S	S	S	S	S	S	S	S	S	S	S
		16:52:35	60301	S	S	S	S	S	S	S	S	S	S	S	S	S	S	S	S
		17:59:59	80521	S	S	S	S	S	S	S	S	S	S	S	S	S	S	S	S
27-May-09	27-May-09	17:58:31	72301	S	S	S	S	S	S	S	S	S	S	S	S	S	S	S	S
		18:06:19	74641	S	S	S	S	S	S	S	S	S	S	S	S	S	S	S	S
		18:21:07	79081	S	S	S	S	S	S	S	S	S	S	S	S	S	S	S	S
01-Jun-09	01-Jun-09	08:50:45	13021	S	S	S	S	S	S	S	S	S	S	S	S	S	S	S	S
		08:53:33	13861	S	S	S	S	S	S	NS	NS	S	S	S	S	NS	NS	NS	NS
		08:55:21	14401	S	S	S	S	S	S	NS	NS	S	S	S	S	S	S	NS	NS
01-Jun-09	01-Jun-09	10:37:16	21781	S	S	S	S	S	S	S	S	S	S	S	S	S	S	S	S
		12:04:52	48061	S	S	S	S	S	S	S	S	S	S	S	S	S	S	S	S
		13:22:28	71341	S	S	NS	NS	S	S	NS	NS	S	S	S	NS	S	S	NS	NS
		14:17:28	87841	S	S	NS	S	S	S	S	S	S	S	S	NS	S	S	S	S
		15:12:28	104341	S	S	S	S	S	S	S	S	S	S	S	S	S	S	S	S
		15:29:04	109321	S	S	S	S	S	S	S	S	S	S	S	NS	S	S	S	S
		15:37:16	111781	S	S	S	S	S	S	NS	NS	S	S	S	S	S	S	S	S

		17:25:16	144181	S	S	S	S	S	S	S	S	S	S	S	S	S	S	S	S
02-Jun-09	02-Jun-09	12:49:10	37141	S	S	S	S	S	S	S	S	S	S	NS	NS	S	S	S	S
		14:36:58	69481	S	S	S	S	S	S	S	S	S	S	S	S	S	S	NS	S
		15:27:34	84661	S	S	S	S	NS	S	S	S	S	S	S	S	S	S	S	S
		16:03:10	95341	S	S	S	S	S	S	S	S	S	S	S	S	S	S	S	S
		16:16:46	99421	S	S	NS	NS	S	S	NS	S	S	S	S	S	S	S	S	S
		16:23:46	101521	S	S	S	S	S	S	S	S	S	S	S	S	S	S	S	S
		16:48:22	108901	S	S	S	S	S	S	NS	NS	S	S	S	S	S	S	NS	NS
		17:04:46	113821	S	S	NS	NS	S	S	NS	NS	S	S	S	S	S	S	S	S
03-Jun-09	03-Jun-09	13:38:10	28501	S	S	NS	NS	S	S	S	S	S	S	NS	NS	S	S	S	S
		14:16:58	40141	S	S	S	S	S	S	S	S	S	S	S	S	S	S	S	S
		14:49:34	49921	S	S	S	S	S	S	S	S	S	S	S	S	S	S	S	S
04-Jun-09	04-Jun-09	11:13:01	11221	S	S	S	S	S	S	S	S	S	S	S	S	S	S	S	S
		11:56:25	24241	S	S	S	S	S	S	S	S	S	S	S	S	S	S	S	S
		12:16:25	30241	S	S	S	S	S	S	S	S	S	S	S	S	S	S	NS	NS
07-Jun-09	07-Jun-09	13:28:01	15241	S	S	S	S	S	S	S	S	S	S	S	S	S	S	S	S
		14:39:25	36661	S	S	S	S	S	S	S	S	S	S	S	S	S	S	S	S
		15:44:37	56221	S	S	S	S	S	S	S	S	S	S	S	S	S	S	NS	NS
08-Jun-09	08-Jun-09	11:02:15	41041	S	S	S	S	S	S	S	S	S	S	S	S	S	S	S	S
		13:01:03	76681	S	S	S	S	S	S	S	S	S	S	NS	S	S	S	NS	NS
		14:27:15	102541	S	S	S	S	S	S	S	S	S	S	S	S	S	S	S	S
		15:02:15	113041	S	S	S	S	S	S	S	S	S	S	S	S	S	S	S	S
		15:47:51	126721	S	S	S	S	S	S	S	S	S	S	S	S	S	S	S	S
17-Jun-09	17-Jun-09	13:24:59	96361	S	S	S	S	S	S	S	S	S	S	S	S	S	S	S	S
		13:55:47	105601	S	NS	NS	S	S	S	S	S	S	S	S	S	S	S	S	S
		18:04:47	180301	S	S	S	S	S	S	S	S	S	S	S	S	S	S	S	S
17-Jun-09	18-Jun-09	12:08:18	74101	S	S	S	S	S	S	NS	NS	S	S	S	S	S	S	NS	NS
		12:49:30	86461	S	S	S	S	S	S	S	S	S	S	S	S	S	S	S	S
		13:17:30	94861	S	S	S	S	NS	NS	NS	NS	S	S	S	S	S	S	NS	NS
		13:41:42	102121	S	S	NS	S	S	S	S	S	S	S	S	S	S	S	S	S

18-Jun-09	18-Jun-09	15:52:34	11881	S	S	S	S	S	S	S	S	S	S	S	S	NS	NS	NS	S
		16:11:22	17521	S	S	S	S	S	S	S	S	S	S	S	S	S	S	S	S
		16:18:10	19561	S	S	S	S	S	S	NS	NS	S	S	S	S	NS	NS	NS	NS
		16:31:46	23641	S	S	S	S	S	S	NS	NS	S	S	S	S	S	S	NS	NS
		18:15:34	54781	S	S	S	S	NS	S	S	S	S	S	S	S	S	S	S	S
		18:29:10	58861	S	S	S	S	S	S	S	S	S	S	S	S	S	S	S	S
19-Jun-09	21-Jun-09	14:13:50	468901	S	S	S	S	S	S	S	S	S	S	S	S	S	S	S	S
		14:58:38	482341	S	S	S	S	S	S	S	S	S	S	S	S	S	S	S	S
		16:51:02	516061	S	S	S	S	S	S	S	S	S	S	S	S	S	S	S	S
		17:41:14	531121	S	S	S	S	S	S	NS	NS	S	S	S	S	S	S	NS	NS
		18:42:14	549421	S	S	S	S	S	S	NS	S	S	S	S	S	S	S	NS	NS
		18:50:14	551821	S	S	S	S	S	S	S	S	S	S	NS	NS	S	S	S	S
		19:48:02	569161	S	S	S	S	S	S	S	S	S	S	S	S	S	S	S	S
	22-Jun-09	00:46:02	658561	S	S	S	S	S	S	S	S	S	S	S	S	S	S	S	S
22-Jun-09	22-Jun-09	01:38:13	185341	S	S	S	S	S	S	S	S	S	S	S	S	S	S	S	S
		12:02:41	189481	S	S	S	S	S	S	S	S	NS	NS	S	NS	S	S	S	S
		14:55:05	237061	S	S	S	S	S	S	S	S	S	S	S	S	S	S	S	S
		16:08:53	259201	S	S	S	S	S	S	S	S	S	S	S	S	S	S	S	S
		16:36:53	267601	S	S	NS	NS	S	S	S	S	S	S	S	S	S	S	S	S
		17:28:17	283021	S	S	S	S	S	S	NS	NS	S	S	S	S	S	S	NS	NS
		23:39:05	394261	NS	NS	S	S	S	S	S	S	S	S	S	S	S	S	S	S

Table A.6 RUN and TREND tests (time lag = 50 sec and N = 12).

Start Date	Date	Time	Point ID	V6.5m				D6.5m				V10m				D10m			
				RUN		TREND		RUN		TREND		RUN		TREND		RUN		TREND	
				Mean	M. Sq.	Mean	M. Sq.	Mean	M. Sq.	Mean	M. Sq.	Mean	M. Sq.	Mean	M. Sq.	Mean	M. Sq.	Mean	M. Sq.
2008																			
28-Oct-08	29-Oct-08	03:43:15	296161	S	S	S	S	S	S	NS	NS	S	S	S	S	S	S	NS	S
		03:51:03	298501	S	S	S	S	S	S	S	S	S	S	S	S	S	S	S	S
		06:38:03	348601	S	S	S	S	S	S	S	S	S	S	S	S	S	S	S	S
		07:15:39	359881	S	S	S	S	S	S	S	S	S	S	S	S	S	S	S	S
		13:14:39	467581	S	NS	S	S	S	S	S	S	NS	NS	S	S	S	S	S	S
29-Oct-08	29-Oct-08	15:28:47	5941	S	S	S	S	S	S	S	S	S	S	S	S	S	S	S	S
		15:30:23	6421	S	S	S	S	S	S	S	S	S	S	S	S	S	S	S	S
		17:10:23	36421	S	S	S	S	S	S	S	S	S	S	S	S	S	S	S	S
	30-Oct-08	05:46:23	263221	S	S	S	S	S	S	S	S	S	S	S	S	S	S	S	S
		09:52:11	336961	S	S	S	S	S	S	S	S	S	S	S	S	S	S	S	S
07-Nov-08	07-Nov-08	17:08:42	125221	S	S	S	S	S	S	S	S	S	S	S	S	S	S	S	S
		18:46:36	154591	S	S	S	S	S	S	S	S	S	S	S	S	S	S	S	S
17-Nov-08	17-Nov-08	13:31:41	35281	S	S	S	S	S	S	S	S	NS	NS	S	S	S	S	S	S
19-Nov-08	20-Nov-08	01:19:47	248791	S	S	S	S	S	S	S	S	S	S	S	S	S	S	S	S
		02:30:29	270001	S	S	S	S	S	S	S	S	S	S	S	S	S	S	S	S
		02:47:29	275101	S	S	S	S	S	S	S	S	S	S	S	S	S	S	S	S
		03:32:47	288691	NS	NS	S	S	S	S	S	S	S	S	S	S	S	S	S	S
		05:52:05	330481	S	S	S	S	S	S	S	S	S	S	S	S	S	S	S	S
		11:41:53	435421	NS	NS	S	S	S	S	NS	S	S	S	S	S	S	S	S	S
		14:05:29	478501	S	S	S	S	S	S	S	S	S	S	S	S	S	S	S	S
21-Nov-08	22-Nov-08	14:09:40	288091	S	S	S	S	S	S	S	S	S	S	S	S	S	NS	S	S
		15:52:58	319081	S	S	S	S	NS	NS	S	S	S	S	S	S	S	S	S	S
	23-Nov-08	04:12:34	540961	S	S	S	S	S	S	S	S	S	S	S	S	S	S	S	S

		05:40:58	567481	S	S	S	S	S	S	S	S	S	S	S	S	S	S	S	S
		05:46:58	569281	S	S	S	S	S	S	S	S	S	S	S	S	S	S	S	S
		07:21:46	597721	S	S	S	S	NS	NS	S	S	S	S	S	S	S	S	S	S
		09:59:40	645091	S	S	S	S	S	S	S	S	S	S	S	S	S	S	S	S
		14:15:40	721891	S	S	S	S	S	S	S	S	S	S	S	S	S	S	S	S
24-Nov-08	25-Nov-08	14:59:06	645481	S	S	S	S	S	S	S	S	S	S	S	S	S	S	S	S
		19:06:54	719821	S	S	S	S	S	S	S	S	S	S	S	S	S	S	S	S
		19:10:06	720781	S	S	S	S	S	S	S	S	S	S	S	S	S	S	S	S
		19:32:06	727381	NS	NS	S	S	S	S	S	S	S	NS	S	S	S	S	S	S
		21:57:54	771121	S	S	S	S	S	S	S	S	S	S	S	S	S	S	S	S
25-Nov-08	26-Nov-08	01:59:46	59101	NS	S	S	S	S	S	S	S	S	S	S	S	S	S	S	S
		05:15:04	117691	S	S	S	S	S	S	S	S	S	S	S	S	S	S	S	S
		05:38:04	124591	S	S	S	S	S	S	S	S	S	S	S	S	S	S	S	S
		06:29:22	139981	S	S	S	S	S	S	S	S	S	S	S	S	S	S	S	S
		09:09:04	187891	NS	NS	S	S	S	S	NS	NS	S	S	S	S	S	S	S	S
		09:27:58	193561	S	S	S	S	S	S	S	S	S	S	S	S	S	S	S	S
		09:43:10	198121	S	S	S	S	S	S	S	S	S	S	S	S	S	S	S	S
		10:12:58	207061	S	S	S	S	S	S	S	S	S	S	S	S	S	S	S	S
2009																			
24-Apr-09	25-Apr-09	13:15:14	396661	S	S	S	S	S	S	NS	NS	S	S	S	S	S	S	S	S
		13:28:50	400741	S	S	S	S	S	S	S	S	S	S	S	S	S	S	S	S
		13:32:26	401821	NS	S	S	S	S	S	S	S	S	S	S	S	S	S	S	S
		13:33:26	402121	S	S	S	S	NS	NS	S	S	S	S	S	S	S	S	S	S
		13:47:14	406261	S	S	S	S	S	S	NS	NS	S	S	S	S	S	S	S	S
		14:02:50	410941	NS	NS	S	S	S	S	S	S	S	S	S	S	S	S	S	S
25-Apr-09	26-Apr-09	11:15:15	263941	S	S	S	S	NS	NS	S	S	S	S	S	S	S	S	S	S
		13:53:39	311461	S	S	S	S	S	NS	S	S	S	S	S	S	S	S	S	S
		15:26:15	339241	NS	NS	S	S	S	S	S	NS	S	S	S	S	S	S	S	S
		16:04:15	350641	NS	NS	S	S	S	S	S	S	S	S	S	S	S	S	S	S
		17:57:39	384661	NS	NS	S	S	NS	NS	S	S	S	S	S	S	NS	NS	S	S

14-May-09	14-May-09	13:02:53	30901	S	S	S	S	S	S	S	S	S	S	S	S	S	S	S	S
		13:14:29	34381	S	S	S	S	S	S	S	S	S	S	S	S	S	S	S	S
		14:09:29	50881	S	S	S	S	S	NS	S	S	S	S	S	S	S	S	S	S
		15:13:29	70081	S	S	S	S	S	S	S	S	S	S	S	S	S	S	S	S
		15:41:17	78421	S	S	S	S	S	S	S	S	S	S	S	S	S	S	S	S
		16:17:17	89221	S	S	S	S	S	S	S	S	S	S	S	S	S	S	S	S
		16:29:41	92941	S	S	S	S	S	S	NS	NS	S	S	S	S	S	S	NS	NS
		17:13:29	106081	S	S	S	S	S	S	S	S	S	S	S	S	S	S	S	S
14-May-09	15-May-09	00:10:17	7081	NS	NS	S	S	S	S	S	S	NS	NS	S	S	S	S	S	S
		01:26:42	30001	S	S	S	S	S	S	S	NS	S	S	S	S	S	S	S	S
		02:06:17	41881	S	S	S	S	S	S	S	S	S	S	S	S	S	S	S	S
		02:53:29	56041	NS	NS	S	S	S	S	S	S	S	S	S	S	S	S	S	S
		03:22:05	64621	S	S	S	S	S	S	S	S	S	S	S	S	S	S	S	S
		12:57:41	237301	S	S	S	S	S	S	S	S	S	S	S	S	S	S	S	S
16-May-09	17-May-09	05:20:12	206401	S	S	S	S	S	S	S	S	S	S	S	S	S	S	S	S
		06:10:24	221461	S	S	S	S	S	S	S	S	S	S	S	S	S	S	S	S
		06:57:00	235441	S	S	S	S	S	S	NS	NS	S	S	S	S	S	S	NS	NS
		08:04:36	255721	S	S	S	S	S	S	S	S	S	S	S	S	S	S	S	S
		10:09:00	293041	S	S	S	S	S	S	S	S	S	S	S	S	S	S	S	S
		10:35:12	300901	S	S	S	S	NS	S	S	S	S	NS	S	S	S	S	S	S
20-May-09	20-May-09	14:18:08	110581	S	S	S	S	S	S	S	S	S	S	S	S	S	S	S	S
21-May-09	21-May-09	12:01:00	28021	S	S	S	S	S	S	S	S	S	S	S	S	S	S	S	S
		14:29:00	72421	S	S	S	S	S	S	S	S	S	S	S	S	S	S	NS	NS
		15:36:12	92581	S	S	S	S	S	S	S	S	S	S	S	S	S	S	S	S
		16:07:12	101881	S	S	S	S	S	S	S	S	S	S	S	S	S	S	S	S
		16:35:12	110281	S	S	S	S	NS	NS	S	S	S	S	S	S	S	S	S	S
		17:14:48	122161	S	S	S	S	S	S	S	S	S	S	S	S	S	S	S	S
22-May-09	22-May-09	09:16:34	16021	S	S	S	S	S	NS	S	S	S	S	S	S	S	S	S	S
		10:44:10	42301	S	S	S	S	S	S	S	S	S	S	S	S	NS	NS	NS	NS
		11:10:26	48181	S	S	S	S	S	S	S	S	S	S	S	S	S	S	S	NS

		12:01:38	63541	S	S	S	S	S	S	S	S	S	S	S	S	S	S	S	S
22-May-09	24-May-09	13:21:41	109081	S	S	S	S	S	S	S	S	S	S	S	S	S	S	S	S
		13:58:53	120241	S	S	S	S	S	S	S	S	S	S	S	S	S	S	S	S
		15:01:29	139021	S	S	S	S	S	S	S	S	S	S	S	S	S	S	S	S
		15:22:29	145321	S	S	S	S	S	S	S	S	S	S	S	S	S	S	S	S
		16:23:29	163621	S	S	S	S	S	S	S	S	S	S	S	S	S	S	S	S
25-May-09	25-May-09	11:40:05	68881	S	S	S	S	S	S	S	S	S	S	S	S	S	S	S	S
		11:55:29	73501	S	S	S	S	S	S	S	S	S	S	S	S	S	S	S	S
		12:41:17	87241	S	S	S	S	S	S	S	S	S	S	S	S	S	S	S	S
		12:55:29	91501	S	S	S	S	S	S	S	S	S	S	S	S	NS	NS	S	S
25-May-09	25-May-09	14:59:35	26401	S	S	S	S	S	S	S	S	S	S	S	S	S	S	S	S
		15:20:11	32581	S	S	S	S	S	S	S	S	S	S	S	S	S	S	S	S
		15:46:11	40381	S	NS	S	S	S	S	S	S	S	S	S	S	NS	NS	S	S
		15:51:35	42001	S	S	S	S	S	S	S	S	S	S	S	S	S	S	S	S
		16:34:35	54901	S	S	S	S	S	S	S	S	S	S	S	S	S	S	S	S
		16:52:35	60301	S	S	S	S	S	S	S	S	S	S	S	S	S	S	S	S
		17:59:59	80521	S	S	S	S	S	S	S	S	S	S	S	S	S	S	S	S
27-May-09	27-May-09	17:58:31	72301	S	S	S	S	S	S	S	S	S	S	S	S	S	S	S	S
		18:06:19	74641	S	S	S	S	S	S	S	S	S	S	S	S	S	S	S	S
		18:21:07	79081	S	S	S	S	S	S	S	S	S	S	S	NS	S	S	S	S
01-Jun-09	01-Jun-09	08:50:45	13021	S	S	S	S	S	S	S	S	S	S	S	S	S	S	S	S
		08:53:33	13861	S	S	S	S	NS	NS	NS	NS	S	S	S	S	S	S	NS	NS
		08:55:21	14401	S	S	S	S	S	S	NS	NS	S	S	S	S	NS	NS	NS	NS
01-Jun-09	01-Jun-09	10:37:16	21781	S	S	S	S	S	S	S	S	S	S	S	S	S	S	S	S
		12:04:52	48061	S	S	S	S	S	S	S	S	S	S	S	S	S	S	S	S
		13:22:28	71341	S	S	S	S	S	S	NS	NS	S	S	S	S	S	S	NS	NS
		14:17:28	87841	S	S	S	S	S	S	S	S	S	S	S	S	NS	NS	S	S
		15:12:28	104341	S	S	S	S	S	S	S	S	S	S	S	S	S	S	S	S
		15:29:04	109321	S	S	S	S	S	S	S	S	S	S	S	S	S	S	S	S
		15:37:16	111781	S	S	S	S	S	S	S	S	S	S	S	S	S	S	S	S

		17:25:16	144181	S	S	NS	NS	S	S	S	S	S	NS	S	S	S	S	S	S
02-Jun-09	02-Jun-09	12:49:10	37141	S	S	S	S	S	S	S	S	S	S	S	S	S	S	S	S
		14:36:58	69481	S	S	S	S	S	S	S	S	S	S	S	S	NS	S	S	S
		15:27:34	84661	S	S	S	S	S	S	S	S	S	S	S	S	S	S	S	S
		16:03:10	95341	S	S	S	S	S	S	S	S	S	S	S	S	S	S	S	S
		16:16:46	99421	S	S	S	S	S	S	S	S	S	S	S	S	S	S	S	S
		16:23:46	101521	S	S	S	S	S	S	S	S	S	S	S	S	S	S	S	S
		16:48:22	108901	S	S	S	S	S	NS	S	NS	S	S	S	S	NS	NS	NS	NS
		17:04:46	113821	S	S	S	S	S	S	S	S	S	S	S	S	S	S	NS	NS
03-Jun-09	03-Jun-09	13:38:10	28501	S	S	S	S	S	S	S	S	S	S	S	S	S	S	S	S
		14:16:58	40141	S	S	S	S	S	S	S	S	S	S	S	S	S	S	S	S
		14:49:34	49921	S	S	S	S	S	S	S	S	S	S	S	S	S	S	S	S
04-Jun-09	04-Jun-09	11:13:01	11221	S	S	S	S	S	S	S	S	S	S	S	S	S	S	S	S
		11:56:25	24241	S	S	S	S	S	S	S	S	S	S	S	S	S	S	S	S
		12:16:25	30241	S	S	S	S	S	NS	S	S	S	S	S	S	S	S	NS	NS
07-Jun-09	07-Jun-09	13:28:01	15241	S	S	S	S	S	S	S	S	S	S	S	S	S	S	S	S
		14:39:25	36661	S	S	S	S	S	S	S	S	S	S	S	S	S	S	S	S
		15:44:37	56221	NS	NS	S	S	S	S	S	S	S	S	S	S	S	S	S	S
08-Jun-09	08-Jun-09	11:02:15	41041	S	S	S	S	S	S	S	S	S	S	S	S	S	S	S	S
		13:01:03	76681	S	S	S	S	S	S	S	S	S	S	S	S	NS	NS	S	S
		14:27:15	102541	S	S	S	S	S	S	S	S	S	S	S	S	S	S	S	S
		15:02:15	113041	S	S	S	S	S	S	S	S	S	S	S	S	S	S	S	S
		15:47:51	126721	S	S	S	S	S	S	S	S	S	S	S	S	S	S	S	S
17-Jun-09	17-Jun-09	13:24:59	96361	S	S	S	S	NS	S	S	S	S	S	S	S	NS	NS	S	S
		13:55:47	105601	S	S	S	S	S	S	S	S	NS	S	S	S	S	S	S	S
		18:04:47	180301	S	S	S	S	S	S	S	S	S	S	S	S	S	S	S	S
17-Jun-09	18-Jun-09	12:08:18	74101	S	S	S	S	S	S	NS	NS	S	S	S	S	NS	NS	NS	NS
		12:49:30	86461	S	S	S	S	S	S	S	S	S	S	NS	NS	S	S	S	S
		13:17:30	94861	S	S	NS	S	NS	NS	S	S	S	S	S	S	S	S	NS	NS
		13:41:42	102121	S	S	S	S	S	S	S	S	S	S	S	S	S	S	S	S

18-Jun-09	18-Jun-09	15:52:34	11881	S	S	S	S	S	S	S	S	S	S	S	S	NS	NS	S	S
		16:11:22	17521	S	S	S	S	S	S	S	S	S	S	S	S	NS	NS	S	S
		16:18:10	19561	S	S	S	S	S	S	NS	NS	S	S	S	S	NS	NS	NS	NS
		16:31:46	23641	S	S	S	S	S	S	S	S	S	S	S	S	S	S	NS	
		18:15:34	54781	S	S	S	S	NS	NS	S	S	S	S	S	S	S	S	S	S
		18:29:10	58861	S	S	S	S	S	S	S	S	S	S	S	S	S	S	S	S
19-Jun-09	21-Jun-09	14:13:50	468901	S	S	S	S	S	S	S	S	S	S	S	S	S	S	S	S
		14:58:38	482341	S	S	S	S	S	S	S	S	S	S	S	S	S	S	S	S
		16:51:02	516061	S	S	S	S	S	S	S	S	S	S	S	S	S	S	S	S
		17:41:14	531121	S	S	S	S	S	NS	S	S	S	S	S	S	S	S	S	S
		18:42:14	549421	S	S	S	S	S	S	S	S	S	S	S	S	S	S	S	S
		18:50:14	551821	S	S	S	S	S	S	S	S	S	S	S	S	S	S	S	S
		19:48:02	569161	S	S	S	S	S	S	S	S	S	S	S	S	NS	S	S	S
	22-Jun-09	00:46:02	658561	S	S	S	S	S	S	S	S	S	S	S	S	S	S	S	NS
22-Jun-09	22-Jun-09	01:38:13	185341	S	S	S	S	S	S	S	S	S	S	S	S	S	S	S	S
		12:02:41	189481	S	S	S	S	S	S	S	S	NS	NS	S	S	S	S	S	S
		14:55:05	237061	S	S	S	S	S	S	S	S	NS	NS	S	S	S	S	S	S
		16:08:53	259201	S	S	S	S	S	S	S	S	S	S	S	S	S	S	S	S
		16:36:53	267601	NS	NS	S	S	S	S	S	S	S	S	S	S	S	S	S	S
		17:28:17	283021	S	S	S	S	S	S	S	S	S	S	S	S	S	S	S	S
		23:39:05	394261	S	S	S	S	S	S	S	S	S	S	S	S	S	S	S	S

APPENDIX B

Detailed Results (Pressures)

This appendix presents supplementary results to Section 6.3.

B.1 Comparison between full-scale and wind tunnel pressure coefficients for individual pressure taps (supplementary to Section 6.3.2)

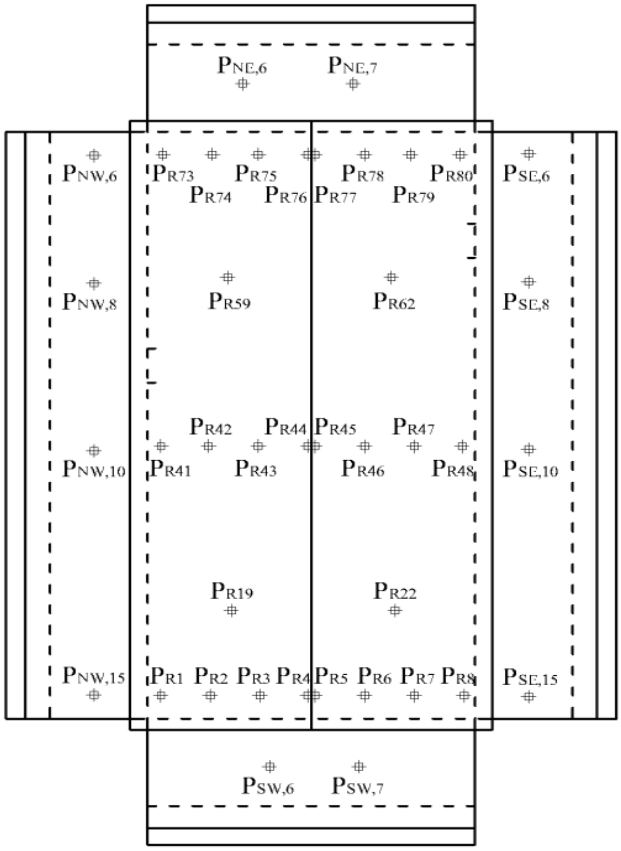

Figure B.1 Wall and roof pressure tap notation.

B.1.1 South-west wall

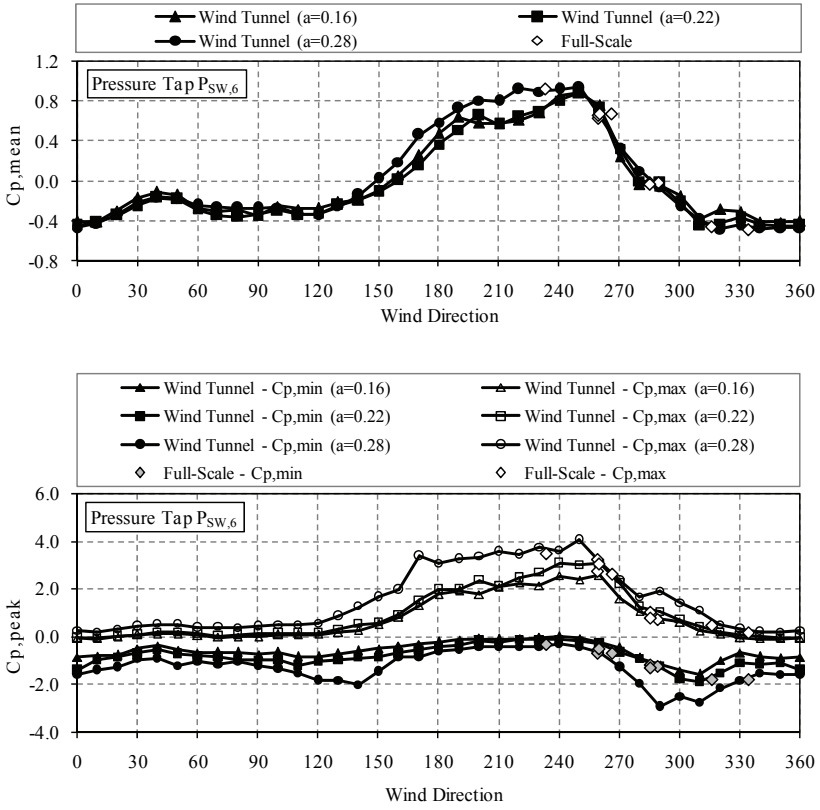

Figure B.2 Mean and peak pressure coefficient variation for pressure tap $P_{SW,6}$.

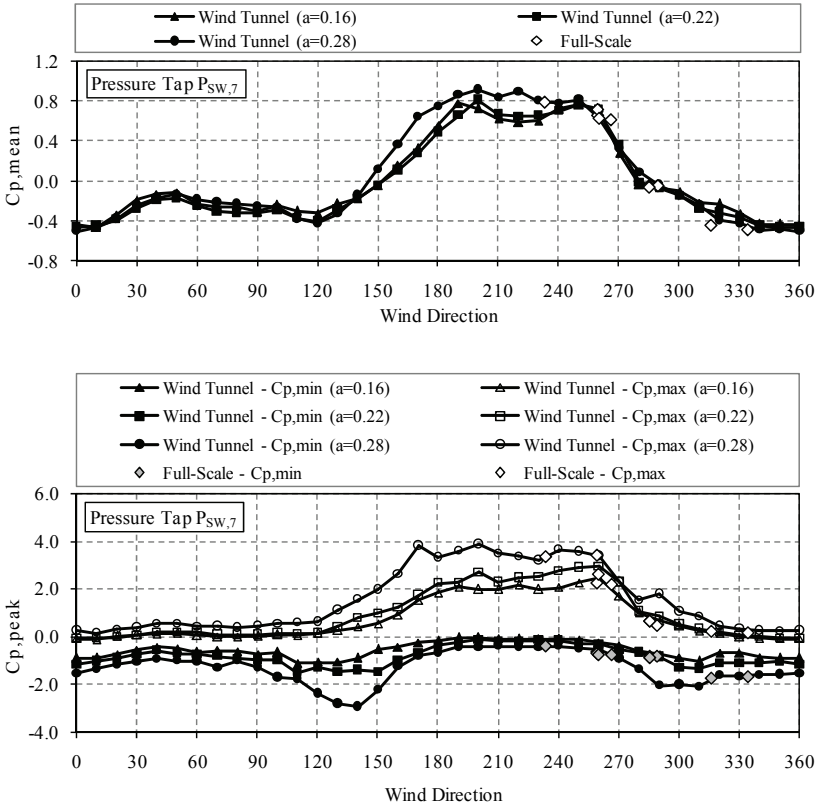

Figure B.3 Mean and peak pressure coefficient variation for pressure tap $P_{SW,7}$.

B.1.2 North-east wall

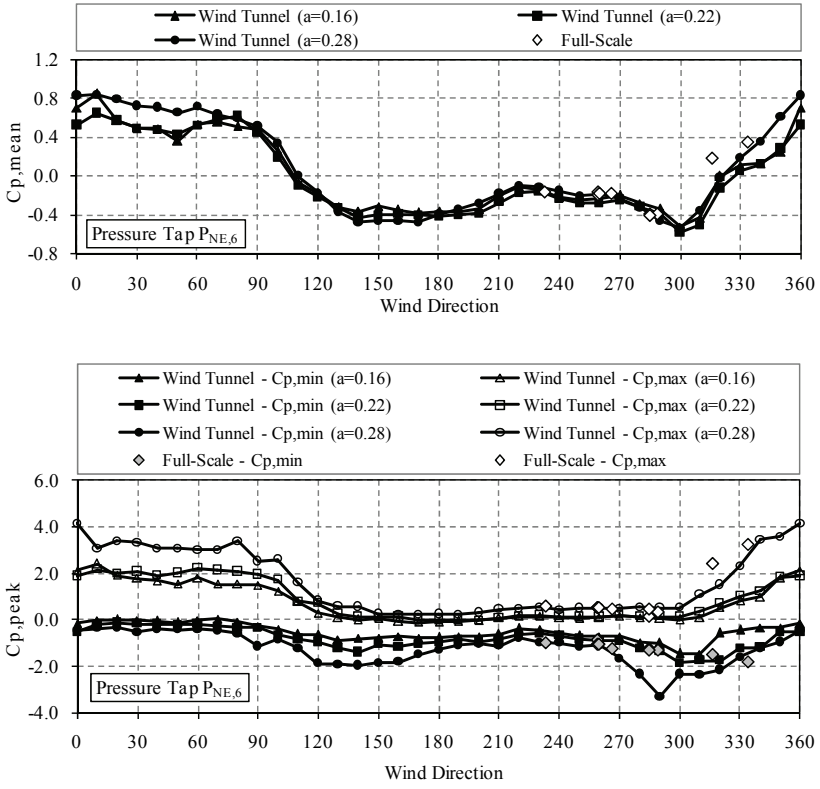

Figure B.4 Mean and peak pressure coefficient variation for pressure tap $P_{NE,6}$.

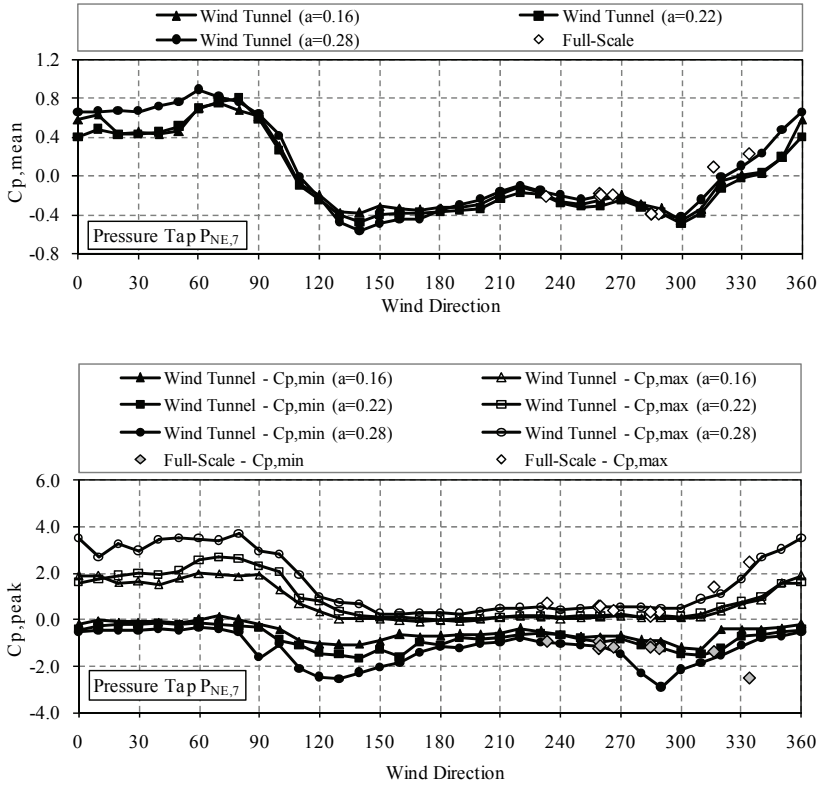

Figure B.5 Mean and peak pressure coefficient variation for pressure tap $P_{NE,7}$.

B.1.3 North-west wall

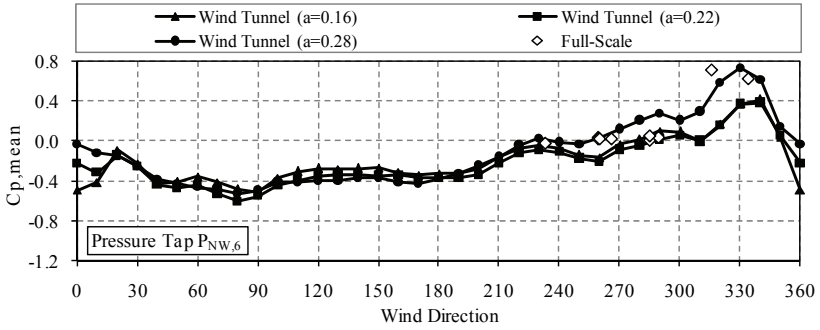

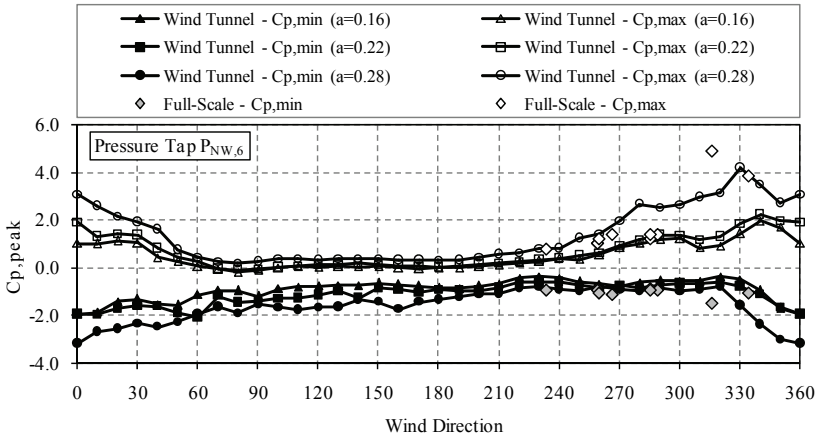

Figure B.6 Mean and peak pressure coefficient variation for pressure tap $P_{NW,6}$.

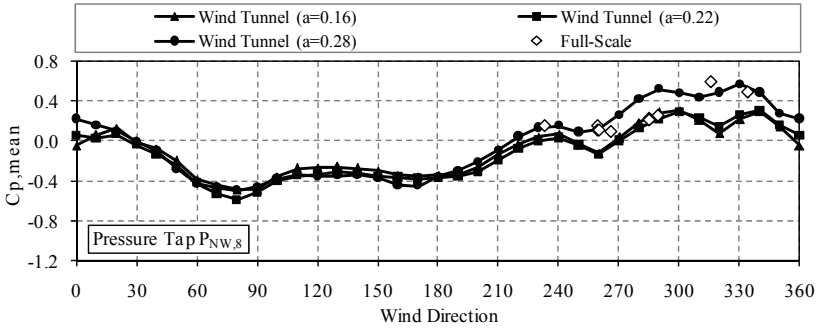

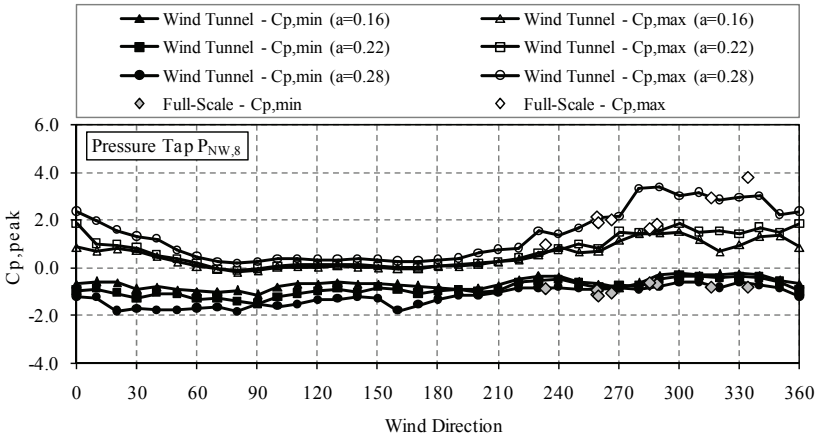

Figure B.7 Mean and peak pressure coefficient variation for pressure tap $P_{NW,8}$.

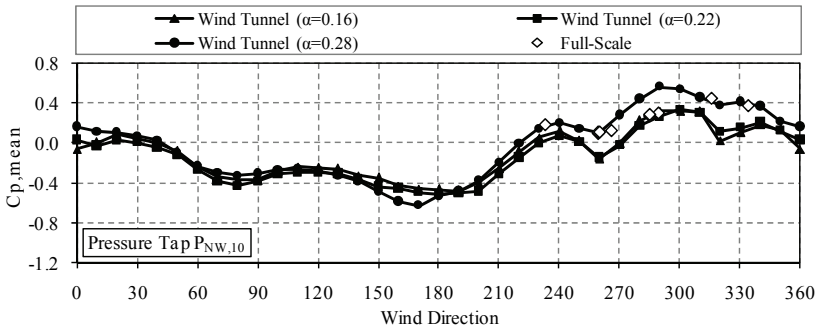

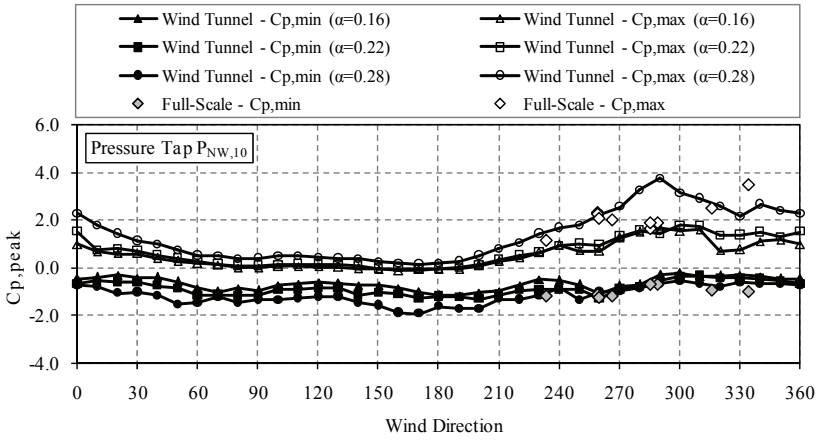

Figure B.8 Mean and peak pressure coefficient variation for pressure tap $P_{NW,10}$.

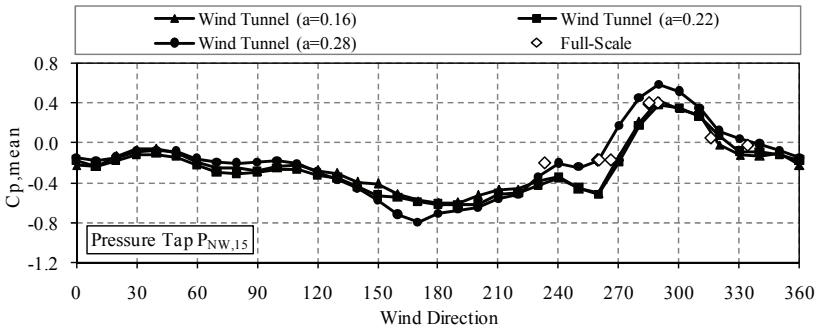

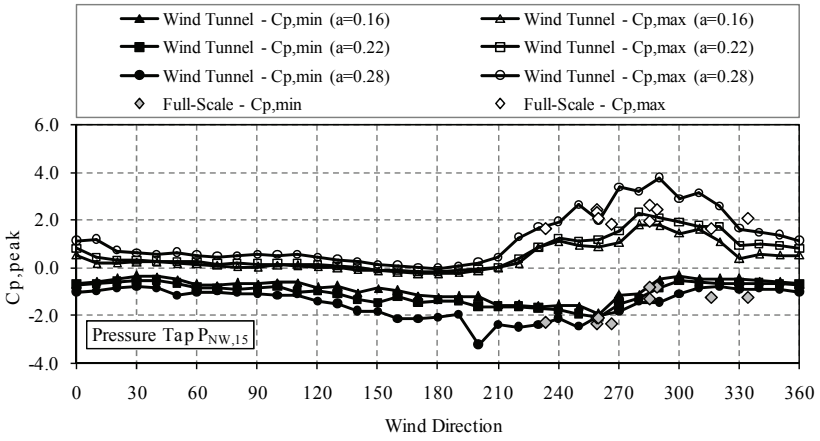

Figure B.9 Mean and peak pressure coefficient variation for pressure tap $P_{NW,15}$.

B.1.4 South-east wall

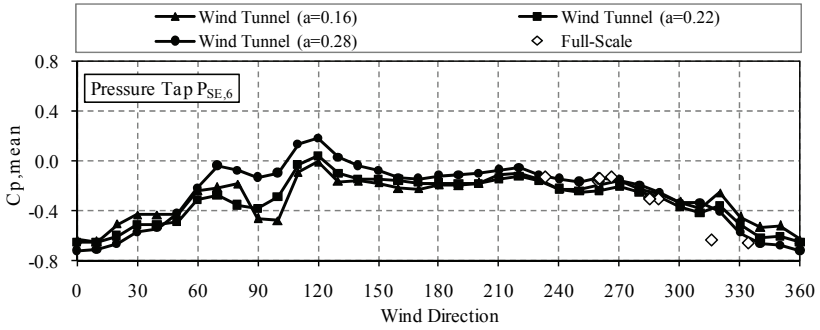

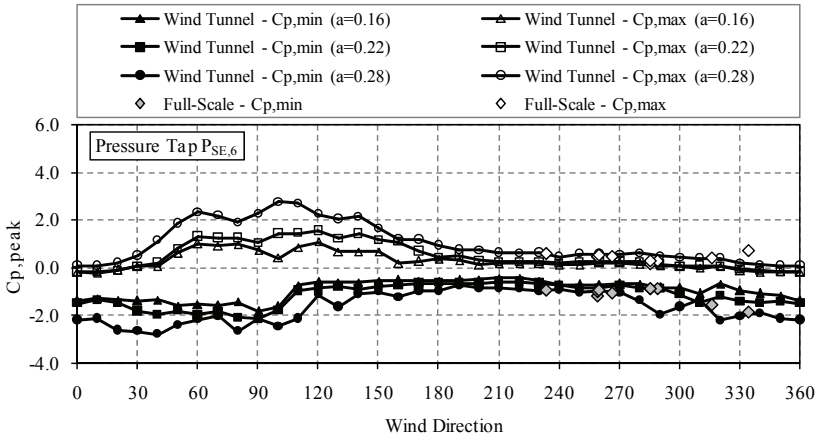

Figure B.10 Mean and peak pressure coefficient variation for pressure tap $P_{SE,6}$.

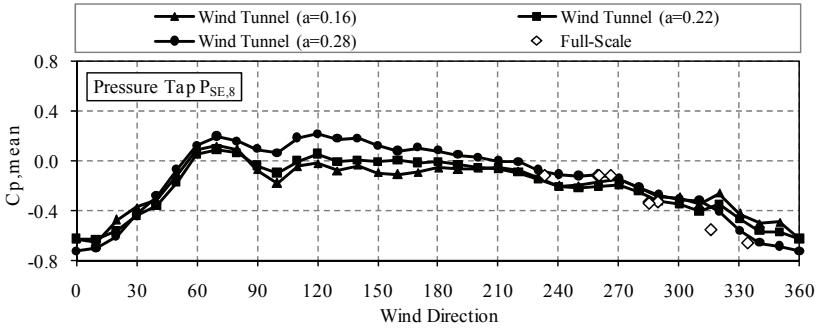

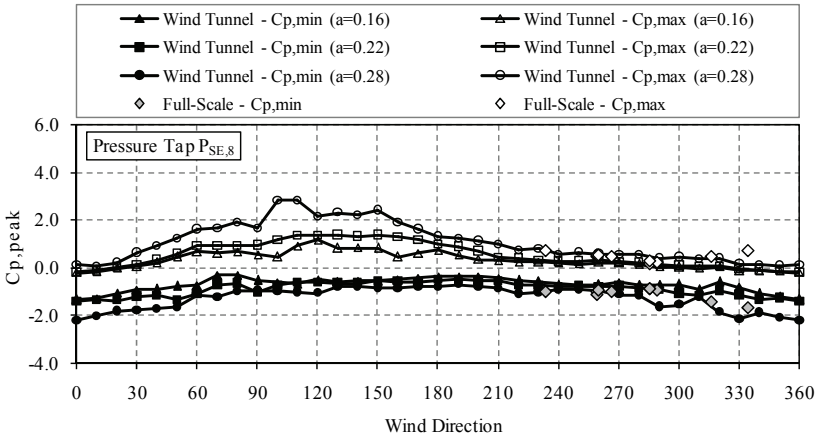

Figure B.11 Mean and peak pressure coefficient variation for pressure tap $P_{SE,8}$.

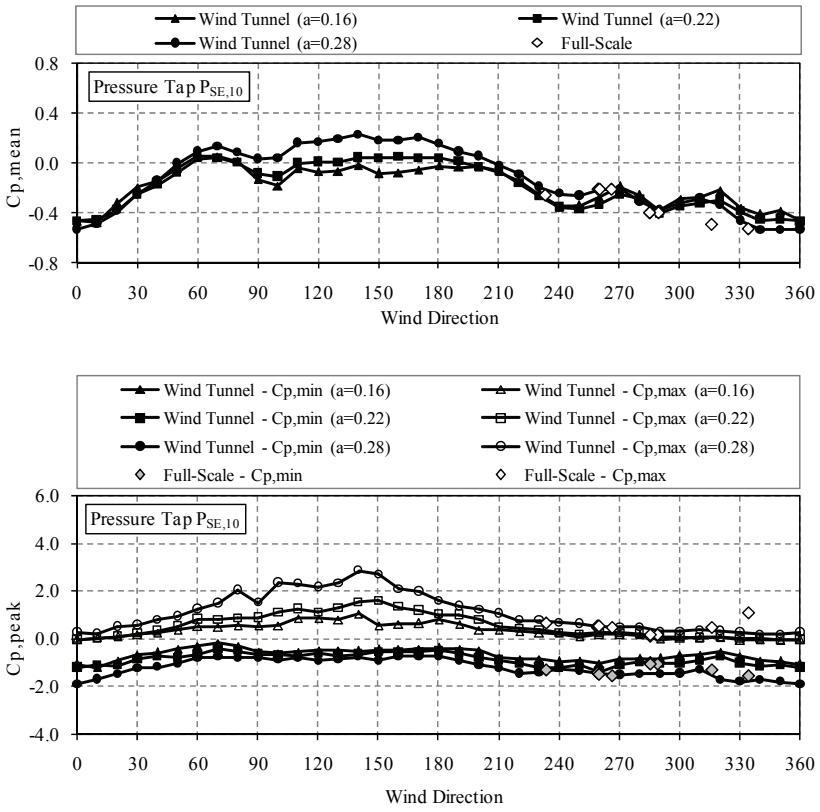

Figure B.12 Mean and peak pressure coefficient variation for pressure tap $P_{SE,10}$.

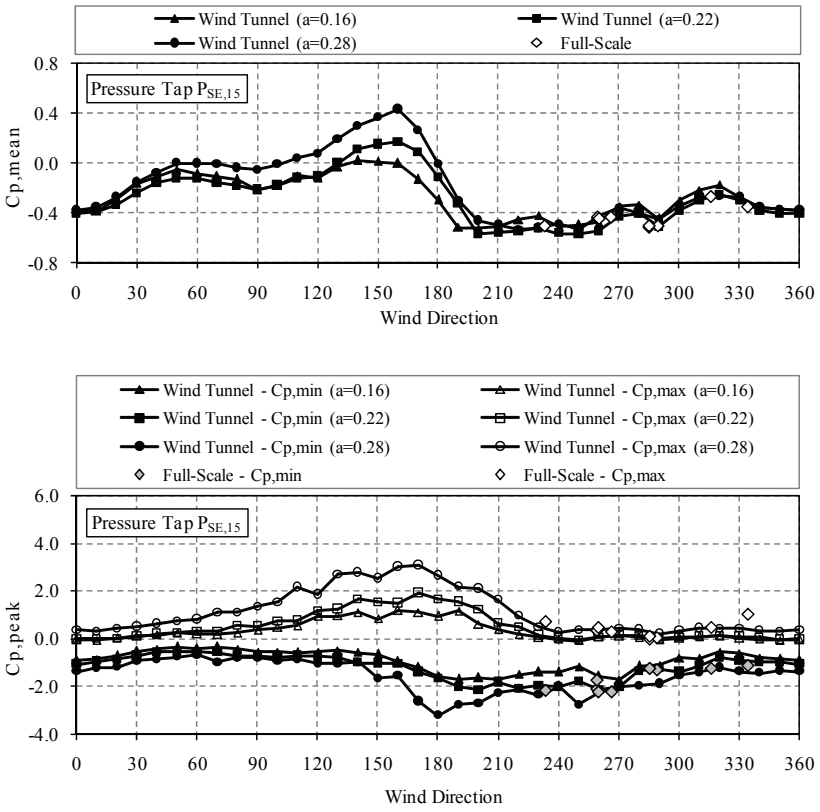

Figure B.13 Mean and peak pressure coefficient variation for pressure tap $P_{SE,15}$.

B.1.5 North-west roof

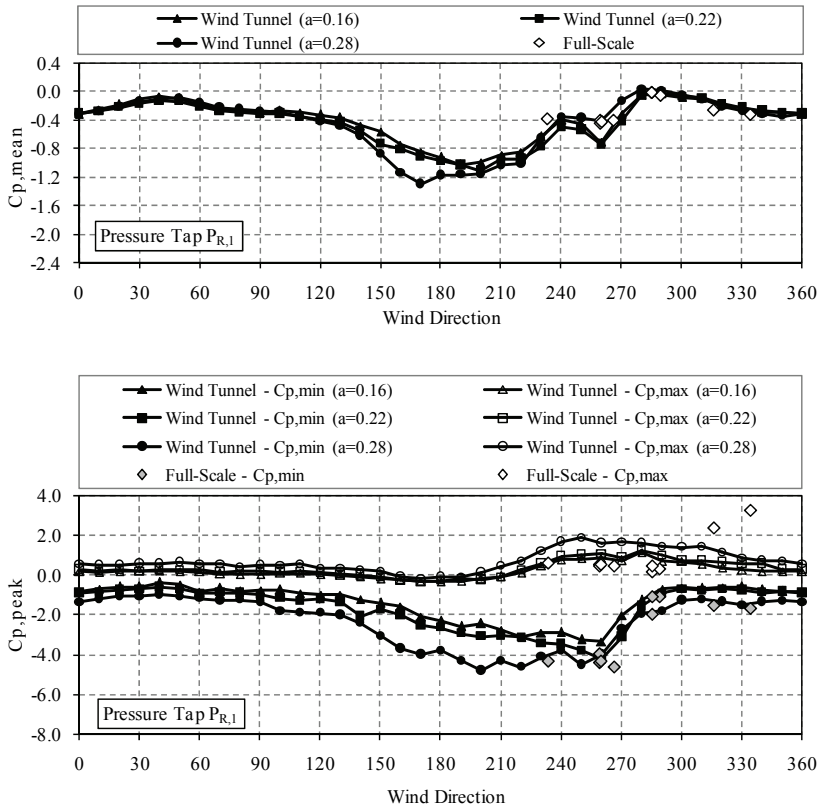

Figure B.14 Mean and peak pressure coefficient variation for pressure tap $P_{R,1}$.

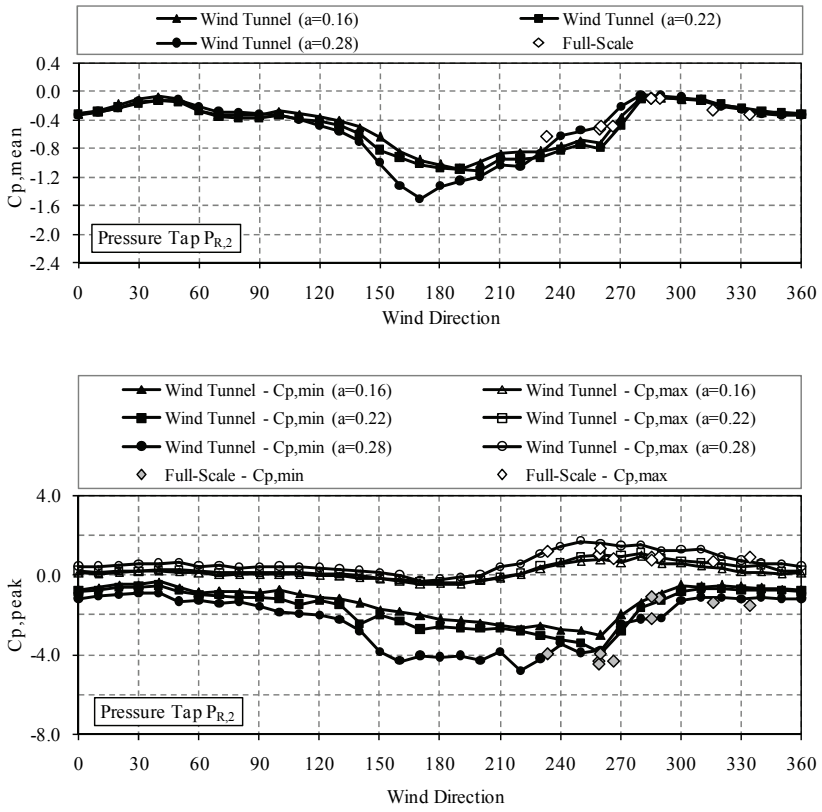

Figure B.15 Mean and peak pressure coefficient variation for pressure tap $P_{R,2}$.

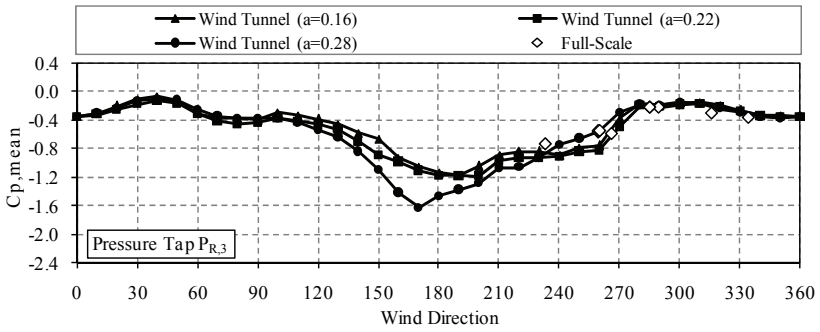

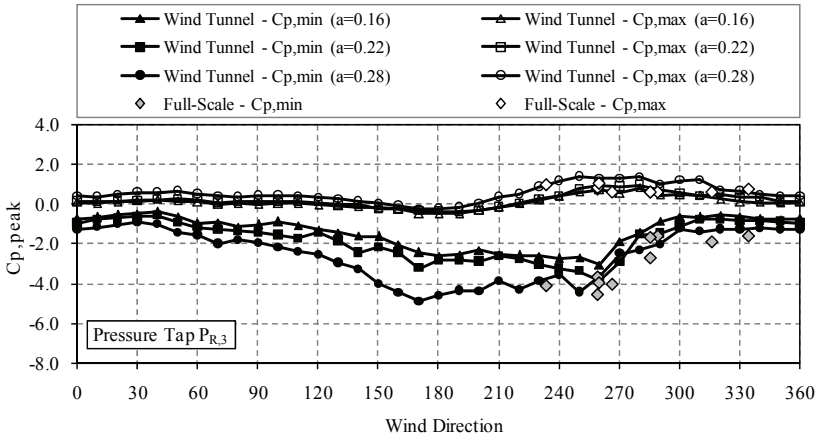

Figure B.16 Mean and peak pressure coefficient variation for pressure tap $P_{R,3}$.

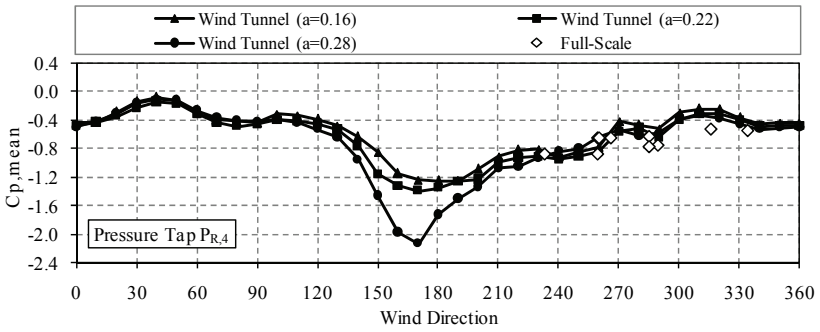

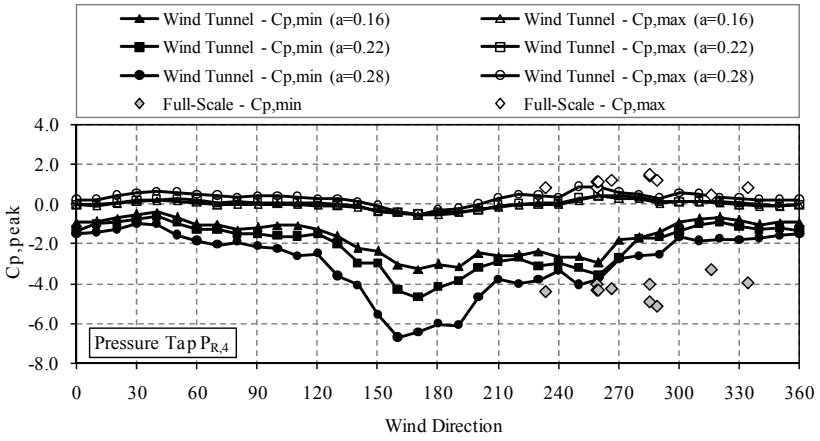

Figure B.17 Mean and peak pressure coefficient variation for pressure tap $P_{R,4}$.

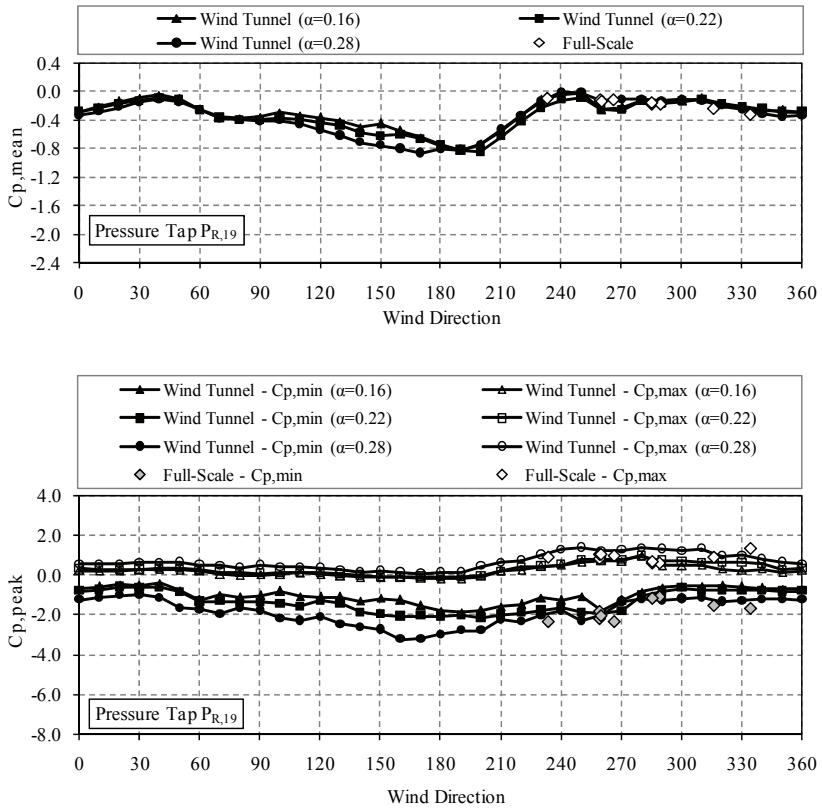

Figure B.18 Mean and peak pressure coefficient variation for pressure tap $P_{R,19}$.

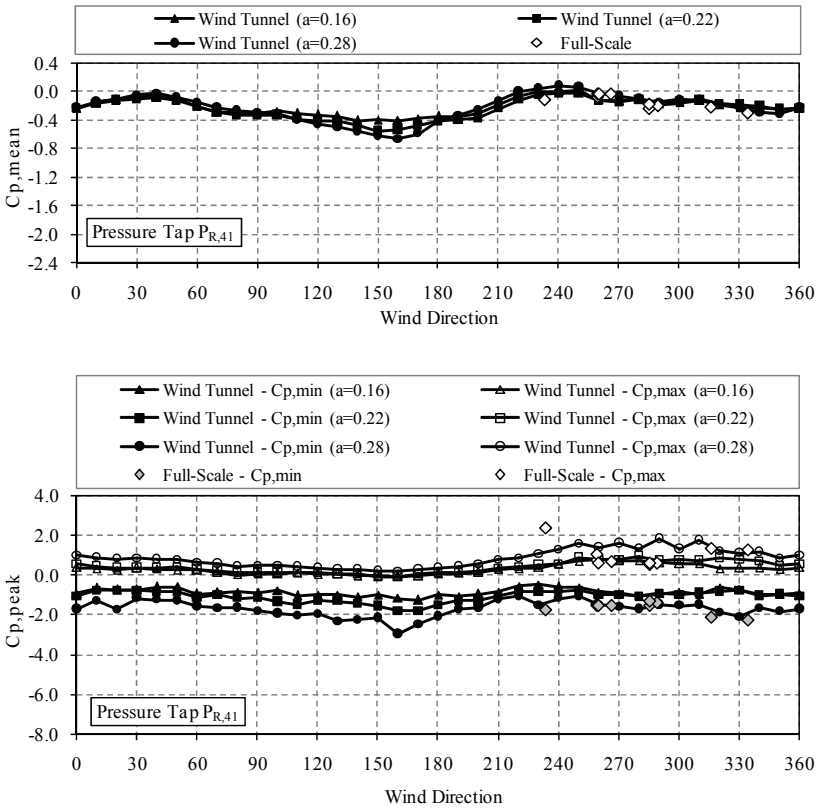

Figure B.19 Mean and peak pressure coefficient variation for pressure tap $P_{R,41}$.

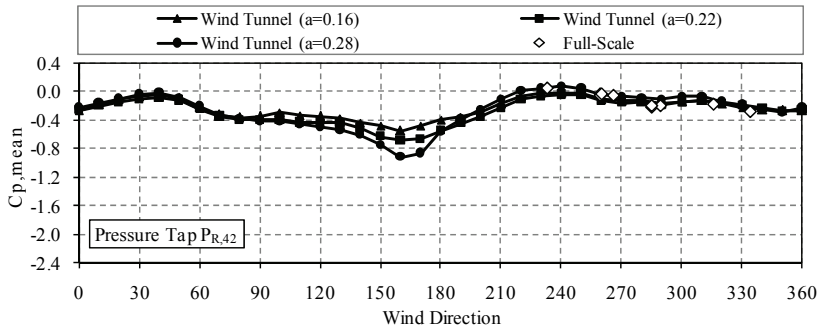

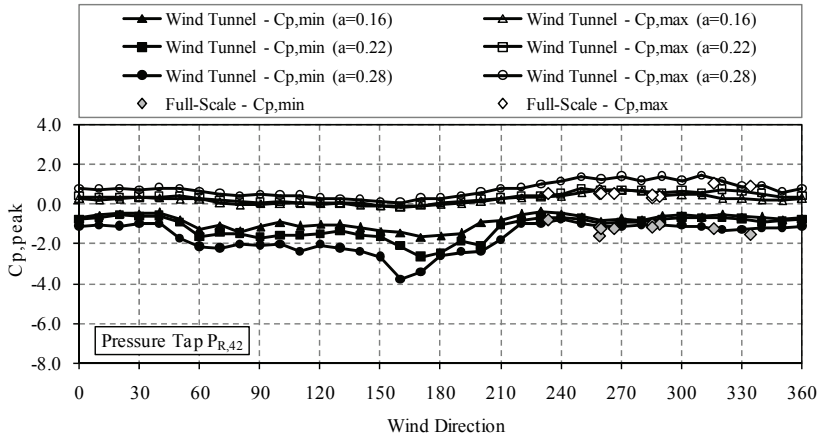

Figure B.20 Mean and peak pressure coefficient variation for pressure tap $P_{R,42}$.

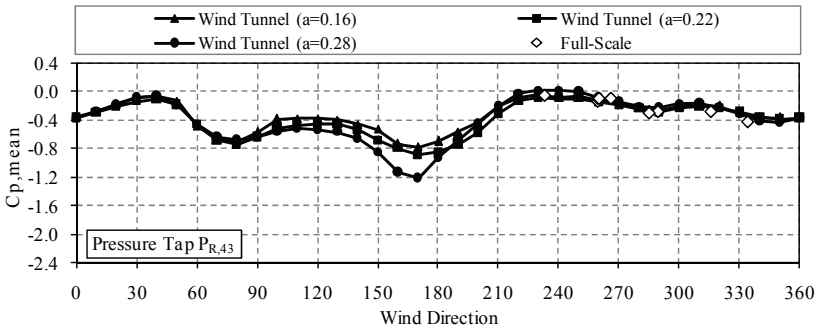

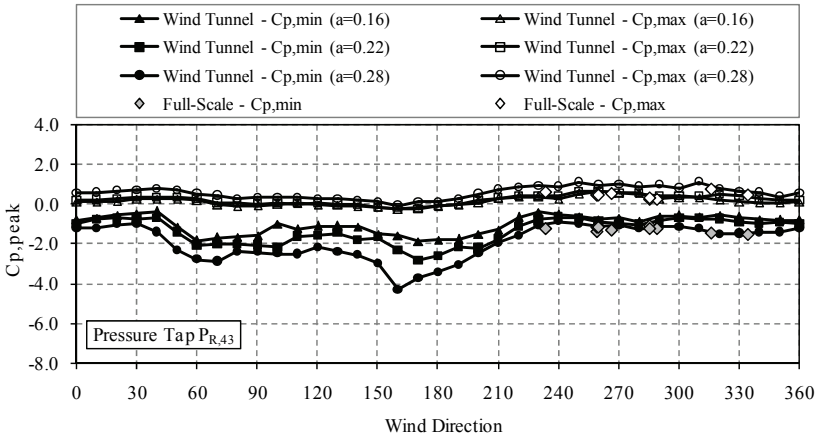

Figure B.21 Mean and peak pressure coefficient variation for pressure tap $P_{R,43}$.

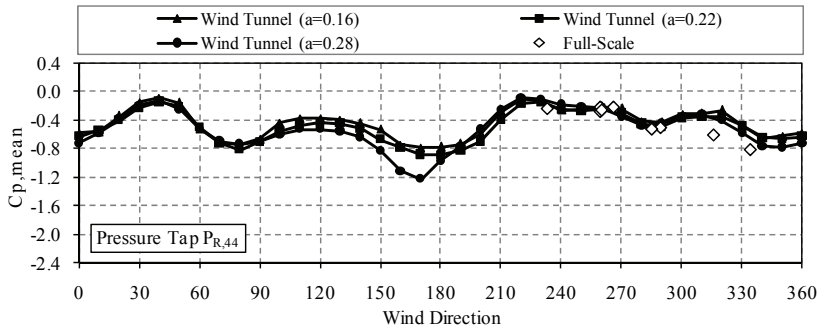

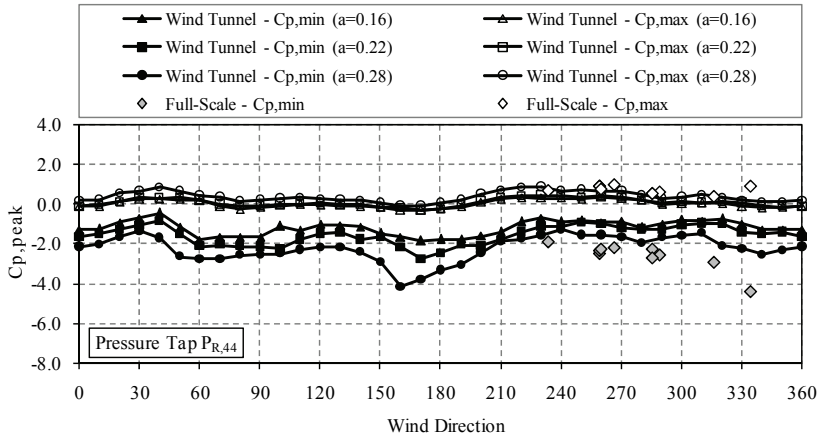

Figure B.22 Mean and peak pressure coefficient variation for pressure tap $P_{R,44}$.

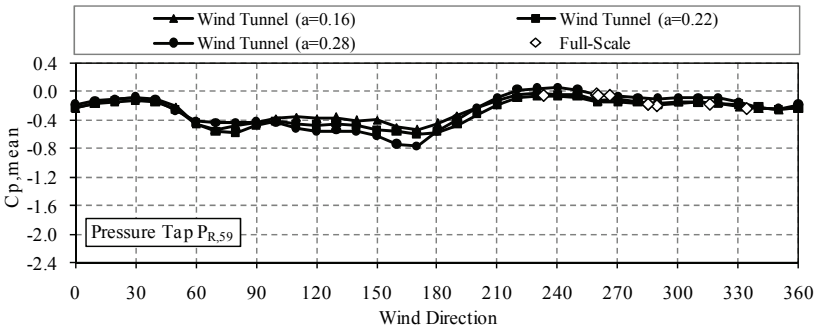

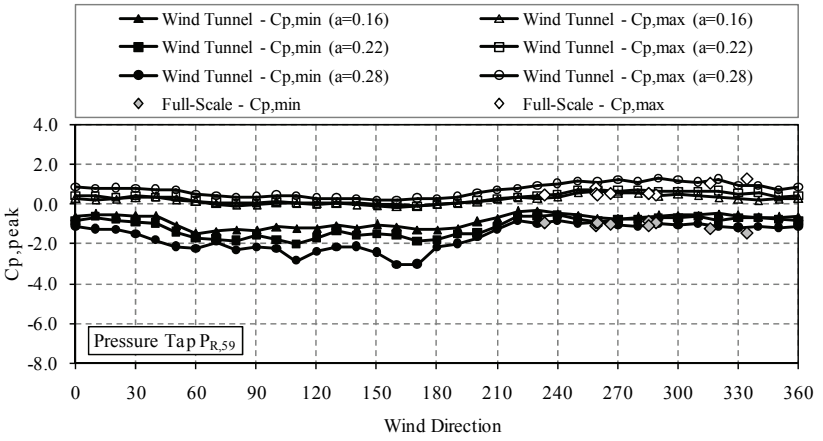

Figure B.23 Mean and peak pressure coefficient variation for pressure tap $P_{R,59}$.

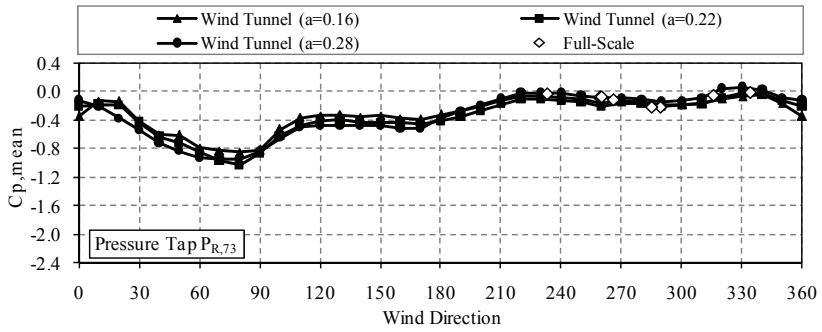

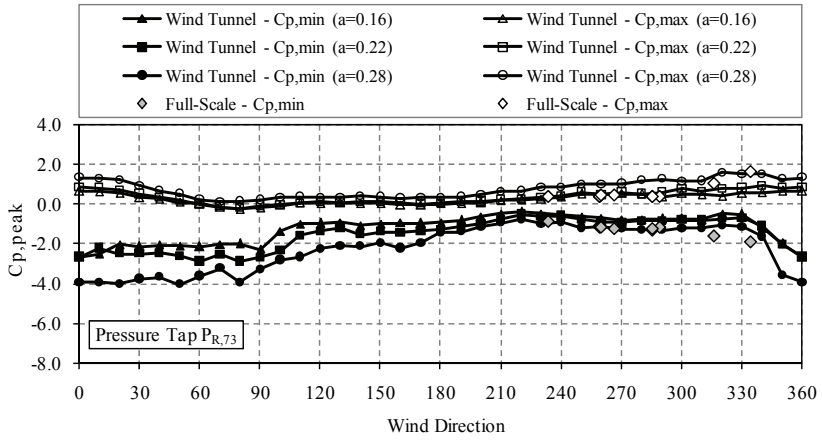

Figure B.24 Mean and peak pressure coefficient variation for pressure tap $P_{R,73}$.

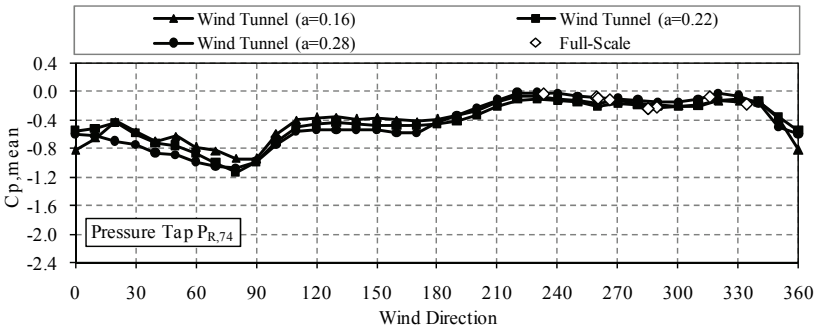

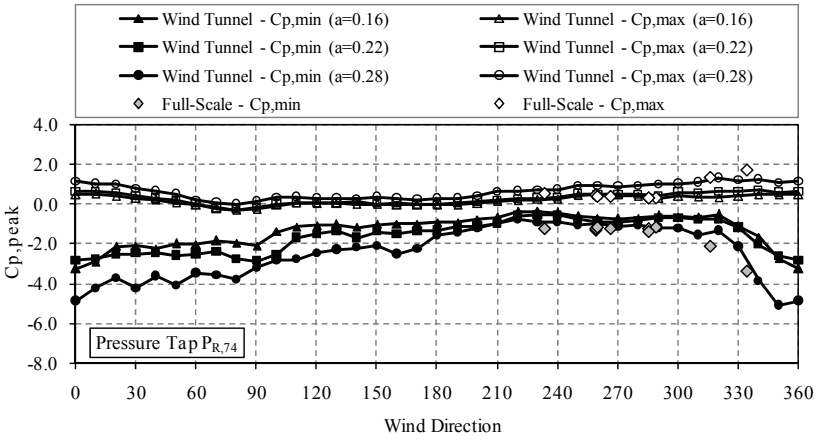

Figure B.25 Mean and peak pressure coefficient variation for pressure tap $P_{R,74}$.

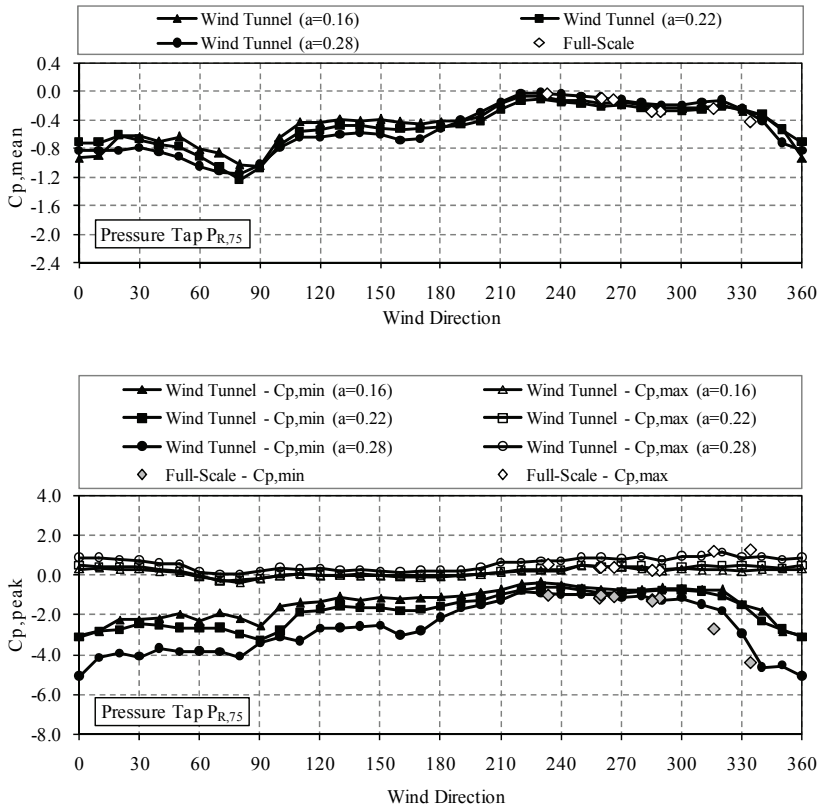

Figure B.26 Mean and peak pressure coefficient variation for pressure tap $P_{R,75}$.

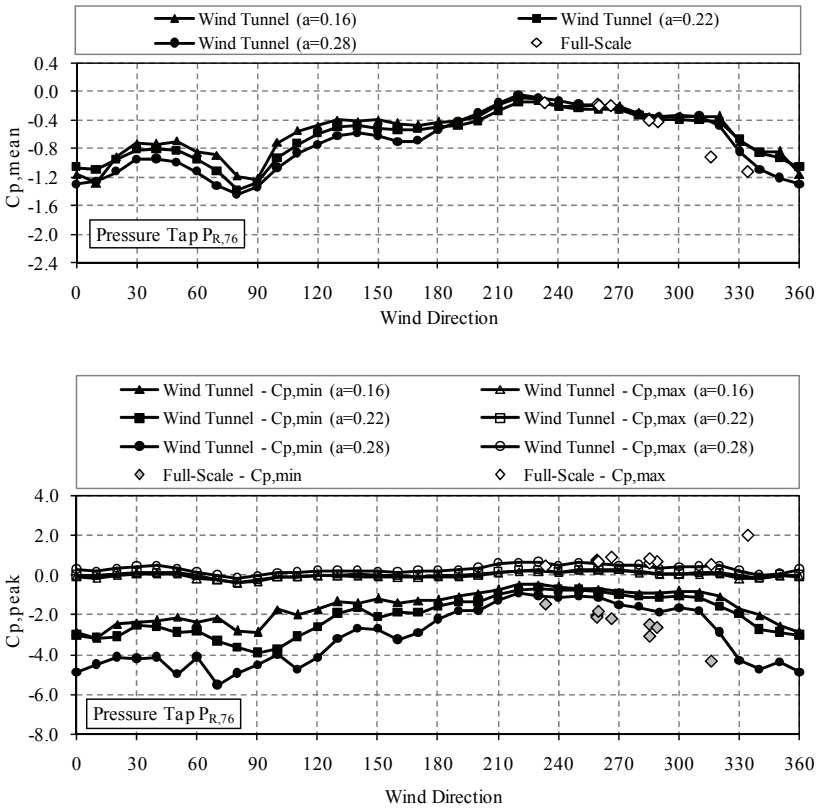

Figure B.27 Mean and peak pressure coefficient variation for pressure tap $P_{R,76}$.

B.1.6 South-east roof

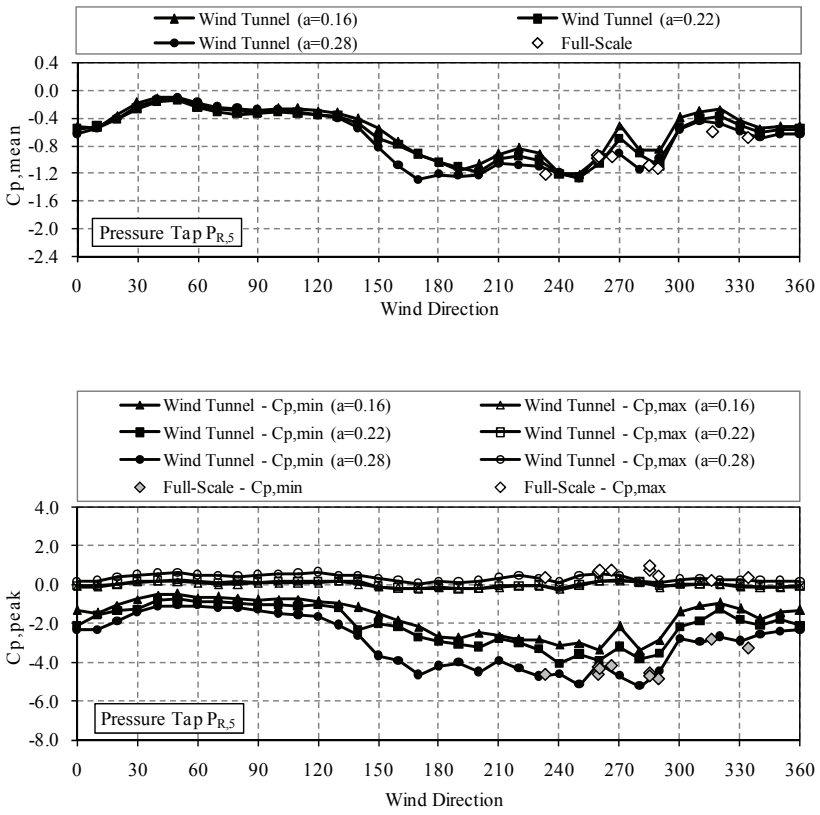

Figure B.28 Mean and peak pressure coefficient variation for pressure tap $P_{R,5}$.

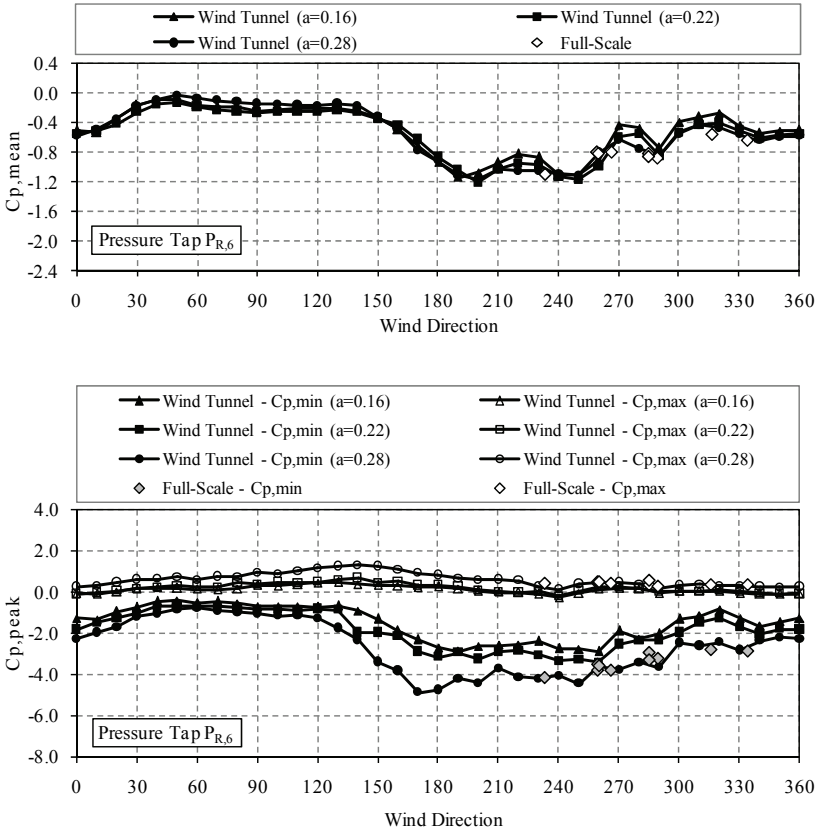

Figure B.29 Mean and peak pressure coefficient variation for pressure tap $P_{R,6}$.

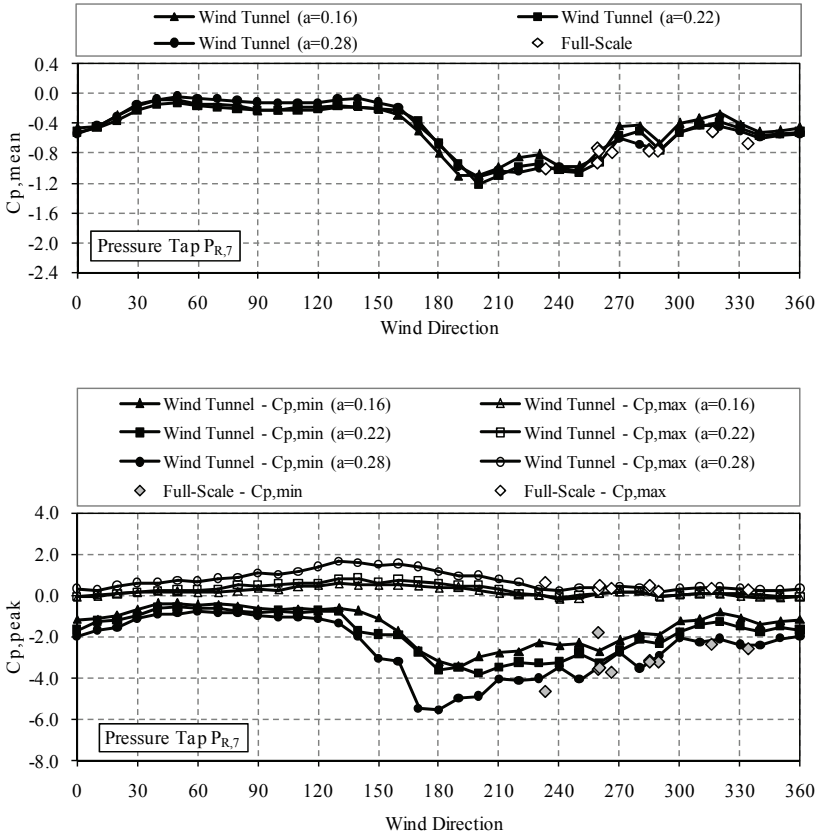

Figure B.30 Mean and peak pressure coefficient variation for pressure tap $P_{R,7}$.

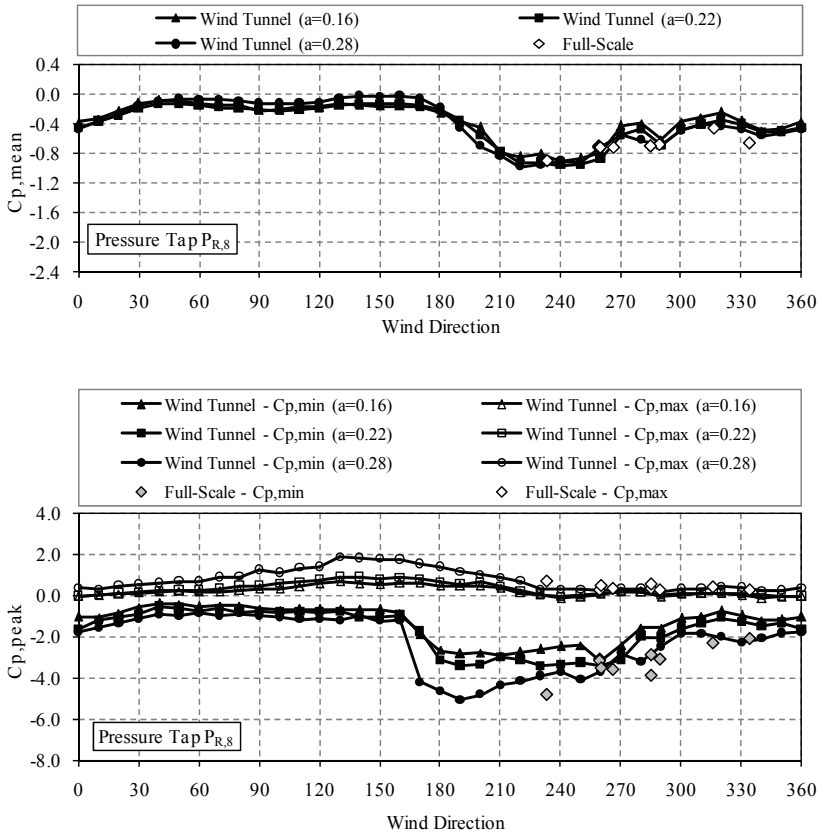

Figure B.31 Mean and peak pressure coefficient variation for pressure tap $P_{R,8}$.

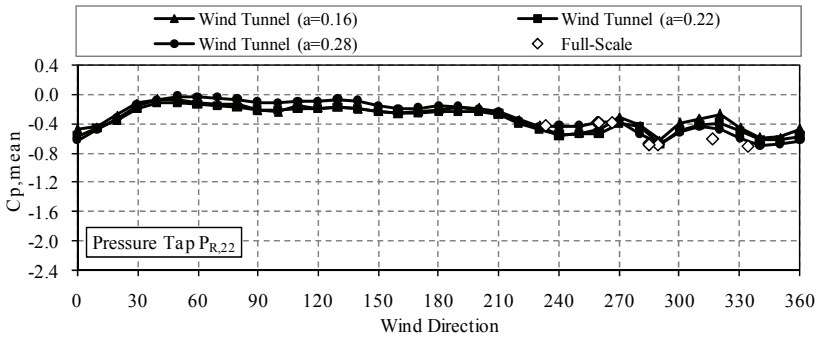

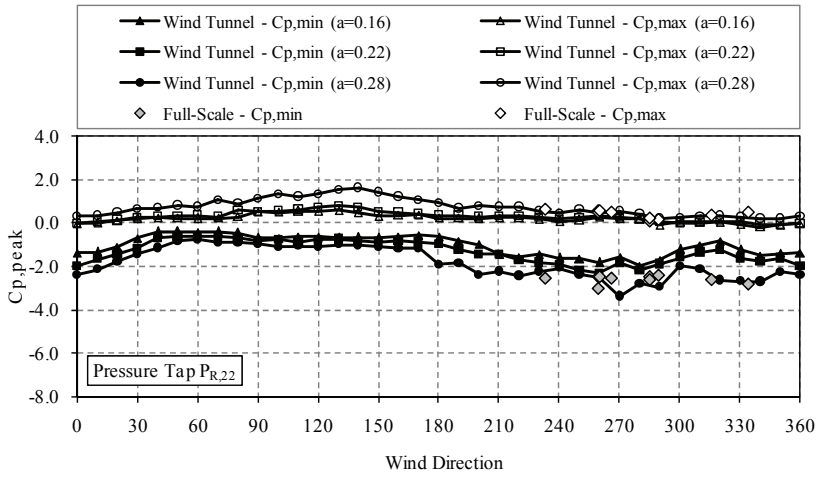

Figure B.32 Mean and peak pressure coefficient variation for pressure tap $P_{R,22}$.

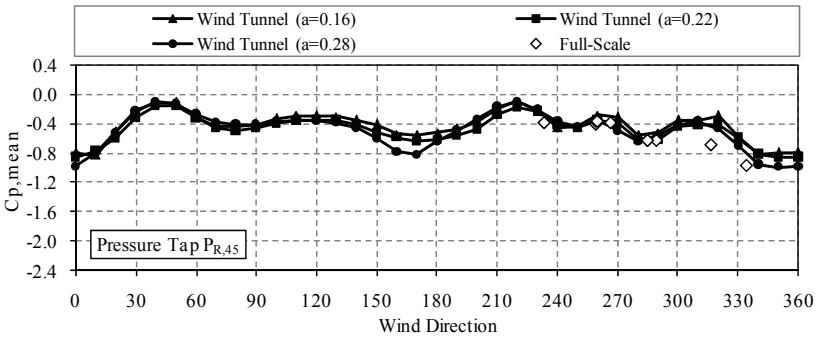

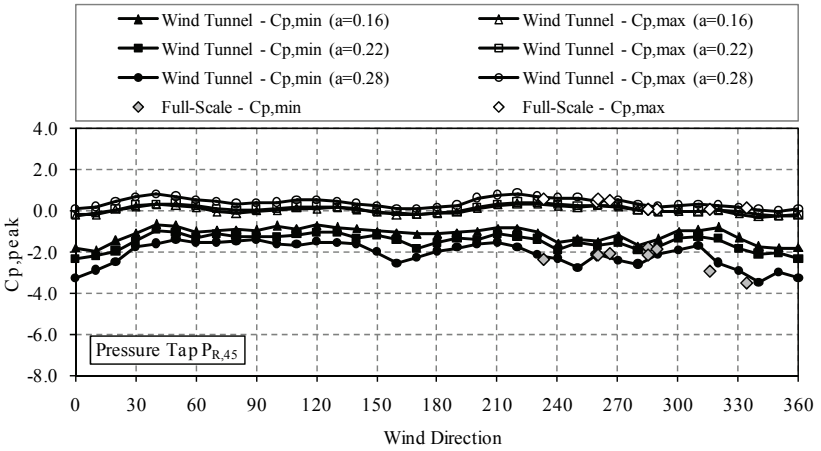

Figure B.33 Mean and peak pressure coefficient variation for pressure tap $P_{R,45}$.

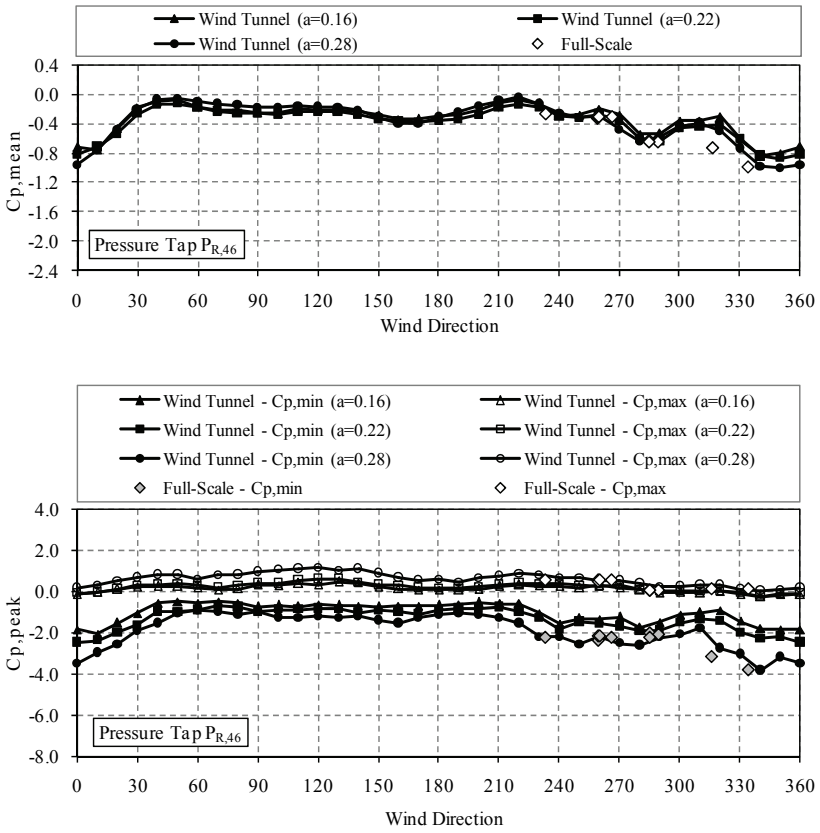

Figure B.34 Mean and peak pressure coefficient variation for pressure tap $P_{R,46}$.

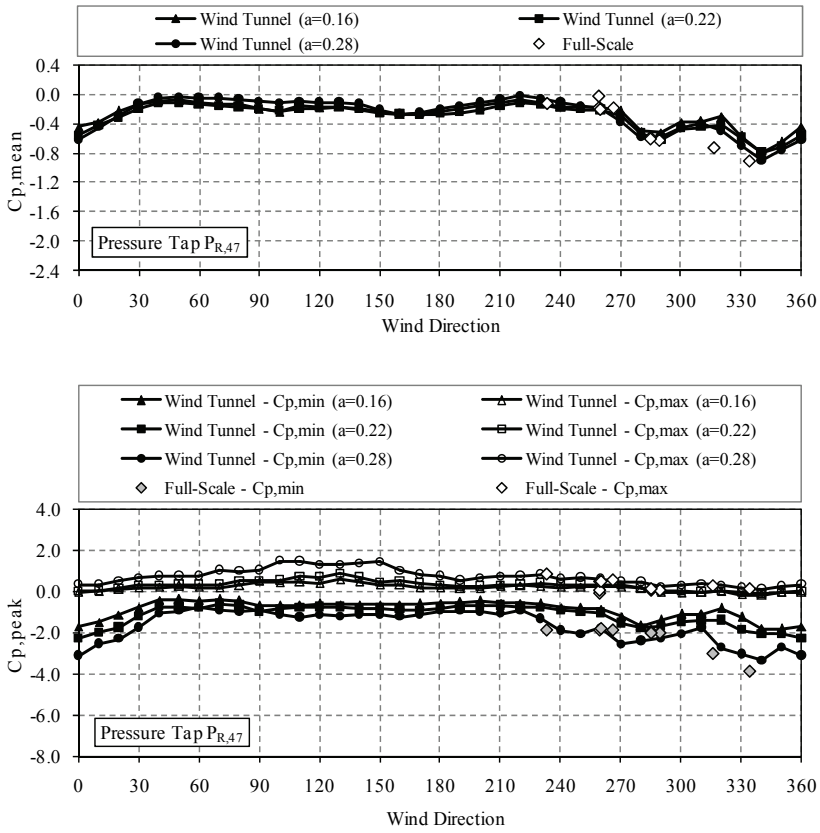

Figure B.35 Mean and peak pressure coefficient variation for pressure tap $P_{R,47}$.

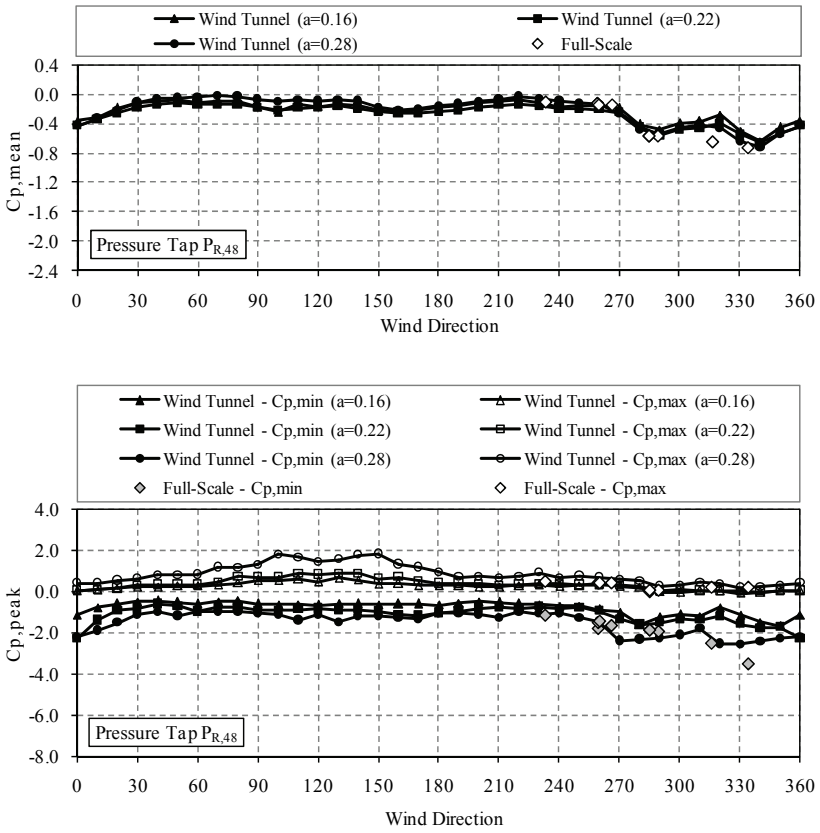

Figure B.36 Mean and peak pressure coefficient variation for pressure tap $P_{R,48}$.

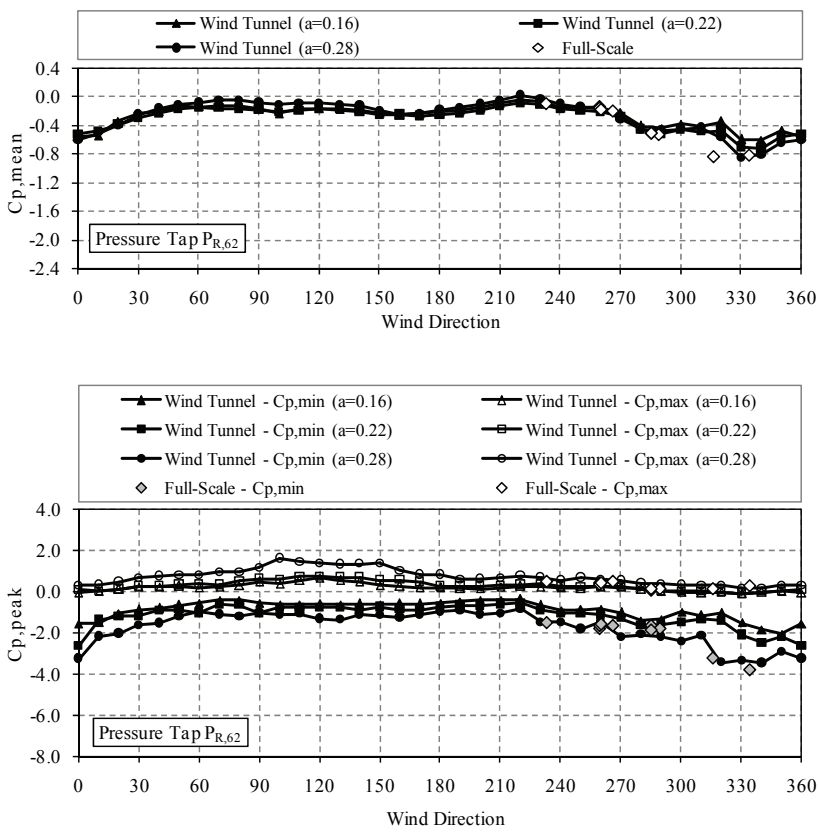

Figure B.37 Mean and peak pressure coefficient variation for pressure tap $P_{R,62}$.

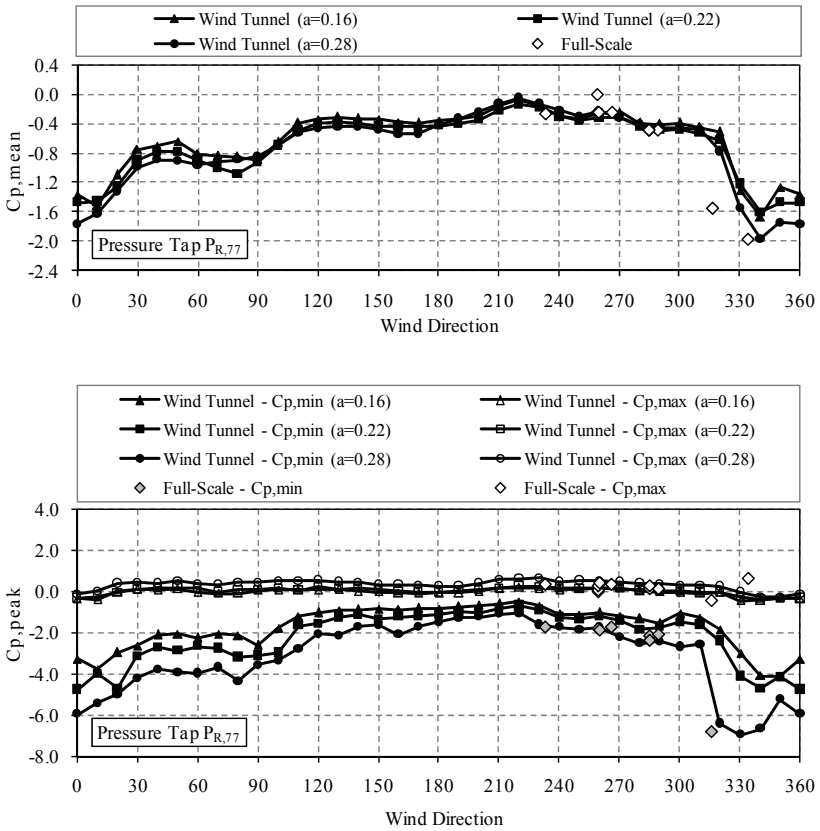

Figure B.38 Mean and peak pressure coefficient variation for pressure tap $P_{R,77}$.

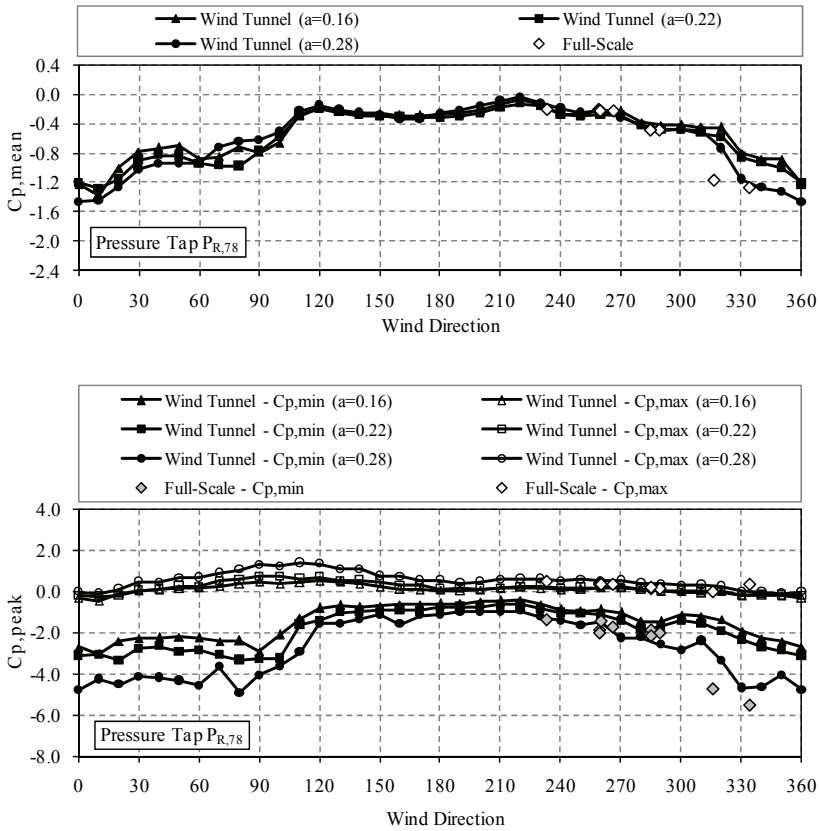

Figure B.39 Mean and peak pressure coefficient variation for pressure tap $P_{R,78}$.

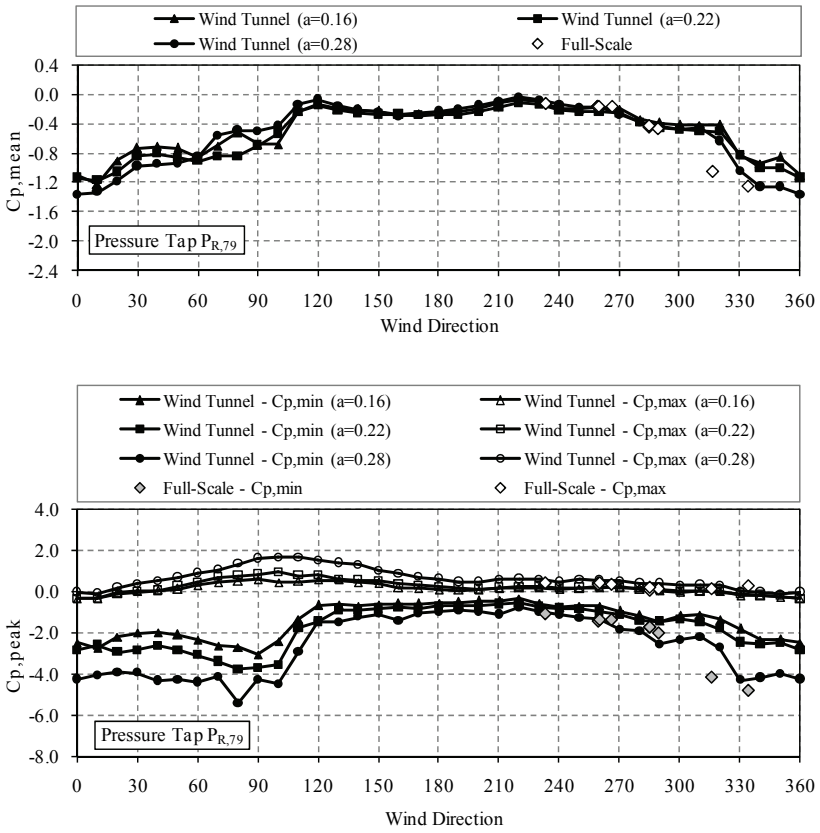

Figure B.40 Mean and peak pressure coefficient variation for pressure tap $P_{R,79}$.

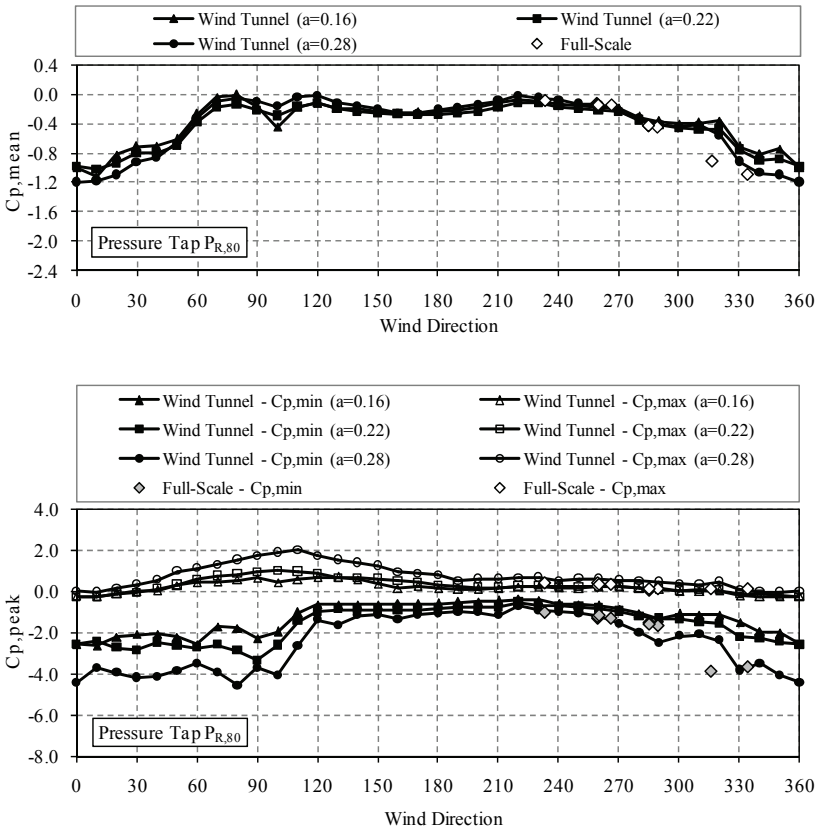

Figure B.41 Mean and peak pressure coefficient variation for pressure tap $P_{R,80}$.

B.2 Wind tunnel and full-scale pressure coefficient comparisons (individual frames - supplementary to Section 6.3.4)

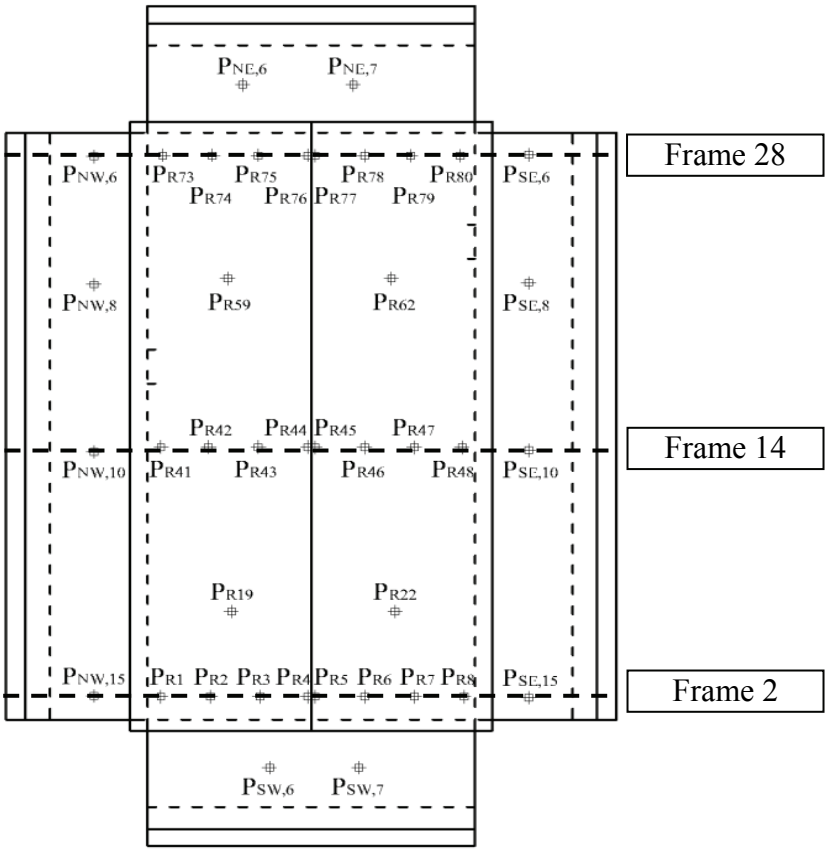

Figure B.42 Instrumented frames in full-scale test building.

B.2.1 Wind direction 240 degrees

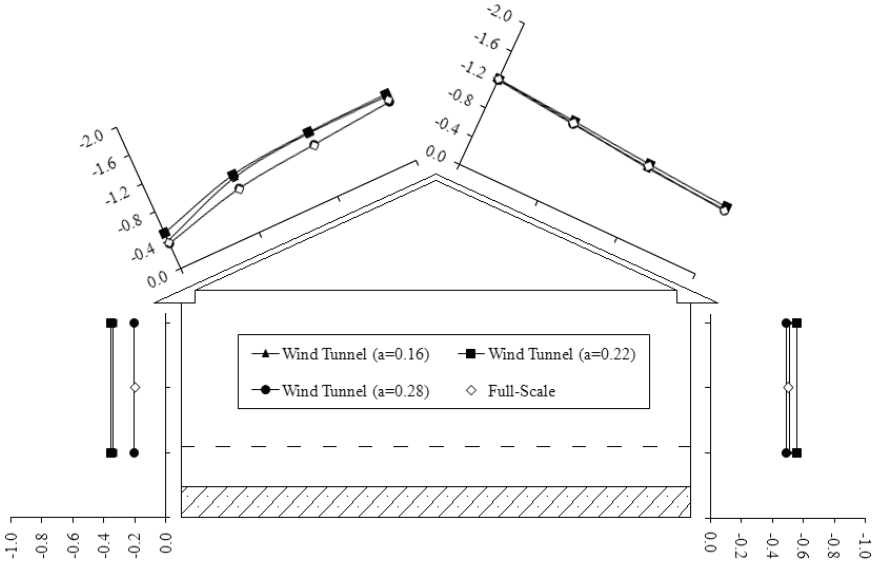

Figure B.43 Mean pressure coefficients for Frame 2.

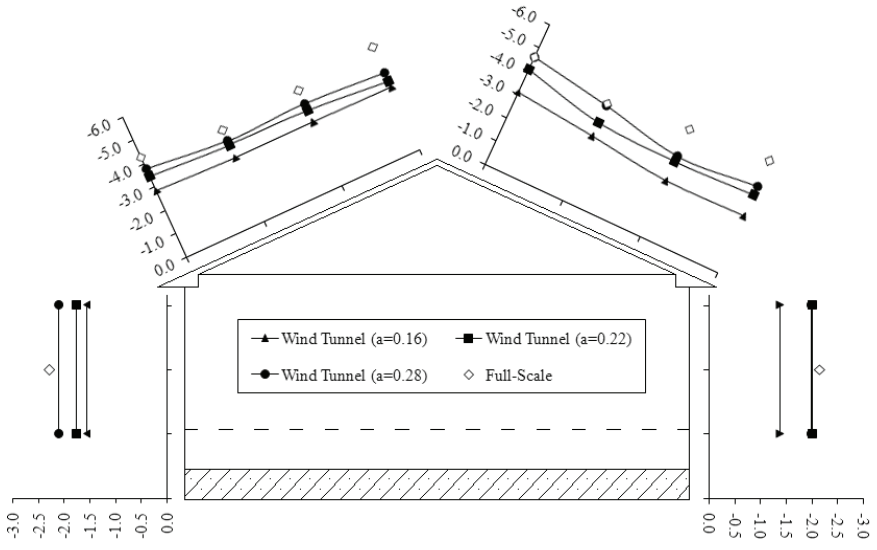

Figure B.44 Peak pressure coefficients for Frame 2.

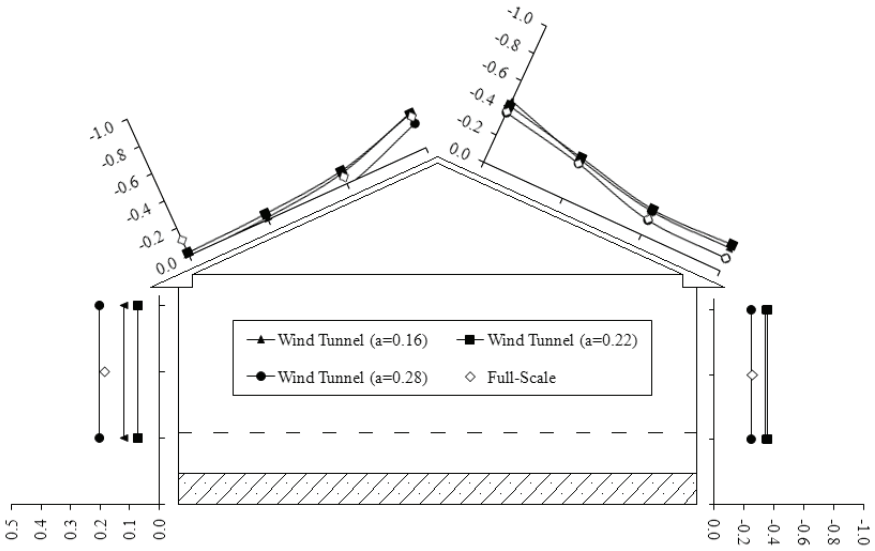

Figure B.45 Mean pressure coefficients for Frame 14.

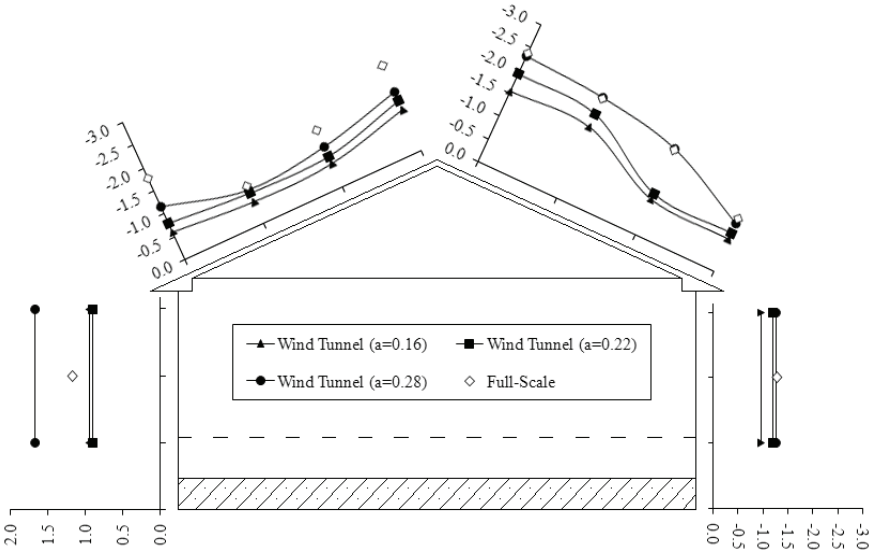

Figure B.46 Peak pressure coefficients for Frame 14.

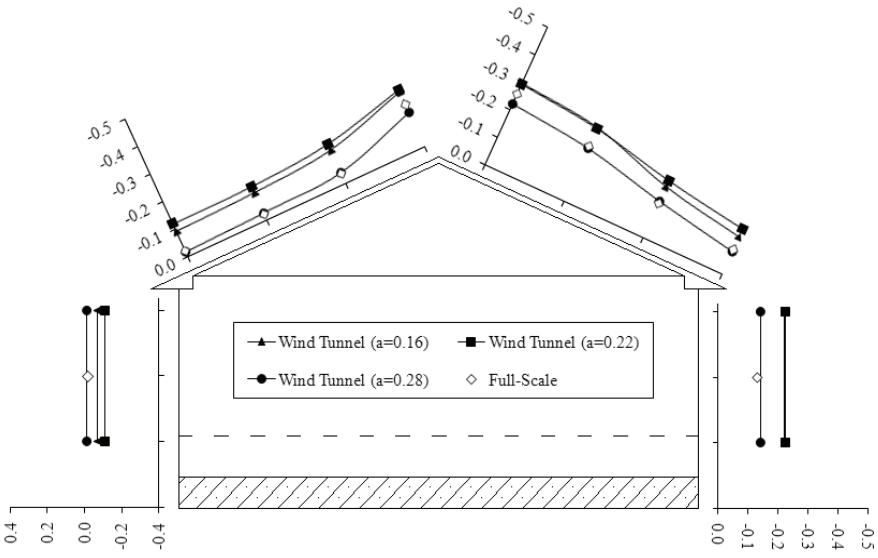

Figure B.47 Mean pressure coefficients for Frame 28.

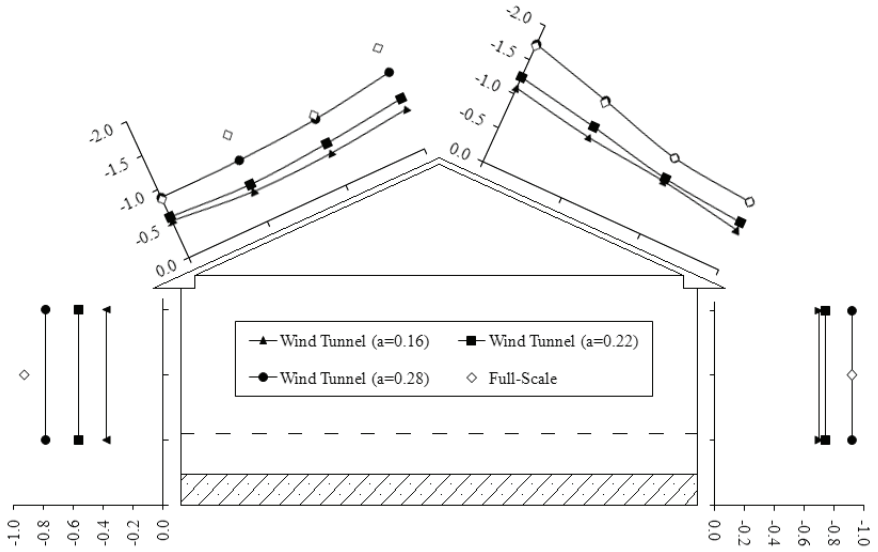

Figure B.48 Peak pressure coefficients for Frame 28.

B.2.2 Wind direction 260 degrees

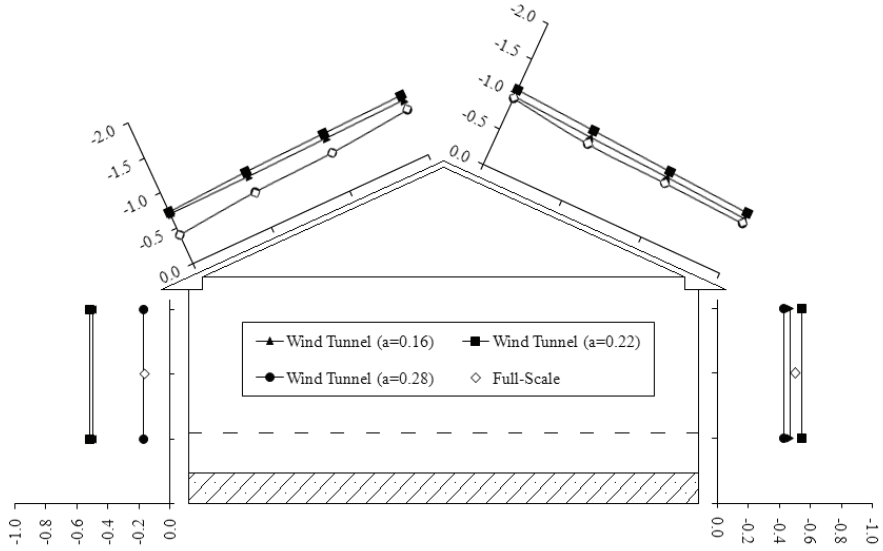

Figure B.49 Mean pressure coefficients for Frame 2.

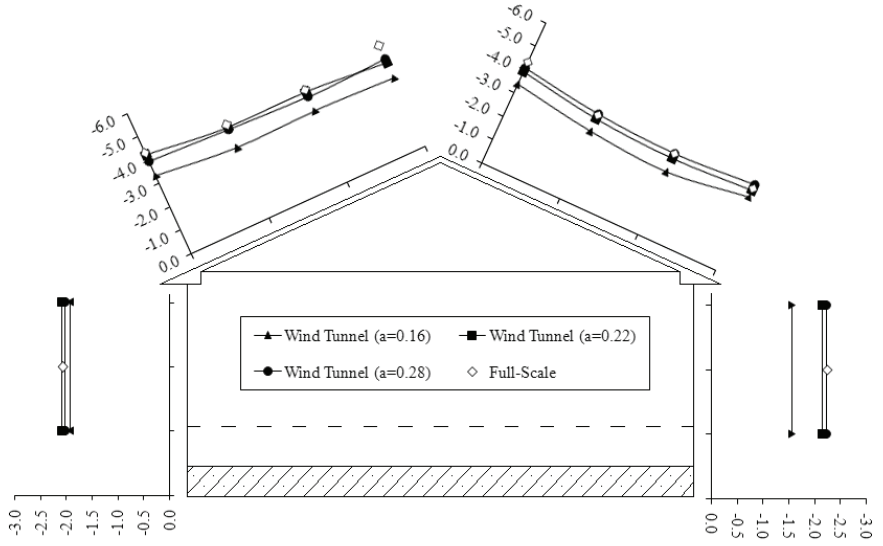

Figure B.50 Peak pressure coefficients for Frame 2.

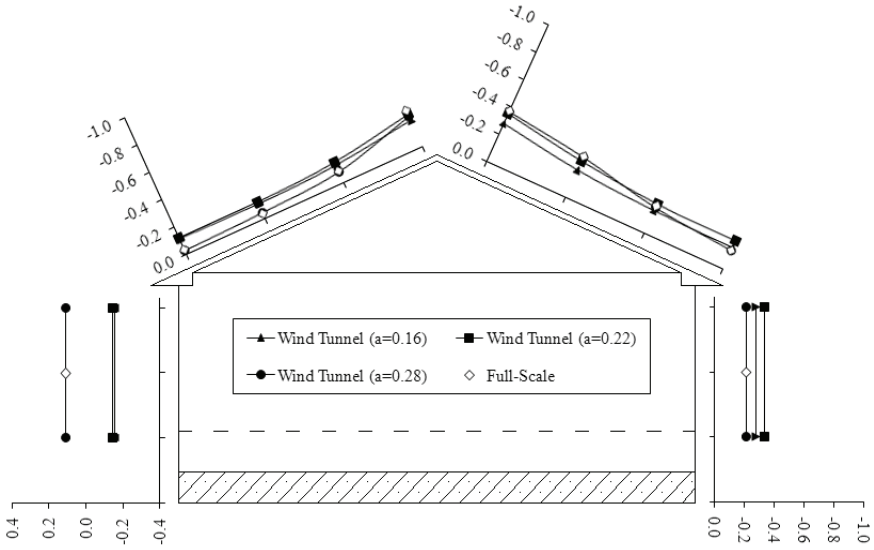

Figure B.51 Mean pressure coefficients for Frame 14.

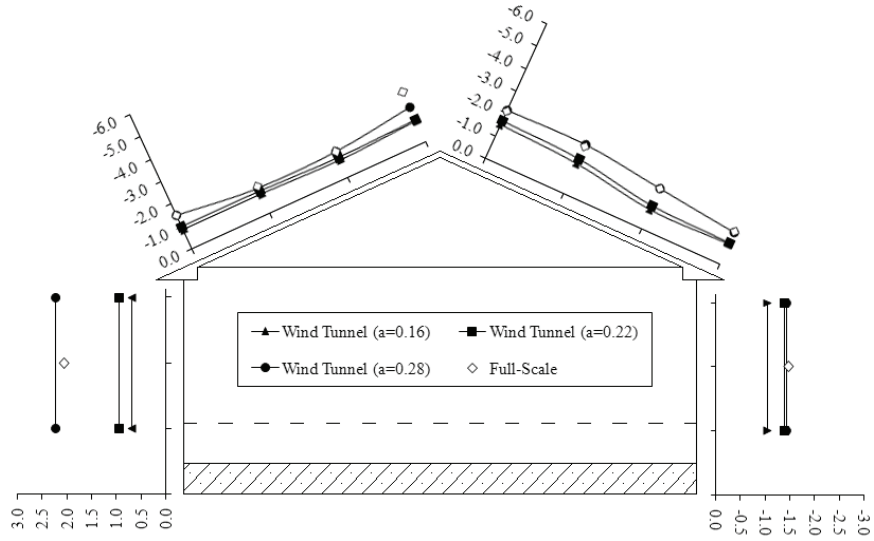

Figure B.52 Peak pressure coefficients for Frame 14.

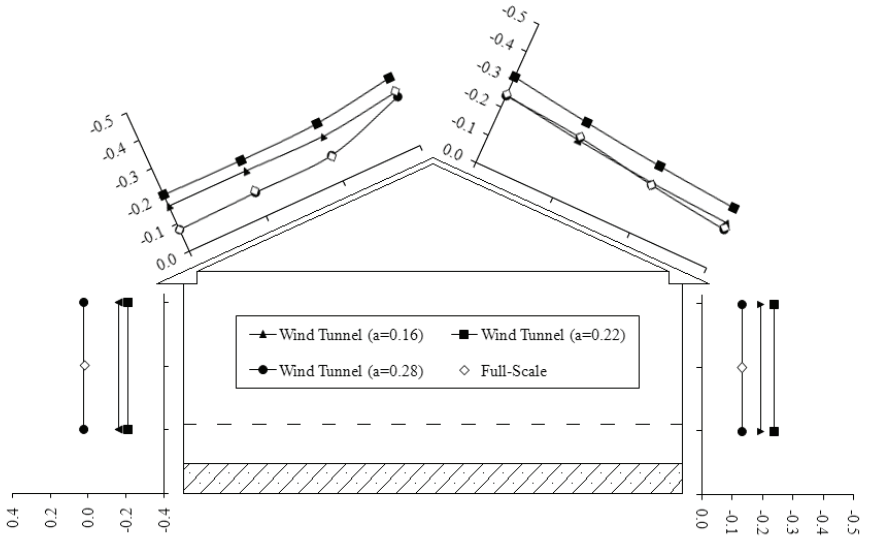

Figure B.53 Mean pressure coefficients for Frame 28.

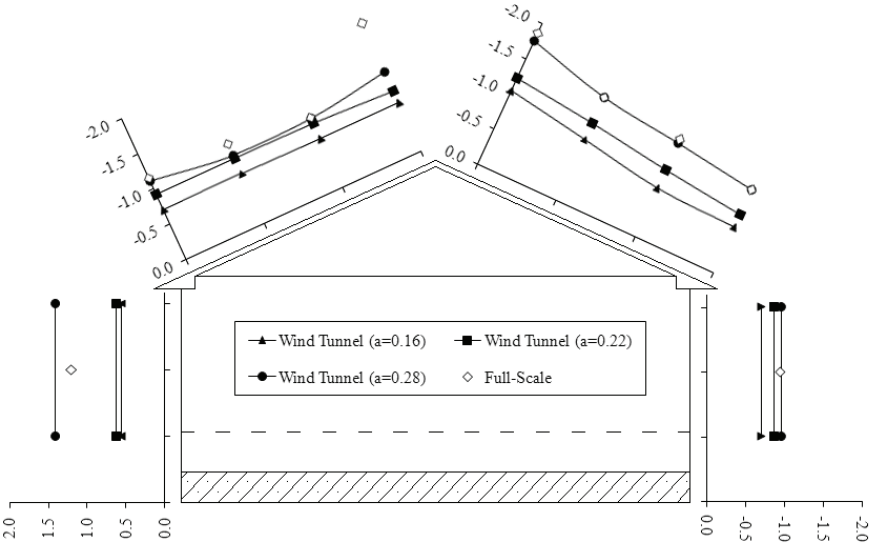

Figure B.54 Peak pressure coefficients for Frame 28.

B.2.3 Wind direction 290 degrees

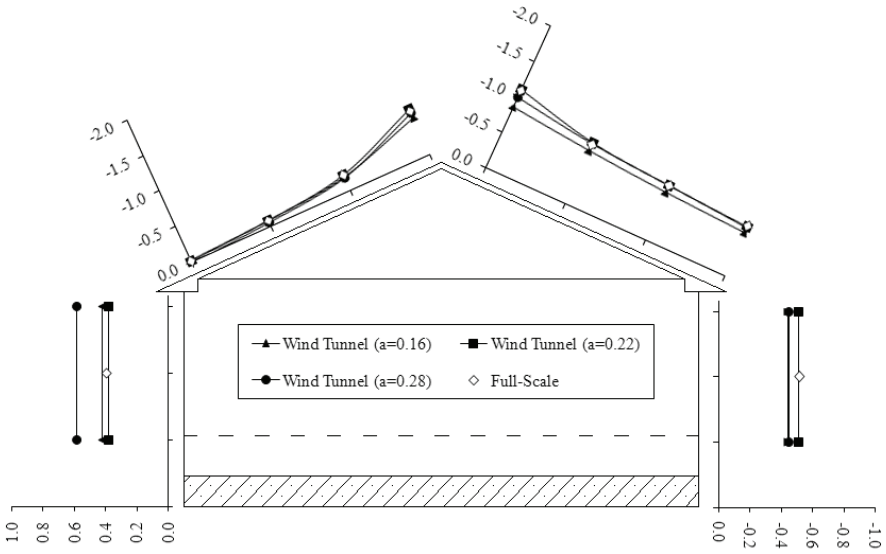

Figure B.55 Mean pressure coefficients for Frame 2.

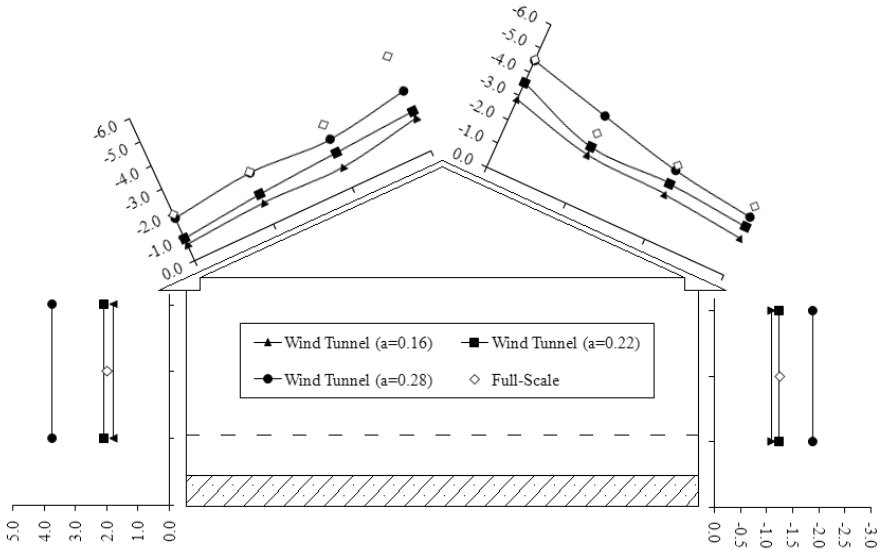

Figure B.56 Peak pressure coefficients for Frame 2.

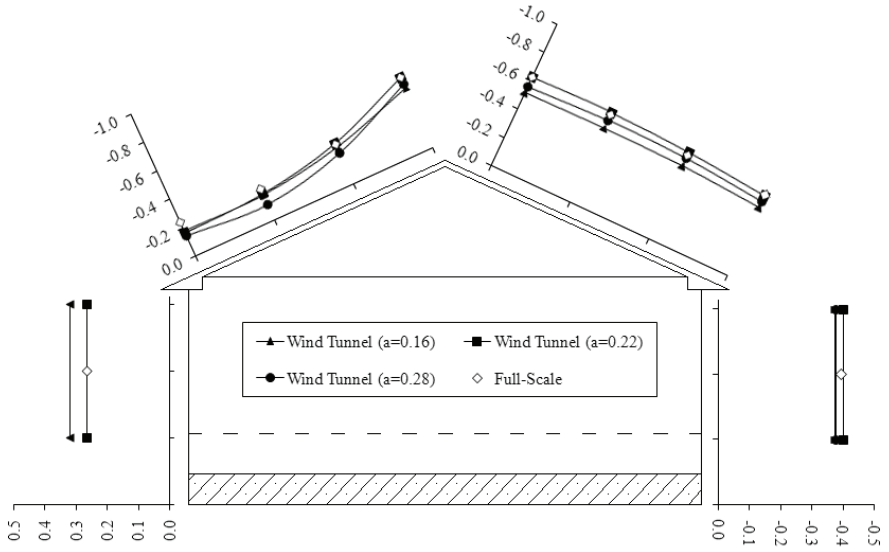

Figure B.57 Mean pressure coefficients for Frame 14.

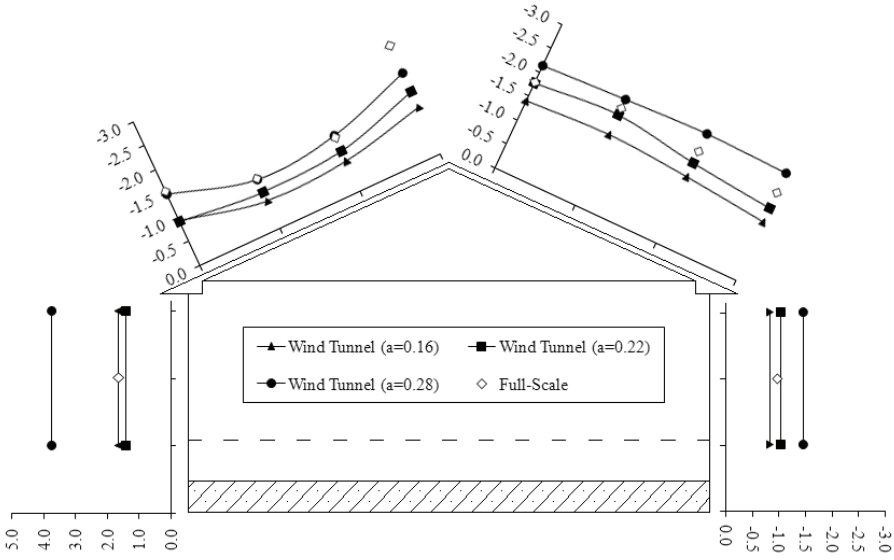

Figure B.58 Peak pressure coefficients for Frame 14.

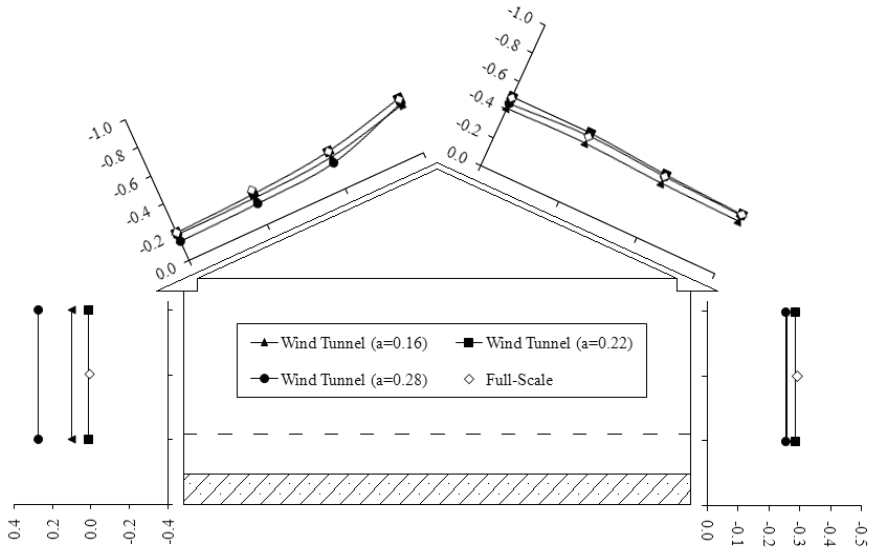

Figure B.59 Mean pressure coefficients for Frame 28.

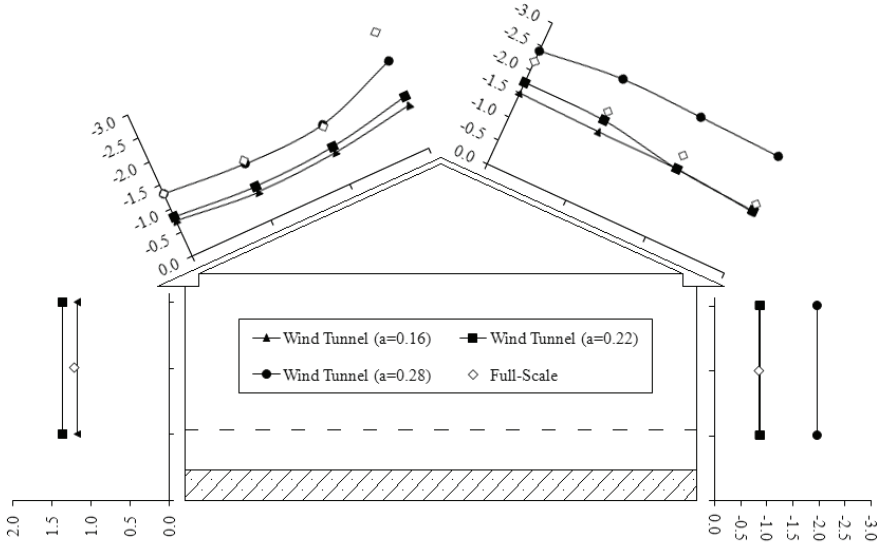

Figure B.60 Peak pressure coefficients for Frame 28.

B.2.4 Wind direction 330 degrees

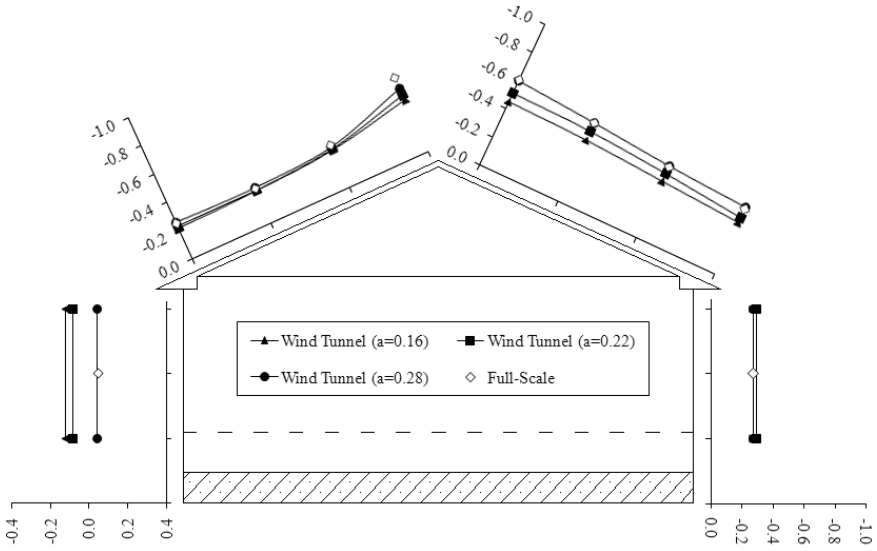

Figure B.61 Mean pressure coefficients for Frame 2.

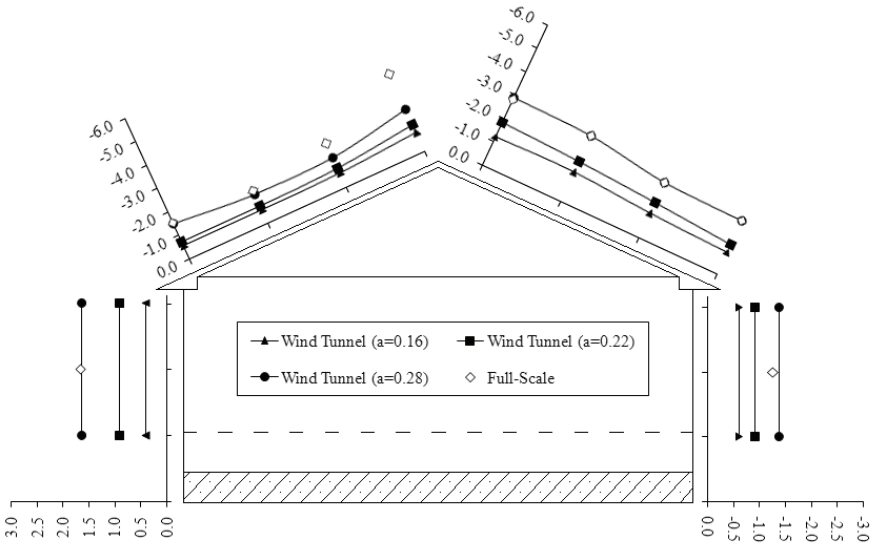

Figure B.62 Peak pressure coefficients for Frame 2.

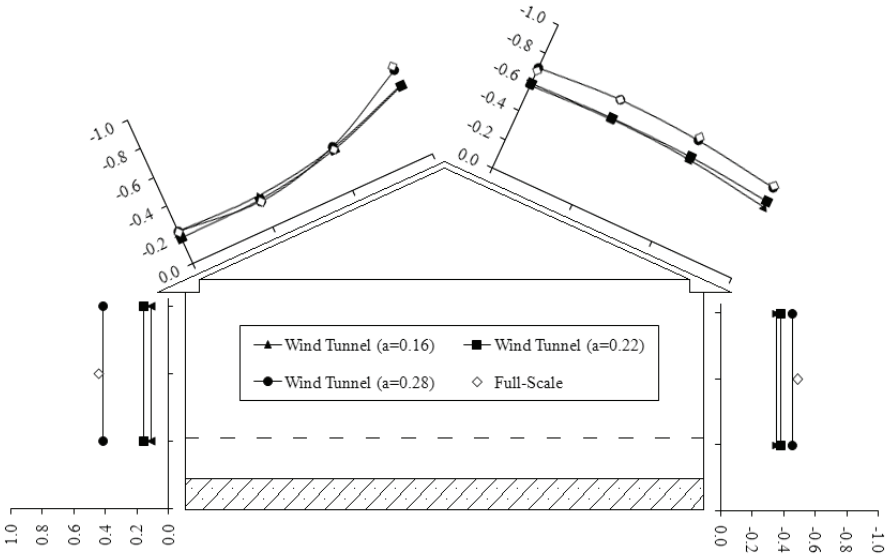

Figure B.63 Mean pressure coefficients for Frame 14.

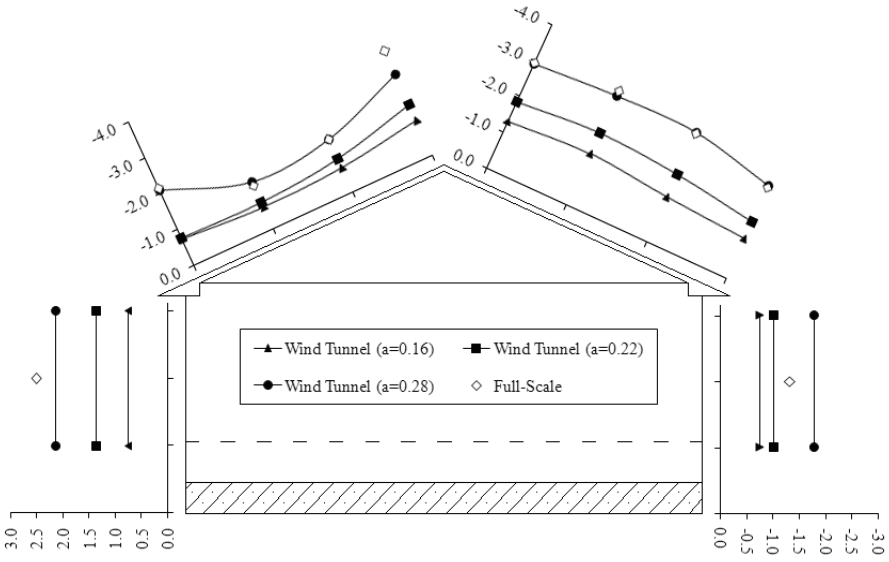

Figure B.64 Peak pressure coefficients for Frame 14.

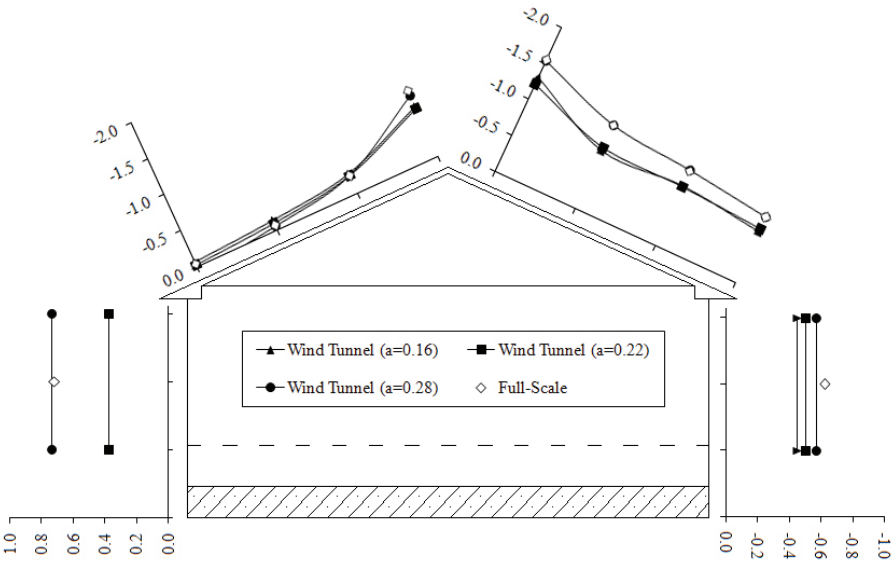

Figure B.65 Mean pressure coefficients for Frame 28.

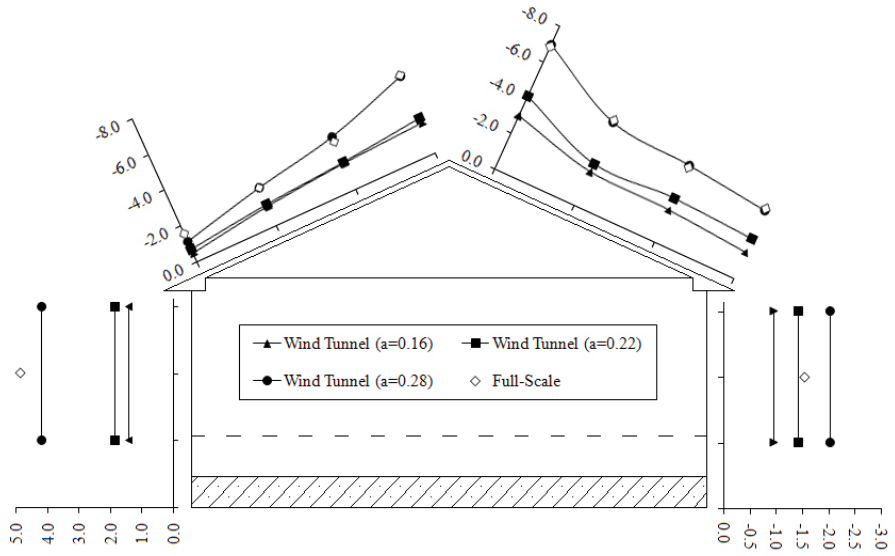

Figure B.66 Peak pressure coefficients for Frame 28.

B.3 Wind tunnel and full-scale pressure coefficient comparisons (all pressure taps - supplementary to Section 6.3.3)

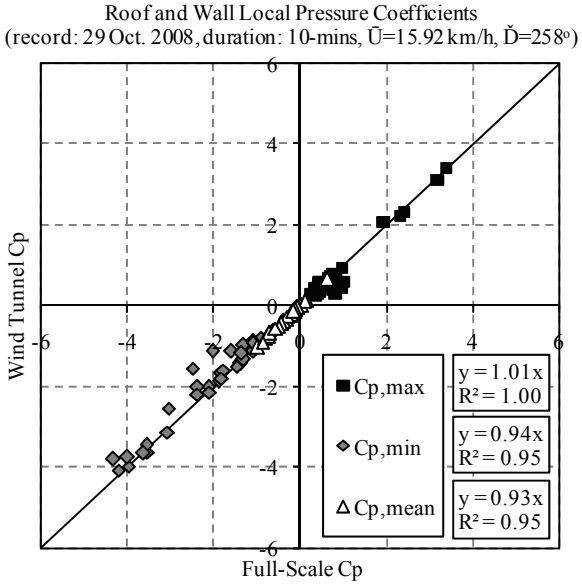

Figure B.67 Comparison of wind tunnel and field mean and peak pressure coefficients (29 October, 2008).

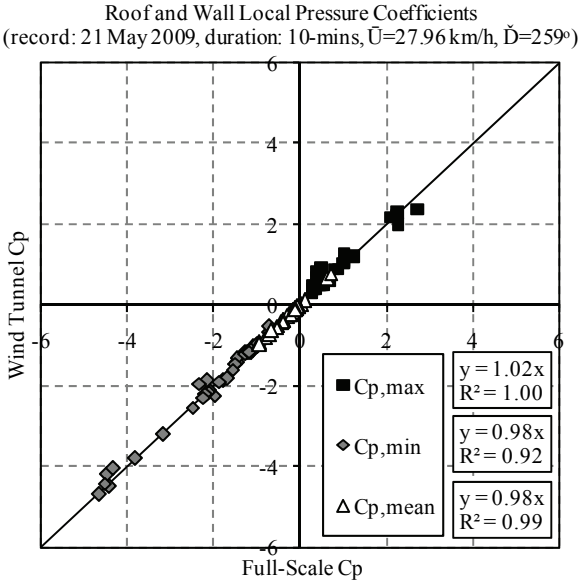

Figure B.68 Comparison of wind tunnel and field mean and peak pressure coefficients (21 May, 2009).

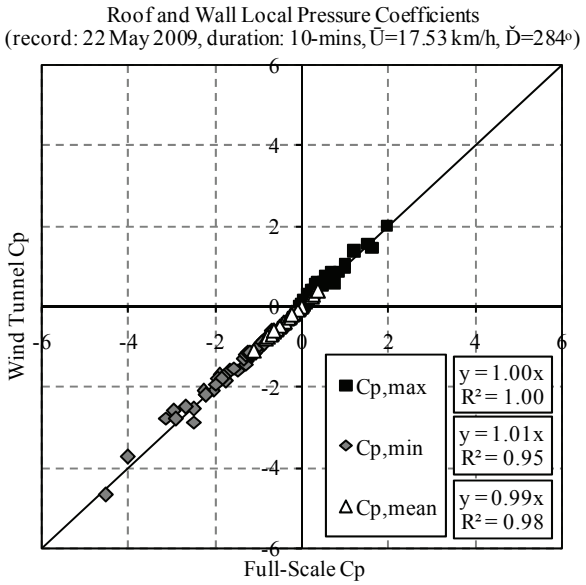

Figure B.69 Comparison of wind tunnel and field mean and peak pressure coefficients (22 May, 2009).

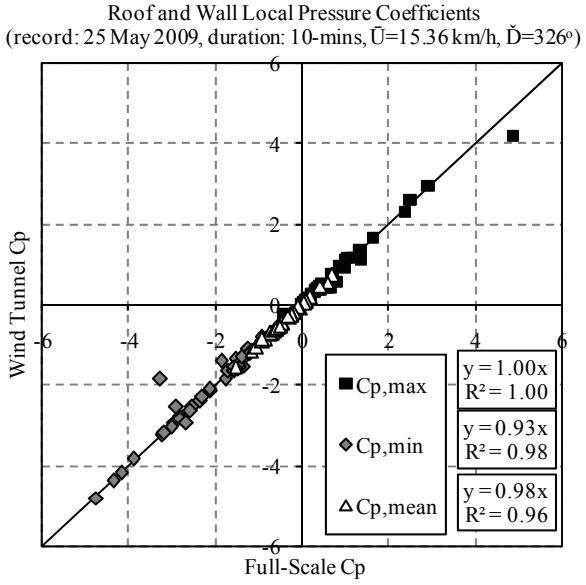

Figure B.70 Comparison of wind tunnel and field mean and peak pressure coefficients (25 May, 2009).

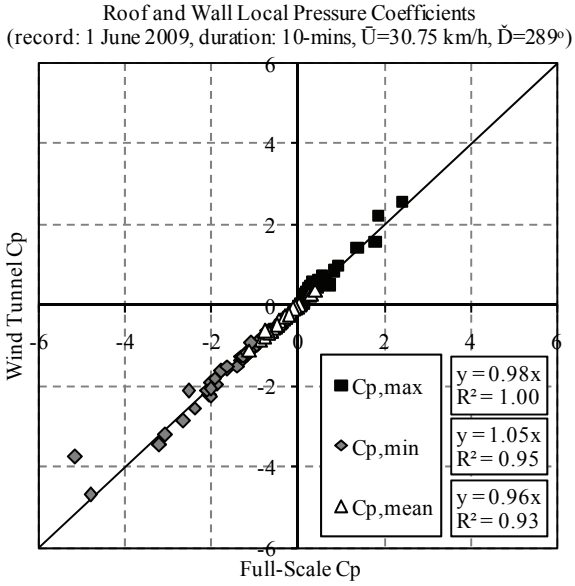

Figure B.71 Comparison of wind tunnel and field mean and peak pressure coefficients (1 June, 2009).

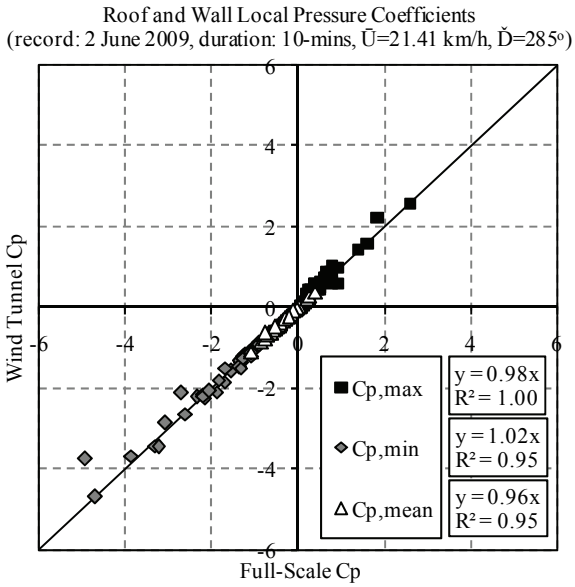

Figure B.72 Comparison of wind tunnel and field mean and peak pressure coefficients (2 June, 2009).

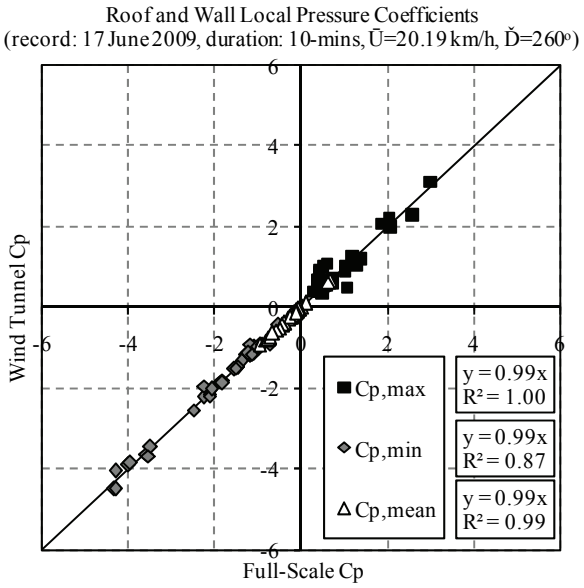

Figure B.73 Comparison of wind tunnel and field mean and peak pressure coefficients (17 June, 2009).

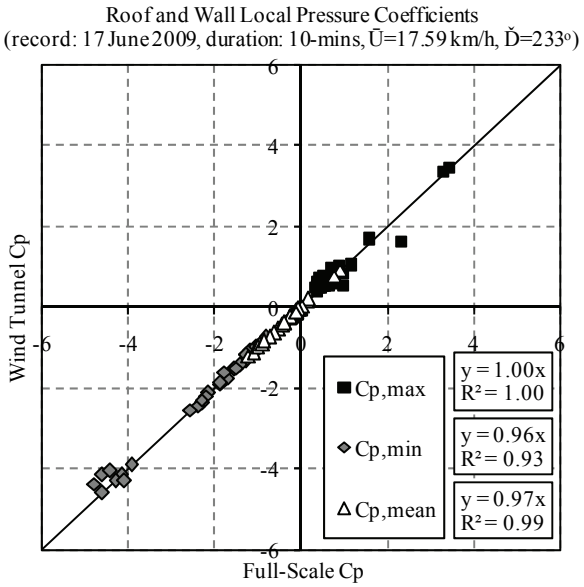

Figure B.74 Comparison of wind tunnel and field mean and peak pressure coefficients (17 June, 2009).

APPENDIX C

Detailed Results (Forces)

This appendix presents supplementary results to Section 6.4.

C.1 Structural attenuation of wind uplift forces

C.1.1 Record October 29th, 2008

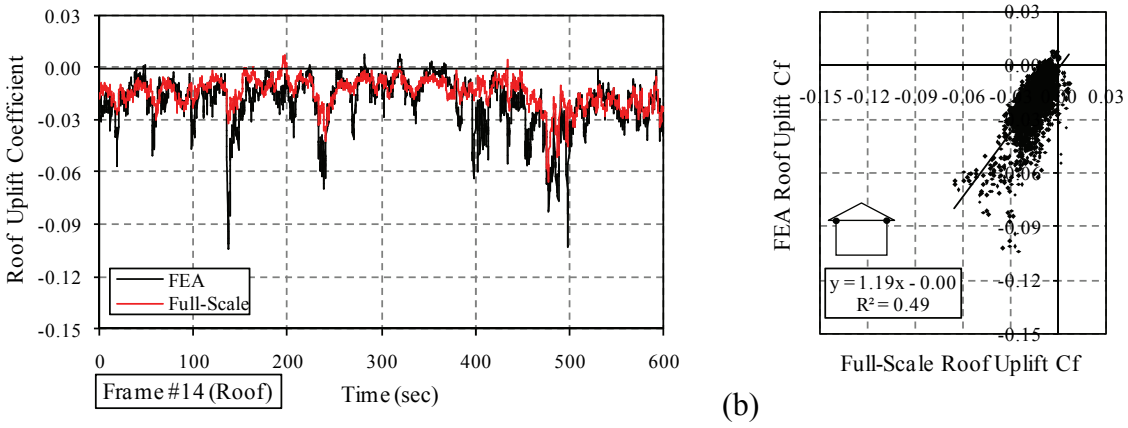

Figure C.1 (a) Frame 14 load cell and finite element roof uplift forces and (b) scatter plots (FEA: finite element model predictions).

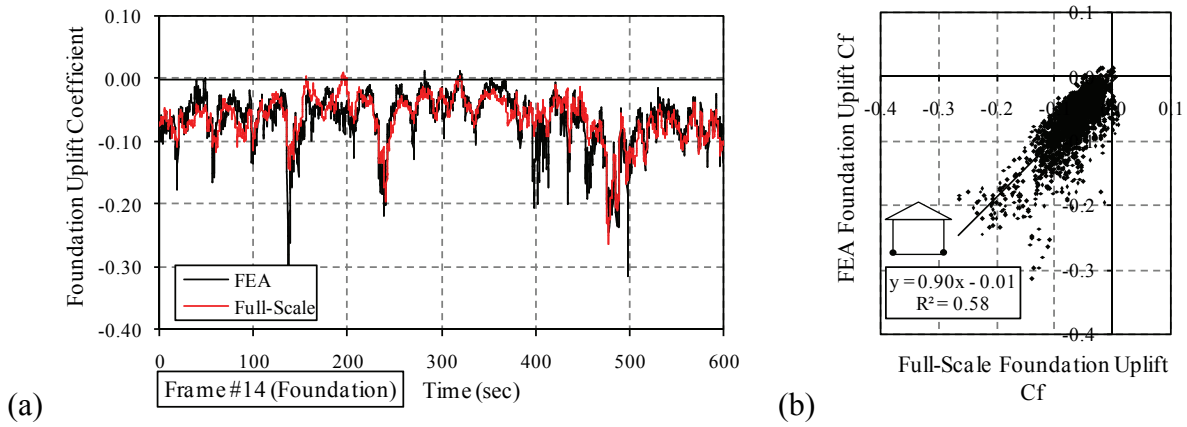

(a) (b)

Figure C.2 (a) Frame 14 load cell and finite element foundation uplift forces and (b) scatter plots (FEA: finite element model predictions).

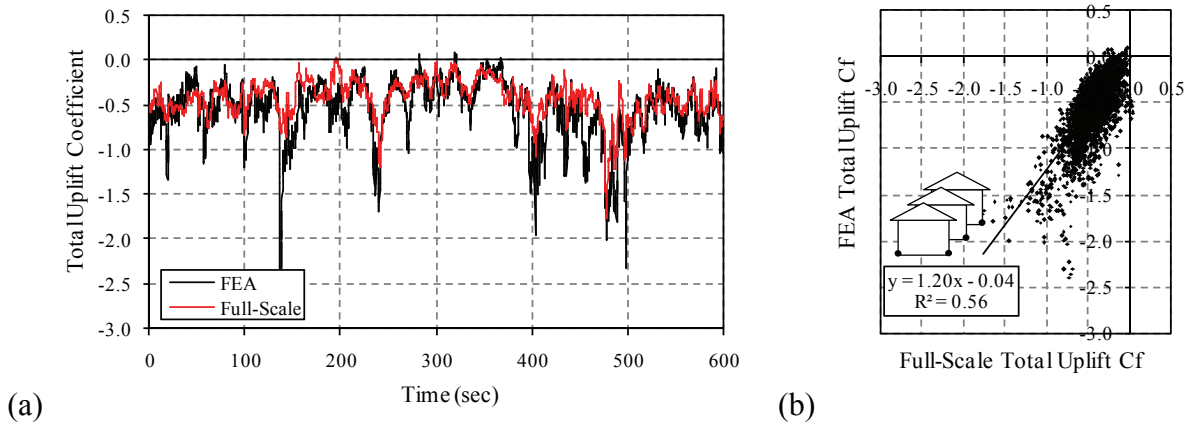

(a) (b)

Figure C.3 (a) Load cell and finite element total foundation uplift forces and (b) scatter plots (FEA: finite element model predictions).

C.1.2 Record May 14th, 2009

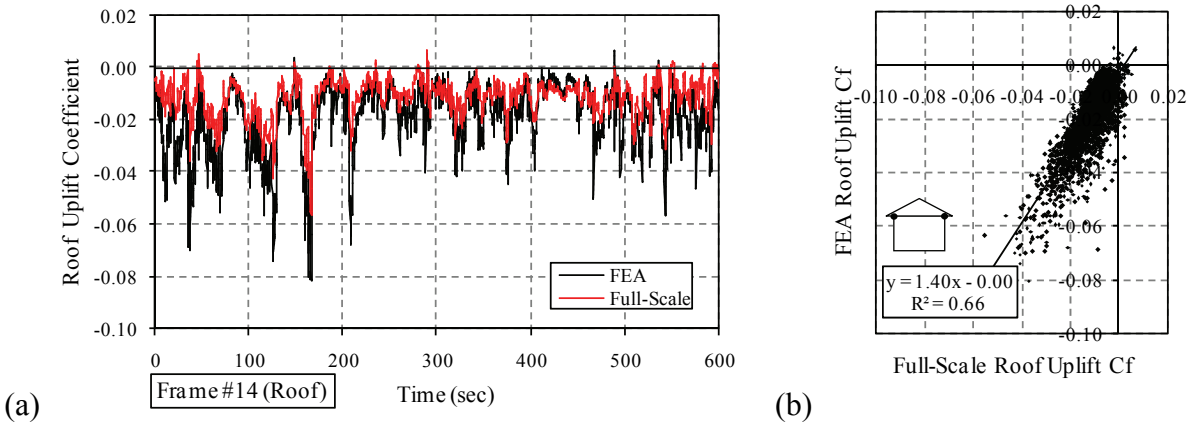

Figure C.4 (a) Frame 14 load cell and finite element roof uplift forces and (b) scatter plots (FEA: finite element model predictions).

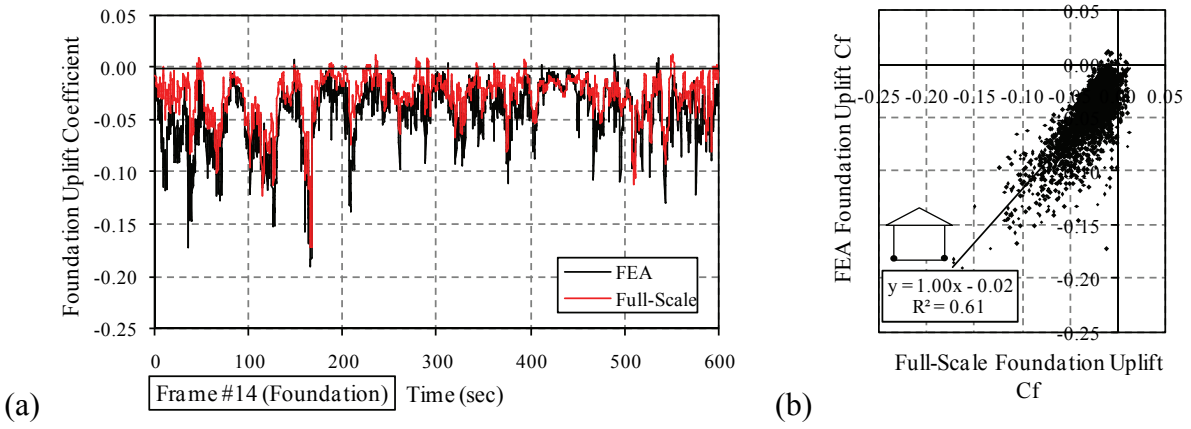

Figure C.5 (a) Frame 14 load cell and finite element foundation uplift forces and (b) scatter plots (FEA: finite element model predictions).

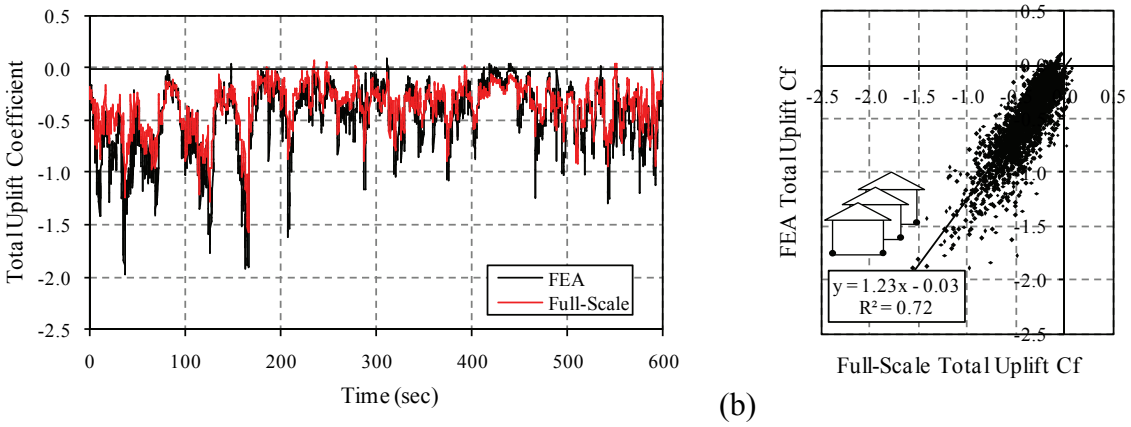

(a) (b)

Figure C.6 (a) Load cell and finite element total foundation uplift forces and (b) scatter plots (FEA: finite element model predictions).

C.1.3 Record May 21st, 2009

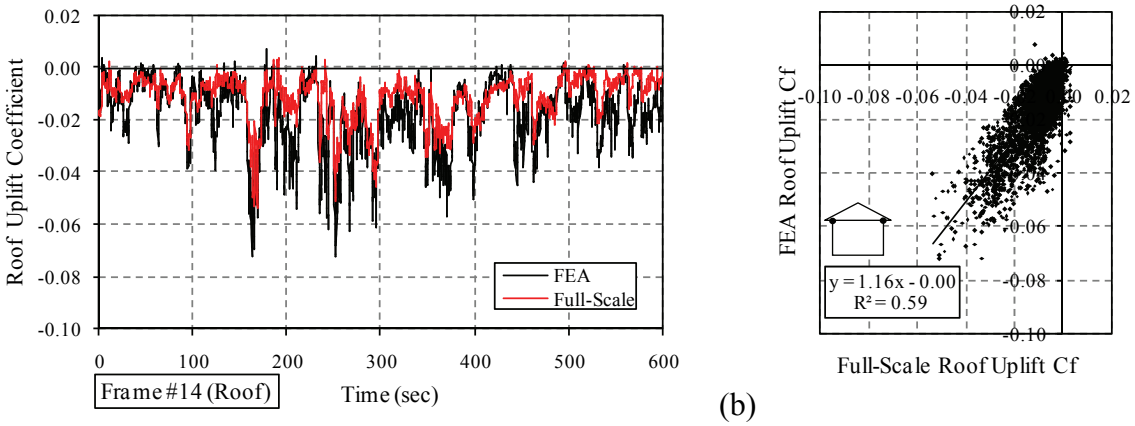

(a) (b)

Figure C.7 (a) Frame 14 load cell and finite element roof uplift forces and (b) scatter plots (FEA: finite element model predictions).

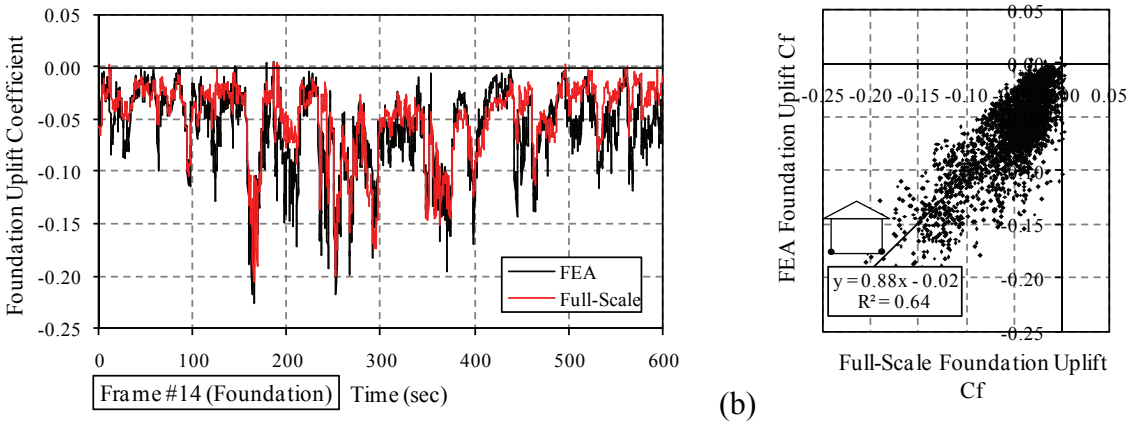

Figure C.8 (a) Frame 14 load cell and finite element foundation uplift forces and (b) scatter plots (FEA: finite element model predictions).

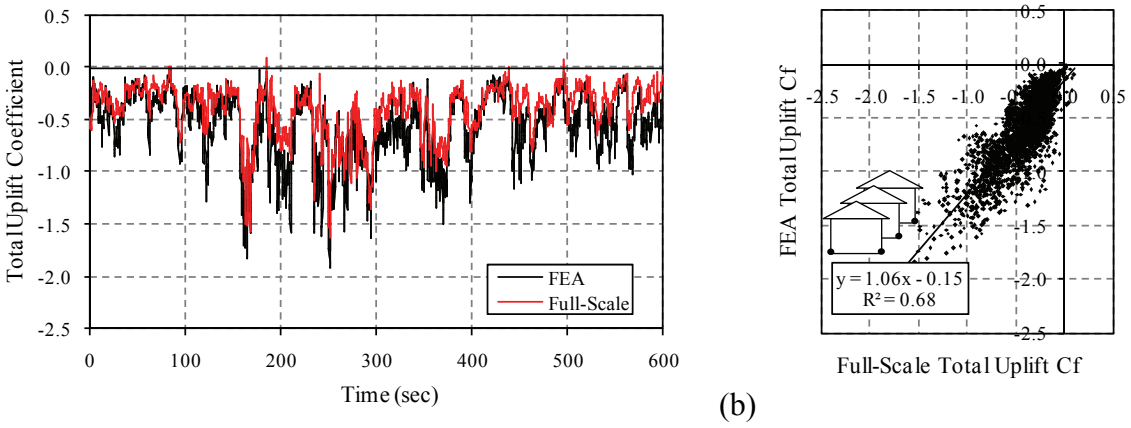

Figure C.9 (a) Load cell and finite element total foundation uplift forces and (b) scatter plots (FEA: finite element model predictions).

C.1.4 Record May 22nd, 2009

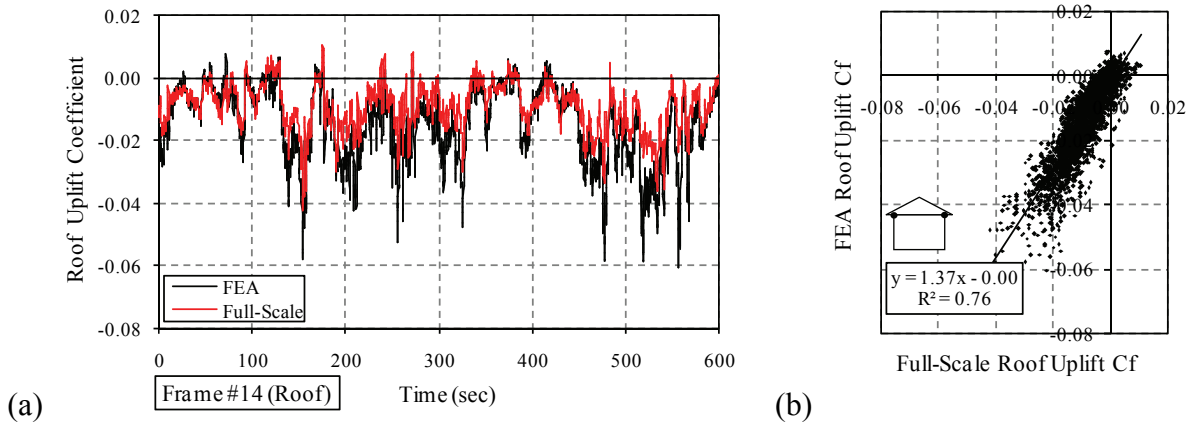

(a) (b)

Figure C.10 (a) Frame 14 load cell and finite element roof uplift forces and (b) scatter plots (FEA: finite element model predictions).

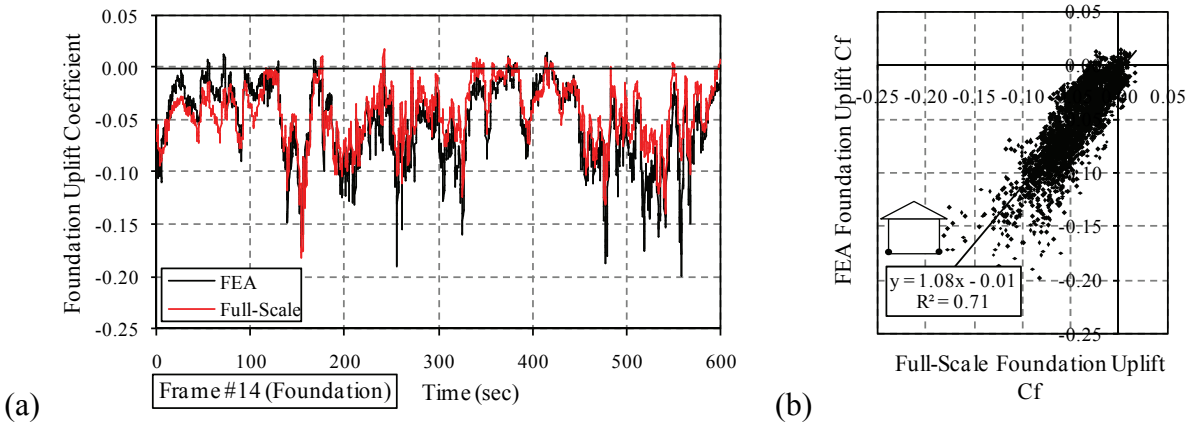

(a) (b)

Figure C.11 (a) Frame 14 load cell and finite element foundation uplift forces and (b) scatter plots (FEA: finite element model predictions).

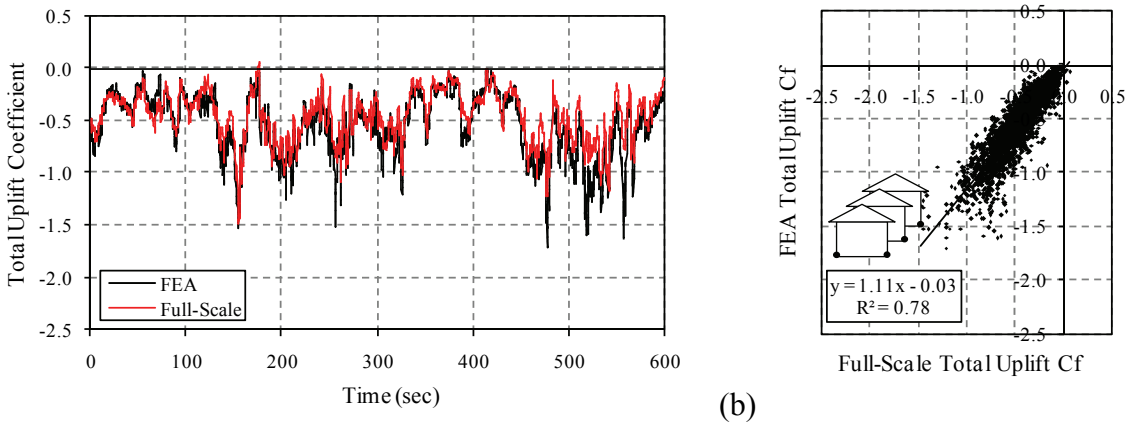

(a) (b)

Figure C.12 (a) Load cell and finite element total foundation uplift forces and (b) scatter plots (FEA: finite element model predictions).

C.1.5 Record June 1st, 2009 (ID 13021)

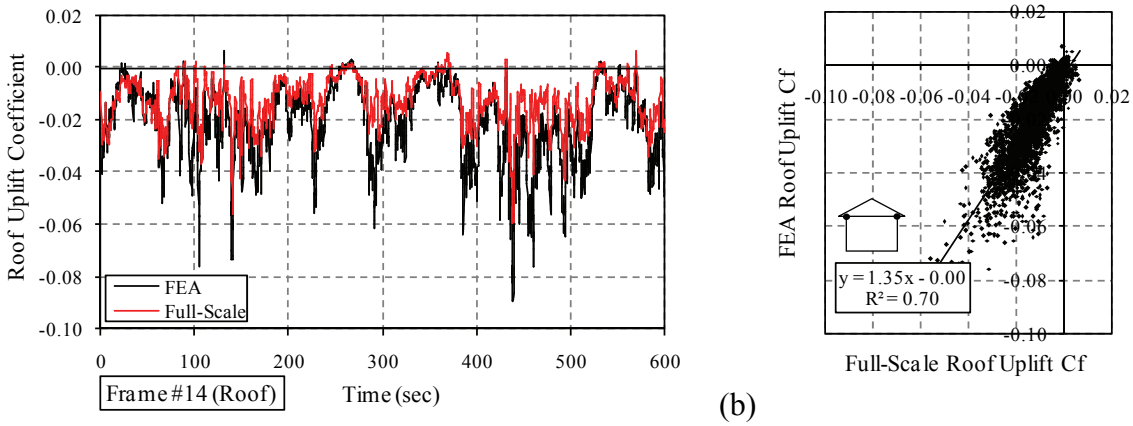

(a) (b)

Figure C.13 (a) Frame 14 load cell and finite element roof uplift forces and (b) scatter plots (FEA: finite element model predictions).

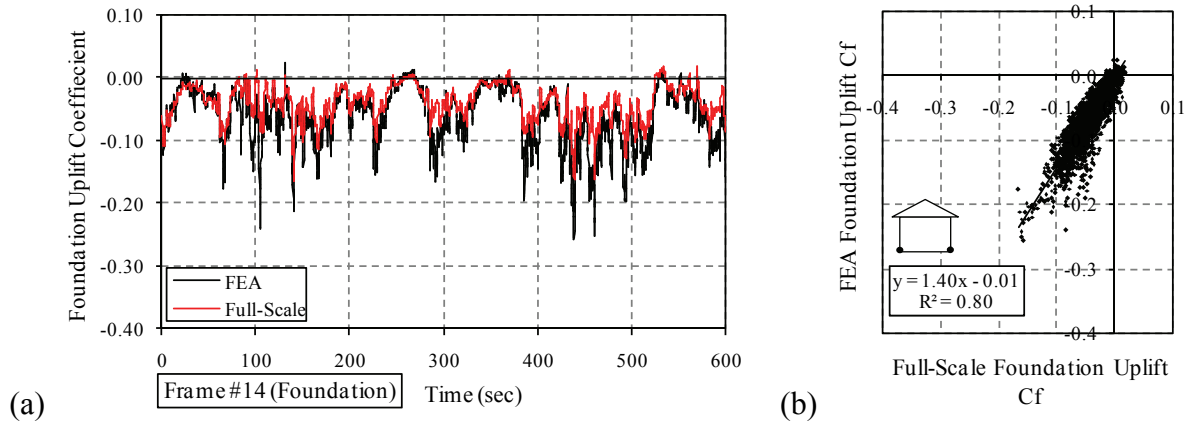

Figure C.14 (a) Frame 14 load cell and finite element foundation uplift forces and (b) scatter plots (FEA: finite element model predictions)).

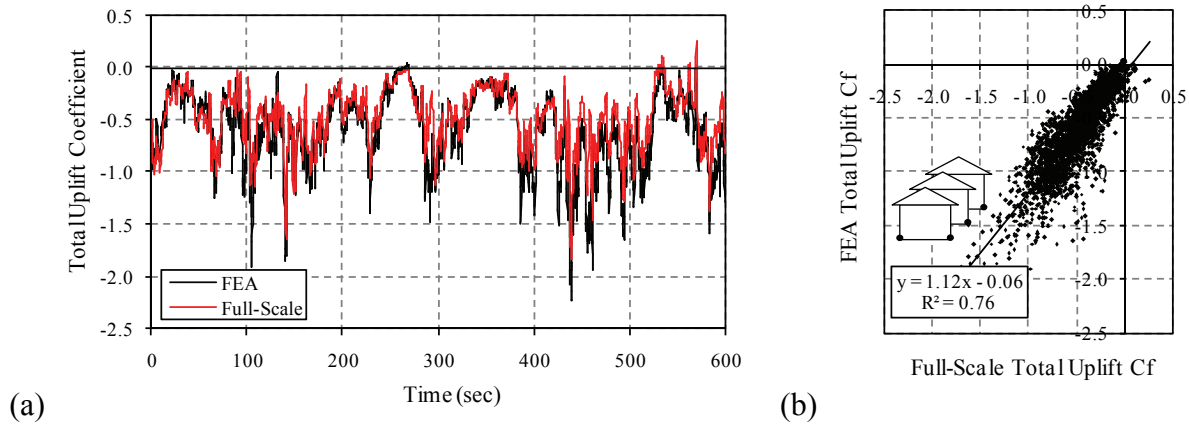

Figure C.15 (a) Load cell and finite element total foundation uplift forces and (b) scatter plots (FEA: finite element model predictions).

C.1.6 Record June 1st, 2009 (ID 109321)

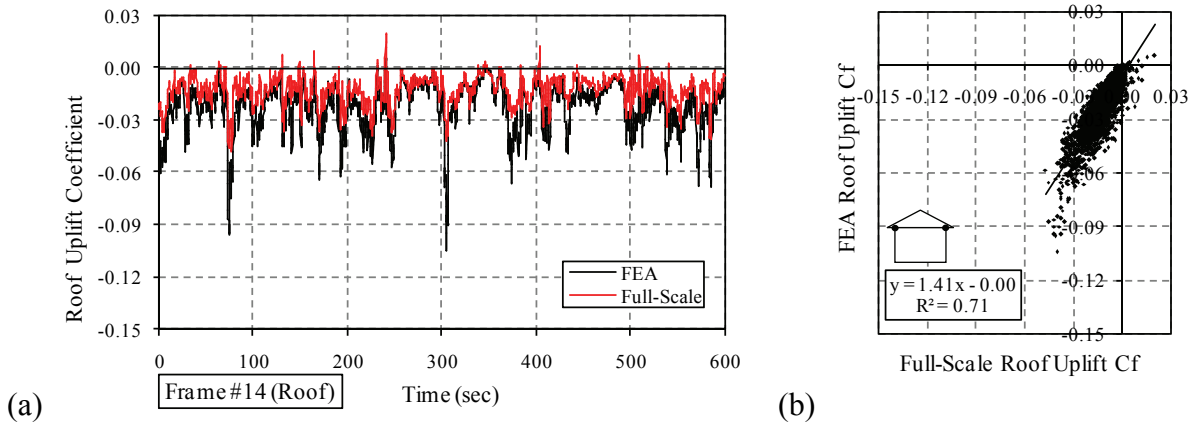

Figure C.16 (a) Frame 14 load cell and finite element roof uplift forces and (b) scatter plots (FEA: finite element model predictions).

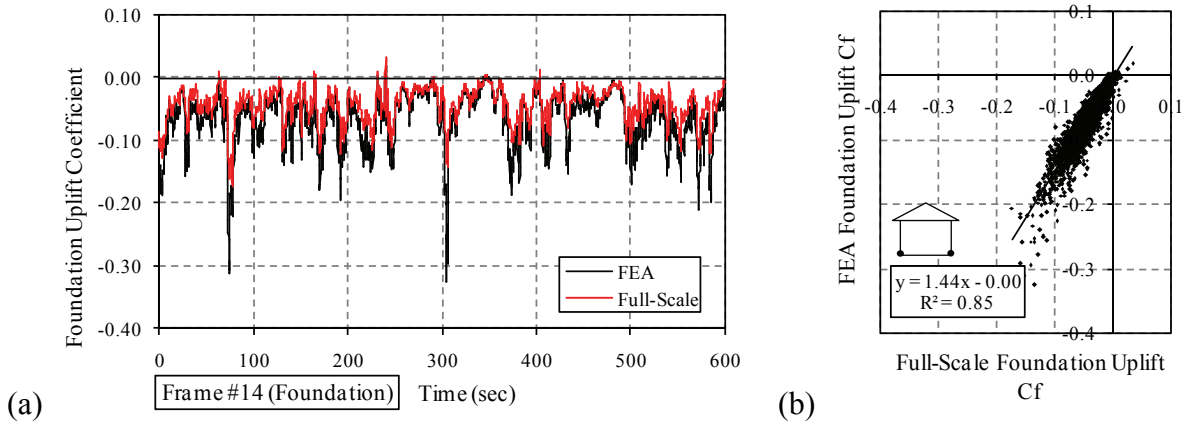

Figure C.17 (a) Frame 14 load cell and finite element foundation uplift forces and (b) scatter plots (FEA: finite element model predictions).

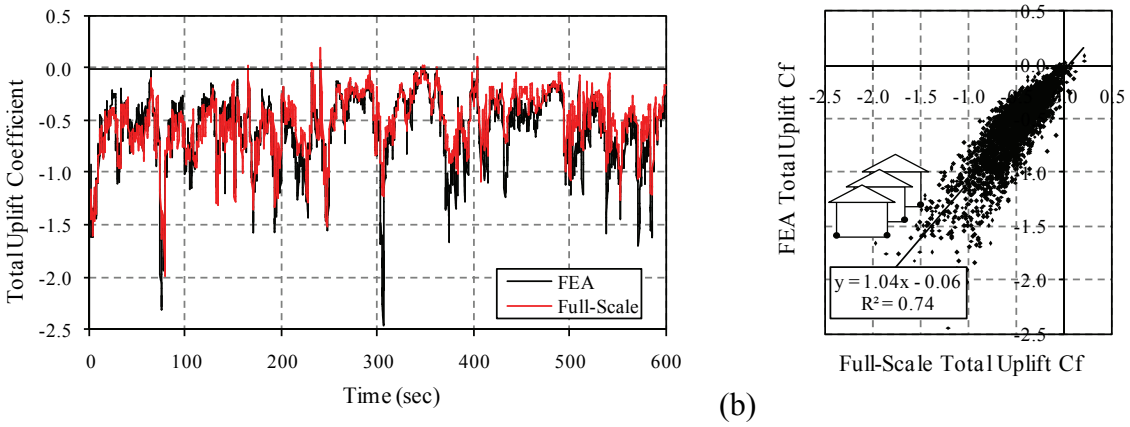

(a) (b)

Figure C.18 (a) Load cell and finite element total foundation uplift forces and (b) scatter plots (FEA: finite element model predictions).

C.1.7 Record June 2nd, 2009

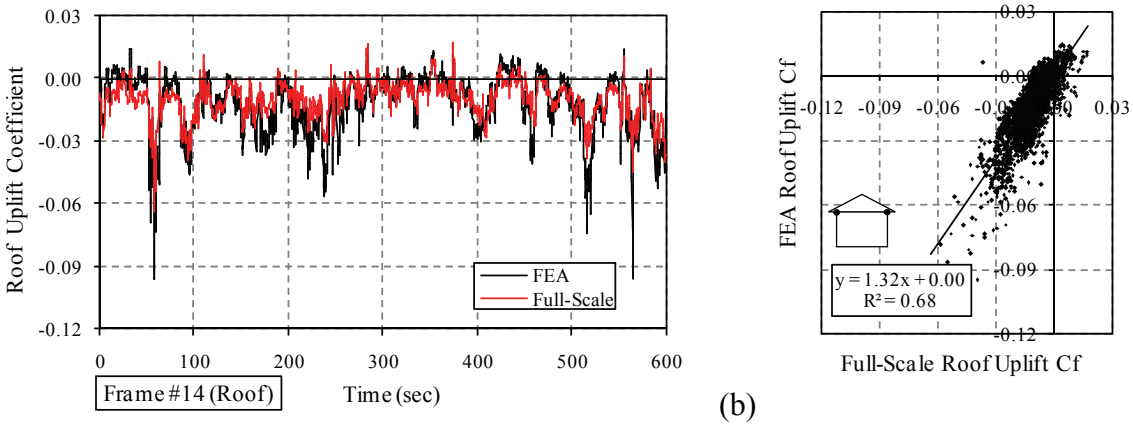

(a) (b)

Figure C.19 (a) Frame 14 load cell and finite element roof uplift forces and (b) scatter plots (FEA: finite element model predictions).

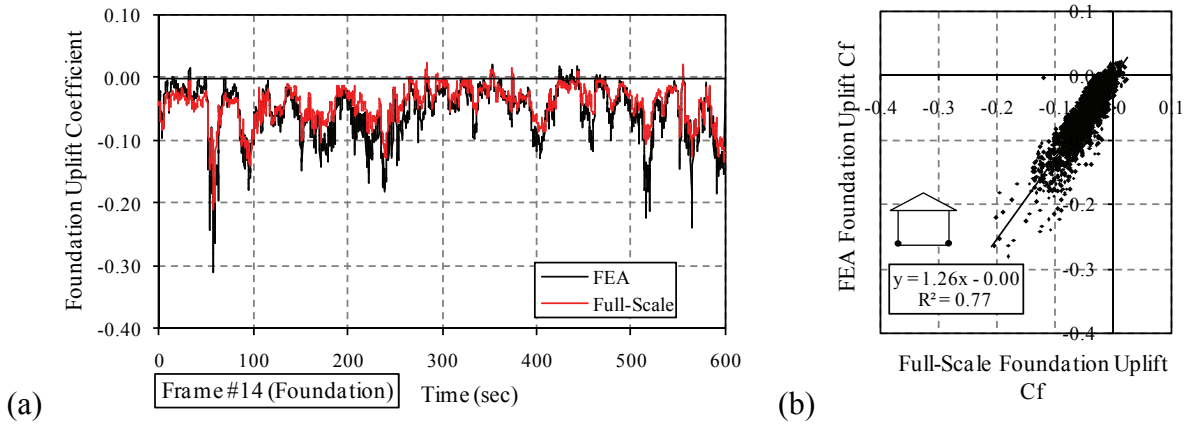

Figure C.20 (a) Frame 14 load cell and finite element foundation uplift forces and (b) scatter plots (FEA: finite element model predictions).

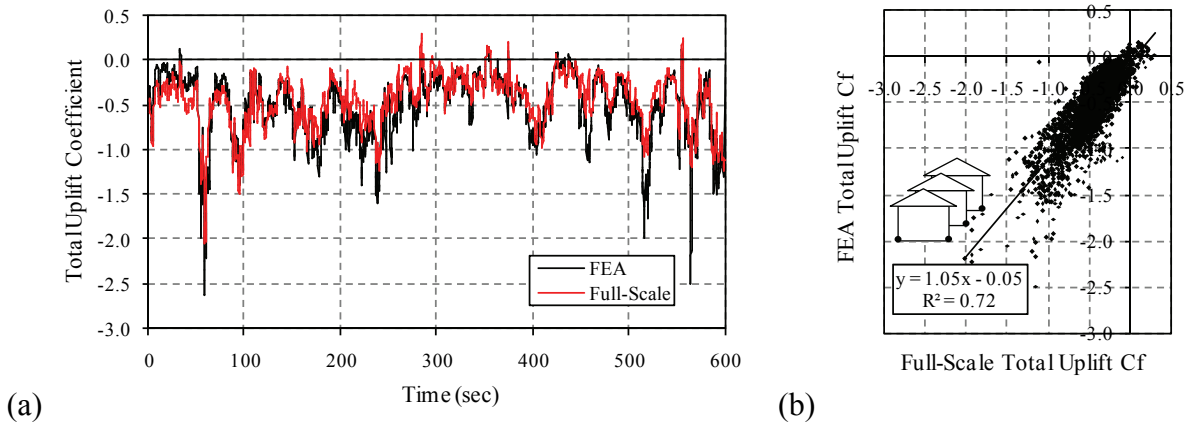

Figure C.21 (a) Load cell and finite element total foundation uplift forces and (b) scatter plots (FEA: finite element model predictions).

C.1.8 Record June 4th, 2009

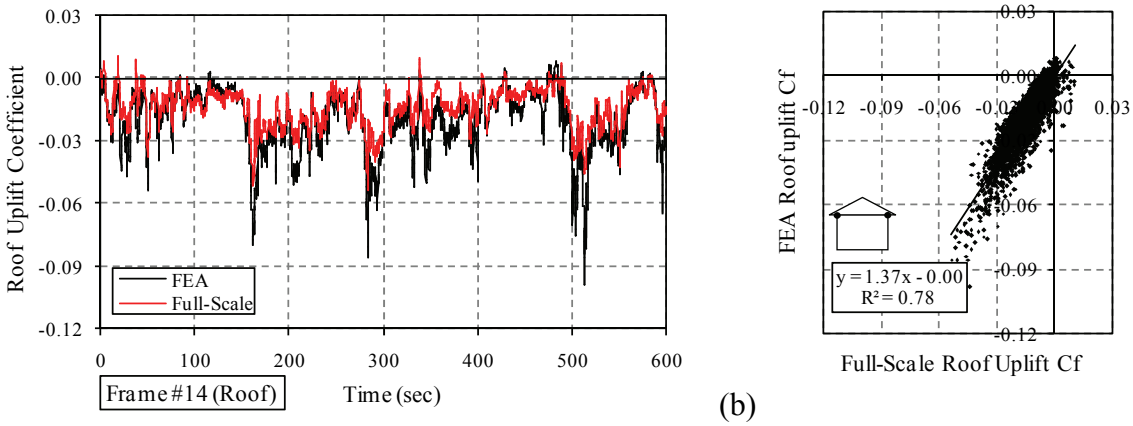

(a) (b)

Figure C.22 (a) Frame 14 load cell and finite element roof uplift forces and (b) scatter plots (FEA: finite element model predictions).

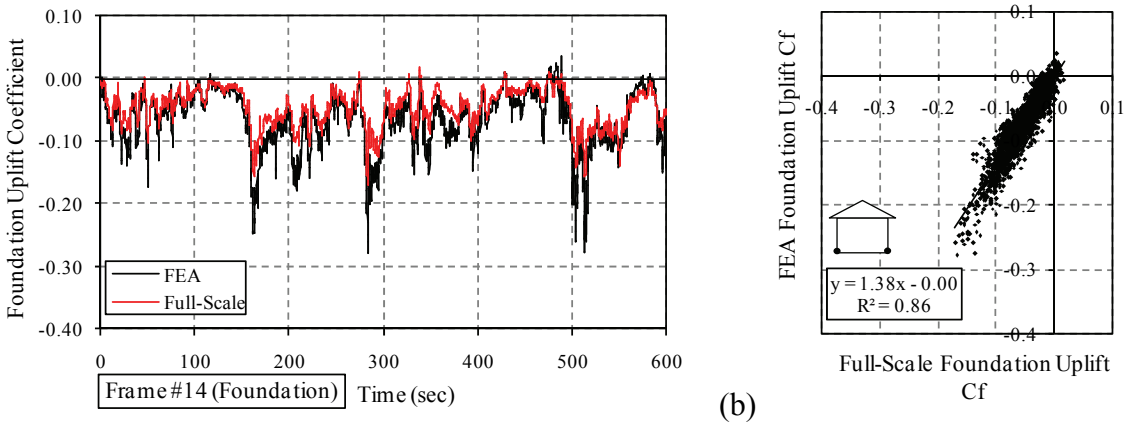

(a) (b)

Figure C.23 (a) Frame 14 load cell and finite element foundation uplift forces and (b) scatter plots (FEA: finite element model predictions).

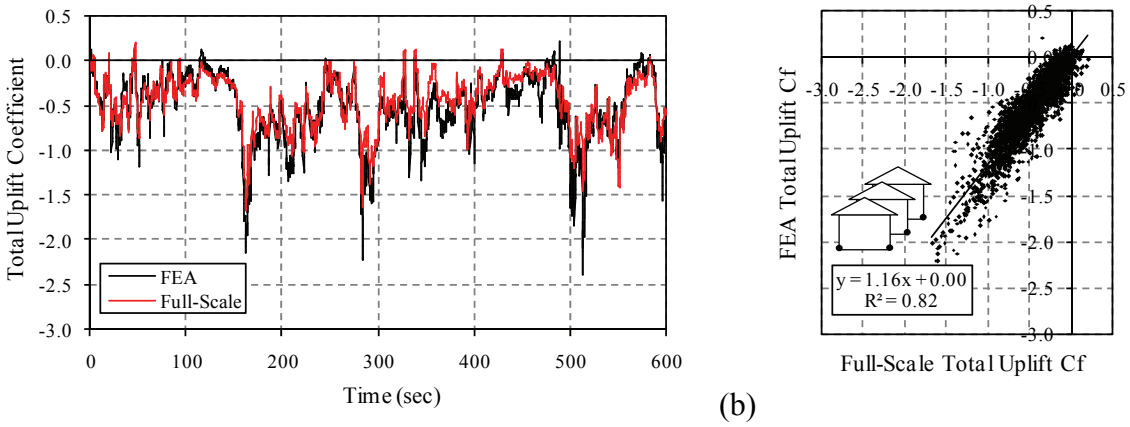

(a) (b)

Figure C.24 (a) Load cell and finite element total foundation uplift forces and (b) scatter plots (FEA: finite element model predictions).

C.1.9 Record June 8th, 2009

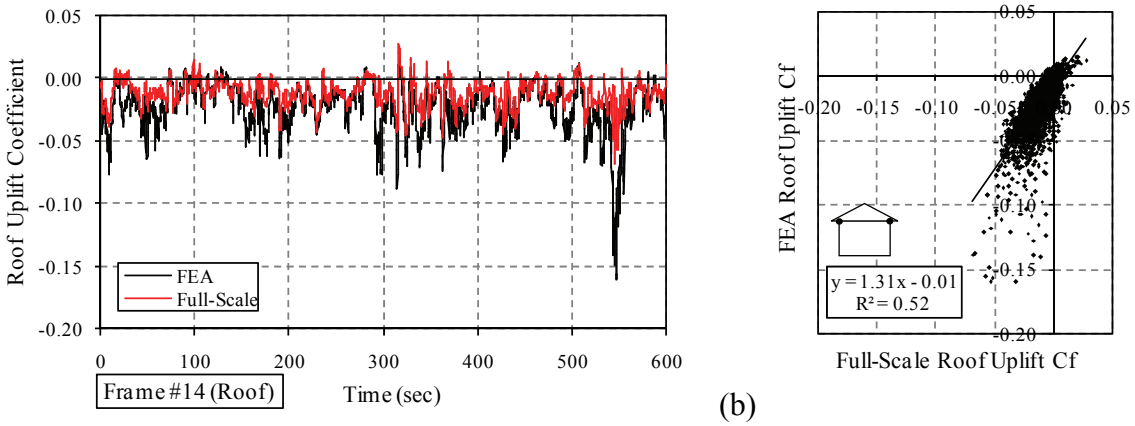

(a) (b)

Figure C.25 (a) Frame 14 load cell and finite element roof uplift forces and (b) scatter plots (FEA: finite element model predictions).

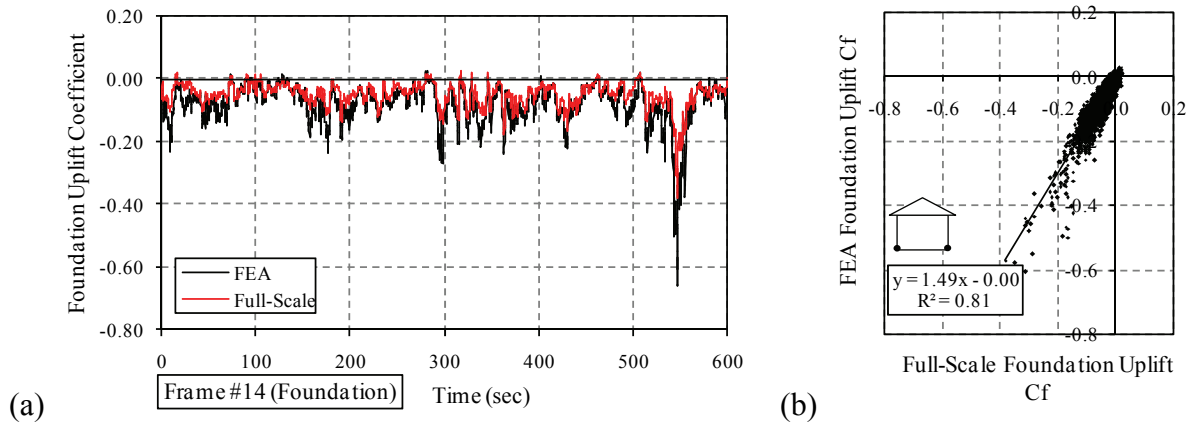

Figure C.26 (a) Frame 14 load cell and finite element foundation uplift forces and (b) scatter plots (FEA: finite element model predictions).

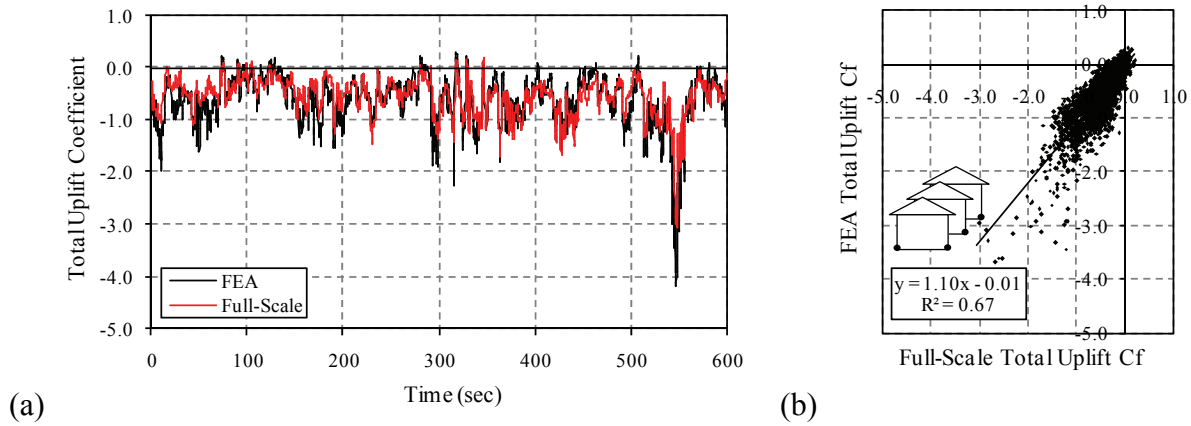

Figure C.27 (a) Load cell and finite element total foundation uplift forces and (b) scatter plots (FEA: finite element model predictions).

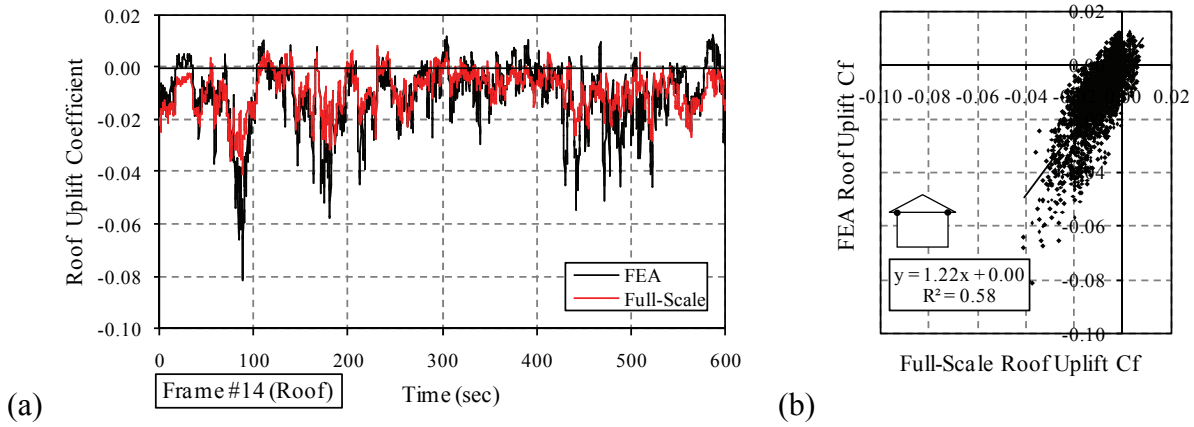

Figure C.28 (a) Frame 14 load cell and finite element roof uplift forces and (b) scatter plots (FEA: finite element model predictions).

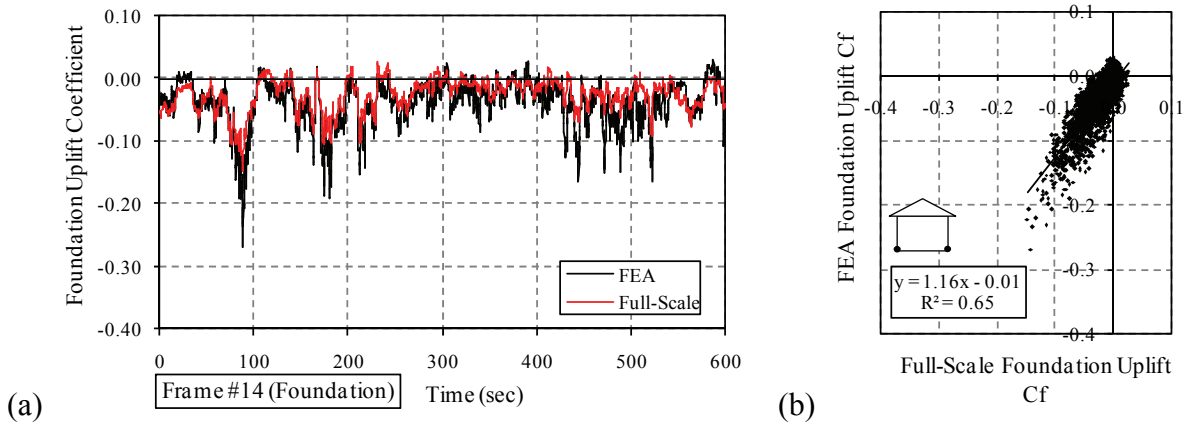

Figure C.29 (a) Frame 14 load cell and finite element foundation uplift forces and (b) scatter plots (FEA: finite element model predictions).

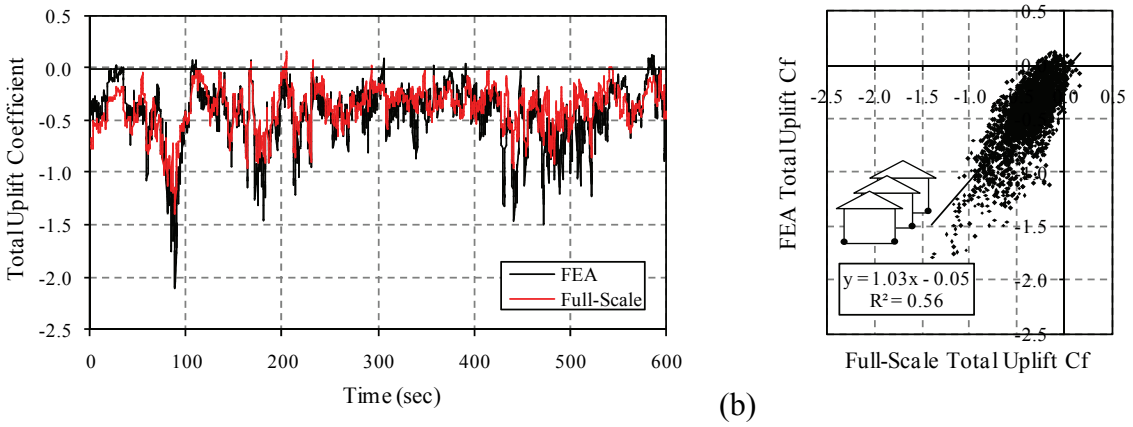

Figure C.30 (a) Load cell and finite element total foundation uplift forces and (b) scatter plots (FEA: finite element model predictions).

C.1.11 Record June 17th, 2009 (ID 102121)

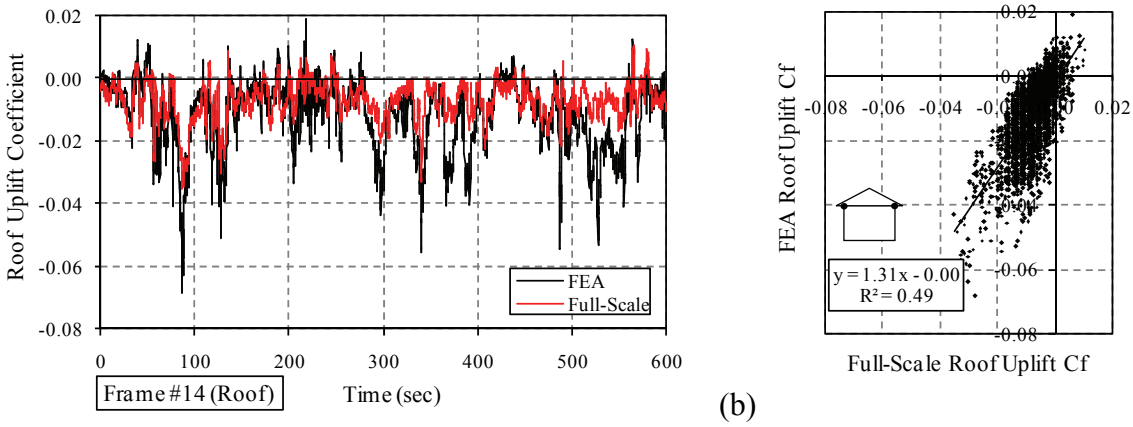

Figure C.31 (a) Frame 14 load cell and finite element roof uplift forces and (b) scatter plots (FEA: finite element model predictions).

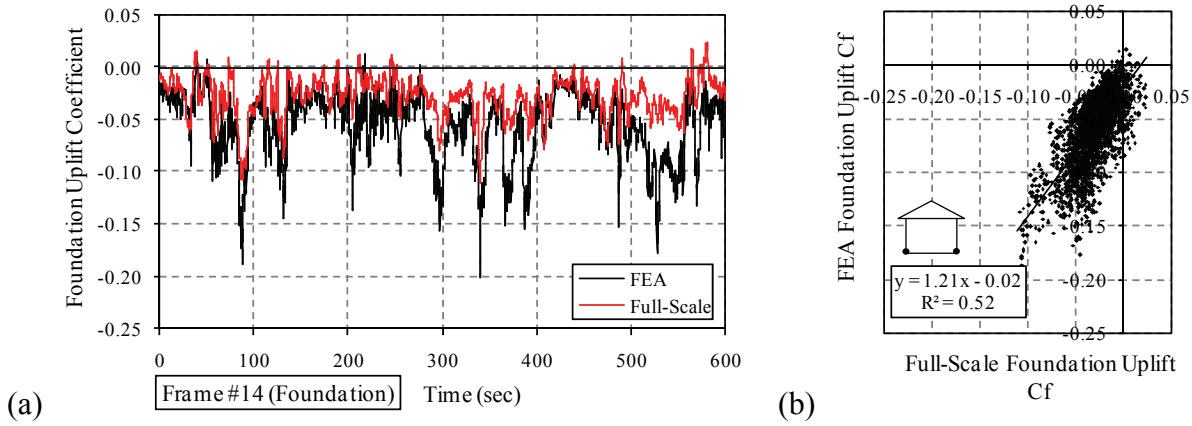

Figure C.32 (a) Frame 14 load cell and finite element foundation uplift forces and (b) scatter plots (FEA: finite element model predictions).

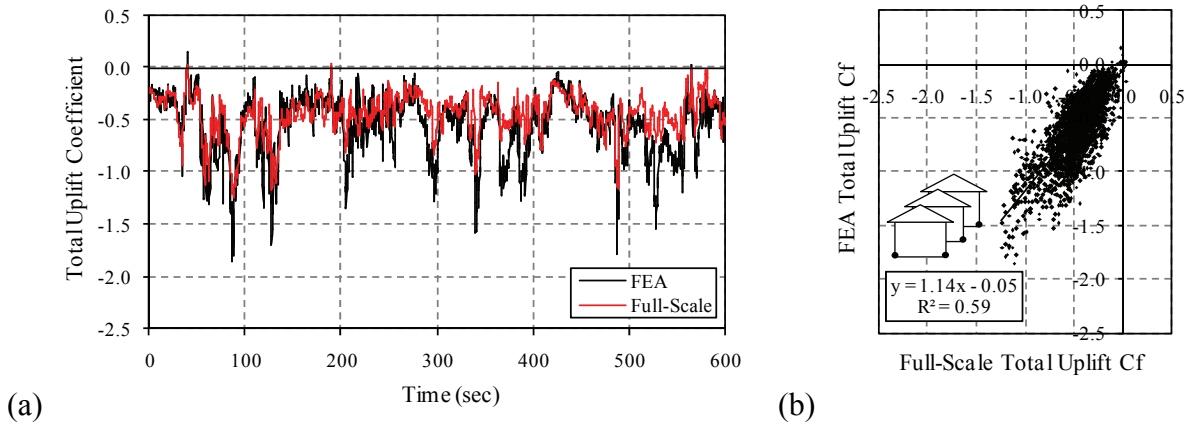

Figure C.33 (a) Load cell and finite element total foundation uplift forces and (b) scatter plots (FEA: finite element model predictions).

C.2 Uplift Force Spectra Comparisons

C.2.1 Record October 29th, 2008

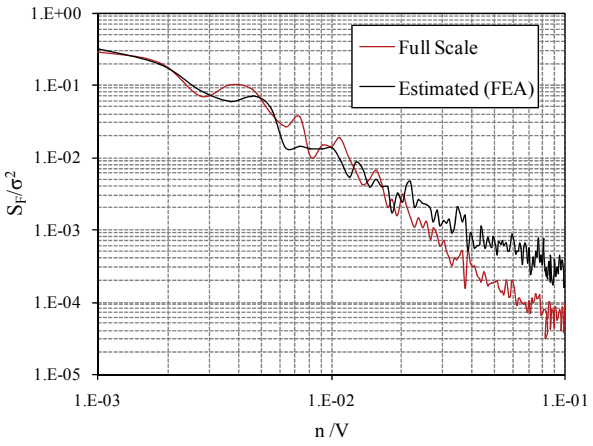

Figure C.34 Field and numerically estimated total uplift force spectra (all foundation load cells).

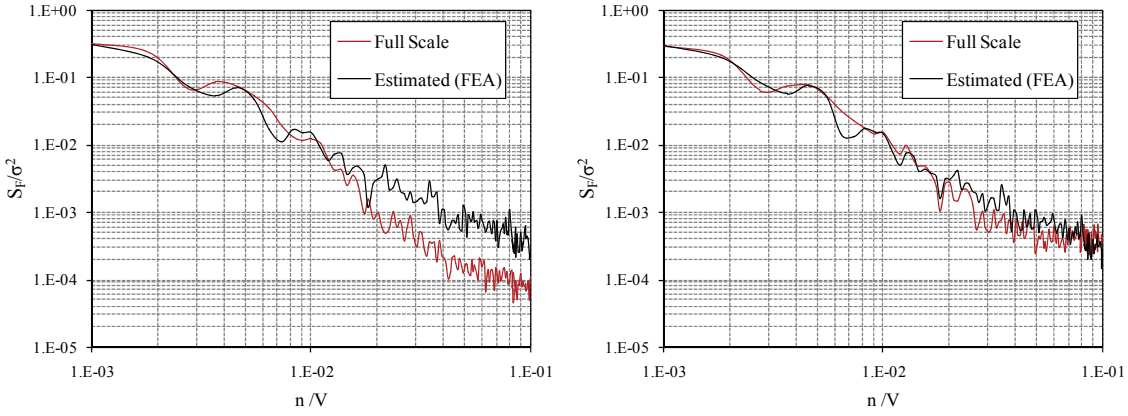

Figure C.35 Field and numerically estimated foundation and roof force spectra at Frame 14 (two foundation and two roof load cells).

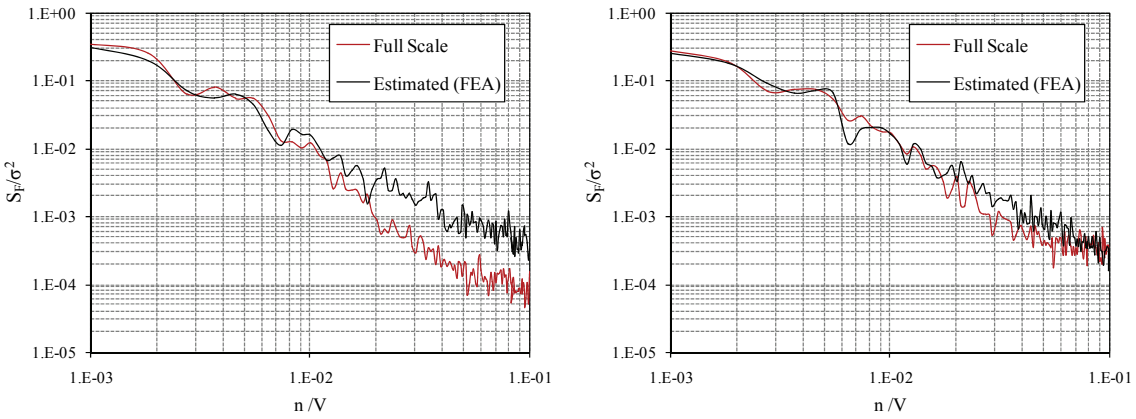

Figure C.36 Field and numerically estimated foundation and roof force spectra at South-East side of Frame 14 (single foundation and roof load cell).

C.2.2 Record May 21st, 2009

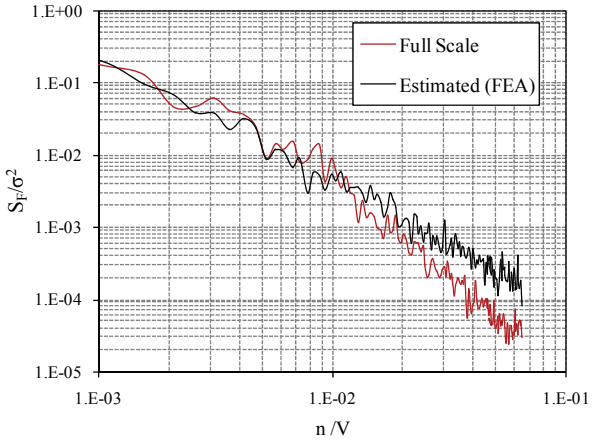

Figure C.37 Field and numerically estimated total uplift force spectra (all foundation load cells).

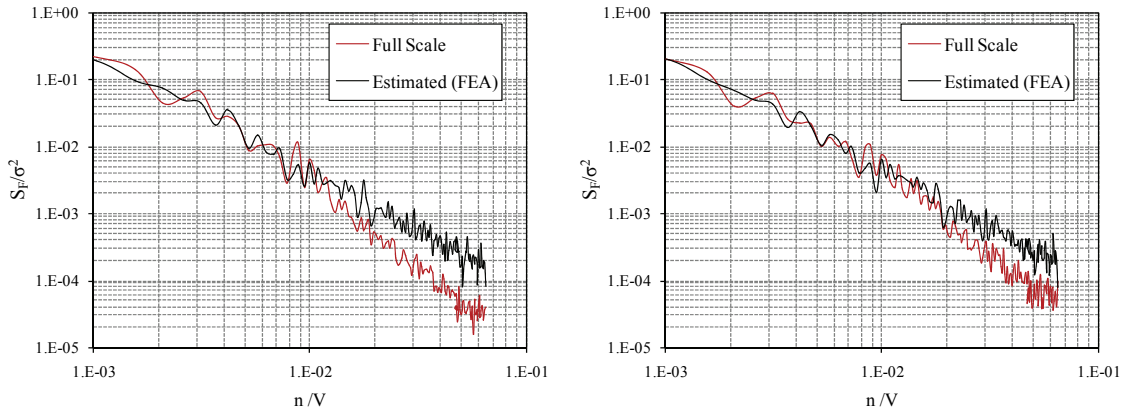

Figure C.38 Field and numerically estimated foundation and roof force spectra at Frame 14 (two foundation and two roof load cells).

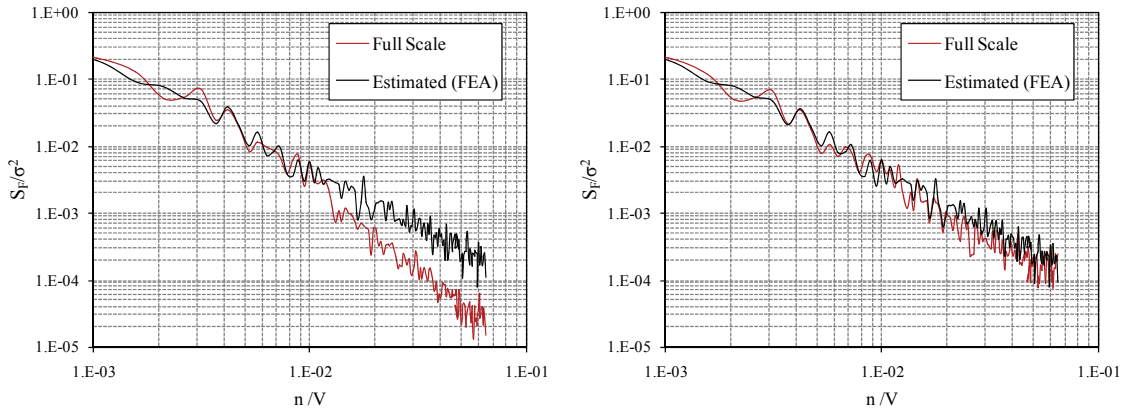

Figure C.39 Field and numerically estimated foundation and roof force spectra at South-East side of Frame 14 (single foundation and roof load cell).

C.2.3 Record May 22nd, 2009

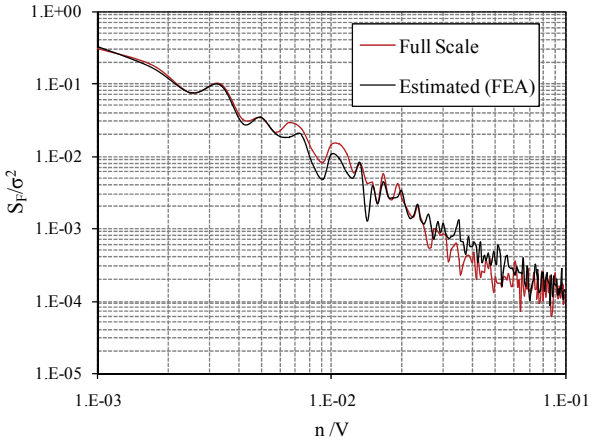

Figure C.40 Field and numerically estimated total uplift force spectra (all foundation load cells).

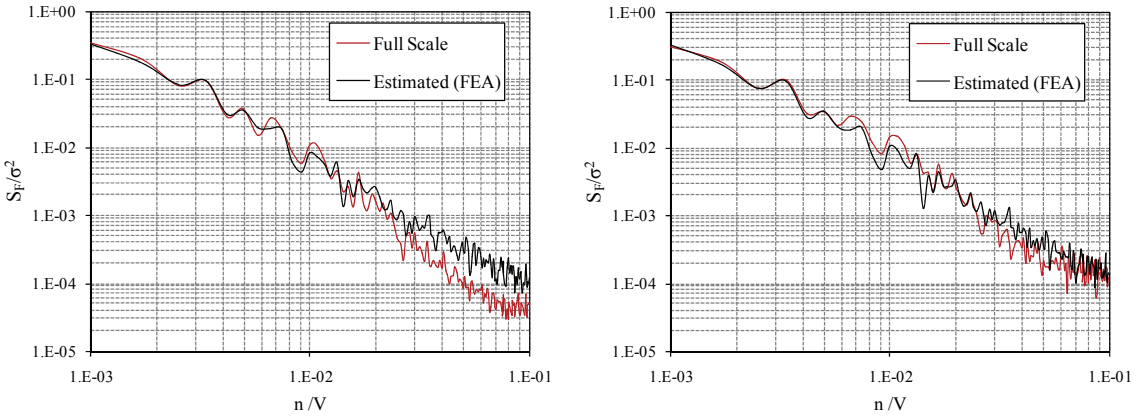

Figure C.41 Field and numerically estimated foundation and roof force spectra at Frame 14 (two foundation and two roof load cells).

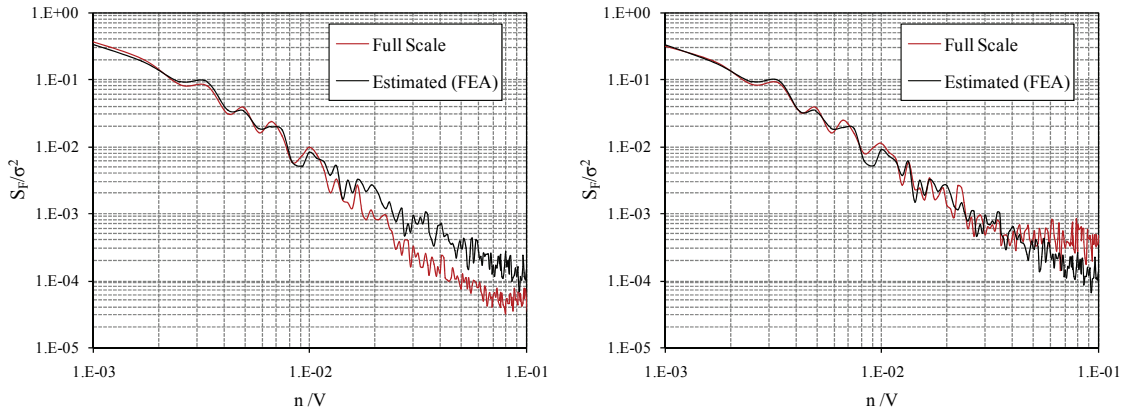

Figure C.42 Field and numerically estimated foundation and roof force spectra at South-East side of Frame 14 (single foundation and roof load cell).

C.2.4 Record June 1st, 2009

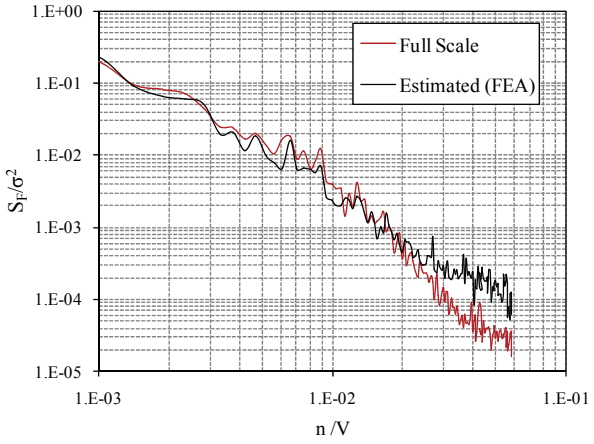

Figure C.43 Field and numerically estimated total uplift force spectra (all foundation load cells).

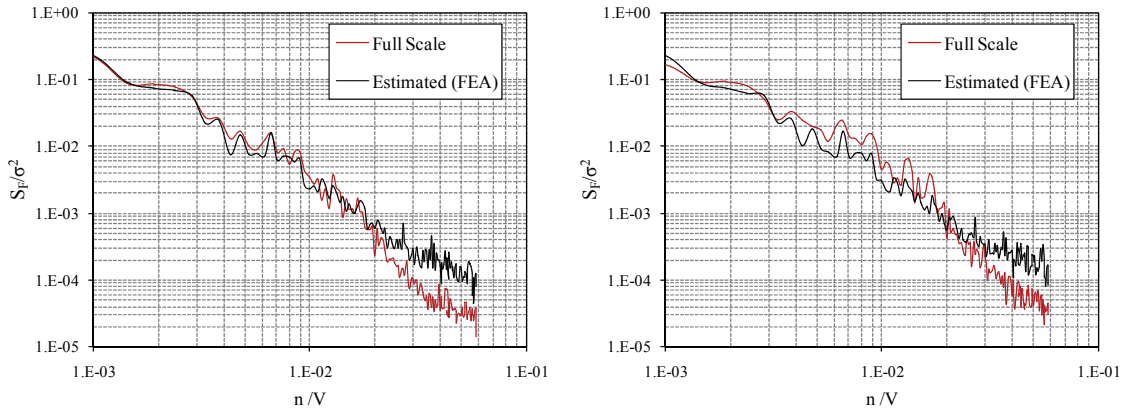

Figure C.44 Field and numerically estimated foundation and roof force spectra at Frame 14 (two foundation and two roof load cells).

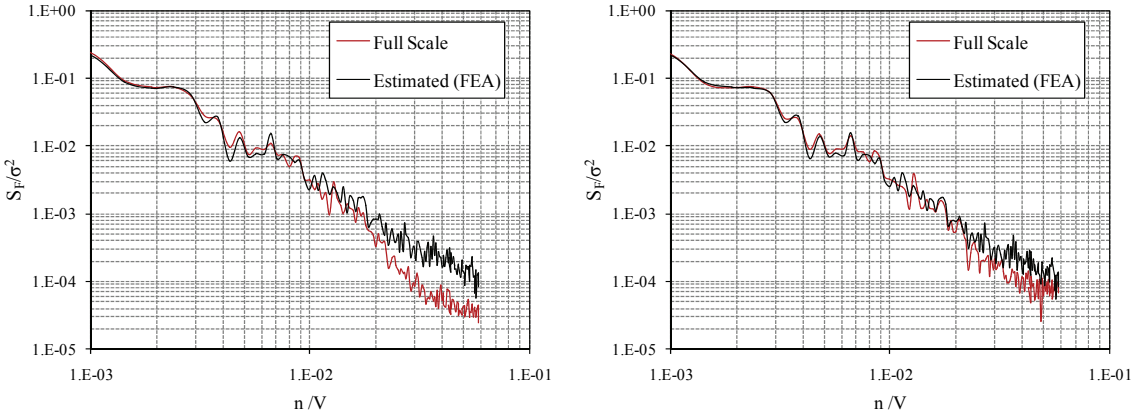

Figure C.45 Field and numerically estimated foundation and roof force spectra at South-East side of Frame 14 (single foundation and roof load cell).

C.2.5 Record June 4th, 2009

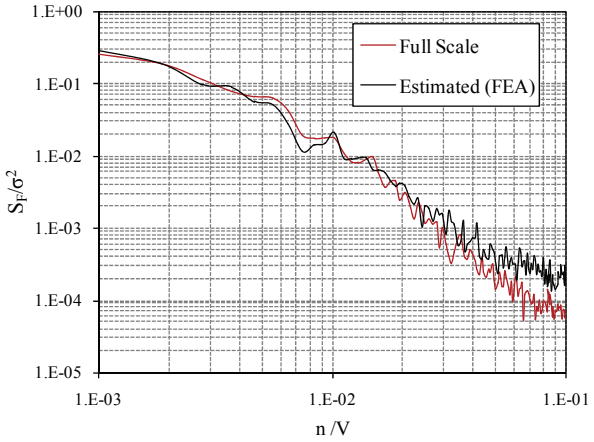

Figure C.46 Field and numerically estimated total uplift force spectra (all foundation load cells).

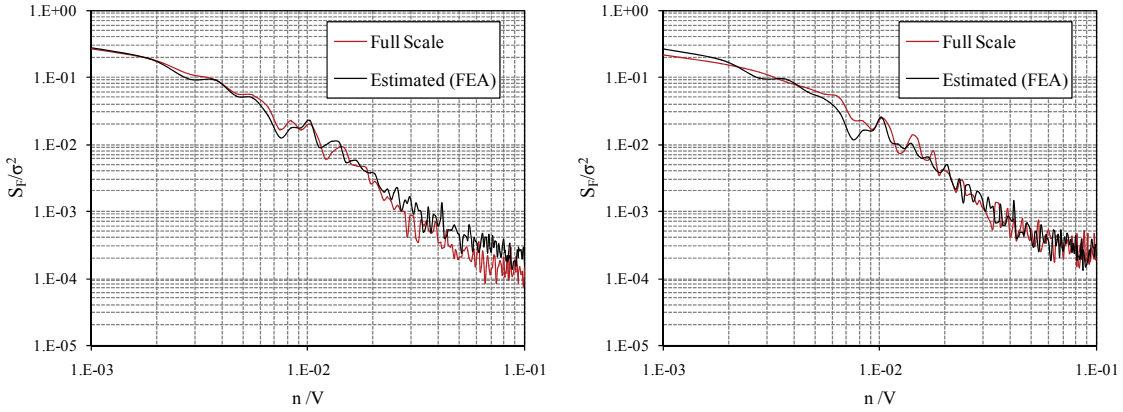

Figure C.47 Field and numerically estimated foundation and roof force spectra at Frame 14 (two foundation and two roof load cells).

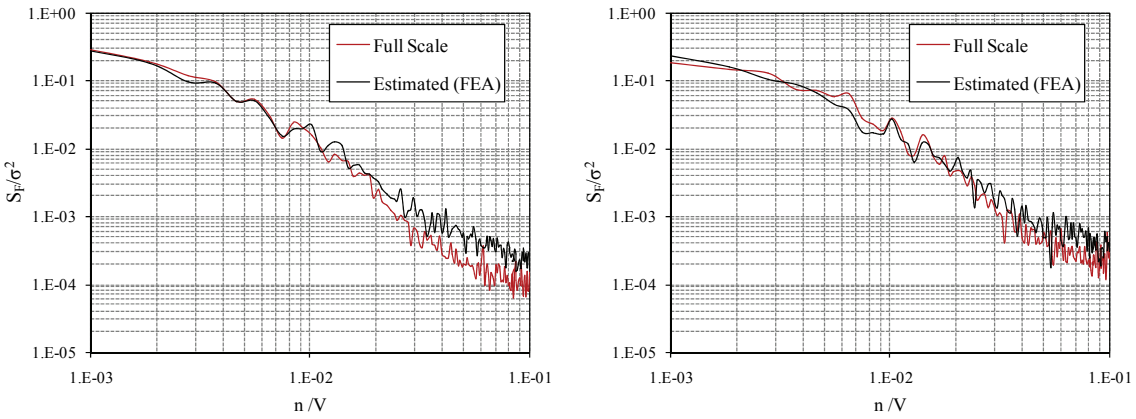

Figure C.48 Field and numerically estimated foundation and roof force spectra at South-East side of Frame 14 (single foundation and roof load cell).

C.2.6 Record June 17th, 2009

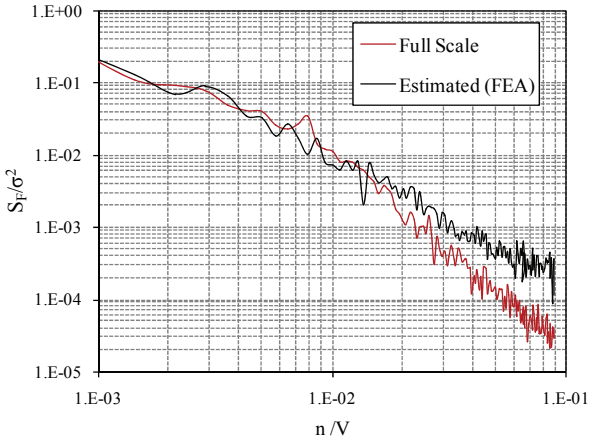

Figure C.49 Field and numerically estimated total uplift force spectra (all foundation load cells).

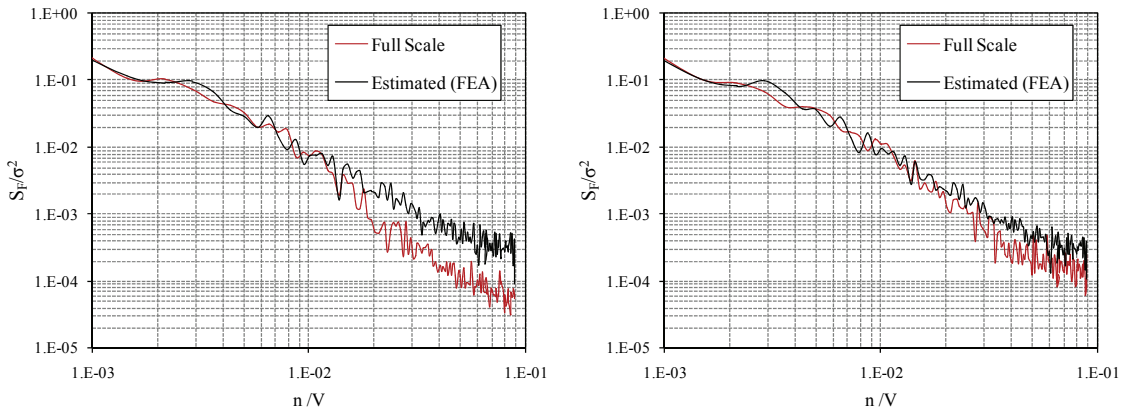

Figure C.50 Field and numerically estimated foundation and roof force spectra at Frame 14 (two foundation and two roof load cells).

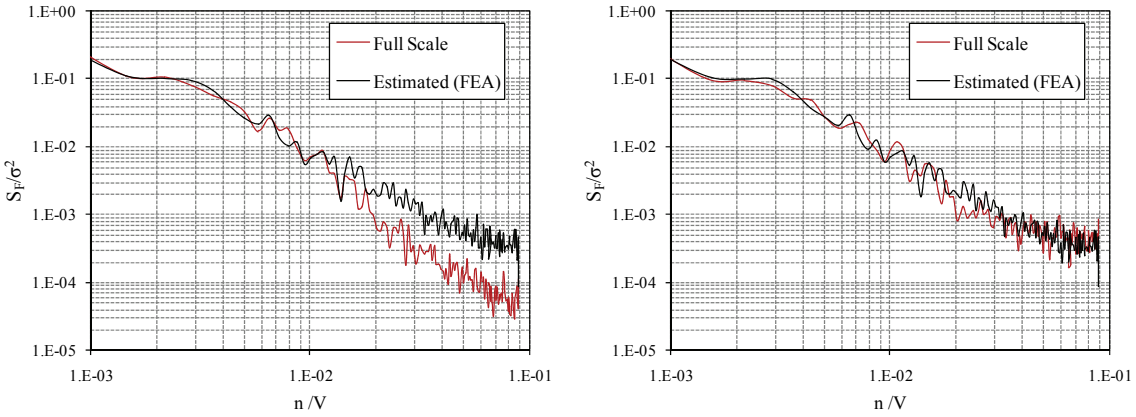

Figure C.51 Field and numerically estimated foundation and roof force spectra at South-East side of Frame 14 (single foundation and roof load cell).